UNIVERSITY OF HONG KONG

Planetary Nebulae in the Galactic Bulge

Author:
Shuyu TAN

Supervisor:
Prof. Quentin PARKER

A thesis submitted in fulfillment of the requirements
for the degree of Master of Philosophy

in the

Department of Physics
Faculty of Science

20 July, 2022

Abstract of thesis entitled

Planetary Nebulae in the Galactic Bulge

Submitted by

Shuyu Tan

for the degree of Master of Philosophy

at The University of Hong Kong

in July, 2022

Planetary Nebulae (PNe) are gaseous layers and dust shrouding dying stars with low- and intermediate-masses, showing predominant emission lines. With the advancement of wide-field and high-precision telescopes, for example, the *HST* and the ESO VLT, both high-resolution images and long-slit spectra became available for a growing sample of PNe. This allows an improvement in our understanding of both the formation of PNe, including the evolutionary history, mass-loss physics, and chemical abundances of their progenitors, furthermore, to analyse the chemical environment in which their progenitors were born. This may give powerful insights into the chemical evolution of the galaxy they reside. The main purpose of this project is to make full use of the observation of 138 PNe in the Galactic bulge from the 8.2m ESO VLT. This set of observational data is comprised of high-resolution images and long-slit spectroscopic observations covering a wavelength range from 3660 to 8450 Å.

With the imaging data, the morphologies, position angles, as well as central star visibilities of PNe in the sample, were investigated in combination with the *HST* observations where available. The excellent resolving power of the VLT reveals many never-seen-before morphological features and central stars of PNe in previous studies.

With the long-slit spectroscopic observations, the chemical abundances of PNe in this sample were derived after a careful data reduction. The oxygen abundance was then used as a metallicity indicator of the central stars of PNe to trace the chemical evolution in the Galactic bulge. An analysis of PN spatial distribution, oxygen abundance gradient and abundance distribution function was carried out. Combining with the previous studies on different stellar populations in the bulge, these results add pieces of evidence to the origin of the bulge as a pseudo-bulge formed through disk instabilities in the inner thin disk. Besides, weak optical recombination lines were also detected in the spectroscopic observations which allow a determination of the abundance discrepancy in these objects. Different nebular and central star properties were investigated to find possible links to the abundance discrepancy in these objects. Our results confirm the relationship between abundance discrepancy factors (ADFs) and central star binarity, chemical abundances as well as electron densities noticed in previous studies.

(373 words)

Planetary Nebulae in the Galactic Bulge

by

Shuyu TAN

B.Sc. Physics *Imperial College London*

A Thesis Submitted in Partial Fulfilment
of the Requirements for the Degree of
Master of Philosophy

at

University of Hong Kong
July, 2022

Declaration

I, Shuyu TAN, declare that this thesis titled, "Planetary Nebulae in the Galactic Bulge", which is submitted in fulfillment of the requirements for the Degree of Master of Philosophy, represents my own work except where due acknowledgment have been made. I further declared that it has not been previously included in a thesis, dissertation, or report submitted to this University or to any other institution for a degree, diploma or other qualifications.

Signed: _Shuyu Tan_

Date: July 20, 2022

Acknowledgements

I would like to give a warm thank you to my MPhil supervisor, Prof. Quentin Parker. Being a student of yours is the biggest surprise in my life so far. I appreciate your continuous guidance and encouragement throughout my study. Thanks for your support in the past two years.

Thanks to all the 'resident' members at the Laboratory of Space Research, HKU, it is my luck to work in this supportive and comfortable environment. Thanks for having me for these two years. I would also give a special thank you to my friend, Yuna. I appreciate your listening and understanding since we know each other. I know myself better as I know you.

Last but not the least, I would thank all PIs for conducting the ESO VLT/FORS2 observations in Chile giving this excellent set of data that I used for my MPhil study.

This thesis includes observations made with the ESO Very Large Telescope. This thesis also makes use of the HASH PN Database.

This thesis was typeset using LaTeX.

Shuyu Tan
University of Hong Kong
July 20, 2022

Contents

List of Figures

List of Tables

Chapter 1

Introduction

1.1   Planetary nebulae as a stage of stellar evolution

For low- to intermediate-mass stars ($M_\star < 8M_\odot$), unlike their high mass counterparts, the temperatures and pressures within them could never be high enough to induce carbon burning at their centres. They pass through a phase of the asymptotic giant branch (AGB) when its core is exhausted of helium, subsequently, stars shed their outer layers and become a planetary nebula (PN) which is the second last stage of their evolution. The central stars then evolve towards the white dwarf cooling sequence before they ultimately turn into, theoretically, a black dwarf.

Fig. 1.1 shows an example evolutionary track of a low-mass star on the Hertzsprung-Russell (HR) diagram. Once a proto-star ignites the hydrogen fusion in its core, it becomes a zero-age main-sequence star (ZAMS). Its MS life lasts as long as the process of fusing hydrogen into helium continues, which would take up most of its life. The track on the HR diagram goes from lower left to upper right on the MS phase as the star is getting cooler and brighter. The length of the MS lifetime depends on both its mass and luminosity, which determines the amount of fuel available for nuclear fusion and the rate of fuel consumption respectively. The mass-luminosity relation in MS stars was found as

$$L \propto M^\eta$$

in which η usually takes 3.5 (Kippenhahn & Weigert 1990). An approximate estimation of MS lifetime, τ_{MS}, could be given by

$$\tau_{MS} \propto \frac{M}{L} \propto M^{1-\eta} = M^{-2.5}$$

which is inversely proportional to the mass of the star.

When the nuclear burning happens, the centres of the MS stars exert radiation pressure outwards and this is balanced by gravitational contraction. The differences in stellar masses would, therefore, lead to different core temperatures, and as a result, different nuclear reactions under such a hydrostatic equilibrium. Stars with masses less than or around $1M_\odot$ would mainly undergo proton-proton (PP) chain in which 4 protons are combined to form a single ^{4}He under their lower core temperatures. For more massive stars ($> 1.3M_\odot$) that have a higher core temperature, the
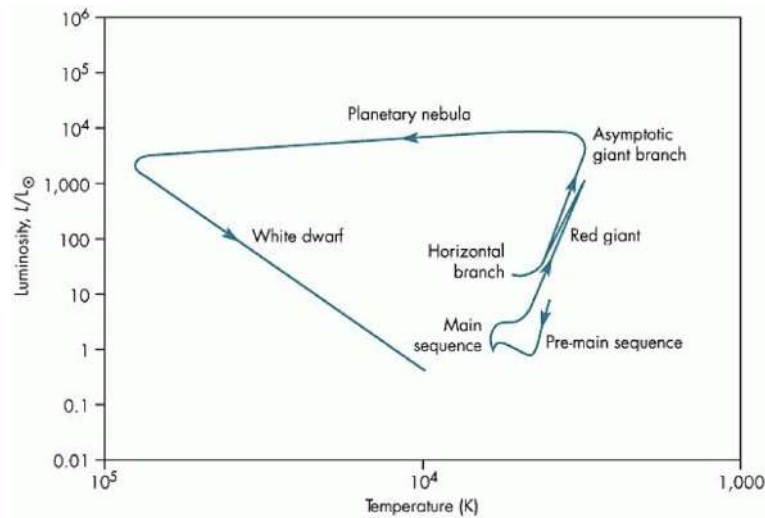
Figure 1.1: The evolution of the Sun on the Hertzsprung-Russell diagram. Image accessed from `http://www.exo.net/~pauld/workshops/Stars/HR$%$20Diagram.pdf` on 13/07/2022.

carbon-nitrogen-oxygen (CNO) cycle will dominate (Nishiyama 2018). In a CNO cycle, carbon behaves like a catalyst for the hydrogen burning into helium processes.

When an MS star runs out of hydrogen in its core, the helium core starts to collapse due to gravity, accompanied by an increase in temperature. The star ascends to the red giant branch (RGB) phase when the core is hot enough to induce the hydrogen burning in the surrounding envelope. Then, for stars with masses less than 1.3 $M_\odot$, the helium ash from the shell of fusing hydrogen falls onto the core and increases the core density. The core finally becomes degenerated from which its volume plateaus as the temperature continues increasing. It was not until the core is as hot as 10^8 K the triple-alpha process commences, in which transformation of $_2^4$He into carbon $_6^{12}$C happens. The rate of helium burning is rapid as well as the temperature increase because of the absence of a pressure change. This is the so-called the helium flash. The lifting of electron degeneracy happens when the helium core is hot enough. Low mass stars then maintain a stable helium burning. For intermediate-mass stars ($1.3M_\odot < M < 8M_\odot$), there will be a deep convective outer envelope, and the helium burning happens slower, creating a carbon-oxygen core.

Then, for both low- and intermediate-mass stars, they climb up to the AGB phase once the cores are exhausted of helium. The core is only left with carbon and oxygen while helium and hydrogen burning continue in concentric shells surrounding the C-O core as shown in Fig. 1.2. The He-burning shell is thermally unstable and produces periodic thermal pulses which create a convective zone in the He-burning shell. The convective zone facilitates the mixture of He-burning shell products and transportation to the bottom of the H-burning shell and causes further nucleosynthesis processes. When the thermal pulses go out, the convective zone penetrates deeply into the star and eventually, brings carbon to the surface of the star.
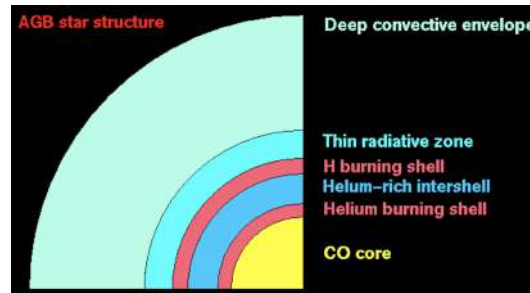
Figure 1.2: The schematic structure of an AGB star. Image accessed from: `https://sparky.rice.edu/astr350/stellar_evolution/m5z02evoln.html` on 13/07/2022.

At the same time, pulsations in an AGB star drive a rapid mass loss and finally stripe off most of its gaseous envelope throughout for 10^4-10^5 years (van Winckel 2003, Paczynski 1971). The ejecting envelope is referred to as a planetary nebula. The expanding nebula that moving away at a typical velocity of $20\,\mathrm{kms^{-1}}$ fades and finally becomes a part of the interstellar medium (Wesson et al. 2008).

1.2 The Morphologies of Planetary Nebulae

Planetary nebulae are observed in various shapes, e.g. elliptical, bipolar (butterfly), round, etc. The diversity in their morphologies indicates that the dynamical processes, such as ejection, collimation, and for certain microscopic structures, precession, during the PN formation are complicated (Kwok 2000, Cliffe et al. 1995, Shaw 2011). The shaping mechanisms of PNe are still not well-understood. Different morphological features have been long attributed to the interacting stellar winds (ISW) in which a fast wind escaping from the central star compresses and collides with the previously ejected envelope from the AGB progenitor (Kwok et al. 1978, Marigo et al. 2001). Other than that, two more factors are also considered to have significant influences on the formation of PNe and are competing to explain the initial asymmetry. One is the binary central star, which is present in numerous PNe in observations (e.g. Jones & Boffin 2017, Chornay et al. 2020). The other is the magnetic field around the central star of the PN (e.g. García-Segura et al. 2018, Balick & Adam 2002).

1.2.1 Interacting Stellar Winds

The ISW model was first introduced in the work of Kwok et al. (1978), in which a fast, collimated wind ejected during the post-AGB stage and before entering the PN phase was proposed. The line-driven stellar wind from the hot central star, expanding at a velocity around $1000\,\mathrm{kms^{-1}}$, accelerates and impacts the heavy remnant of the AGB circumstellar envelope moving at about $10\,\mathrm{kms^{-1}}$ (Kwok et al. 1978). The swept-up AGB materials then become ionized, resulting in the bright rims of the PN (Fig. 1.3). The generalised ISW (GISW) model was used to explain the observed aspherical, e.g. the bilobed PNe, morphologies of PN in Balick (1978) and Icke (1988), in which the slow AGB winds could have a pole-to-equator density contrast and the aspherical morphology is formed because of shocks generated from "inertial confinement"
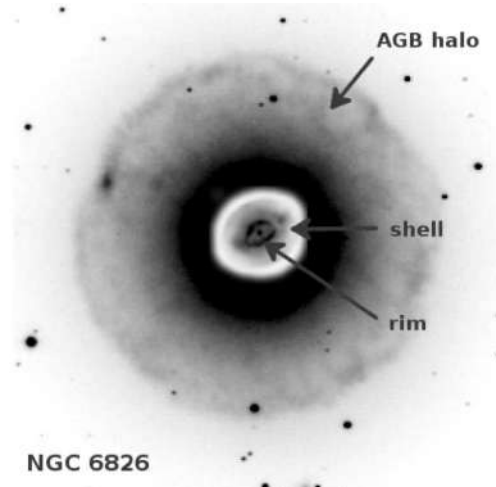
Figure 1.3: [O III] images of the planetary nebula NGC 6826 The rim and shell features are labelled on the image. The nebula is expanding into the outer large and slow-expanding spherical halo consisting of ionised AGB-wind materials (Fig.1 in Schönberner et al. 2014).

during the collision between a spherical fast wind and the aspherical slow wind.(Frank et al. 2018)

A synthetic model was presented in Marigo et al. (2001) which combines the AGB super-wind, wherein the central stars eject $20-80\%$ of their mass which terminates the high luminosity AGB, and prescriptions for different phases in the stellar evolution including the dynamics in the primary shell and surrounding ejecta, the photoionisation of H and He by the central star and a few nebular line emissions. It reproduced certain general properties of PNe including shell thickness and electron densities and showed consistency with the observations of two PNe. A recent stellar wind model by Krtivcka et al. (2020) focused on predicting the wind structure parameters including the rates of mass-loss, wind terminal velocities and emerging nebular fluxes and they investigated the influences of metallicity and wind clumping. They noticed a bistability jump at around 20 kK at which mass-loss rate decreases which could explain additional shell structures in PNe. Although the simulation results are promising, the challenge in the ISW models is to explain the origin of the equatorial overdensities. In addition, as a myriad of new PN morphological features were revealed in high-resolution observations, more physical processes are expected to be included, e.g. the heat transfer through convection. This brings extra challenges to the GISW models.

1.2.2 Binary Central Stars

A fraction of low- and intermediate-mass stars are observed as in binary systems and more are revealed in the data coming from recent high-resolution observing surveys (e.g. Jacoby et al.2021, Chornay et al. 2021). Thus, the model assuming a single star would be insufficient to understand and explain all properties observed in PNe. For close binaries (binary stars with a separation of a few AU or less), theoretical studies in Marco 2009 predicted that a PN could be formed during a common-envelope (CE) evolution. During this stage, the progenitor of the PN engulfs its companion, which exhibits a clear route to an aspherical bipolar shape (Ivanova et al.

2013, Jones et al. 2017). A full CE evolution simulation performed by Frank et al. (2018) shows that the CE evolution ejecta could have strongly aspherical features and the bipolar structures obtained in the generalised ISW models could also be reproduced.

There are two major limitations in the CE evolution hypothesis. One is that the computation time restricts the spatial resolution, and thereby, the inner part materials could not be taken into consideration to probe e.g. the formation of the waist of bipolar PNe (García-Segura et al. 2018). The other is that, for binaries with wider separation in which the CE is absent, they would either follow a similar evolutionary track as a single star or be affected by gravitational interactions with its companion star. These processes have not yet been studied in detail, however, the morphologies of their PN matched the bipolar or ringed PN shapes because of strong binary-induced shaping (Tyndall et al. 2013). The binary interaction is promising in explaining the aspherical slow wind, but more observational and theoretical attempts are required to add constraints on the binary system configurations, reveal more structural details and better understand the influence of the companion stars.

1.2.3   Magnetic Fields

Magnetic fields have been found in oxygen-rich AGB, post-AGB stars and central stars of PNe through either maser polarization observations or spectropolarimetry (Vlemmings 2013, Jordan 2005). 3D magnetohydrodynamic simulations in García-Segura & Guillermo (1997) shows that magnetic collimation of fast wind from the central post-AGB star could create jets and ansae as a result of magnetic tension caused by the magnetized winds. Moreover, in a wide binary system, the magnetic collimation around a precessing star could lead to rotating jets and point-symmetry features. A 2D simulation of the interaction between magnetised winds and a 2D envelope drawn from a 3D CE phase model shows that the magnetic field strength of red giant stars is enough to cause disk winds after a CE event and the disk could store kinetic energy as high as the observed protoplanetary nebula outflows (García-Segura et al. 2020). Magnetised winds behaved as 'tapered' regardless of the type of wind source.

The possibility of forming a bipolar PN from a single star under the effects of star rotation of magnetic torques was tested in García-Segura et al. (2014). A rotating single star was not able to account for an envelope rotating fast enough to form a bipolar PN as the angular momentum of the star was largely removed during AGB or the later phase, therefore, the magnetic braking effect cannot speed up the envelope rotation in effect. The magnetic field is, therefore, less likely to be the main shaping mechanism in single stars. Apart from this, although all current models could produce a jet-like axial flow, the detailed features vary (Balick et al. 2020). More high-resolution observations are required to constrain the mass-loss process, the bipolar outflow formation processes as well as the influence of the external field.

In conclusion, the ISW was the dominant explanation for different morphologies observed in PNe, but as it assumes an aspherical slow wind which cannot be well-explained, the alternating PN shaping mechanisms emerged. The binarity of the central star of PNe is promising

in understanding the aspherical features observed in PNe as the CE evolution could naturally possess aspherical features. Furthermore, the binary central stars combing the magnetic fields around the central stars of PNe could explain the observed fast protoplanetary nebula outflow. However, more observation from the advanced telescope and surveys is expected to help to better constrain these mechanisms as well as better understand the formation of PNe from a single star.

From an observational aspect, the interpretation of PN morphologies largely depends on the morphological classification. The first morphological study was carried out by Curtis in 1918 based on the photographic observations of 78 PNe. He divided the observed morphological features into helical, annular, disk-shaped, amorphous and star-like groups. The classification scheme was improved and modified in a number of following studies in Westerlund and Henize (1967), Greig (1971), Stanghellini et al. (1993) and so on. PNe were then commonly divided into round, elliptical, bipolar, irregular, stellar and point symmetry groups. As more micro-morphological structures of PNe were revealed in observations, e.g. from IPHAS in Sabin et al. (2014) and the *HST* in Sahai et al. (2011), sub-classifiers were employed to describe the bipolar lobes (close end or open end), the point symmetry, outer shells, ring structures, etc.

1.3 The Spectroscopic Characteristics of Planetary Nebulae

By definition, a PN is shrouding a hot, low-mass CS with a temperature of at least 20 kK and up to approximately 250 kK and a mass between 0.55 and $0.9M_\odot$ derived from empirical studies (Frew & Parker 2010). The spectral types of CS range from ON and sdO through DAO and DA for the great majority of PNe. A number of PNe show prominent wide emission lines of ionised helium, nitrogen or carbon in their spectra, known as Wolf-Rayet features which indicating a dense stellar wind. These stars are of a spectral type [WR] with sub-types including [WC], [WO] and [WN]. Additionally, H-deficient stars including weak emission-line stars (*wels*), and the PG 1159 classifications contemplate the [WC] and [WO] stars (Weidmann et al. 2020, Frew & Parker 2010).

During a PN stage, ultraviolet radiation from the hot exposed central star will ionise the ejecta before it becomes a white dwarf. The PN emissions were studied in multi-wavelength observations including optical, infrared and radio ranges. The electromagnetic emission from a PN has little if any continuum emission and prominent emission lines. The continuum radiation is mainly from the interaction between free electrons and H and He ions through free-free radiation (also referred to as bremsstrahlung) giving thermal radiation of a wide range of wavelengths. The continuum emission dominates the near-infrared region (Pottasch 1984, Terzian 1978). Meanwhile, emission lines dominate in the optical regions. The emission of a distinct wavelength is a result of electron transits from a higher energy level to a lower by releasing energy in the form of a photon. Collisional excitation and recombination are the main mechanisms producing emission lines.
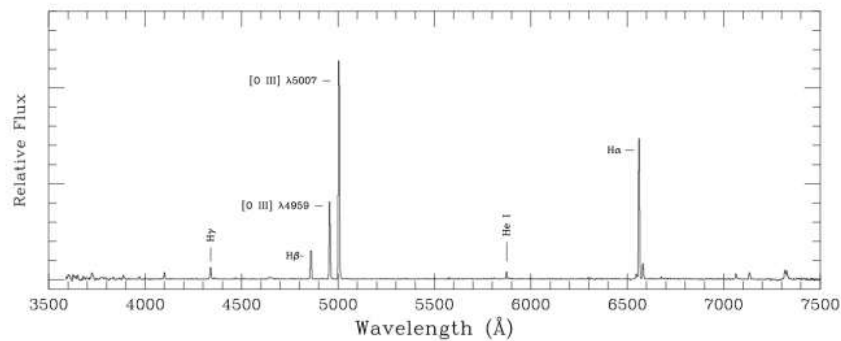
Figure 1.4: A typical spectrum of planetary nebulae in the optical range. Image accessed from `https://www.e-education.psu.edu/astro801/book/export/html/1756` on 13/07/2022.

1.3.1 Collisionally Excited Lines (CELs)

In a PN, the atom density is too low for atom-atom collisions, however, atom-electron collisions could happen. There are free electrons that come from the photoionisation of hydrogen in the gas. When bound electrons in the lower levels of e.g. O^+ or the O^{2+} ions are excited to higher energy levels during collisions with free electrons, the colliding electrons lose their kinetic energy. More importantly, the low gas density in a PN allows electrons in meta-stable fine structure states to de-excite collisionally before jumping downward through spontaneous de-excitation, such a transition emitting a forbidden-line photon. There is a critical density for each forbidden line at which the usual spontaneous de-excitation is quenched while collisional de-excitation allows its emission. This also makes forbidden lines suffer little collisional de-excitation and has a long path length. PNe are therefore easily discernible even at larger distances.

1.3.2 Recombination Lines (RLs)

A recombination line occurs when a free electron is captured by an ion. The difference between the initial energy before the encounter and the energy of the level it resides would be released by emitting a photon. The electron could go directly to the ground state of the ion if the ion was just ionised, or more likely, the electron would be caught in an intermediate state, emitting a photon of lower energy, then de-excite quickly through several energy levels until it goes to the ground state, known as cascade transitions. A photon is emitted every time the de-excitation occurs.

1.4 Thesis outlines

This study is motivated by the set of observational data of 138 PNe in the Galactic Bulge obtained with the FORS2 instrument on the 8.2m ESO Very Large Telescope (VLT). This data set is significant as it provides the high-resolution images and spectra for the majority of the objects for the first time. More macro- and micro- morphological features were resolved and more weak emission lines got detected compared with previous observations obtained from 2-4m telescopes

10-20 years ago. This allows for more accurate morphological classifications and more precious chemical abundance determinations from either CELs or RLs. The outline of the thesis is in the following.

Chapter 2 presents the full data reduction procedure in which the limitation of the FORS2 pipeline was discussed as well as the substituting programming scripts or software employed. Except for the standard cosmic-ray removal, bias subtraction, flat-fielding, wavelength calibration, flux calibration, sky-line removal, and spectrum extraction. We include a method to correct the saturated emission lines, line fitting and quality check. The steps in the calculation of chemical abundances are given, including the interstellar extinction correction, physical condition determination, ionic abundances derivation as well as the principle of ionisation correction factor.

A detailed study of morphologies of PN in this sample is present in Chapter 3. This involves observation from the *Hubble Space Telescope* (*HST*) as well, where available. A chosen set of classifiers was used to describe the macro- and micro- morphological structures of each PN and compared with the results in the HASH Database. The central star visibilities were checked and the position angle of each PN was measured where possible.

In Chapter 4, as the current largest and homogeneously processed PN sample in the Galactic bulge, the PN chemical abundances were used to trace the chemical evolution in the bulge. The aims include testing whether an abundance gradient could be measured, estimating an age distribution of PNe and obtaining an abundance distribution function to compare to the results from other stellar populations. These measurements and results were used to disentangle the formation scenarios of the Galactic bulge.

Chapter 5 looks at a long-lasting conundrum in nebular science, the abundance discrepancy. Chemical abundances measured from CELs and RLs were compared to check the consistency. Different nebular and central star properties were considered to find a clue to the mechanism that causing the abundance discrepancy.

Then, the results of each chapter are briefly summarised in Chapter 6, the findings in this project are present as well as the further investigation of the problems we currently do not understand well.

Chapter 2

The observations of PNe in the Galactic Bulge from the ESO 8.2 m Very Large Telescope

2.1 The FORS2 Instrument on the ESO Very Large Telescope

The observations analyzed in this work were obtained with the FOcal Reducer and low dispersion Spectrograph (FORS2) instrument mounted on the ESO Very Large Telescope (VLT) UT1 (Antu) Cassegrain focus in Chile. FORS2 is a multi-mode instrument optical instrument capable of imaging, polarimetry, long-slit and multi-object spectroscopy in a wavelength range of 3000-11000 Å according to the FORS2 user manual. A schematic of main instrument optics is shown in Fig. 2.1. FORS2 equips 2k × 4k MIT CCDs, each with 15 μm pixels. The Standard Resolution (SR) collimator giving a 44.5 mm diameter pupil was employed with the standard 2×2 binning. The imaging (IMA) and the long-slit spectroscopy (LSS) mode were used for the observations.

2.2 Observation

We obtained observations of 135 planetary nebulae under program IDs 095.D-0270(A), 097.D-0024(A), 099.D-0163(A), and 0101.D-0192(A). The sample is within the central $10^{\circ} \times 10^{\circ}$ region towards the Galactic bulge which accounts for 25 per cent of known PNe in this region. The programs were designated as a filler program and designed to observe all PNe that are extended between 2 to 10 arcsec to allow the observations can be performed even under bad weather (e.g. clouds and/or high humidity) and poor seeing. The observing dates, amount of time and number of the object covered are summarized in Table 2.1.

According to HASH database, after careful check of line ratios including Hβ/[O III]5007, Hγ/[O III]4363 and [N II]/Hα, the objects PN G 005.9-02.6 and PN G 007.5+04.3 are now candidates of symbiotic star and were excluded from this study. Details about the sources are summarized in Table. A.1.
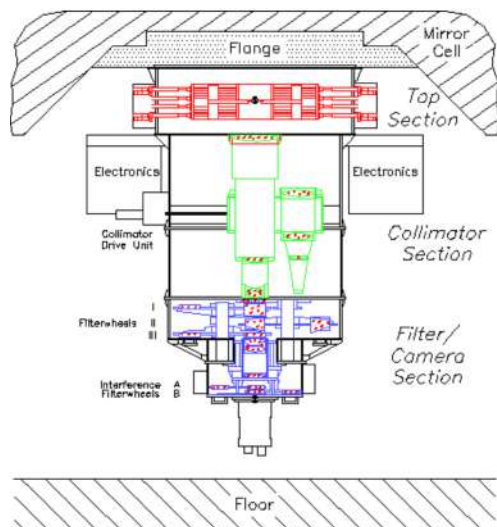
Figure 2.1: A schematic view of FORS2 instrument taken from ESO FORS2 web page: `https://www.eso.org/sci/facilities/paranal/instruments/fors/img/cut_col.gif`. Accessed on 01/02/2022

Program ID	Obs. Date	# of PNe Observed	Amount of Time
095.D-0270(A)	Apr - Aug 2015	62	25 nights, 74 hours
097.D-0024(A)	May - Sep 2016	42	23 nights, 54 hours
099.D-0163(A)	Jun - Sep 2017	16	9 nights, 19 hours
101.D-0192(A)	May - Jul 2018	23	11 nights, 31 hours
Total:		138*	68 nights, 178 hours

* Observations of faint PN G 005.8-06.1, PN G 007.5+04.3, PN G 355.9-04.2, PN G 357.3+04.0 and PN G 358.9+03.4 were repeated because of the saturation as the long 1000s exposure was used or weak emission line measurements.

Table 2.1: Summary of observation programs.

2.3 Imaging Data

2.3.1 The VLT observations

The VLT PN imaging data were taken for the pre-imaging purpose for the spectroscopy of PNe in the Galactic bulge. The FORS2 instrument has a 2048×1024 pixel CCD delivering a field view of 4.2 arcmin $\times$ 4.2 arcmin (0.126 arcsec/pixel). (see FORS2 manual, `http://www.eso.org/sci/facilities/paranal/instruments/fors/inst/pola.html`) Two narrow-band filters, Hα and [O III] were used for the pre-imaging. Imaging data were taken for 112 of the 136 PNe with Hα and/or [O III] narrow-band filters. Faint or small objects are difficult to resolve any shape other than a point, thus, images are not obtained. The same is for the unavailable filter images. Among the 112 PNe, 80 PNe have images with both Hα and [O III] filters, 16 PNe have an image with Hα filter only and 16 have an image with [O III] filter only. The integration times range from 0.36 s to 240 s.

The FORS2 instrument was identified as a versatile instrument with exchangeable blue-optimized

and red-optimized filters and relatively short exposure times (less than 26 s) were used for most of PNe, which could result in issues because of read-out noise of the CCD provided the photon-noise is limited . The rotator in ANTU was continuously moving to keep the instrument in the same alignment with the sky so did the image orientation. For the comparison with the HASH DB, the images were rotated to match the WCS coordinates. The near stars were used for the cross-check as well.

The Hα filter employed has a central wavelength of 6563 Å with an FWHM of 61 Å, while the [O III] filter has a central wavelength of 5001 Å and the FWHM is 57 Å. For the 80 objects with both Hα and [O III] narrow-band images, a colour-composite image was created for each PN. The images were obtained with red from the Hα image, both green and blue from the [O III] image because of the lack of green images. The scales and pixel distributions of the observational data were adjusted to give the best quality of images with a visual inspection.

2.3.2 The *HST* observations

Searching through the HASH database, imaging data from the *Hubble Space Telescope* (*HST*) for 41 PNe are available. The observations were made using the Wide Field and Planetary Camera 2 (WFPC2) of *HST* with 800 × 800 pixel silicon CCD with an angular resolution of up to 0.04 arcsec. Only Hα images taken with the F656N filter are available. The F656N filter has a central wavelength of 6560 Å and an FWHM of 30 Å, giving an image scale of 0.046 arcsec/pixel. Because of the high resolution, only the *HST* imaging data were used for PN image analysis in Chapter 3 where available.

2.4 Long-slit Spectroscopic Data

The long-slit spectroscopic images were obtained using the VLT FORS2 GRIS1200B+97 (G1200B) and GRIS600RI+19 (G600RI) grisms in long-slit spectroscopy (LSS) mode. The slit is 0.5 arcsec in width and 6.8 arcmin in length. The G1200B grism covers the blue spectral range 3360-5110 Å with a medium spectral resolution up to 1420, while the G600RI grism covers the red spectral range 5120-8450 Å with a medium resolution ($\lambda/\Delta\lambda$ up to 1000). Exposure time varies from 2s to 1500s. A log of the observations is shown in Table. B.1. In general, one object has two exposures for blue and red grisms respectively: 30s and 1000s. The shorter and longer exposures are for very bright and faint emission lines to avoid saturation or no observation. The data of observations contain 545 spectroscopic data in total of which 247 have saturated emission lines. The saturation is resolved either by scaling the shorter exposure measurement or repeating observation or correcting using unsaturated lines and theoretically predicted line ratios where possible. For 18 objects, as information from their spectra is not enough for any correction, they were excluded from the study in this project. Details in saturated emission line correction are discussed in §2.4.2.

2.4.1 Data Reduction

The data reduction procedure was devised to diminish the contamination as possible and maximize the signal-to-noise ratio (S/N) in the final spectrum. It includes a standard process: cosmic ray rejection, bias subtraction, flat-fielding, wavelength calibration, geometric correction and flux calibration. The ESO FORS2 reduction pipeline in the ESOReflex environment was employed for most of the reduction steps. This provides an effective and graphical workflow engine and allows to check intermediate results and change parameters for its improvement at each step. However, after a preliminary check of reduced spectra and intermediate spectroscopic images of reduction, for the following reasons, additional steps are required for a careful and consistent reduction:

- Ineffective cosmic ray cleaning. The removal of cosmic rays by the pipeline is generally good. However, because of the random nature of cosmic rays, they could hit the region of skylines, the stellar continuum or even worse, the emission lines, and the pipeline then unable to remove without any mistaking cleaning. Besides, the pipeline would overlook cosmic rays that are relatively weak and below a certain threshold value. The left-overs are clear in the images and would cause large errors, especially for weak line regions.

- Lack of stellar continuum removal. Either the CSPN or nearby stars will end up with a bright continuum in the spectroscopic image. This could be attempted by excluding rows in the image corresponding to the star emission. However, this would reduce the measurement from weak lines significantly and limit the amount of information that could be obtained from the image. The situation is generally true for compact PNe.

- Problematic skyline removal. In the ESO FORS2 pipeline, the skyline removal was done by first asking users to select sky windows below and above the object, then perform and subtract a fitting polynomial in the vertical direction. One problem is that skylines are usually bright in red spectra where many nearby stars are in the field. The bright sources in the sky windows could possibly lead to and over-subtraction of skylines. The other problem is that the object window in the pipeline is automatically selected for stars, then for a PN, it needs to be customised. However, with the small-scale image in the program window, it is difficult to determine the edges of the emission lines.

Self-developed `Python` scripts to perform cosmic ray removal, stellar continuum removal and skylines removal were then used in combination with the ESO FORS2 pipeline.

Cosmic ray removal with `L.A.Cosmic`

High energy cosmic rays moving through space could result in the generation of a cluster of signal charges when hitting on the CCD. Cosmic rays have to be removed before any reduction process because their random distributions and positions in the image could affect the cosmetic quality of CCD images and cause a glitch in fitting results.

L.A.Cosmic, an algorithm based on a variation of the Laplacian edge detection, was used

for this purpose in its `Python` implementation. Specifying signal-to-noise thresholds for detection (`cr_threshold`) and neighboring pixels (`neighbor_threshold`), a number of maximum iteration is required. However, as emission lines from PNe are distinct and bright, a mask for emission lines was applied in case of any wrong identification as cosmic rays. The masks for red and blue were obtained by summing pixel values of all frames available, then pixels with an average pixel value above 50000 are set to 1 for masking and the rest pixels are set to 0 for cosmic ray removal. The chosen value was not aimed to mask all regions possible for an emission line, but to cover the brightest central pixels of emission lines. In the first round of removal, thresholds are set for spectroscopic images according to their mean pixel value (MPV). The threshold values applied are derived from multiple testing and are shown in Table. 2.2.

Grism	Condition	Yes	No
G1200B	MPV > 700	[20, 5]	[4, 2]
G600RI	MPV > 500	[(MPV/25)+10, 3]	[(MPV/20), 3]

Table 2.2: Chosen [`cr_threshold`, `neighbor_threshold`] values in `L.A.Cosmic`

Spectroscopic images with cosmic ray removed using these given parameters are generally well-cleaned, but still has the following issues:

- Cosmic rays below the threshold intensity are not removed, which is usually worse at the noisy blue end.

- The edge of the cosmic ray bright cluster was not removed.

- Bright pixels of skylines or emission lines, either hit by cosmic rays or not, were removed.

Those with either residual at blue ends or bright cluster edges underwent another cleaning process with bright emission lines and skylines masked. The missed removed clusters of skylines were corrected by taking the average values of the same shape and size of pixels below and above. Careful treatments were given to cosmic rays hitting near or on the emission lines. First, the raw spectroscopic image was cleaned for cosmic rays with a precise mask covering pixels that are considered as emission lines. The mask was obtained through an inspection of pixel value variation in this region. After that, any pixel in emission lines cleaned for cosmic rays was set to the mean value of neighbouring pixels.

ESO FORS2 Pipeline

After the cosmic ray removal, the spectroscopic images were reduced using the FORS2 reduction pipeline in the `ESOReflex` workflow. The associated raw calibration files were selected automatically and downloaded together with the scientific observations through the ESO Archive download portal. The reduction was done with 3 recipes in the pipeline working in succession: `fors_bias`, `fors_calib` and `fors_science`.

First, with `fors_bias`, a set of raw bias frames (normally greater than 7 bias exposures) was stacked by rejecting the highest and lowest pixel values and taking the median of the rest, giving a master bias frame. The `fors_calib` recipe then, with parameters from the grism table, traces
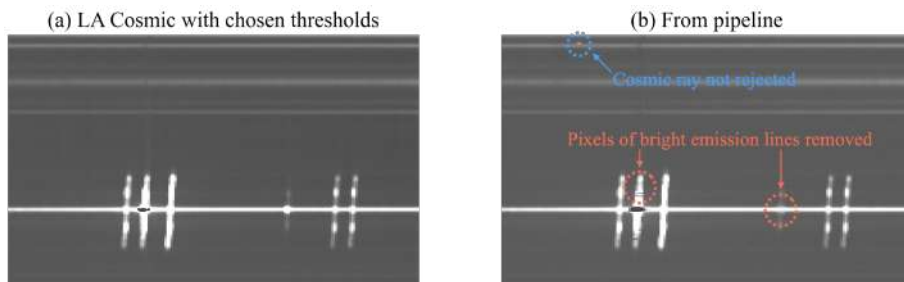
Figure 2.2: A comparison between cosmic ray rejection with *L.A.Cosmic* and the ESO pipeline. The spectrum is of PNG004.3+01.8 taken with G600RI grism and an exposure time of 1000S near the Hα lines. As CR rejection and sky line removal were conducted simultaneously in ESO pipeline, two images are both cosmic-ray and sky-line removed. CR rejection algorithm in the pipeline failed to reject a weak cosmic rays in the blue circle and mistakenly removed bright pixels of emission lines. This demonstrates the importance of customising CS rejection parameters and applying masks to the emission lines.

the slit and determines the coefficients for wavelength calibration through the identification of reference lines on the raw arc lamp exposure with a line catalogue. It also creates a normalized flat field frame from a set of raw flat frames using the same stacking method as the master bias. Then, with the `fors_science` recipe, the instrument spectrophotometric response curve for flux calibration was created from a standard star observation on the same night as the scientific data. The spectroscopic images are wavelength-calibrated, rectified and mapped in the `fors_science` recipe using results from previous recipes and were cropped to 500 pixels in spatial direction with the CSPN at the centre for the skyline removal in the next step.

Skyline subtraction with `starlink.figaro`

The skylines were subtracted using `starlink.figaro.polysky` routine which performs a polynomial fitting in the spacial direction of two defined sky windows on either side of the scientific object, i.e. a PN. The sky windows start where the bright emission lines go to a background level while the ends were selected to cover the no-source region as possible. The degree of polynomial fitting was set to 3 and 10% of sky window spacial sizes of extreme values were rejected for the fitting. The end products were checked and either new sky windows would be selected or fitting parameters would be modified if the skylines were not well-removed (e.g. residuals or emission line affected).

Stellar continuum removal

Stellar continuum were fitting using `iraf.noao.ondespec.continuum`. The fitting function is a high-order cubic spline and fitting points are created by combining each 10 sample points and taking the median. Only the high rejection limit = 3 was applied and the number of rejection iterations was 15.

After all contamination of skylines and stellar continuum was removed, to maximize the S/N, the background level was determined with sigma-clipped statistics, all pixels with a value below
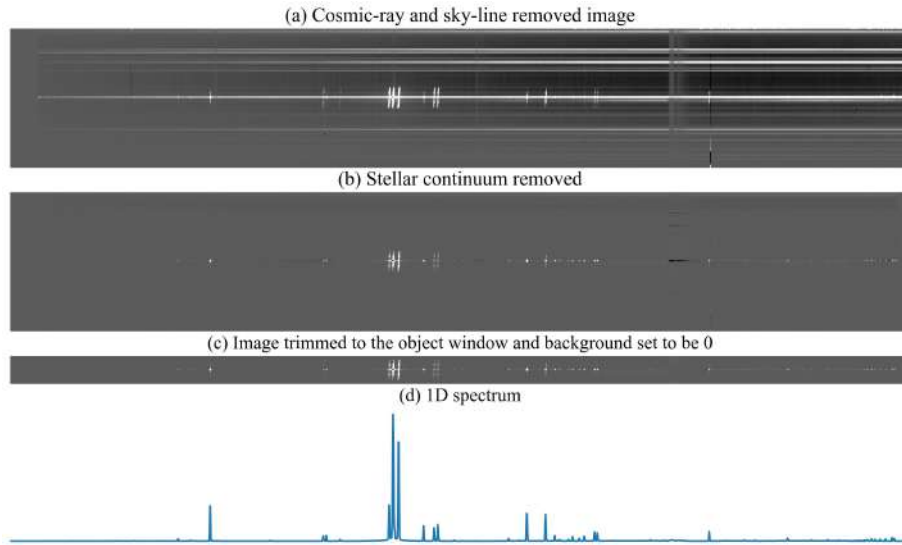
Figure 2.3: An example of the data reduction process. The spectroscopic images are of PNG004.3+01.8 taken with G600RI grism for 1000s. Panel (a) shows the image after cosmic ray rejection and sky line removal. The interim end products were visually inspected and fitting parameters were adjusted where residuals are present. Panel (b) presents the images after stellar continuum removal and setting the background pixels to zero. Panel (c) is the image trimmed to the object window that will be used to obtained the object spectrum. Images at this stage are usually free of contamination, positions of any residuals away from the middle nebulae region were measured and set to be zero with `Python` scripts. Pixel values in the object window were then summed up to give the final 1D spectrum as shown in Panel (d).

the 3-sigma limit were set to 0. Flux calibration was performed at this stage with the spectrophotometric table obtained from the FORS2 pipeline, converting the count/s on CCD to an energy unit. Then, by summing all pixels values in the chosen object window according to wavelength, the data reduction is completed and the resulting spectra are ready for scientific study.

Line Fitting and Flux Measurement with `ALFA`

Line fitting methods are usually employed to measure the emission line fluxes in the spectra. An automated line fitting algorithm (`ALFA`) was used in this project for this purpose. `ALFA` performs a Gaussian fit to the input spectrum by constructing a synthetic spectrum using an atomic line list. The parameters of the synthetic spectrum are optimised through a generic algorithm: It first fits the spectrum in smaller sections, then determines an approximate expansion velocity and resolution with a subset of brightest lines. The two values were then used as initial guesses and vary in the fitting process of smaller sections through a two-pass approach in which the first pass allows larger variation and the second pass is used for fine-tuning.

A fitted line list and the optimized synthetic spectrum were the output from `ALFA`. The emission fluxes were given with their observed wavelength, rest wavelength, error from fitting, peak value and FWHM. Due to the noise at the blue ends of spectra, false emission lines that fit beyond the spectrum wavelength coverage were deleted from the final results.

One problem noticed in `ALFA` fitting is the ineffective deblending of [N II] $\lambda 6548$ and Hα lines of the low-excitation nebulae with weak [N II] emissions. A preliminary check of [N II] $\lambda 6583/6548$ line intensity ratios were first conducted to check spectra with possible deblending problems. Careful measurements of [N II] $\lambda 6548$, Hα and [N II] $\lambda 6583$ fluxes were performed manually using the deblending method in `iraf.splot`.

The uncertainties in bias subtraction, flux calibration and sky subtraction were estimated with the error frame of the final output fits file from the ESO pipeline. The average is 5%. The uncertainties in `ALFA` line fitting, which are the RMS of residuals, are 10% on average, giving a total uncertainty of 15% in our line fluxes. However, for weaker emission lines and [N II] $\lambda 6458$ the uncertainties in line measurements could be up to 30%.

2.4.2   Saturation, Saturation

The ESO VLT CCD has a 16-bit dynamic range, each pixel has gray values ranging between 0 and 65535 ADU. The saturation was examined with cosmic-ray-cleaned raw spectroscopic images by finding pixels having the grey value equal to 65535, the saturation level, within the spatial range of PN emissions. As a result, saturated emission lines were found in 247 spectroscopic images for 110 PNe (80% in this sample). For most of the objects, saturation happens for the brightest lines in the long exposure, which allows a correction to be made by taking the measurements from the short exposure. This was done with self-developed `Python` scripts.

For each saturated spectroscopic image, the number of saturated lines, n_{sat} were first determined with a procedure shown in Fig. 2.4. An image with saturated pixels only was first generated by setting all unsaturated pixels to be 0, then by summing pixels along the dispersion direction, a 1D distribution of saturation in that direction was obtained. n_{sat} was found using a peak finding algorithm on this distribution plot. The interval for peak finding was chosen according to an average FWHM value computed from the spectrum fitting using `ALFA` and in case of any fluctuation caused by multiple saturated pixels of a single emission line, which usually happens for [N II], Hα, Hβ and [O III] lines, the maximum number of peaks was set to 1 in the corresponding pixel coordinate ranges. The preliminary wavelengths of saturated emission lines were considered as that of the top n_{sat} fluxes measured in the shorter unsaturated exposures. A careful visual inspection of saturated lines, as well as the lines affected during cosmic-ray removal, were then carried out, giving the accurate number of lines to be corrected and the corresponding wavelengths.

As the astronomical seeing may vary between different exposures, the fluxes measured in the shorter exposures were not used as direct replacements and instead a scaling was applied. For a saturated emission line, the scale factor was derived by averaging the flux ratios of at least 5 adjacent strong emission lines which are not saturated in both exposures with an inverse-error weighting. The uncertainty in flux was from both the scale factor and the shorter exposure measurement. To minimise the uncertainty in the scale factor, a set of the emission lines giving
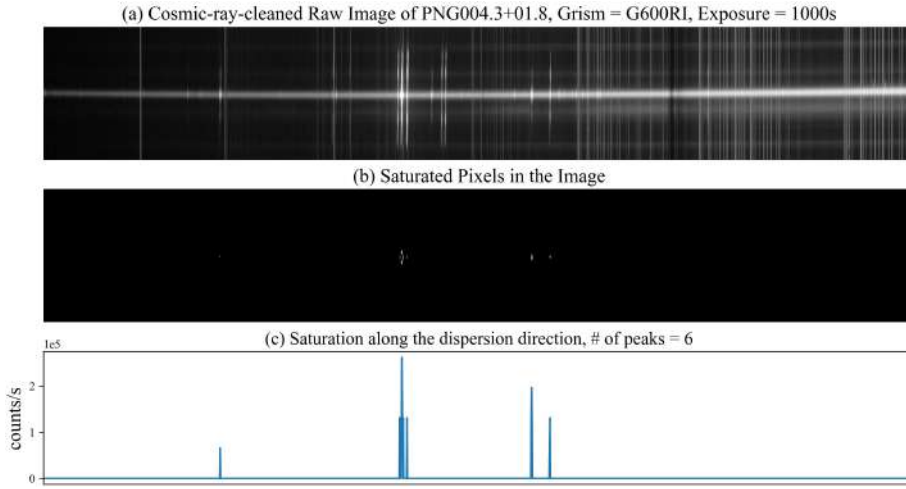
Figure 2.4: The steps of finding the number of saturated lines in a cosmic-ray-cleaned spectro-scopic image. Panel (a) shows row spectroscopic image frame after the cosmic ray removal. The bright vertical lines running full width of the image are sky lines.

the most consistent scale factors obtained by varying the threshold and S/N cut-off were used. An average error in the scale factor is 0.5%, for which the correction does not influence the precision of the overall line flux measurement of a frame.

For object with both exposures in either blue or red arm saturated, a more careful correction was applied to the short exposure. For red frames, a correction was first made to saturated [N II] λ6583.5 Å lines only using the theoretical ratio of [N II] λ6583.5/6548.1 and line flux of unsaturated [N II] λ6548.1 Å line. If Hα line is saturated in a red frame, the first check was made to see if the literature line ratios are availble. The lines [N II] $\lambda\lambda$6548, 6583, [He I] $\lambda\lambda$6678, 5875, [S II] $\lambda\lambda$6715, 6731 were used to check the consistency between this work and the literature. The line ratios were then adopted to correct for the saturated Hα line if both agree with each other with the measurement uncertainty. As Hα is used for the calibration between blue and red spectra in later analysis, those with all the line flux measurements deviate from the literature or without literature measurement were excluded from this study due to the potential large uncertainty. The similar were applied for blue spectra, short exposures with [O III] λ5006.84 Å line saturated only were corrected with the theoretical ratio of [O III]5006.84/4958.91 and [O III]4958.91 flux. Then literature line fluxes were first checked the consistency with this work then applied to correct Hβ line. The object have either inconsistent measurements or no literature data were not further studied in this work. In addition, the PNG 003.9+01.6 was also excluded as no Hγ line was not detected in its observations.

The final data set includes 118 PNe in which 23 are unsaturated in both exposures and 95 were corrected for saturated lines with before-mentioned methods. This doubled sample size in Gorny (2009).

2.4.3   Quality Check

The measured Hβ fluxes were compared with that measured from the spectrophotometric observations in Strasbourg-ESO Catalogue from Acker (1992) with error bars as shown in Fig. 2.5. The catalogued data were observed with the ESO 1.52m telescope and the PHP CARELEC telescope. The slit employed for their spectroscopic observations has widths of either 2.5 or 4 arcsec and heights ranging from 4.1 to 7.7 arcsec. In the plot, the slope of the lines of best fit is 0.94±0.05, indicating a general agreement. The catalogued fluxes are on average fainter than that measured in this work by 0.11±0.67 dex, which is possibly due to the difference in slit sizes and slit positions relative to the objects. Larger uncertainties are seen for weaker line fluxes which used for the catalogued data and the ESO VLT observations in this work.
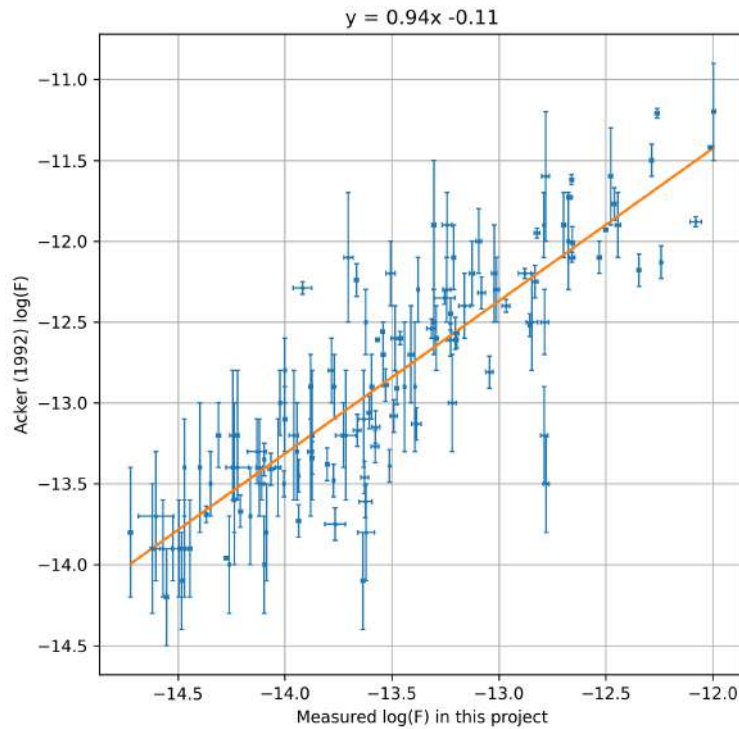
Figure 2.5: Hβ log fluxes in the unit of erg $\cdot$ cm^{-2}s^{-1} compared to the Strasbourg-ESO Catalogue Hβ log fluxes.The line of best-fit is in orange with a slope of 0.94± 0.05 and an intercept of -0.11± 0.67.

2.5   Plasma Diagnostics and Chemical Abundance

The Nebular Empirical Analysis Tool (`NEAT`) was employed for ionic and elemental abundance calculation (Wesson et al. 2012). `NEAT` corrects for the interstellar extinction and calculates electron temperatures and densities. Ionic abundances are then calculated from collisionally

excited lines (CELs) using the derived temperature and density corresponding to their ionization potential.

2.5.1 Interstellar extinction correction

The emission from a PN was first corrected for the interstellar extinction caused by the micron-sized dust particles. Dust dims the light from an object and preferentially scatters and absorbs shorter-wavelength bluer light, thus, the spectral line at the blue ends lessened in intensity while the object appears to be redder. The Balmer series of hydrogen line ratios, specifically the Hα λ6563, Hγ λ4340 and Hδ λ4102 lines relative to Hβ λ4861 are usually used from such correction by comparing the measure line ratios to the predicted values from atomic physics. The theoretical ratios from Osterbrock (1989) of hydrogen Balmer lines under typical conditions (at electron density, T_e = 10,000K and electron density, n_e = 100cm^{-2}) in PNe are Hα/Hβ = 2.86, Hγ/Hβ = 0.47 and Hδ/Hβ = 0.26.

Because of the reddening effect, the measure Hα/Hβ ratios are always higher than the theoretical value while Hγ/Hβ and Hδ/Hβ are always lower. Taking Hγ as an example, to correct the spectra, the colour excess, E(B-V) was first determined with the equation

$$E(B - V) = \frac{E(H\beta - H\gamma)}{[\kappa(H\beta) - \kappa(H\gamma)]}$$
$$= \frac{-2.5}{[\kappa(H\beta) - \kappa(H\gamma)]} \times \log_{10}\left[\frac{(H\gamma/H\beta)_{int}}{(H\gamma/H\beta)_{obs}}\right]$$

where $\kappa(\lambda)$ is the extinction coefficient at particular wavelength derived from the Galactic extinction law in Fitzpatrick (1999) with $R(V)$ = 3.1. The absolute extinction at λ can be derived by

$$A(\lambda) = \kappa(\lambda) \cdot E(B - V) = \frac{A(\lambda)}{A(V)} \cdot R(V) \cdot E(B - V)$$

where $A(V) = R(V) \cdot E(B - V)$ is the total extinction at the V-band. Then, the optical depth , $\tau(\lambda)$ is given by

$$\tau(\lambda) = A(\lambda)/1.086$$

The logarithmic extinction $c(H\beta)$ is then calculated with

$$c(H\beta) = -\log[e^{-\tau(H\beta)}].$$

Intrinsic Balmer line ratios vary with physical environments in the nebulae. In this work, NEAT first assumes an intrinsic Balmer line ratios under T_e = 10,000K and n_e = 100cm^{-2}. The de-reddened emission lines were then used to derive the electron temperatures and densities, which were then used to recalculate the intrinsic Balmer line ratios. These values will then be used for the extinction correction. c(Hβ) was calculated with Hγ/Hβ and Hδ/Hβ intensity ratios and the flux-weighted results were adopted for the spectrum correction. The variation in intrinsic Hydrogen Balmer line ratios with T_e and n_e could lead to an error in c(Hβ) up to 0.04 dex as

discussed in Giammanco et al (2011). As such a contribution is small, this is not included in the quoted uncertainties in the following chemical abundance analysis.

2.5.2   Electron densities and temperatures

The ions O^{2+} and N^{+} have optical collisional excited lines that originated from excitations to two upper energy levels and have a large difference in their excitation energies. The relative rates of excitations to these two upper levels strongly depend on electron gas temperature, T_e, resulting in that the relative strength of such CELs is sensitive to T_e. For O^{2+}, the lines $\lambda 5007$, $\lambda 4598$ occurring from the ^1D level and $\lambda 4364$ occurring from the ^1S are used to determine T_e. The line intensity ratio $I(5007 + 4958)/I(4363)$ depends on T_e up to an electron density N_e of $10^5 cm^{-3}$ and the range of sensitivity is $5000-20000K$ as shown in Fig. 2.6. Similarly, for N^{+}, the line intensity ratio $I(6548 + 6583)/I(5755)$ could be used.
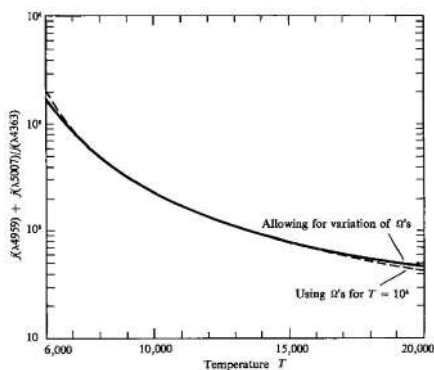
Figure 2.6: [O III] $I(5007 + 4958)/I(4363)$ line intensity ratios as a function of gas electron temperature in low-density limit ($N_e \rightarrow 0$). Solid line are values calculated from the statistical weights, Ω of different energy levels; dashed line shows the commonly used approximation is which the Ω is represented by its mean value. Figure from Osterbrock (1974).
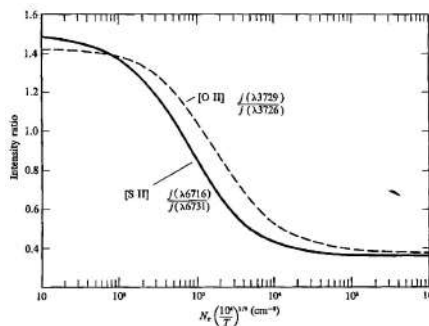
Figure 2.7: The variation of [OII] (solid line) and [SII] (dashed line) as a function of electron density N_e. The [OII] ratio measures N_e best around $N_e \approx 10^3 \ cm^{-3}$ while [SII] ratios measure best when $N \approx 2^3 \ cm^{-3}$. In the low-density limit $N_e \rightarrow 0$, and the high-density limit $N_e \rightarrow \infty$, the intensity ratios tend to constant values. Figure from Osterbrock (1974).

For certain ions, they have CELs from the same lower level to two upper levels with energies close to each other. The relative transitional probability is then unaffected by collisions but depends on the actual gas electron density, N_e. The line intensity ratios [O II] $\lambda 3729/\lambda 3726$, [S II] $\lambda 6716/\lambda 6731$, [Cl III] $\lambda 5517/\lambda 5537$ and [Ar IV] $\lambda 4711/\lambda 4740$ are such density-sensitive lines and could be used to estimated N_e. The change in [O II] and [S II] ratio with N_e is shown in Fig. 2.7.

NEAT adopts an iterative way for the determination of electron temperature and densities because of their dependence on each other. An electron density is first estimated assuming an electron temperature of 10,000 K. The electron temperature is then calculated with the density

derived from temperature-sensitive line ratios and a new electron density is estimated based on the results of the temperature diagnostics. The process is repeated until self-consistency is reached.

2.5.3 Ionic Abundance Ratio Determination

With the local physical conditions derived, including electron temperatures and densities, ionic abundances are determined by comparing the de-reddened intensity of an ionic emission line to the de-reddened intensity of an H recombination line. The ratio is to be compared with the ratio of theoretical emissivities. The equation is given by

$$\frac{N(X^i)}{N(H^+)} = \frac{I_\lambda}{I_{H\beta}} \frac{\epsilon_{H\beta}}{\epsilon_\lambda} \tag{2.1}$$

where N is the number density of the respective ions, I, ϵ are the line intensity and emissivity of the respective lines.

The theoretical emissivities for collisionally excited ions in the low-density limit are

$$\epsilon = N_i N_e h\nu \frac{8.629 \times 10^{-6}}{T^{1/2}} \frac{\Omega_{12}(T)}{g} e^{-\chi/kT_e} \tag{2.2}$$

where N_i is the number density of the ion of interest, N_e is the electron density, h is the Planck's constant, ν is the photon frequency of the transition, Ω is the average electron collisional strength from the lower level and is a constant and calculated quantum mechanically, g is the statistical weight of the lower level, k is the Boltzmann' constant, T_e is the electron temperature, and χ is the energy difference between the two energy levels. For recombination ionic abundance derivation, the emissivity calculation is far more complicated, and the temperature and density dependence is fitted with appropriate power laws. (Aparicio et al. 1998)

The calculated values of transition probabilities and collision strengths in the literature adopted in `NEAT` were summarized in Table. 1 in Wesson et al. (2018) and is present in Table.2.3.

2.5.4 Ionisation Correction Factor

The total elemental abundance is given by the sum of the ionic abundances. This is straightforward if emission lines from all of the relevant ionic states were detected and measured. However, emission lines of ionic states might either be too weak to detect or lie out of the observational wavelength coverage. The ionisation correction factors (ICFs) derived empirically were then employed to calculate elemental abundance from available observations. The ICF scheme of Kingsburgh & Barlow (1994) was used in this study which is in the incorporation of He I recombination coefficients calculated by Porter et al. (2012).

Taking oxygen as an example, for cases when only the emission lines of O^+ and O^{2+} are detected, which is true for optical observations, the unobserved O^{3+} state is corrected for by

Ion	Transition probabilities	Collision strengths
O^+	Zeippen (1982)	Pradhan (1976)
S^{2+}	Mendoza & Zeippen (1982)	Mendoza & Zeippen (1983)

Ion	Recombination coefficients
H^+	Storey & Hummer (1995)
He^+	Porter et al. (2012, 2013)
He^{2+}	Storey & Hummer (1995)
C^{2+}	Davey, Storey & Kisielius (2000)
C^{3+}	Pequignot, Petitjean & Boisson (1991)
N^{2+}	Escalante & Victor (1990)
N^{3+}	Pequignot et al. (1991)
O^{2+} (3s–3p)	Storey (1994)
O^{2+} (3p–3d, 3d–4f)	Liu et al. (1995)
Ne^{2+} (3s–3p)	Kisielius et al. (1998)
Ne^{2+} (3d-4f)	Storey (unpublished)

Table 2.3: Table 1 is Wesson et al. (2018) is adopted: atomic data used in `NEAT`. For collisionally excited lines, collision strengths and transition probabilities for ions not listed in this table were taken from version 9.0 of the `CHIANTI` database in the version v2.3 (Dere et al. 1997, 2019).

assuming that the O^{3+} zone is coincident with the He^{2+} zone O^{3+} because of the coincidence of their ionization potentials, O^{3+} state is corrected via

$$ICF(O) = \left(\frac{He^+ + He^{2+}}{He^+} \right)^{2/3} \tag{2.3}$$

The total elemental abundance is the product of the ICF and the ionic abundances of ions observed

$$A(O) = ICF(O) \left(O^+ + O^{2+} \right) / H^+ \tag{2.4}$$

Chapter 3

A Revisit of PN Morphologies, CSPN visibilities and Position Angles

3.1 Introduction

Planetary nebulae (PNe) remain some of the most fascinating astronomical objects, the reasons for which include the wide diversity of their shapes. The understanding of their morphologies plays a key role in the study of the mass-loss processes, the interaction with the ISM and the physical and chemical properties of the progenitor stars of PNe (Nishiyama 2018). An accurate classification of PN morphology could help to project the fraction of ISM interactions and central-star properties and give information on their formation mechanism: whether a stellar wind is formed at the end of the AGB phase (Kwok 2015, Frank et al. 2018), whether the binarity of the central stars of planetary nebulae (CSPNe) causes the aspherical slow wind (Ivanova et al. 2013, Santander et al. 2018), whether the magnetic fields influence the shaping process (Vlemmings et al. 2013, García-Segura et al. 2018). Answers to these questions will give a better understanding of the late stage evolution of their progenitors - the low- and intermediate-mass stars and any possible advantages and biases of using planetary nebulae to trace the chemical evolution of the Galactic bulge.

Unlike other physical parameters, the morphology of PNe is difficult to qualify and being rather subjective. Several schemes of PN morphologies were introduced and modified by Hromov (1968), Schwarz et al. (1992) and Sahai et al. (2011), to distinguish their morphological properties. The common features of PNe could then be summarised into six main morphological types which are known as the 'ERBIAS' classifier. This stands for Elliptical ('typical' PNe), Round (spherical), Bipolar (elongated, axially symmetric with two extended lobes departing from an 'equatorial' waist), Irregular (does not fit in any class above) and Asymmetric. The extra quasi-Stellar classifier is used for the PNe observed as point-like whose detailed morphology haven't been revealed in current observations (Parker et al. 2006, Corradi & Schwarz 1995).
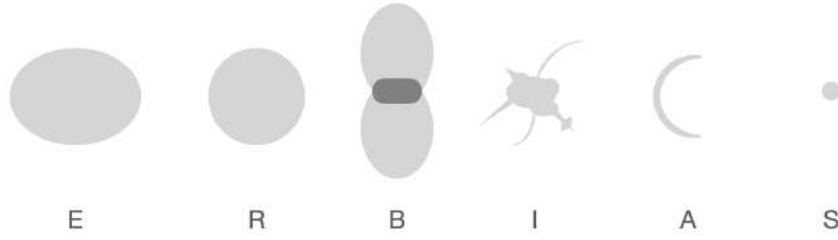
Figure 3.1: The basic 'ERBIAS' classifier for indicating the PN morphology (Parker *et al.*2016, Corradi & Schwarz 1995).

For a detailed description, certain common features in PN morphologies could be indicated with a sub-classifier 'amprs' which is used to describe that the object exhibits an enhancement on one-sided brightness asymmetry 's' (also referred to as an enhanced concavity arc in Ali et al., 2000), shows multiple shells or external structure 'm', possesses a point symmetry 'p', has a sharp ring structure or annuals 'r' or exhibits its internal structure with details, e.g. filaments, knots, 's'.

The 'ERBIAS' plus 'amprs' classifier is used for the PN morphological description in the HASH database which currently provides the most up-to-date and accurate information (positions, sizes, images and etc.) of all at-present discovered PNe of which 2681 are identified as true PNe. HASH contains observational data from over 30 large surveys (optical: SDSS; near infrared: 2MASS/UKIDSS, VVV; mid infrared: MSX, *Spitzer*/MIPSGAL, GLIMPSE, WISE; Parker, 2020). Images of PNe from such wide-field optical narrow-band surveys have revealed more PN structural details to us which allows a more accurate morphological classification (Parker et al. 2006). Meanwhile, studies of PN morphology would be compared with the ongoing high-resolution images from large telescopes, one of which is the ESO Very Large Telescope (VLT) in northern Chile that could achieve a resolution of 0.126 arcsec/pixel in the IMAGE mode. This recent new observational data by the VLT contains images of 111 PNe which could improve the current morphological classification of PNe in this sample in HASH DB.

The objective of this chapter is to make a comparison between images of PNe in the Galactic Bulge from this VLT imagery supplemented by *HST* images of 36 objects and those existing in the HASH DB. With full use of the narrow-band images in either Hα or [OIII] filter, the structures of some PN samples are more resolved which allows a better understanding of their structures. For some of the objects, the CSPNe could be observed. This was used to improve the position and information of CSPN. Further to this, the position angles of PNe were also measured on the VLT images as well as the *HST* images where available.

3.2   Observations

The date of observation and exposure time of each object are shown in Fig. 3.2. Images of objects with exposure time less than 5s were mainly taken between July and August in 2015. The possible reasons as follow: bright object may saturate for long exposures, some fields of

interest have sufficient imaging through *HST* or other telescopes already or the infra-red position is different from those at optical wavelengths for the same source.
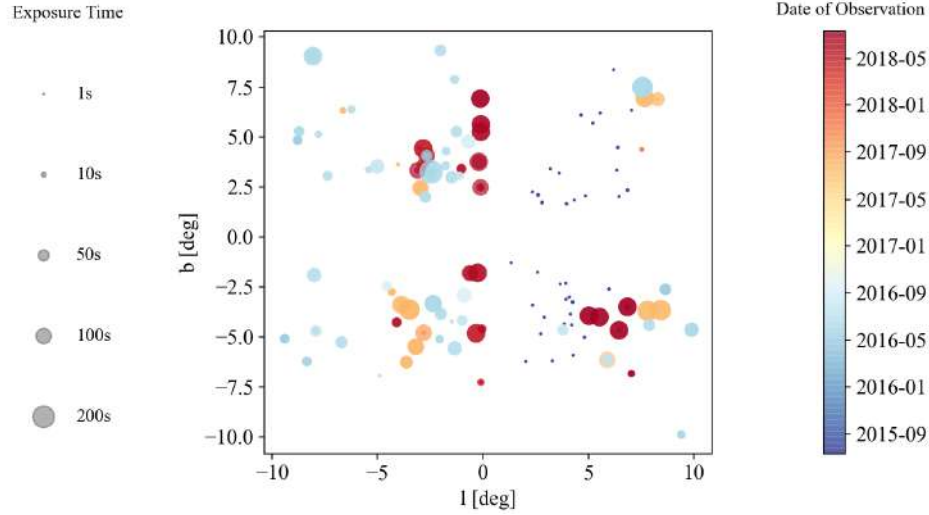
Figure 3.2: The Galactic coordinates of the VLT pointing for all 111 objects and the dates of observation.

3.3 Image Analysis with DS9

The astronomical image viewer SAOImage DS9 was applied for PNe imaging observation analysis, including a morphological classification, a search for central stars (CSPN) and a measurement of position angle (EPA). As only qualitative studies were involved, data reduction is not required and raw images were used. The scaling options and parameters was varied to resolve the structural details of PNe as possible. Color-composite images were used when both Hα (red) and [OIII] (green and blue) images are availble.

3.4 Results

In the new set of observational data from the ESO VLT, the improvement is evident on the aspects of the quality of image, the PN morphological structural and the central star information. Nearly all the images of PNe from the VLT have a better resolution. The new discoveries are illustrated in the following sections.

The positions, morphological classifications, central star coordinates, if availble, and position angles of 111 PNe obtained with the VLT data are summarized in Table. 3.1 and details are discussed in §3.4.1, §3.4.2 and §3.4.2 respectively. After a careful recheck with the new observations, the morphologies of 47 objects were classified differently from the HASH DB (42%).

Table 3.1: Summary of VLT PN observational results

No.	PN G	Centroid Coords.		Morph.	Central Star Coords.		EPA	Tele.
		RA(J2000)	DEC(J2000)		RA(J2000)	DEC(J2000)	$(\pm5^\circ)$	
1	001.3-01.2	17:53:47.7	-28:27:10.3	E	-	-	-	VLT
2	002.0-06.2	18:15:07.2	-30:15:26.5	Es	-	-	146	VLT
3	002.3+02.2	17:42:30.6	-25:45:19.1	Bps	17:42:30.0	-25:45:26.8*	68.5	VLT
4	002.3-03.4	18:04:28.3	-28:37:26.3	Rars	18:04:28.8	-28:37:38.2*	149	*HST*
5	002.5-01.7	17:58:31.1	-27:36:55.0	Rps	17:58:31.1	-27:37:06.4*	109	VLT
6	002.6+02.1	17:43:39.4	-25:36:42.5	Baps	17:43:39.3	-25:36:39.6*	70	VLT
7	002.7-04.8	18:11:04.2	-28:58:53.0	Bamprs	18:11:04.9	-28:58:59.2	41	*HST*
8	002.8+01.7	17:45:38.9	-25:39:58.7	E	-	-	9.5	*HST*
9	002.8+01.8	17:45:27.7	-25:38:05.1	Bas	-	-	44.7	VLT
10	002.9-03.9	18:08:04.9	-28:26:09.5	Baps	18:08:05.7	-28:26:10.6*	50	*HST*
11	003.1+03.4	17:40:08.1	-24:25:36.4	Ea	17:40:07.4	-24:25:42.7*	152.5	*HST*
12	003.2-06.2	18:17:42.0	-29:08:12.4	Bmps	-	-	146	VLT
13	003.6+03.1	17:41:56.4	-24:11:12.4	Ear	17:41:57.2	-24:11:16.3	-	*HST*
14	003.6-02.3	18:03:12.4	-26:58:21.4	E	-	-	24	VLT
15	003.7-04.6	18:12:33.7	-27:58:05.9	Ea	-	-	34	VLT
16	003.8-04.3	18:11:28.9	-27:46:05.8	Bps	18:11:29.2	-27:46:15.9*	79	*HST*
17	003.9+01.6	17:48:27.9	-24:41:14.7	Ea	-	-	142.5	VLT
18	003.9-02.3	18:03:39.8	-26:43:26.0	E	-	-	164.5	VLT
19	003.9-03.1	18:06:49.1	-27:06:14.8	Eas	18:06:50.0	-27:06:19.5*	15.5	*HST*
20	004.0-03.0	18:06:41.8	-26:54:53.8	E	18:06:40.9	-26:54:56.5	175	*HST*
21	004.1-03.8	18:10:11.3	-27:16:35.4	E	-	-	139.5	*HST*
22	004.2-03.2	18:08:00.7	-26:53:54.8	Bs	-	-	50	VLT
23	004.2-04.3	18:12:25.3	-27:29:02.6	Es	-	-	-	VLT
24	004.2-05.9	18:18:37.6	-28:07:52.6	E	-	-	131.5	VLT
25	004.3+01.8	17:48:35.8	-24:16:27.3	Bap	17:48:36.5	-24:16:33.0*	37.5	VLT
26	004.6+06.0	17:33:37.2	-21:46:14.9	E	-	-	69	VLT
27	004.8+02.0	17:48:59.8	-23:42:49.1	Emr	17:49:00.5	-23:42:54.9*	2.5	*HST*
28	004.8-05.0	18:16:10.5	-27:14:59.4	E	18:16:11.4	-27:14:57.0*	30.5	VLT
29	005.0-03.9	18:12:22.6	-26:32:44.7	Eamrs	18:12:27.8	-26:36:28.5*	148.8	VLT
30	005.2+05.6	17:36:23.4	-21:31:08.0	Ers	-	-	165.5	VLT
31	005.5+06.1	17:35:20.6	-20:57:17.4	Ears	-	-	127.1	VLT
32	005.5-04.0	18:13:40.5	-26:08:28.4	E	-	-	125.1	VLT
33	005.8-06.1	18:22:54.1	-26:49:17.1	Emps	-	-	64.0	VLT
34	005.9-02.6	18:09:12.4	-25:04:22.1	Bs	18:09:12.3	-25:04:34.5	69	VLT
35	006.1+08.3	17:28:57.5	-19:15:41.7	E	-	-	92.5	*HST*
36	006.3+03.3	17:47:33.2	-21:47:16.9	E	-	-	-	VLT

Table 3.1: Summary of VLT PN observational results (continued)

No.	PN G	Centroid Coords.		Morph.	Central Star Coords.		EPA	Tele.
		RA(J2000)	DEC(J2000)		RA(J2000)	DEC(J2000)	(±5°)	
37	006.3+04.4	17:43:29.1	-21:09:40.1	E	17:43:28.7	-21:09:51.8	115	*HST*
38	006.4+02.0	17:52:40.5	-22:21:58.2	Eas	17:52:41.4	-22:21:57.1	26.7	*HST*
39	006.4-04.6	18:18:12.9	-25:37:57.7	E	-	-	2.5	VLT
40	006.8+02.3	17:52:22.2	-21:51:02.3	Bmps	-	-	4.7	VLT
41	006.8-03.4	18:14:29.6	-24:43:36.4	Bs	-	-	69	VLT
42	007.0+06.3	17:38:10.8	-19:37:31.6	Bms	-	-	14.4	VLT
43	007.0-06.8	18:27:58.7	-26:06:46.0	Bm	-	-	173	VLT
44	007.5+07.4	17:35:10.2	-18:34:20.4	Ramr	-	-	-	VLT
45	007.6+06.9	17:37:22.6	-18:46:36.7	Bams	-	-	62.6	VLT
46	007.8-03.7	18:17:15.9	-23:58:53.6	Baps	-	-	170.8	VLT
47	007.8-04.4	18:20:08.8	-24:15:05.0	E	18:20:08.8	-24:15:05.3	25	*HST*
48	008.2+06.8	17:38:56.9	-18:17:25.9	E	17:38:57.3	-18:17:35.9	66.5	*HST*
49	008.4-03.6	18:18:24.7	-23:24:51.0	Eamps	18:18:09.6	-23:26:41.4*	157.4	VLT
50	008.6-02.6	18:14:51.7	-22:43:51.0	Bap	18:14:50.9	-22:43:55.5*	162	*HST*
51	009.4-09.8	18:44:43.0	-25:21:34.8	Emrs	-	-	85	VLT
52	009.8-04.6	18:25:04.9	-22:34:52.6	Ears	-	-	30	VLT
53	350.5-05.0	17:42:53.3	-39:36:17.4	Er	-	-	123	VLT
54	351.1+04.8	17:03:47.7	-33:29:39.2	E	17:03:46.8	-33:29:44.6	138	*HST*
55	351.2+05.2	17:02:19.0	-33:10:04.9	Bp	-	-	120.5	VLT
56	351.6-06.2	17:50:44.5	-39:17:25.9	Eaps	-	-	129.5	VLT
57	351.9+09.0	16:50:17.1	-30:19:55.4	B	16:50:17.0	-30:19:55.9*	7.5	VLT
58	351.9-01.9	17:32:59.6	-36:43:52.1	Emps	17:33:00.6	-36:43:52.9*	50	*HST*
59	352.0-04.6	17:45:07.6	-38:08:44.9	Bmps	-	-	157	VLT
60	352.1+05.1	17:05:31.1	-32:32:00.2	Bmrs	-	-	124	VLT
61	352.6+03.0	17:14:42.5	-33:24:37.5	Bprs	-	-	141.5	*HST*
62	353.2-05.2	17:50:44.6	-37:23:45.7	Bmprs	-	-	43	VLT
63	353.3+06.3	17:04:18.3	-30:53:28.8	Bp	-	-	32.6	VLT
64	353.7+06.3	17:05:13.9	-30:32:07.7	Eamrs	17:05:14.0	-30:32:19.3	2.5	VLT
65	354.5+03.3	17:18:52.1	-31:38:56.7	E	-	-	101	*HST*
66	354.9+03.5	17:19:19.2	-31:12:41.2	E	17:19:20.2	-31:12:40.9*	104.5	*HST*
67	355.1-06.9	18:02:31.4	-36:39:08.8	R	-	-	5	VLT
68	355.4-02.4	17:44:21.3	-34:06:36.1	Bps	17:44:20.6	-34:06:40.8*	148.5	*HST*
69	355.6-02.7	17:46:06.3	-34:03:45.3	E	-	-	-	VLT
70	355.9+03.6	17:21:31.5	-30:20:37.7	Eps	-	-	108.4	*HST*
71	355.9-04.2	17:52:58.9	-34:38:11.4	E	17:52:58.9	-34:38:22.9	10.4	*HST*
72	356.1-03.3	17:49:51.4	-34:00:23.1	Bas	-	-	49.8	*HST*

Table 3.1: Summary of VLT PN observational results (continued)

No.	PN G	Centroid Coords.		Morph.	Central Star Coords.		EPA	Tele.
		RA(J2000)	DEC(J2000)		RA(J2000)	DEC(J2000)	(±5°)	
73	356.3-06.2	18:02:32.7	-35:13:08.2	Eas	-	-	71.1	VLT
74	356.5-03.6	17:51:50.0	-33:47:27.0	Bas	-	-	58.2	*HST*
75	356.8+03.3	17:25:05.1	-29:45:12.7	Ers	-	-	170.3	*HST*
76	356.8-05.4	18:00:18.0	-34:27:27.4	E	-	-	68.7	VLT
77	356.9+04.4	17:21:03.8	-29:02:52.2	E	-	-	39.4	*HST*
78	357.0+02.4	17:28:49.7	-30:07:37.3	Ears	-	-	104.3	VLT
79	357.1+03.6	17:24:33.6	-29:24:10.5	E	-	-	-	VLT
80	357.1+04.4	17:21:37.0	-28:55:14.7	E	-	-	33.7	VLT
81	357.1-04.7	17:58:15.3	-33:47:32.5	Ers	-	-	75.5	*HST*
82	357.2+02.0	17:31:08.0	-30:10:27.9	Rar	-	-	-	*HST*
83	357.3+04.0	17:23:24.5	-28:58:56.4	E	-	-	-	VLT
84	357.5+03.1	17:27:24.3	-29:21:14.5	S	-	-	167.5	VLT
85	357.5+03.2	17:26:59.7	-29:15:31.8	Bs	-	-	132	VLT
86	357.6-03.3	17:53:16.7	-32:40:38.5	Bs	17:53:16.8	-32:40:38.4	33	VLT
87	357.9-03.8	17:56:14.2	-32:37:19.4	Ers	17:56:13.9	-32:37:23.2★	66	VLT
88	357.9-05.1	18:01:21.2	-33:17:37.8	Bas	-	-	31.5	VLT
89	358.0+09.3	17:05:43.7	-25:24:59.9	Emps	17:05:44.5	-25:25:02.1★	14	VLT
90	358.2+03.5	17:27:32.5	-28:30:57.2	E	-	-	64.5	VLT
91	358.2+04.2	17:24:52.1	-28:05:54.6	S	-	-	166	VLT
92	358.5+02.9	17:30:30.7	-28:35:45.1	Bp	17:30:30.4	-28:35:54.9★	158.5	*HST*
93	358.5-04.2	17:59:03.2	-32:21:39.4	E	17:59:02.5	-32:21:43.6★	116.5	*HST*
94	358.6+07.8	17:12:39.6	-25:43:28.7	Bs	17:12:39.2	-25:43:38.6★	13.5	VLT
95	358.6-05.5	18:04:55.4	-32:54:00.6	Es	18:04:56.3	-32:54:01.6★	130.5	VLT
96	358.7+05.2	17:22:29.2	-27:08:40.5	Es	17:22:28.2	-27:08:42.5★	67.5	*HST*
97	358.8+03.0	17:31:08.3	-28:14:48.8	Ears	17:31:09.4	-28:14:50.9★	60.5	VLT
98	358.9+03.4	17:30:02.2	-27:59:05.9	E	-	-	74.5	*HST*
99	359.0-04.1	17:59:55.9	-31:54:19.5	Bps	-	-	40	VLT
100	359.1-02.9	17:55:05.1	-31:12:07.2	Bs	-	-	65.5	VLT
101	359.2+04.7	17:25:44.0	-26:57:35.7	E	17:25:44.0	-26:57:48.0★	138.5	*HST*
102	359.3-01.8	17:51:18.3	-30:23:45.3	Bps	17:51:28.2	-30:27:01.1	54.3	VLT
103	359.6-04.8	18:04:08.6	-31:39:06.2	Bs	-	-	66.4	VLT
104	359.7-01.8	17:52:06.4	-30:05:05.2	Rmr	17:51:54.4	-30:07:59.5★	-	VLT
105	359.8+02.4	17:35:47.2	-27:43:20.0	E	-	-	126.1	VLT
106	359.8+03.7	17:30:45.9	-27:05:55.8	E	-	-	11.9	VLT
107	359.8+05.2	17:25:23.2	-26:11:44.1	Bmps	17:25:28.9	-26:15:24.9★	28.8	VLT
108	359.8+05.6	17:24:01.0	-25:59:14.8	Bps	-	-	75.5	VLT

Table 3.1: Summary of VLT PN observational results (continued)

No.	PN G	Centroid Coords.		Morph.	Central Star Coords.		EPA	Tele.
		RA(J2000)	DEC(J2000)		RA(J2000)	DEC(J2000)	(±5°)	
109	359.8+06.9	17:19:14.0	-25:17:13.0	Bps	-	-	68.4	VLT
110	359.8-07.2	18:14:51.1	-32:36:44.6	Bmps	-	-	151.7	VLT
111	359.9-04.5	18:03:52.0	-31:17:38.9	E	-	-	139.0	VLT

* Not previously catalogued

Most of the VLT images that were taken with short exposure time (42 less than 10s in which 23 less than 5 s) because of the pre-imaging purpose, resulting in poorer image quality compared with the HASH DB. However, 19 CSPNe could be discerned in which 15 CSPNe have not been catalogued in previous studies. Also, among the 111 PNe in the new ESO VLT observation, 36 objects also have observational data available from the *Hubble Space Telescope* (*HST*). The high-resolution *HST* images supplement the CSPN coordinates of 24 PNe in which 1 were observed in the VLT as well. In total, 43 CSPN were seen and 29 of them were newly discovered. The image showing the CSPN from the VLT could be found in Appendix C. The improvements with the VLT data are summarised in Table 3.2.

Table 3.2: Improvement of the combined VLT and *HST* observation

Improvement	Description
Morphology Classification	Resolved 7 point-like and 7 elliptical PNe, 5 round PNe, 28 PNe have clearer sub-structures observed
Central Star	19 new CSPNe observed from the VLT, 24 from the *HST*

3.4.1 Morphological Classification Revisit

With the 'ERBIAS' morphological classifier, the total number and ratio of each main class are shown in Fig. 3.3. In total, the morphological classifications of 29 PNe, using the VLT data, deviate from the HASH DB. The main morphological classifications of 19 PNe are different from the HASH DB, in which 7 objects that were originally identified as 'S' show clear morphologies with the better image quality and 7 elliptical PNe now show clear bipolar features.

Also, for 28 objects, although their main morphological classes remain the same as in HASH DB, they are seen with more structural details. Among them, 8 PNe have one-sided enhancement in brightness ('a'), 5 were observed with multiple shells ('m'), the point-symmetry features of 8 PNe were revealed ('p'), 2 show a ring structure in their internal regions ('r') and 18 of them were first time seen with a resolved internal structure ('s'). These result in more accurate classifiers for their morphologies. Nonetheless, several PNe have images with no obvious improvement and the possible reasons include the lack red images, the short exposure time as well as the small size of the object. PNe with improved morphological classifications are summarized in the following.
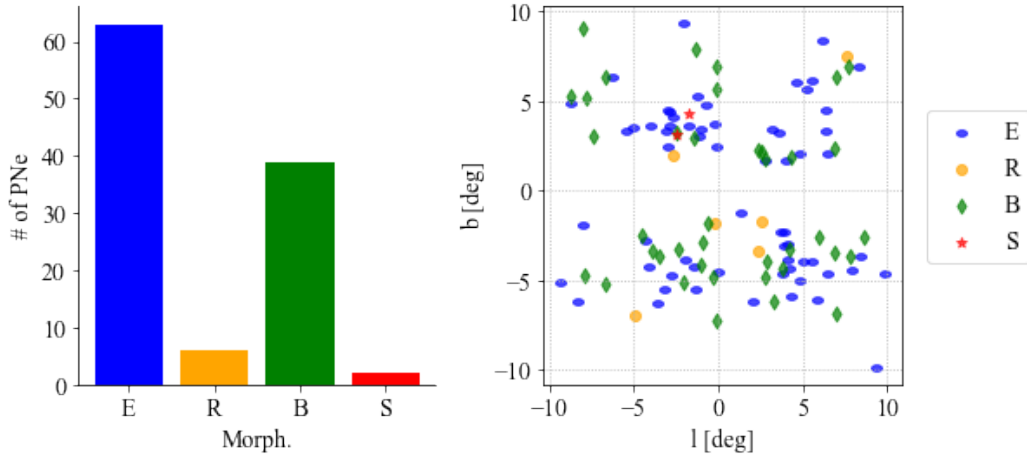
Figure 3.3: Total number and proportion of morphological classifications for the VLT data (upper panel) and the distribution of PNe with different morphologies in the Galactic coordinate system (lower panel).

Change in Main Classifiers

No.	PN G	Morph.	Characteristics
23	004.2-04.3	E → Bs	The image is like the equatorial torus-like structure of a bipolar PN, internal over-densities are resolved.
29	005.0-03.9	Rrs → Eamrs	Clear multiple-shell structure and out elliptical envelope is slightly elongated along EW.
32	005.5-04.0	R → Ears	The elliptical nebulosity is seen with over-densities like a ring structure, slightly elongated along SW to NE.
33	005.8-06.1	R → Emps	A point-symmetrical multiple-shell structure is seen. One of the outer envelopes is elongated along NS, another span along WE.
39	006.4-04.6	S → Eas	The nebula is seen in an elliptical shape elongated along SW to NE. An over-density seen on SW which is like an arc structure but unclear.
40	006.8-03.4	S → B	The image shows the central regions of two faint lopes and over-densities in the internal region are discernible.
41	006.8+02.3	R → Bmps	Clear bipolar feature seen with a point-symmetric structure. The outer envelope is elongated along NS.
43	007.0-06.8	E → Bms	Clear bipolar feature with a multiple-shell structure. Two faint lopes (not quite point-symmetric) elongated along NS, the central regions is bright.
46	007.8-03.7	Em → Baps	A elongated point-symmetric bipolar feature is seen and over-densities in the internal region are in the directions of elongation.

No.	PN G	Morph.	Characteristics
53	350.5-05.0	S → Er	The elliptical nebulosity is seen with an internal ring structure in the color image.
57	351.9+09.0	R → Eamps	A multiple-shell elliptical structure is seen, the outer envelope is elongated along NS. The over-densities in the internal regions is seen in the SW and NE directions. The central star is discernible.
59	352.0-04.6	E → Bmps	Two outer elongated elliptical envelopes along SN and SW to NE respectively. The bright central region is like a torus of a bipolar PN.
60	352.1+05.1	Em → Bmrs	The outer envelope is faint, which might be two lopes of a bipolar PN. A bright central ring structure is seen in the H\alpha image.
63	353.3+06.3	S → Bp	Can only seen a point-symmetric nebulosity, might be a bipolar PN.
64	353.7+06.3	S → Eamrs	Clear arc around the inner region together with inner structures and over-densities. The outer envelope of elliptical and slightly elongated.
89	358.0+09.3	Em → Emps	An elliptical outer envelope is seen and internal structures is resolved. The over-densities are exhibiting a S-shape. The central star is discernible.
94	358.6+07.8	S → Es	Possible elliptical shape and internal structures is slightly resolved. Might be able to see the central star in a better resolution.
106	359.8+03.7	E → Bmps	The bipolar features are discernible together with a point-symmetric structure.
108	359.8+05.6	S → Bps	Clear bipolar lopes are seen which are elongated along SN with nearly perfect point-symmetry.

Change in Sub-Classifiers

No.	PN G	Morph.	Characteristics
2	002.0-06.2	Em → Ems	The multiple shells and internal over-densities are discernible, however, unclear.
6	002.6+02.1	Bms → Baps	The bipolar feature is clear with two jets along NW to SE which has a point symmetry. The internal structure is see with over-densities, filaments and knots.
9	002.8+01.8	Bs → Bas	Two outflows along NW to SE could be observed, therefore, a bipolar PN. Internal over-densities seen on the E direction.

No.	PN G	Morph.	Characteristics
12	003.2-06.2	Bmp → Bmps	A equatorial torus-like structure is seen with two point-symmetric outflows having a S-shape. Over-densities are seen in the outflows.
15	003.7-04.6	E → Ea	Slightly elongated elliptical PN with stronger surface bright-ness in the N direction.
17	003.9-02.3	Ea → Eas	Elliptical PN with two arcs and irregularities in the brightness. The arcs in the SW is brighter.
18	003.9+01.6	E → Ea	The elliptical structure of PN is obvious with a pair of symmetric jets from NE to SW in PA = 140°. The internal region have a higher surface brightness towards SE.
25	004.3+01.8	Ba → Bap	Two lobes with closed ends is seen and the overall shape of lobes exhibits a point symmetry.
28	004.8-05.0	E → Emr	Elliptical PN with two outer shells discernible, the ring-structure is clear.
30	005.2+05.6	Er → Ers	Elliptical PN with two jets along NW. Two symmetric arcs could be easily identified. The inner region shows irregularities in brightness with a faint central star.
34	005.9-02.6	B → Bs	Bipolar PN with two huge jet-like features clearly visible with over-densities and irregularities in brightness. The central star is bright.
44	007.5+07.4	Rar → Ramr	Bright PN with a round appearance. It has a faint external elliptical shell and an internal ring structure with a higher density in the NW.
51	009.4-09.8	Er → Emrs	A bright elliptical ring-like internal structure is seen withe filaments. An outer elliptical envelope with two jest along EW is easily discernible.
52	009.8-04.6	Ear → Ears	It shows an elliptical envelope with a possible internal ring structure of filaments and irregularities in brightness.
55	351.2+05.2	B → Bp	Clear multipolar appearance with two symmetric jets in N and S and another two in the E and W. The central region is bright.
56	351.6-06.2	Er → Eaps	A clear bipolar-core PN with outer elliptical nebulosity. The core exhibits a point symmetry with irregularities in brightness.
62	353.2-05.2	Brs → Bmprs	The outer lopes is clear with a point symmetry and arcs. The internal structure is a bipolar core with higher brightness towards NE and SW.

No.	PN G	Morph.	Characteristics
73	356.3-06.2	E → Eas	An outer elliptical envelope is seen with arc structures. The arc at N has a higher surface brightness. The internal filaments is resolved.
80	357.1+04.4	Er → Ers	The outer elliptical nebulosity with two internal arcs are seen. The arc structure has a point-symmetry. Internal filaments is discernible.
85	357.5+03.2	B → Bs	A bipolar PN with no obvious symmetry. There are irregularities in the waist.
86	357.6-03.3	Ba → Bs	A bipolar PN with a filamentary waist that looks like a torus. The CSPN is evident.
88	357.9-05.1	B → Bas	The huge outer jets and irregularities in brightness in the central region are resolved and impressive in the red image.
97	358.8+03.0	Ear → Ears	A ring-like internal structure is observed with irregularities and an enhancement in brightness towards SE, the central star is evident. The shape is more likely to be round.
99	359.0-04.1	B → Bps	Possible bipolar PN with two pairs of symmetric jets. The prominent pair of jets have a PA = 56° and another has a PA = 11°.
100	359.1-02.9	B → Bs	A bipolar with no obvious symmetry. Two filamentary lobes is seen. The waist has over-densities at the edges.
102	359.3-01.8	B → Bps	Two lopes along the SN direction, indicating a bipolar PN. The waist has a certain spiral structure. The central star is discernible.
104	359.7-01.8	R → Rmr	An outer round envelope with ring structures is clear and another elliptical shell in the inner region. The central star is discernible. There is an enhancement in surface brightness in the NE.
107	359.8+05.2	B → Bps	Two giant outflows in N and S directions are seen, therefore, a bipolar PN. The over-densities in the waist is resolved and the central star is evident.

3.4.2   Central Stars of PNe

Combined with the *HST* data, 38 CSPNe were discovered, in which 19 are from the VLT and 24 are from the *HST*. More excitingly, 29 of the observed CSPNs have not been previously catalogued in Weidmann et al. 2020.

For 19 PNe observed with the VLT, the central stars are discernable, which allowed us to measure the central star coordinates. Moreover, one of the CSPNe (that of PN G358.5-04.2)

were observed through both VLT and *HST*, which allows a brief comparison between the observational results. The differences in the RA and DEC, (Δ RA, Δ DEC) in the unit of arcsecs, measured is (0.03, 1.42) respectively. After checking of the coordinates of three close stars to the object, the resultant errors between the VLT and *HST* images is (0.05, 1.46). Thus, the coordinate of the CSPN obtained with two telescopes are consistent. The difference may come from the data reduction pipelines.

Also, for the 13 previously cataloged CSPNe, three of them were measured through the VLT (PNG005.9-02.6, PNG353.7+06.3, and PNG357.6-03.3). The coordinates obtained with the VLT images were compared with the catalogue of CSPNe (Weidmann et al. 2020) which give a derivation of (0.6, 1.2), (0.2, 0.3), (0.0, 0.0) respectively.

3.4.3   Position Angles

The orientations of each PNe were measured with images from both the VLT and the *HST* where available. The position angle (PA) of the projected major axis was measured from the north towards the west which is in the equatorial coordinate system. Thus, these angles are also referred to as EPA. The elongated axes were determined visually and the line that can better represents the long symmetry axis of the PN was chosen.
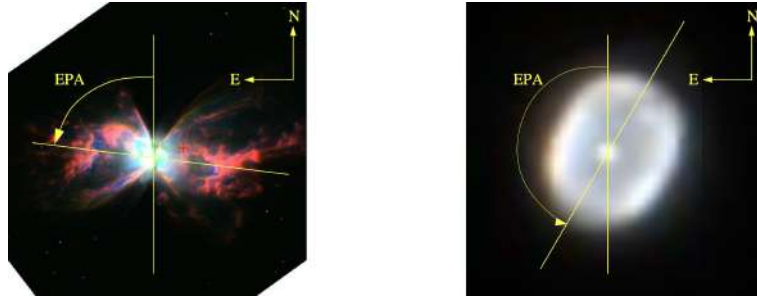
Figure 3.4: Typical examples of measuring the Equatorial Position Angle. [100]

To determine the uncertainties in the PA measurements, the PAs of 3 PNe were measured independently by two people. This gives the largest difference between the two measurement is 5° which was considered as the random error in the PA measurement. The measuring approach is illustrated in Fig. 3.5.

Among 111 samples from the VLT, the position angles of 10 PNe (PNG 001.3-01.2, PNG 003.6-02.3, PNG 004.2-04.3, PNG 006.3+03.3, PNG 007.5+07.4, PNG 355.6-02.7, PNG 357.1-04.7, PNG 357.2+02.0, PNG 357.3+04.0 and PNG 359.7-01.8) were not measurable. This is because that the objects PNG 001.3-01.2, PNG 006.3+03.3, PNG 355.6-02.7, PNG 357.1-04.7 and PNG 357.3+04.0 have fuzzy and point-like images, the morphologies of PNG 007.5+07.4, PNG 359.7-01.8 and PNG 003.6-02.3 are nearly round, the object PNG 357.2+02.0 shows a perfect ring structure and the object PNG 004.2-04.3 has an unclear outer structure. For 27 PNe with *HST* images, the measured PA with the *HST* images were compared with that from the
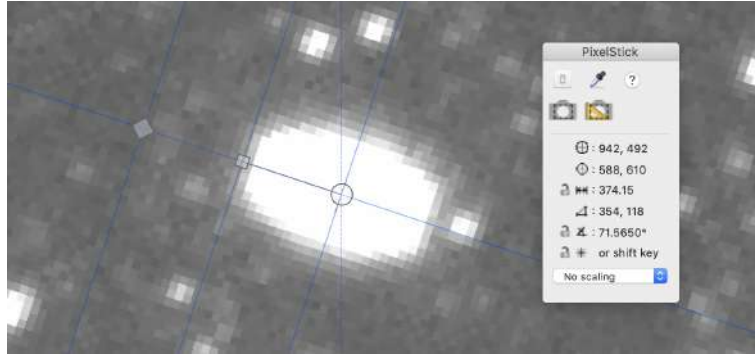
Figure 3.5: Example of measuring criteria for the object PNG003.2-06.2. The image is in the WCS and the N is up and E is left.

VLT. For most of the object, the difference between PA measured from two telescopes is less than $10°$ which is within the random error of the measurement, and therefore these results can be concluded as accurate.

However, for 7 objects (PNG 007.8-04.4, PNG 351.1+04.8, PNG 352.6+03.0, PNG 355.9+03.6, PNG 356.8+03.3, PNG 357.1-04.7 and PNG 358.5-04.2), the differences are relatively large. The images of these objects are shown in Appendix D. For the object PNG 007.8-04.4, the near stars show a relatively uniform orientation, thus, there would be a degree of distortion for the image which could possibly result from the flat-fielding in the data reduction pipeline. For the objects PNG 351.1+04.8 and PNG 352.6+03.0, PNG 355.9+03.6, PNG 356.8+03.3 and PNG 357.1-04.7 the *HST* images give a more accurate result because of the image quality, so for the VLT, the short exposure time resulting in insufficient emission from the outer jets accumulated for these objects. Besides, for the object PNG 358.5-04.2, as the F656N $H\alpha$ narrow-band filter was applied, the *HST* image was compared with the $H\alpha$ image from the VLT, the outer shells of the PN are not visible in the VLT image.

Chapter 4

Chemical abundances in the Galactic Bulge from PN observations

4.1 Introduction

PNe, as the ejected envelope of AGB stars, effectively log any modification of chemical composition at its progenitor surface. They trace both the products of hydrogen and helium burning, i.e., He, C, N, O, Ne, S, Cl, and Ar. The alpha elements O, Ne, S, Ar and Cl produced in massive stars are believed unaltered during the evolution of CSPNe so used to characterize the ISM at the time of formation of the progenitor stars of PNe. Elements including He, C, and N that are produced in low-to-intermediate mass stars in PNe allow tracing chemical evolution in their progenitors.

Different mixing episodes happen during the evolution of a PN progenitor. When the stellar core is exhausted of hydrogen, helium burning turns into a core of carbon and oxygen during the red giant (RGB) phase, meanwhile, the outer convective envelope deepens as the star expands, resulting in the bringing up of hydrogen burning products into the convective envelope. This is referred to as the first dredge up leading to an enhancement in surface N abundance of the progenitor at the expense of C. Similarly, the second dredge-up happens when a star with a mass higher than $4M_\odot$ is exhausted of helium and enters the AGB phase, resulting in excesses of He/H at the surface and decreases of C and O relative to N. Thermal pulses produced during the AGB phase creates convective envelopes. The third dredge-up (TDU) occurs every time in the aftermath of a thermal pulse and the convective envelope penetrates deep into the shells of hydrogen and helium burning, transporting helium, and more importantly, carbon to the surface. For stars more massive than $\sim 4\ M_\odot$, the convective envelope could extend all the way down to the H-burning shell during the 'inter-pulse' phase, resulting in nucleosynthesis from a hot bottom burning (HBB). The HBB process converts C at the surface to N.

As a result, the amount of N and C changes with the evolution of PN progenitors while the

elements O, Ne, S, and Ar are also known as the α-elements undergo virtually no variation from the environment as the PN progenitor forms, as well as Cl. Therefore, these elements could be used to trace the chemical evolution at the position of PNe, here, the Galactic Bulge.

This chapter aims to help to disentangle the formation scenario in the Galactic Bulge using PNe. The Galactic bulge is dominated by old stars and some are the oldest stars in the Galaxy. However, few studies on Galactic archaeology show the existence of a young population with super-solar metallicities in the bulge, eg. Bensby et al. (2017) and Ferraro et al. (2020). This brings a long dispute on the origin of the bulge on whether it is a classical bulge made by a major galaxy merger, or it is a pseudo-bulge built from secular stellar evolution in a precursor disk as these two models lead to entirely different metallicity distribution and star formation history (SFH) (Bensby et al. 2018). Previous studies of bulge PNe show a generally sub-solar metallicity, indicating an overall old population as expected from a classical bulge. This spectroscopic and imaging data of a significant sample of compact PNe taken from the ESO VLT in this study is providing the current largest sample of this population with a much better resolution than previous attempts. With careful data reduction, this chapter is going to give an accurate line of evidence for bulge formation models from a PN perspective.

4.2   Data reduction and Analysis

A log of the observations is shown in Table. B.1. The two-dimensional long-slit spectra were reduced with an adopted multi-step method. The cosmic rays were removed using a python implementation of the `L.A.Cosmic` algorithm. The standard reduction procedure including bias subtraction and wavelength calibration was carried out using the ESO pipeline with a `Reflex` workflow. As the bright skylines such as [OI]$\lambda\lambda$ 5577, 6300 and 6363 become strongly inhomogeneous in long red exposures in the spatial direction. A careful sky subtraction was performed using the `STARLINK` package `figaro` through spline line fitting in sky windows chosen below and above the object. In addition, the Galactic bulge has a dense stellar population, the spectra are contaminated by star continua. The background source and the central star emissions were removed with the `iraf` task `continuum`. The sky-subtracted and continuum-removed spectra were then flux-calibrated again with the ESO pipeline. Before extracting 1D spectra, to maximise the signal-to-noise ratio in the frame, especially for weaker lines, the methods here were adopted: a signal was considered to be attributed to an emission line only when it and at least half of its neighboured pixels are stronger than 2σ of the average background noise while the remaining background pixels were set to zero before extracting 1D spectra. 1D spectra were obtained after summing the frame perpendicular to the dispersion direction. The mean systematic errors associated with the wavelength calibration and flux calibration were estimated to be 5%.

The emission lines fluxes were measured using the `ALFA` algorithm from the extracted one-dimensional spectra (Wesson 2016). `ALFA` derives fluxes through performing Gaussian fits with parameters optimized through a generic algorithm, together with uncertainties from the RMS of residuals after subtracting the fitted lines. Saturated emission lines on long exposures were

identified by locating saturated pixels on the raw images and corrected using either the short exposure measurements multiplying a scale factor between two exposures or theoretically constant line intensity ratios and the corresponding unsaturated line measured from the same spectrum. The correction is effective, generally giving an uncertainty up to 2%. For objects with both long and short exposures saturated, literature values of line ratios in Acker (1992) were used for the correction provided that unsaturated strong emission fluxes agree within the uncertainty estimates. The line fluxes of 118 out of 138 observed PNe were derived while the remaining 19 PNe are either with no published measurements or the fluxed measured from our spectra exhibit a certain derivation from the literature.

The code `NEAT` was then used to compute the ionic and elemental abundances (Wesson et al. 2018). For the reduced 1D flux-calibrated spectra, `NEAT` first corrected for the interstellar extinction assuming the extinction law of Fitzpatrick (1999). The final logarithmic extinction took the flux-weighted results from ratios Hγ/Hβ and Hδ/Hβ from the blue spectra by assuming S/N is good enough for both line ratios while Hα was using to derive scale factor between the red arms and the blue arms. The red arms were scaled such that the measurements of Hα relative to Hβ match the extinction measured from the blue arms. Accurate measurements of hydrogen Balmer ratios are crucial to this study. Methods other than line fitting through `ALFA` were applied to obtain the Hα, Hβ, Hγ and Hδ line fluxes which include a manual deblending of Hα and [N II] emission lines and line fitting performed using the `iraf.splot` task, summing flux-calibrated frame pixels corresponding to the emission lines and subtracting the average background taking from the neighbouring pixels on the left and the right and line fitting on the wavelength length range of Hβ, Hγ and Hδ lines through a self-developed Gaussian fitting `Python` script. The derived line fluxes using different methods are consistent with each other. Thus, it can be concluded that the extinction values obtained are reliable.

4.2.1 Evaluation of Data Quality

For all PNe, certain forbidden lines originated from the same energy level having their line-intensity ratios theoretically predicted to be constant according to their transition probabilities were used to evaluate the quality of spectroscopic observations, reduction procedures as well as the line fitting method used in this work. One of them is the [O III] $\lambda5007/\lambda4959$ with the theoretical value of 2.98. This was used to correct the saturated [O III] $\lambda5007$ line when [O III] $\lambda4959$ is unsaturated. The observed reddening-corrected [O III] $\lambda5007/\lambda4959$ intensity ratios measured from non-saturated spectra with error bars is shown in Fig.4.1 together with the 10% uncertainty interval from flux calibration of the two emission lines. Larger deviations of the line intensity ratios are due to either weak [O III] emissions or the uncertainties in extinction correction because of faint Hβ lines. For most of the PNe, [O III] line ratios agree with the theoretical value within an uncertainty of 1.8%.

The comparison was also performed between the observed [N II] $\lambda6584/\lambda6548$ doublet line intensity ratio and its theoretical value of 3.05 as shown in Fig.4.2. Although a certain scattering for intermediate brightness lines, the mean observed [N II] $\lambda6584/\lambda6548$ ratios agrees with the
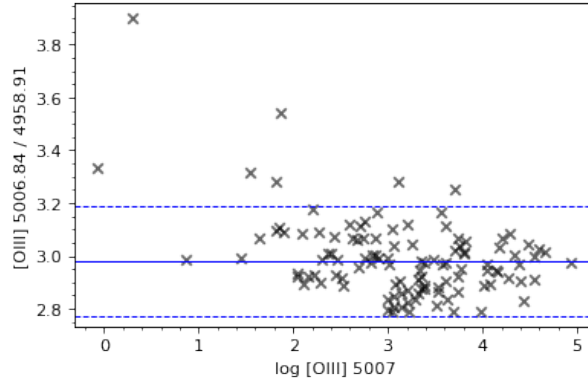
Figure 4.1: Intensity ratios of the [O III] λ5007 and λ4959 emission lines against the log([O III] λ5007) flux in erg cm^{-2}s^{-1} for 112 PNe. Any saturated spectrum was excluded. The solid line represents the theoretical value 2.98 while dashed lines correspond to 7% deviation from it, corresponding to a typical uncertainty in the data reduction. Outliers are due to either weak [O III] emissions or the uncertainties in extinction correction because of faint Hβ lines.

theoretical value within 0.4% with a standard derivation of 0.25. Large uncertainties are mainly from blending of [N II] λ6548 line with Hα lines which might lead to an underestimation of the λ6548 line when Hα is prominent in low-excitation PNe or an overestimation when Hα line is saturated and results in 'overflowed' pixels. We present the unsaturated spectral observations in the region of [N II] and Hα lines for six PNe with [N II] λ6583 greater than 100 and the deviation in [N II] line ratios from the theoretical values larger than 1 in Fig.4.3, in which the reddening has not been corrected. One could see that most of the PNe are suffering from large residuals in their flux measurement, this could not be resolved if we repeat measurement or change configurations (population size or detection limit) in `ALFA`. However, such uncertainties are well-reflected in the errors in line fluxes. For PNG 359.8+05.2, it is a faint source with the emission lines passed across by 3 nearby stars as well as multiple skylines, [N II] line ratio measured is 2.24$^{+1.45}_{-0.95}$ which containing the theoretical value.

Fig.4.4 presents the derived logarithmic extinction values, c($H\beta$) against literature values available. For 101 PNe, the catalogued Hα and Hβ fluxes are available in the Strasbourg-ESO Catalogue (Acker et al. 1992), this gives the largest set of data for the comparison in this work. Their extinction values were derived from catalogued Hα/Hβ line ratios in a consistent manner, however, showing large deviation when comparing multiple results of the sample object (e.g. Giammanco et al. 2011). This might be due to the theoretical value of Balmer line ratios (theoretical Hα/Hβ ratio = 2.85 in their calculation) adopted and the extinction law and constants used could also have a minor influence. The catalogued data is, therefore, used for an overall statistical consideration only. In Fig.4.4, a considerable spread is seen between the observed and catalogued extinction values, however, due to the quality of the catalogued data, the data is usually used for statistical consideration only. The Pearson's correlation coefficient of the observed and catalogued extinction values is 0.8, which indicates a strong correlation.
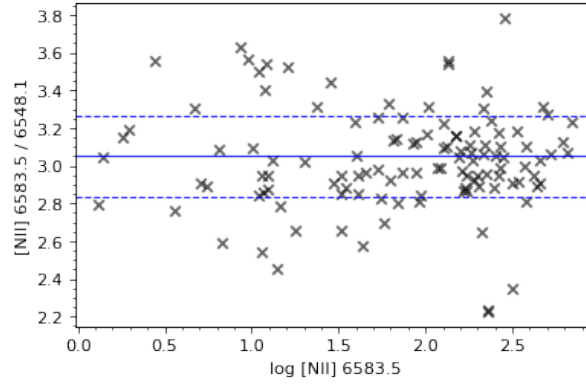
Figure 4.2: Intensity ratios of the [N II] λ6584 and λ6548 emission lines against the log [N II] λ6584 flux in erg cm^{-2}s^{-1} measured in 117 PNe. Any saturated spectrum was excluded. The solid line represents the theoretical value 3.05 while dashed lines correspond to 7% (the uncertainty in our data reduction) deviation from it. Derivations from the theoretical value mainly come from blending of [N II] and Hα lines.
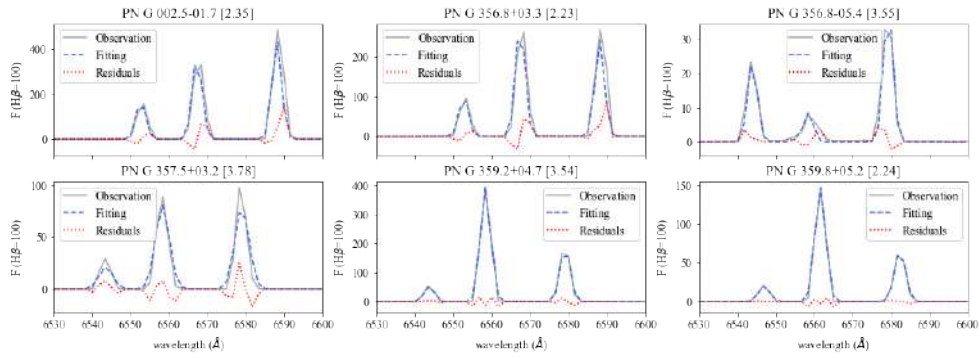
Figure 4.3: Unsaturated spectra of 6 PNe with [N II] ratios greater than 3.55 or less than 2.55 in the wavelength range from 6530 to 6600 Å (interstellar extinction has not been corrected). The value in the square bracket is the [N II] line ratio measured in this object.

Comparisons of obtained extinction values made with those derived from deep high/medium-resolution spectra in previous works are presented in Fig.4.5. 20 PNe in this sample have data available in Escudero et al. (2004), 35 available in Gorny et al. (2009), 6 available in Gorny (2014) and 2 available in García-Rojas et al. (2012), hereafter ECM04, GCS09, G14 and GPM12 respectively.

For ECM04, there is a good overall agreement between our derived C(Hβ) values with 75% values agreeing within ±0.27. The outliers are either possessing bright central stars or weak Hβ fluxes, one of which the extinction value is measured as 0.0 in ECM04, thus, it is considered unreliable. For GCS09 and G14, except few large deviations at low extinction in either observed or literature values, the observed results have a typical difference of −0.3 from the literature results. Such derivation is attributed to the difference in slit aperture sizes. The 0.7" wide slit aperture employed in this work allows a higher spectral resolution of PNe with little influence on the blending of the Hα line at 6563 Å with the [N ii] line at 6548 Å while such
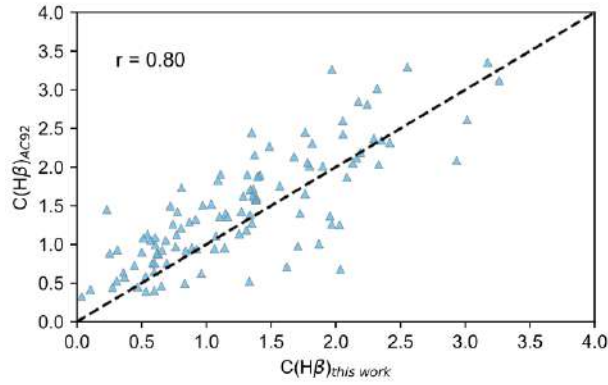
Figure 4.4: The logarithmic extinction c(Hβ) measurements in this work are plotted against data in Acker (1992). The Pearson correlation coefficient is 0.8.
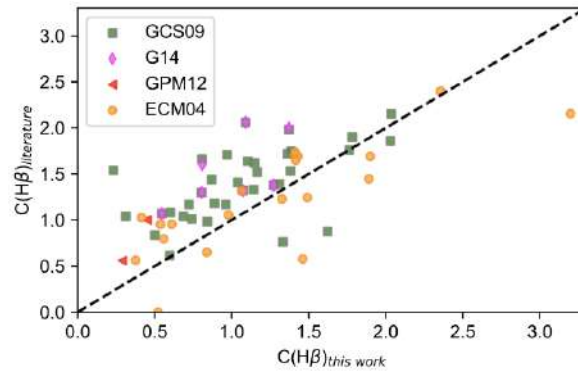
Figure 4.5: Measure logarithmic extinction c(Hβ) compared against other measured $C(H\beta)$ from the literature. The green squares are data from GCS09, pink diamonds are those from G14, two red triangles are data from GPM12 and the yellow dots are those from ECM04. The systematic difference seen in the comparison with GCS09 and G14 might be due to their spectrum background removal method.

effects are substantial for the 2" wide slit aperture. The Hα fluxes were corrected in GCS09 by subtracting from the measured sum of Hα and [N II] λ6548 intensities the value of the [N II] λ6584 intensity divided by 3.05, however, not reddening corrected, there will be some over-subtractions in the Hα fluxes. Other possible reasons are: difficulty in separating nebular emissions from extremely bright stellar continuum spanning along the dispersion direction, the uncertainties in flux calibrations and measurements for weak Hβ lines and treatment of saturated lines in the latter work. Although different extinction laws were adopted, such influences on extinction values are insignificant. A comparison was made between the red arm spectra in Fig. 6 in GCS09 and in this work where available. It shows that our spectra have either a higher S/N even for line intensities below 0.6% of Hα lines or more weak emission lines resolved while such weak lines are noisy in GCS09, this indicates an overall higher background noise level used to differentiate emission lines was present in GCS09. Thus outer weak pixels of emission lines in their spectroscopic image might be set as the background, the actual flux could

therefore be underestimated. Such effect would be smaller in this work as the S/N of 2D spectroscopic images increases. This should have a greater effect in weak lines (Hβ and Hγ in this case) and cause a larger fraction of reduction in fluxes, therefore, a higher Hα/Hβ or Hβ/Hγ ratio.

The extinction values are also systematically lower than that in GPM12 in which the MIKE instrument on the Clay 6.5-m telescope with a 1"×5" slit was employed. In Fig.4.6, the derived line intensities relative to Hβ of two PNe in common were compared to that published in GPM12 with combined errors. The lines were chosen between the wavelength range 4000-7700 Å, within which flux calibration is usually reliable. As can be seen in Fig.4.6, most of the fluxes agree with each other within the quoted uncertainties. Outlying points are the lines with intensities <10% of Hβ, such relatively weaker lines are brighter in the measurement using the VLT. Thus, the difference is mainly for the difference in slit aperture size and the quality of spectroscopic observations.
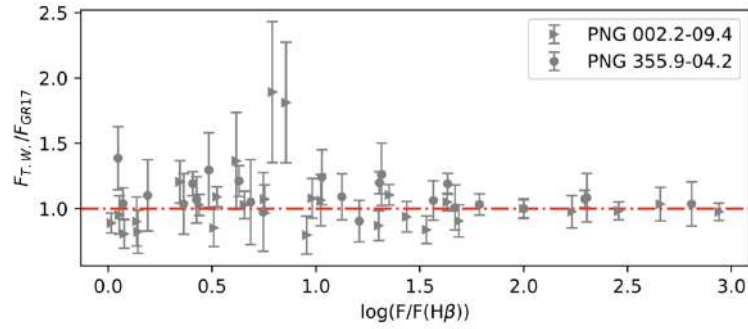
Figure 4.6: Measured line intensities compare against those from GPM12. Two outlying points are I([O II] λ7319)=6.83 and I([O II] λ7330)=5.87.

4.3 Physical conditions and chemical abundances

4.3.1 Electron temperatures

The physical conditions in the sample nebulae were determined from flux ratios of collisional excited lines (CELs) using `NEAT` through an iterative way. `NEAT` uses atomic data for CELs primarily from `CHIANTI 9.0` in Dere et al. (2019) with the exception of data for O^+ and S^{2+}, which documented errors were reported. The transition probabilities and collision strengths of O^+ were adopted respectively from Zeippen (1982) and Pradhan (1976) instead. For S^{2+}, transition probabilities from Mendoza & Zeippen (1982) and collision strengths from Mendoza (1983) were used. The atomic data for recombination lines (ORLs) in `NEAT` are from various sources, for details refer to Table 1 of Wesson et al. (2012). For the calculation of the [N II] temperature, the contribution of recombination excitation of N^{2+} was subtracted from the [N II] λ5754 auroral line intensity, this was implemented in `NEAT` through taking into account expressions in Liu et al. (2000). `NEAT` derived the uncertainties in electron temperatures and densities using a Monte Carlo approach through 10,000 iterations.

Comparisons between electron temperatures derived in Gorny et al. (2009) and in this work are shown in Fig.4.7 and Fig.4.8. T_e([O III]) obtained in this work agree well with the results in Gorny et al. (2009) as the slope of best fit is close to 1 as well as the R^2 value. Meanwhile, large scattering and large uncertainties are seen in T_e([N II]) results. The high and uncertain T_e([N II]) derived might be related to the measurement of weak [N II] $\lambda\lambda6548$, 6583 lines relative to Hα (high temperature corresponds to lower I(6583+6548)/I(5755) ratio) for both studies. At T_e([N II]) < 10000 K, most of the measurements in Gorny et al. (2009) and a few of our measurements also have large error bars, this could be caused by [N II] $\lambda5755$ line flux measurement. We see that for T_e([N II]) < 10000 K (relatively high line ratios), our results are generally higher and more widespread than the literature values which indicate a higher [N II] $\lambda5755$ flux was derived (fluxes for bright emission lines will generally consistent among multiple studies). For this case, our results are more reliable.
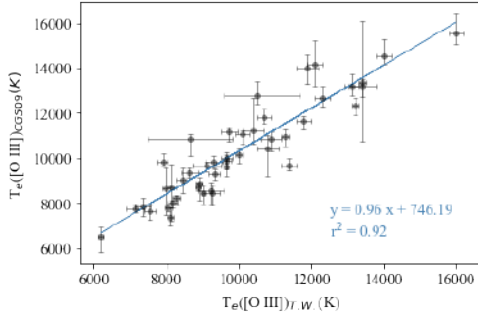
Figure 4.7: A comparison between electron temperature derived from [O III] line ratios in this work and Gorny et al. (2009). The equation of the best-fit line together with the R^2 value is shown in the lower right corner
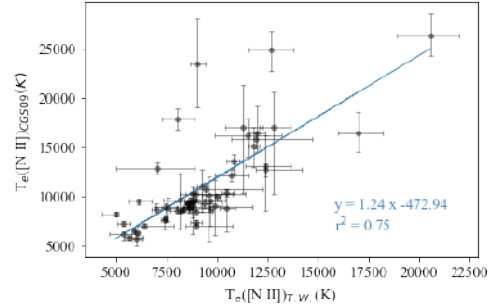
Figure 4.8: A comparison between electron temperature derived from [N II] line ratios in this work and Gorny et al. (2009). The equation of the best-fit line together with the R^2 value is shown in the lower right corner.

Electron temperatures derived from the [O III] lines, T_e([O III]), is plotted against that from the [N II] lines, T_e([N II]), in Fig.4.9. The overall behaviour of these two electron temperatures is similar to that in Gorny et al. (2009):

  (a) For most of the objects, T_e([N II]) and T_e([O III]) are inconsistent. As discussed in Kaler (1986), T_e([N II])/T_e([O III]) could vary from 0.7 to 1.1 depending on the nebular excitation level and the He^{2+} ionic abundance. More nebulae have T_e([N II]) > T_e([O III]). High T_e([N II]) usually have larger uncertainties, which could result from the uncertainties in fitting the [N II] lines as discussed earlier;

  (b) The largest derivation between T_e([N II]) and T_e([O III]) is seen at $\log T_e$([O III])$\sim$ 4, just below the temperature sensitivity limit. [O III] line ratio starts to change more slowly with the temperature (seen the line ratios as a function of temperature in Osterbrock & Ferland, 2006, p. 110).

  (c) A concentration of data points at $\sim$(3.9, 3.9) in the $\log T_e$([O III])-$\log T_e$([N II]) plot. This is more obvious in our results. One probability comes from the initial guess in the iterative

physical condition calculations. NEAT uses 10000K as the initial temperature, which is also the case with GCS09, this might lead to a preferential convergence to the initial value when the temperature changes moderately with line ratios and uncertainties in line fluxes are large. This has not yet been further investigated;

However, a few inconsistencies between our $\log T_e$([O III])-$\log T_e$([N II]) plot and that in GCS09 are noticed. Firstly, more objects measured with T_e([O III]) < T_e([N II]) in our results. Secondly, in GCS09, PNe with high oxygen ionisation ($O^{++}/O^{++}+O^+$ > 0.8), [N II] lines measure higher temperatures than [O III] lines. However, such a relationship is weak in this study (seen in the right panel of Fig.4.10): T_e([O III]) < T_e([N II]) is also measured for some objects with $O^{++}/O^{++}+O^+$ < 0.8. This could be due to the presence of temperature fluctuations in the PNe.
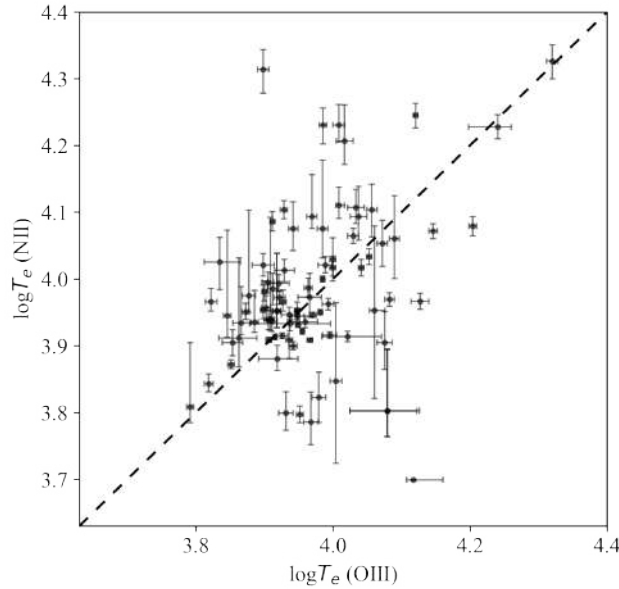
Figure 4.9: Electron temperatures derived from [O III] $\lambda 4363/\lambda 5007$ versus [N II] $\lambda 5755/\lambda 6584$ lines of 90 PNe. T_e([O III]) ranges from 6230 to 20,900 K with a typical uncertainty of 160 K while T_e([N II]) is within 5070 to 21,200 K and the uncertainties are less than 600 K for 69 out of 88 PNe and could be up to 5,100 K for few measurements. The Pearson correlation coefficient, r, between T_e([O III]) and T_e([N II]) is 0.50.

For few objects, [S II] $\frac{\lambda 6717+\lambda 6731}{\lambda 4068+\lambda 4076}$, [O II] $\frac{\lambda 7319,20+\lambda 7330,31}{\lambda 3726+\lambda 3729}$ and [O I] $\frac{\lambda 6363+\lambda 6300}{\lambda 5577}$ line ratios were used to determine electron temperature for the low-ionization zone when T_e([N II]) is not available and [Ar III] $\frac{\lambda 7135+\lambda 7751}{\lambda 5192}$ and [Ar v] $\frac{\lambda 6435+\lambda 7005}{\lambda 4625}$ lines were used for the medium-ionization region where [O III] lines are too weak to be detected.

4.3.2   Electron densities

The histogram of electron densities derived from [S II] $\lambda 6731/\lambda 6717$ line ratios, N_e([S II]) is shown in Fig.4.11(a). For the object PNG 359.8-07.2, the density could not be obtained from
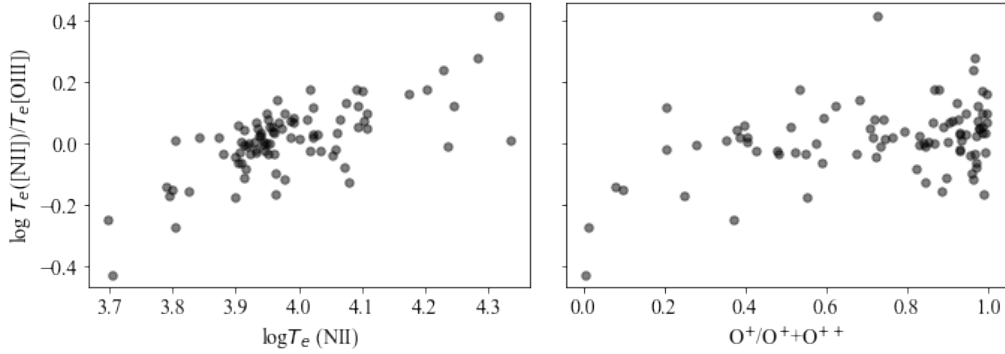
Figure 4.10: <u>Left panel</u>: the ratios between electron temperatures determined using [O III] and [N II] line ratios versus T_e([N II]), both are in log scale. In general the ratio increases as T_e([N II]) increases. <u>Right panel</u>: the T_e([N II])/T_e([O III]) for different values of $O^{++}/O^{++}+O^+$ in 117 PNe. No differentiation between high oxygen ionisation ($O^{++}/O^{++}+O^+ >0.8$) PNe and the rest is seen.
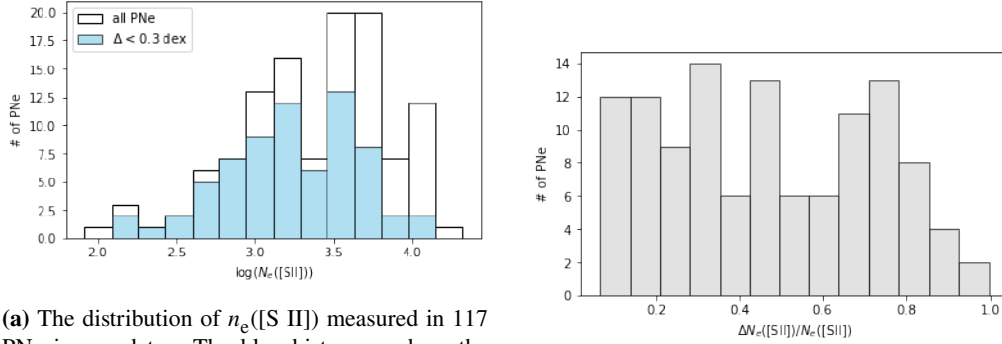
(a) The distribution of n_e([S II]) measured in 117 PNe in our data. The blue histogram show the measurement with an uncertainty less than 0.3 dex which contains 69 PNe. For $\log(n_e$([S II]))>3.5, most of the measurements are highly uncertain.

(b) Fractional uncertainty in n_e([SII]) of 117 PNe in this work. Each value of uncertainty is an average of the lower and the upper error.

Figure 4.11: Electron density derived from [S II] line ratios in this study. The results are suffering from large uncertainties which are mainly due to flux measurement.

the [S II] line ratios and instead is initially assumed 1000 cm^{-3}. The spectrum fitting has large uncertainties when deblending this [S II] doublet which results in uncertain measurements of N_e([S II]) for most of the PNe as shown in Fig.4.11(b). Besides, the saturation correction step could also increase the uncertainty when deriving the scaling factor between the short- and long-exposure observations. The lower limit of N_e([S II]) for 40 PNe is in the low-density limit.

4.3.3 Chemical abundances

The derived plasma diagnostics, elemental abundances of He, N, O, Ne, S, Ar and Cl (relative to hydrogen) along with estimated errors for each PN are listed in Table.F.1. Ionic abundances were first determined from the de-reddened intensities of the lines listed in Table.4.1. The total elemental abundances were obtained from the ionic abundances calculated from CELs and the ionization correction factors (ICFs) derived in Kingsburgh & Berlow (1994, hereafter KB94)

based on detailed photoionization models of 10 PNe to correct for the undetected ionization stages of ions. This 'classical' ICF scheme instead of a more recent in Delgado-Inglada et al. (2014) was chosen as it was used in most the previous works. This allows an examination of other factors that may influence the chemical abundance determination and the reliability of our results. ICF scheme in Delgado-Inglada et al. (2014) will be applied in our paper on this PN abundance catalogue (Tan et al. in prep). The use of ICFs is discussed in §2.5.4. Using usually low S/N [O I] λ6300, [O II] $\lambda\lambda$7320, 7330 lines is because, for some of the objects, the flux calibration is not available for [O II] $\lambda\lambda$3727, 3729 while the O abundance is crucial for ICF calculations. Uncertainties in chemical abundances adopted the statistical uncertainties derived from line fluxes measurements.

X^{+i}	Line
He^+	[N II] $\lambda\lambda$4471, 5876, 6678
He^{+2}	[N II] $\lambda\lambda$4686, 5412
N^+	[N II] $\lambda\lambda$5754, 6584
O^0	[O I] λ6364
O^+	[O II] $\lambda\lambda$3727, 3729, 7319, 7330
O^{+2}	[O III] $\lambda\lambda$4363, 5007
Ne^{+2}	[Ne III] λ3868
Ne^{+3}	[Ne IV] $\lambda\lambda$4714, 4715, 4724, 4725
S^+	[S II] $\lambda\lambda$6716, 6731
S^{+2}	[S III] λ6312
Cl^{+2}	[Cl III] $\lambda\lambda$5517, 5537
Cl^{+3}	[Cl IV] λ7531, 8046
Ar^{+2}	[Ar III] $\lambda\lambda$7135, 7751
Ar^{+3}	[Ar IV]λ4740
Ar^{+4}	[Ar V]$\lambda\lambda$6435, 7005

Table 4.1: Collisional excitation lines used for ionic abundances determinations in this work.

Comparison of general patterns of abundances with previous data sets

The derived chemical abundances for the sample of 118 Bulge PNe were compared with results of GBPNe in Chiappini et al. (2009), referred to as CGS09, which combined the data sets from Górny et al. (2004), a merger of the PNe data from Cuisinier et al. (2000), Escudero & Costa (2001), and Escudero et al. (2004), Górny et al. (2009) and Wang & Liu (2007). The abundances values with an uncertainty greater than 0.3 dex were rejected from comparison. The median, the 25th and 75th percentile values of [He/H], [N/H], [O/H], [Ar/H], [Ne/H], [S/H], [Cl/H] derived in this work and in CGS09 is presented in Table.4.2 together with the number of objects with each measurement available and a summarizing box plot is shown in Fig.4.12. The standard logarithmic form of 12+log(X/H) was used, where *X* is the abundance values of an element.

Table 4.2: Median chemical abundance values and the 25th and 75th percentile values for all the Bulge PNe measured in this work. The number of object measurements is shown in the bracket.

	This work		CGS09				Sun
He/H	11.06	[10.97, 11.14]	(117)	11.11	[11.05, 11.19]	(144)	10.93
N/H	8.13	[7.65, 8.60]	(118)	8.11	[7.76, 8.50]	(123)	7.83
O/H	8.75	[8.47, 8.91]	(118)	8.57	[8.40, 8.72]	(117)	8.69
Ne/H	8.27	[7.94, 8.42]	(93)	7.93	[7.71, 8.17]	(77)	7.93
S/H	6.95	[6.61, 7.31]	(117)	6.79	[6.54, 7.04]	(94)	7.12
Ar/H	6.49	[5.99, 6.69]	(118)	6.34	[6.05, 6.56]	(120)	6.40
Cl/H	5.13	[4.89, 5.37]	(114)	6.22	[6.00, 6.50]	(47)	5.50
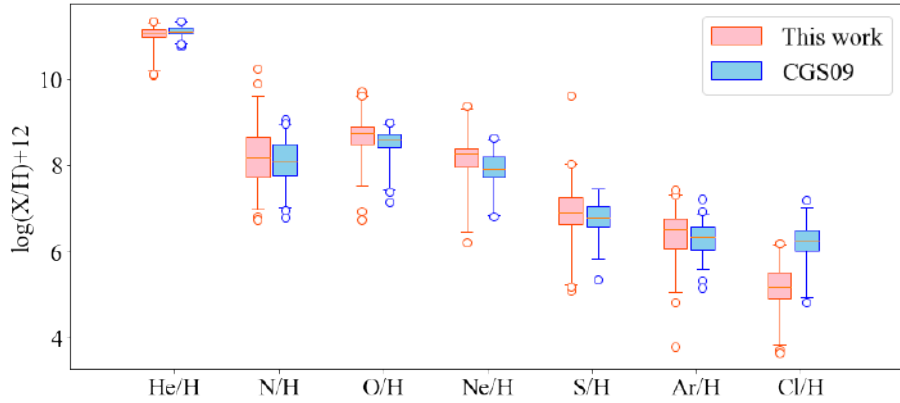
Figure 4.12: Box plot summarising the abundance values measured in this work and in CGS09. Boxes extend from the 25th to 75th percentiles, breaking by a horizontal line indicating the median. Whiskers extends to the 1st and 99th percentiles.

All bar one of the elemental abundances derived in this work shows a more fat-tailed distribution than the results in CGS09. For the nitrogen abundances, the median value derived in this work is higher than the literature values by 0.2 dex while there are longer tails on both sides. The helium abundances derived are systematically lower in our results by approximately 0.05 dex (upper left panel in Fig. 4.13). The abundance values of the α-elements: argon, sulfur, oxygen and neon are systematically higher than the results in CGS09 and the increase in median values are 0.15, 0.16, 0.18, and 0.34 dex respectively. The medium values of [Ar/H], [O/H] and [Ne/H] become super-solar with a tail of abundance value distribution towards lower values. For for chlorine, the median value is measured lower than the literature value by 1.08 dex and all [Cl/H] values are sub-solar in our results.

The chemical abundances of 68 PNe that are included in this work and CGS09 were recomputed using the emission fluxes obtained in this work and the same line list as in CGS09 to verify whether such differences in the abundance distributions are attributed to the use of different line lists and the selection of objects. A comparison between the measured and literature individual abundance values of helium, nitrogen, sulfur, argon, oxygen and neon for this subsample is shown in Fig.4.13 (not including for chlorine which will be discussed later in §4.3.3), in which the red crosses representing abundance values that are not within 2σ interval of the literature

results. Only high-quality measurements with an uncertainty less than 0.3 dex bin this work were included. The systematical shifts of [He/H], [O/H], and [Ne/H] are seen and a considerable fraction of our results are higher or lower than the literature values by more than 2σ. For [N/H], [S/H] and [Ar/H], there are no systematic differences between our results and the literature data, however, the data points scatter with large variances.

The box plot summarizing the distributions of abundances calculated in this way and in CGS09 of objects in common only is shown in Fig.4.14 and Table.4.3 reports the median, the 25th and 75th percentiles of abundance values. In CGS09, for this subsample, the median values are all higher than that of the complete sample, [Ar/H] is now super-solar, while for our results, the median values are generally lower for this fraction of the sample. The median values of [N/H], and [S/H] are measured higher in CGS09 by 0.17 and 0.12 dex respectively. No object with [He/H] measured lower than 10.96 in CGS09 for this subsample, resulting in a much narrower range of values, other than that, the overall wider distribution of the results in this work is still present in this subsample, but much less significant. The more fat-tailed distribution of our chemical abundance, therefore, could be due to the use of different line lists, the inclusion of different objects and measurement uncertainties.

Table 4.3: Median chemical abundance values and the 25th and 75th percentile values for 68 PNe that are included both in this work and in CGS09. The number of object measurements is shown in the bracket.

	This work			CGS09			Sun
He/H	11.05	[10.97, 11.15]	(68)	11.15	[11.06, 11.19]	(58)	10.93
N/H	8.11	[7.64, 8.49]	(51)	8.28	[7.82, 8.58]	(55)	7.83
O/H	8.75	[8.61, 8.87]	(50)	8.63	[8.41, 8.75]	(46)	8.69
Ne/H	8.16	[7.99, 8.40]	(43)	7.94	[7.73, 8.23]	(34)	7.93
S/H	6.79	[6.59, 7.19]	(42)	6.91	[6.54, 7.11]	(38)	7.12
Ar/H	6.50	[6.10, 6.71]	(65)	6.45	[6.13, 6.62]	(45)	6.40
Cl/H	5.18	[4.90, 5.46]	(63)	6.24	[6.04, 6.57]	(20)	5.50

Although the overall distribution agrees well with this subsample, large inconsistencies in individual abundance values are seen in Fig.4.13. Such derivations could be originated from flux measurements, determination of extinctions, physical conditions, and thereby the ionic abundances. A detailed comparison between ionic abundances derived in this work and CGS09 is required to explain and assess the quality of this data. However, as most of the objects in CGS09 were adopted from Gorny et al. (2004) and GCS09 in which the detailed ionic abundances are not available, we compare these detailed measurements for 7 PNe in Wang & Liu (2007) (WL07 hereafter) in the following section.
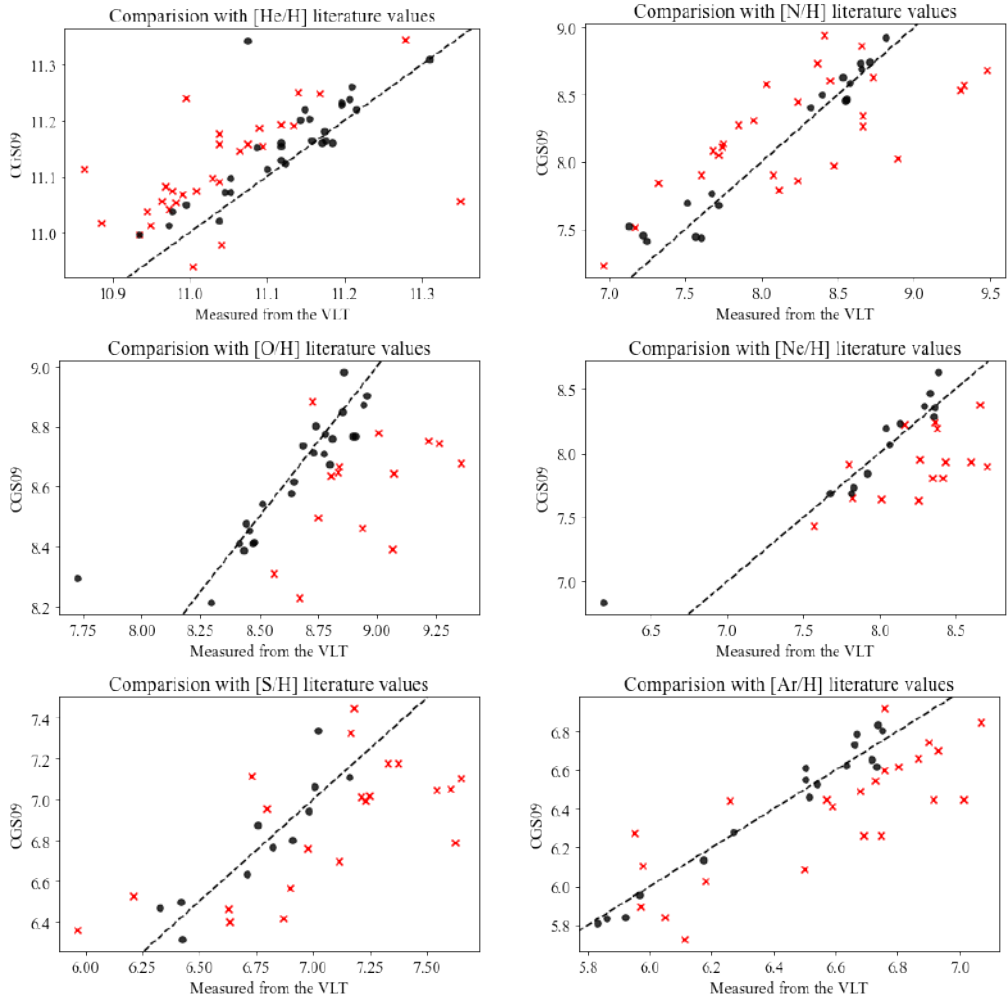
Figure 4.13: A comparison between elemental abundances derived in this work and in CGS09. Black dots are the values in our results that agree with its literature value within twice the literature uncertainty, 2σ while red crosses show the results in this work that deviate from the literature value for more than 2σ. The dashed lines indicate the $y = x$.
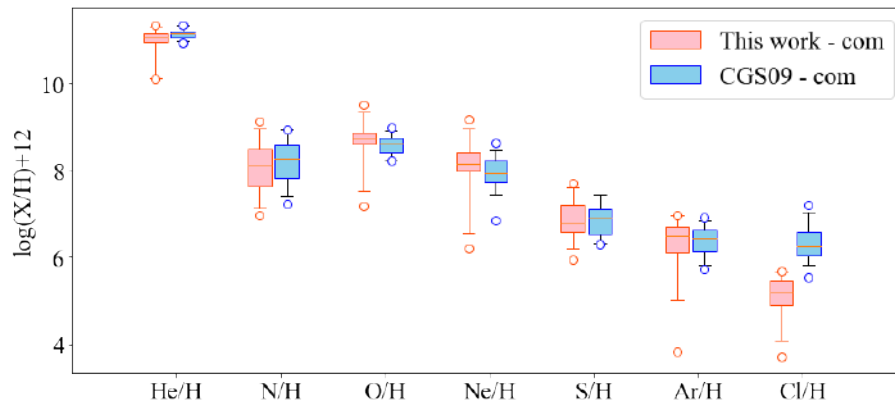
Figure 4.14: Box plot summering the chemical abundances of 68 PNe that are studied in this work and in CGS09. The abundance values shown derived from this work used the ICF in KB94 for all elements. The box plot is configured in the same manner as Fig.4.12.

Comparison of ionic abundances with the literature results in WL07

The objects that are available both in this work and in WL07 are PNG002.0-06.2, PNG 002.2-09.4, PNG 005.8-06.1, PNG 006.1+08.3, PNG 007.0-06.8, PNG 009.4-09.8, and PNG 353.3+06.3. The differences in elemental and ionic abundances between results from this work and in WL07 on a log scale for each PN are present in Fig.4.15, together with the uncertainties from measurements in this work. This includes the elements He, N, O, Ne, S, Ar and Cl.

(a) He

(b) N

(c) O
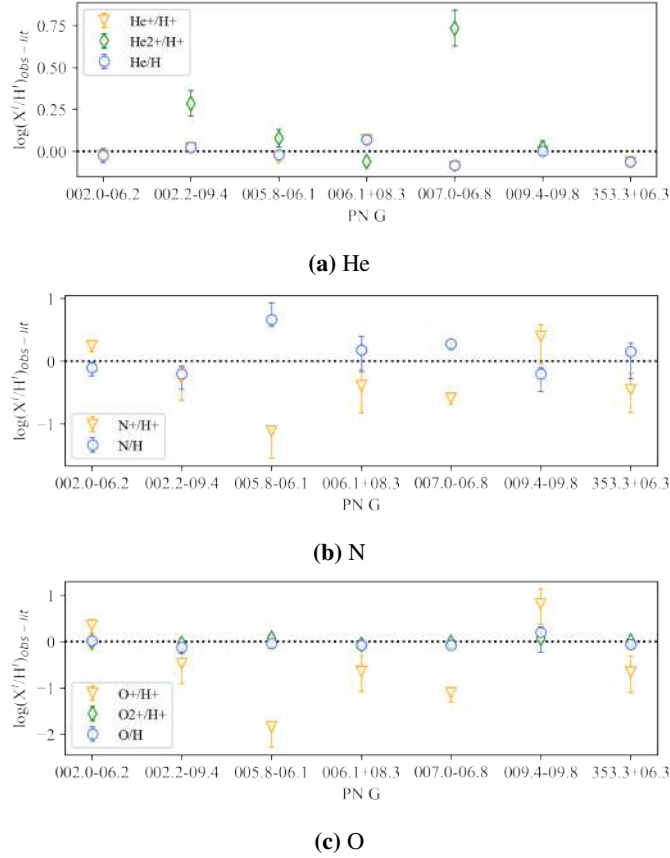
Figure 4.15: The differences in elemental and ionic abundances derived in this work and in WL07 for the elements helium, nitrogen, oxygen, neon, sulfur, argon, chlorine respectively. Error bars are from uncertainties in this work. Green circles represent elemental abundances while orange triangles, green diamonds, purple crosses, pink stars indicate the ionic abundances of X^+/H, X^{2+}/H, X^{3+}/H, and X^{4+}/H respectively.

Helium - the abundance value is simply the sum of He^+/H^+ and He^{2+}/H^+ (usually 2-3 dex weaker than He^+/H^+). The slight difference between [He/H] values are mainly from He^{2+}/H^+ measurements as seen in Fig.4.15(a). He^2/H^+ calculated in this work uses flux-weighted results of He I λ4686 and 5412 lines while WL07 used He I λ4686 line only. Thus, the derivation in [He/H] could mainly be attributed to the use of line lists. The objects PNG 007.0-06.8 and PNG 353.3+06.3 are two of the objects with inconsistent results seen in the upper left panel in Fig.4.13, while most of those are from GCS09 and Gorny et al. (2004).
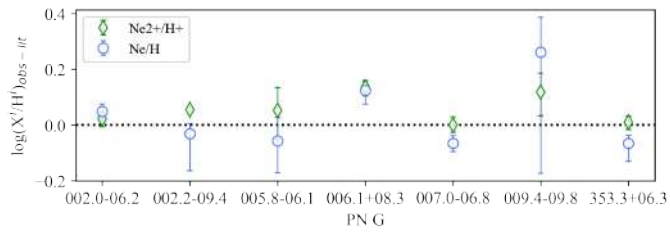
(d) Ne
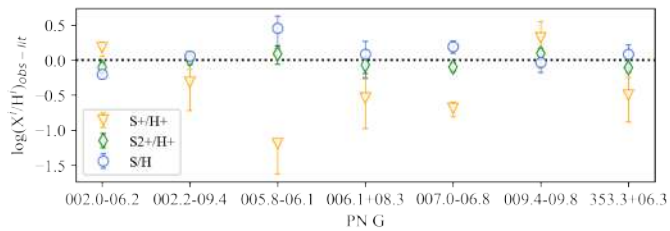
(e) S
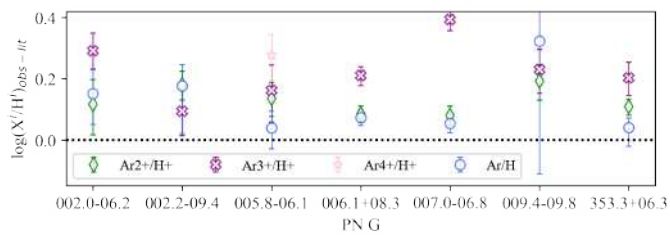
(f) Ar
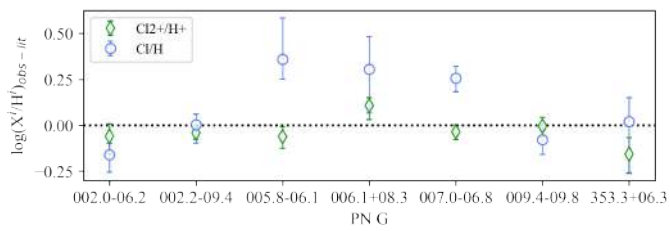
(g) Cl

Figure 4.15: continued:

For the results in GCS09 and Gorny et al. (2004), the de-reddened fluxes were compared with our results. It was noticed that nearly all the [He I] $\lambda5876$ intensities in GCS09 works are measured with higher fluxes than in this work. The ratio of line intensity in literature to that in this work of individual objects as a function of the ratio of [He/H] is shown in Fig.4.16. Generally, a higher line intensity measurement leads to a higher helium abundance. Thus, helium abundance between the results in previous studies of Gorny and co-authors and this work could largely be due to the differences in [He I] $\lambda5876$ line intensities which possibly come from the errors in flux measurement and extinction correction.
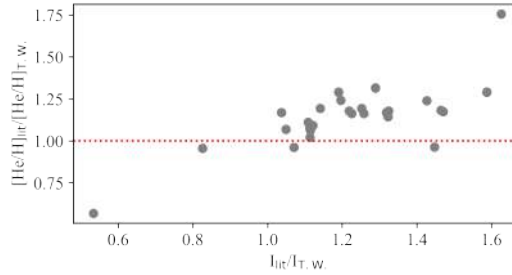
Figure 4.16: The ratio of [He I] $\lambda5876$ line intensity in GSC09 and Gorny et al. (2004) to that in this work as a function of the ratio of the corresponding [He/H] to that measured in this work.

Nitrogen - for the samples in both CGS09 and WL07, larger variations are seen for N^+/H^+ of which the measurement is dominated by the bright [N II] $\lambda6583$ line. The quality of spectra would not lead to any significant difference in the measurements of such bright lines. The differences in electron density and temperature used for its derivation could be the primary cause of variation. The N^+ abundance can partly account for the deviation in [N/H], the ICF of nitrogen which is calculated from oxygen ionic and elemental abundances would also contribute because large differences in oxygen abundance between our results and the literature also present.

Oxygen - the ionic abundance largely depends on the abundance of the dominated ion O^{2+} which emits usually the brightest lines [O III] $\lambda5007$. Other than the [O III] $\lambda5007$, the [O III] $\lambda4363$ line was included in our determination. The O^{2+}/H^+ determined from these two lines agree well and because the [O III] $\lambda4363$ lines is much weaker than the [O III] $\lambda5007$ lines, it would not cause any variation in the ionic abundance $> 10\%$. Thus, the difference in O^{2+}/H^+ is mainly from the physical condition parameters derived. O^+/H^+ shows a larger difference (1.4 dex at the worst) between our results and that in WL07. Although this usually causes a minor change in the [O/H] abundance derived, O^+ abundance is important in ICF calculation of other elements, thus, a detailed consideration is required. The O^+ derived in this work used two pairs of [O II] lines: the blue pair, $\lambda3727+29$ and the red pair, $\lambda7319+7330$. It was noticed in previous works (e.g. Viegas & Clegg 1994, Escudero et al. 2004 and Exter et al. 2004) that using the red pair usually leads to a systematically higher abundance up to 1 dex, even when the intensity of recombination [O II] $\lambda\lambda7319,30$ lines was subtracted, the two pairs can still give results differing by a factor greater than 2, for which the main cause is still an open issue. Thus, in most of the

previous works, only the $\lambda\lambda3727+29$ pair was used because its conversion to abundance is less sensitive to the physical conditions and this is the case for Wang & Liu (2007). Nevertheless, after comparing O^+/H measured from the blue and the red pairs that are simultaneously available for 26 PNe (seen in Fig.4.17), the measurement from the red pair is expected to have higher quality in this work for the following reasons:

(a) The two pairs give consistent abundance within the measurement errors for 16 out of 26 objects. 4 of the rest 10 PNe have abundances measured higher from the blue doublet with uncertain flux measurements and the O^+/H values are lower than 10^{-5}, as a result, suffering from a lower uncertainty of 100% (0.434 dex). The other 8 PNe which have higher abundance measured from the red doublet have either a bipolar morphology and are compact or exhibit point-symmetric and/or asymmetric features, the results could vary largely if the coverage and relative position of the slit changes. In Fig.4.17, one feature to notice is that, except for these 10 outliers, the blue pair tends to give a slightly higher measurement of O^+ abundance values $< 10^{-4}$ while measures lower when $O^+/H > 10^{-4}$. This is contrary to Fig. 5 in Escudero et al. (2004) in which the recombination contribution to the red pair has not been subtracted. The feature observed is then likely originated from the recombination subtraction.

(b) Although deriving the O^+ using the blue pair depends less on the physical parameters, the accuracy of flux measurement is crucial, especially the line ratios of the doublet. The observations in CGS09 used spectra that covered the wavelength range ~3500-7500 Å, thus, both the two pairs are at the blue and red end respectively where the instrumental response was dropping steeply. While the wavelength coverage in this work is ~3700/3750-8300 Å, the blue pair in our spectra, where available, is near the edge of the spectral range, however, the red pair is around the middle of the red spectra where the flux calibration should be with decent accuracy.

The [O/H] abundance derived in this work generally agrees with that in WL07, except for PNG 002.2-09.4 which is measured 3.2σ lower in this work. The inconsistent results seen in the middle left panel in Fig.4.13 are of the objects in the GCS09 and Gorny et al. (2004). It shows that nearly all oxygen abundances derived in this work are higher than the literature value. The bright [O II] lines $\lambda3727$ line was used in GCS09 and Gorny et al. (2004), for some objects, the [O II] $\lambda3727$ fluxes were scaled according to O^+ derived from the [O II] $\lambda7325$ line because of problematic accuracy of the flux measurement. The same explanation and conclusion for WL07 should apply to inconsistent oxygen abundance values with previous works of Gorny and co-authors. Exceptions are: (i). for a few dim objects, $I(\lambda5007)$ increases by more than 20% in our results, the new flux measurement then leads to a significant change in [O/H]; (ii). few compact PNe, as mentioned before, would have high O^+/H using the red pair. For O^+, through comparison, the sum of [O II] $\lambda\lambda7319,30$ de-reddened fluxes obtained in this work is higher than that of [O II] $\lambda7325$ measured in GCS09 for most of the objects (by 500% for the maximum), this could cause higher O^+ abundance values measured in our results and higher ICF computed for other elements.
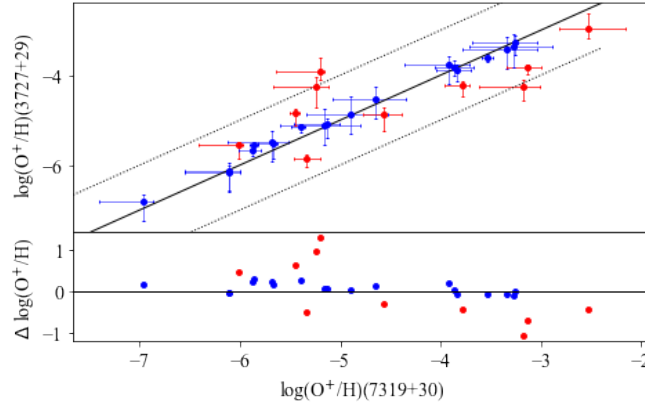
Figure 4.17: The relationship between ionic abundances of O^+ derived from [O II] $\lambda\lambda 3727+29$ and [O II] $\lambda\lambda 7319+30$ of 26 PNe in this work. In the upper panel, the solid line shows $y = x$ while two dotted lines show the ± 1 dex interval respectively. Red dots represent data that do not agree with the measurement uncertainties. In the lower panel, the difference between O^+/H derived from the blue doublet and the red doublet is plotted versus the red doublet O^+ results. The blue and the red dots correspond to that in the upper plot.

Neon - a slight deviation in neon abundance is seen compared to that in WL07. One thing to notice is that the Ne^{+2} abundance is generally higher in our results while the total Ne abundance is lower for most of the objects. The difference in Ne^{+2}/H could result from uncertainties in flux measurements, extinction correction and different parameters of physical conditions derived which could also lead to variation in the ICFs calculated and thereby the [Ne/H] values. Though in the middle right panel in Fig.4.13, our results are significantly higher than the objects adopted from GCS09 and Gorny et al. (2004), by 0.8 dex the most, the uncertainties in flux measurements would also be the main reason. The flux of [Ne III] $\lambda 3868$ underwent a correction to account for the inconsistent ratios of Balmer lines at the blue end with the theoretical values in GCS09. The resulting errors were not reported, but when comparing the fluxes of [Ne III] $\lambda 3868$ lines measured in this work and GCS09, we found: i). 4 out of 19 objects that are common in these two studies and with Ne^{+2} observations have the [Ne III] $\lambda 3868$ flux measured without the before-mentioned correction in which [Ne/H] of only one objects is inconsistent and 0.12 dex lower than our result; ii). for 4 of the rest 15 objects, the Ne^{+2} observations are not available in GCS09, but present in our data; iii). for the corrected [Ne III] $\lambda 3868$ fluxes of the rest of the objects, 8 were measured higher in our results of which 2 were doubled and they are the two objects with the largest deviations.

Sulfur - Same lines were used to derive S^+ and S^{+2} as in CGS09, WL07 and this work. In Fig.4.15(e), the values of S^+/H derived in WL07 and this work show a large difference, which is related to the adopted literature values of collisional strength and differences in derived physical conditions. As S^{+2} usually contributes more to the total abundance, the derivations in [S/H] mainly come from S^2 and ICF for sulfur. The S^{+2}/H determined in WL07 and this work agree within 0.1 dex while larger differences between the values of sulfur elemental abundances are seen, which primarily comes from the ICFs calculated. Same as nitrogen, the ICF of sulfur

depends on the O/O$^+$ ratio, the difference in [S/H] is then a reflection of the inconsistent results of O$^+$/H. The [S/H] values that do not agree within 2σ of the literature are for PNG 002.0-06.2, PNG 005.8-06.1 and PNG 007.0-06.8. However, the results of the latter two objects, which are higher in this work, are within 2σ of our measurement and it is generally true that higher [S/H] usually suffers from large uncertainties. This also applies to the objects with [S/H] > 7.3 in our results in Fig.4.13. As the line intensities of sulfur ions measured in GCS09 are generally higher than in this work, so higher ionic abundances would be expected because similar physical conditions were derived. The differences in ICFs estimated would then also be the cause for the derivation in [S/H] seen for the complete sample in CGS09. Besides, a strong blending of [S II] $\lambda\lambda6731$, 6716 lines in the spectrum in GCS09, which spoil the precision of line flux measurement (40% was suggested) could also account for the deviation between these two measurements.

Argon - both the individual ionic and total elemental abundances of argon obtained in this work are systematically higher than that derived in WL07 as shown in Fig.4.15(f), within 0.38 dex. The same was also noticed in argon abundances in WL07 when comparing with other literature values and in Gutenkunst et al. (2008) in which possible explanations suggested are the ICF schemes, whether the Ar^{+3} ion is observed and the uncertainties in T$_e$. Although these factors could result in large variations in [Ar/H] derived, as (i). the same ICF scheme from KB94 was used in this work as in WL07; (ii). all objects have [Ar IV] $\lambda4740$ observed; (iii). T$_e$([O III]) derived in this work agree within 3% for 6 out of 7 objects (11% for PNG 009.4-09.8), they are not enough to explain the systemic differences. The higher [Ar/H] measurement should come from higher ionic abundances derived and the possible reason for the differences in ionic abundance results is the atomic data used for abundance calculation.

For Ar IV, the collisional data are taken from Ramsbottom, Bell, & Keenan (1997) in `CHIANTI 9.0`, when these data were added to `CHIANTI` in Dere et al. (2019), it was compared to the calculations in Zeippen, Le Bourlot & Butler (1987) which was used in WL07 and significant differences are seen. There is a similar story for [Ar III] which was noticed in Griffin et al. 1998. In the lower right panel in Fig.4.13, larger derivations in [Ar/H] are seen when compared to GCS09 and Gorny et al. (2004) in which the same atomic data and lines were used as in this work. The difference is mainly related to the ICFs. More objects have measurements of weaker [Ar IV] $\lambda4740$ and [Ar V] $\lambda7006$ lines in our measurement, ICFs for argon calculated in GCS09 are to account for unobserved Ar^{+3} and Ar^{+4} for these objects. Thus, the differences in argon abundances are likely due to the improved quality of spectra and atomic data used in this work.

Chlorine - the determination of chlorine abundance is challenging, the dominated ion in the optical region, Cl^{2+}, have the [Cl III] $\lambda\lambda5517,37$ line intensities (the scaled flux such that I(Hβ) = 100) usually less than 1 and are normally the only lines measured. Compared with WL07, the Cl^{+2} ionic abundances agree well. The ICF scheme for chlorine in this work is from Liu et al. (2000) which is the same as in WL07 and is normally used in the literature. It is simply the S/S$^+$ ratio, therefore, the variation in [Cl/H] can correspond to the difference between S^{+2}/H values measured in these two works. Among all the elements examined here, the largest deviation is seen in the chlorine abundance. It was stark in the comparison between the general pattern of

chlorine abundance derived CGS09 and in this work and that all literature results are higher than ours. The median abundance value of chlorine in our results is almost 1.09 dex lower than that obtained in the CGS09. A similar derivation was noticed in Smith et al. (2017) that the chlorine abundances of 2 PNe in their results measured using the observations from the UVES/VLT are lower than that in CGS09 by 1.3-1.5 dex. Therefore, the uncertainties in atomic data, physical conditions and flux measurement of the S^+ doublet and weak chlorine lines are likely to be the main cause.

Conclusion on the abundance calculation

Considering the generally high S/N of our spectra, the employment of more emission lines and ionisation stages for ionic abundance calculations of helium, nitrogen and chlorine, the correction of RP effect, i.e. the effect that flux measurements of weak lines with S/N less than 6 are strongly biased upwards and the actual measurement uncertainty cannot be well represented by a Gaussian observed in Rola & Pelat (1994), in our spectral fittings and the updated atomic data in `CHIANTI 9.0` we used which have better agreement with the observations, our bulge PN abundances from these elements are more accurate than previous studies. For most of the measurements in this work, although a difference greater than 2σ is sometimes seen when compared with the literature values, the literature values are still within 2σ of our measurements.

The larger uncertainties are mainly from the spectral fitting of older published data, whenever strong line blending is present, the uncertainties in flux measurement would be greater than 20%. Such effect should also exist in previous studies, though is not taken into account into their final errors. Extra flux measurements were taken for important diagnostic lines using *iraf.splot* to assess uncertainties and the results approach the higher limit values but are still within the uncertainties. Thus, these uncertainties are valid estimates. Overall, the chemical abundance derivation in this work and GCS09 are more reliable than in WL07, these could be largely due to the difference in derived extinction correction coefficients. Our O^+/H, however, does not show better accuracy than the literature values for compact PNe as the results from the blue and the red doublet could differ by ~1 dex with large error bars as seen in Fig.4.17, though this would not lead to a large change in [O/H], such influence will be considered where relevant.

4.3.4   The alpha-element abundances

In contrast to low- to intermediate-mass stars, massive stars experience a class of nuclear fusion reactions converting helium into elements heavier than carbon, known as the alpha process. Elements that are produced in the alpha process only, such as O, Ne, S, Cl, and Ar, are referred to as alpha elements. Their chemical abundances are expected to vary in lockstep due to their common synthesis sites in massive stars. (Henry et al. 2008) As PNe are descendants of low- to intermediate-mass stars, the abundances of alpha elements remain constant in their progenitors and could be used to trace the chemical environment at the time when the progenitor of a PN was born. Also, one should expect that the alpha element abundances are directly proportional to each other because of their lockstep evolution. In the following, the abundances of Ne, S, Ar and Cl were compared with oxygen abundance to test such a lockstep behaviour, and thereby, to

see whether oxygen abundance in PNe could be used to indicate the chemical environment in the Galactic bulge over time.

The abundances of alpha elements Ne, S, Ar together with Cl are plotted against O abundance in Fig.4.18. Each element-versus-oxygen plot is fitted with a straight line through the least squares fitting method. The slopes, intercepts and r^2 values of best-fit lines are summarised in Table.4.4a. The oxygen and other elemental abundances exhibit a broad range spread with scatters at considerably subsolar and super-solar abundances.

The lockstep for alpha element variation is demonstrated as the correlations between [Ne/H] and [O/H], and between [Ar/H] and [O/H] are tight and positive, especially for [Ne/H], the slope is very close to the unity. The sulfur anomaly, the anomalously low S/O found in PNe (e.g. Henry et al. 2004, 2012), is evident in our result as the data points do not fall along a narrow linear track and instead, the scatter at the solar oxygen abundance is large and the measured sulphur abundances are systemically lower than solar (solar abundances are taken from Scott et al. (2015) and indicated by red dotted lines in Fig.4.18).

The correlation between chlorine and oxygen abundances is also seen in the plot, however, in Table.4.4a, the r^2 value is relatively low which indicates a poor linear relationship. In stellar evolution, the two stable Cl isotopes, ^{35}Cl and ^{37}Cl, are produced during the explosive oxygen burning process in core-collapse supernovae, with ^{35}Cl produced primarily from proton capture on ^{34}S and ^{35}Cl primarily from the radioactive decay of ^{36}Ar. In Fig.4.19, [Cl/H] is plotted against [S/H] and [Ar/H] respectively, the corresponding coefficients of the best-fit lines are indicated in Table.4.4b. For the [Cl/H] vs. [S/H] plot, the data points are somewhat scattered in a wide band. The slope of the best-fitting is 0.70, which deviates from the unity, with a moderate r^2 value of 0.6. The lockstep between chlorine and sulfur is, therefore, not shown in our data. This is also true for [Cl/H] vs. [Ar/H] in which the slope and the r^2 value of the best-fitting is 0.66 and 0.65 respectively. There are scatters at lower [Ar/H] and the positive correlation between [Ar/H] and [Cl/H] is slightly stronger than that of sulfur.

Table 4.4: Least Squares Fit Parameters For α Elements

a Elemental abundance versus [O/H]

[X/H] vs. [O/H]	Slope	y-Intercept	r^2	# of PNe
[Ne/H]	1.03 ± 0.01	-0.79 ± 0.19	0.81	100
[S/H]	0.75 ± 0.01	0.45 ± 0.47	0.44	118
[Cl/H]	0.69 ± 0.01	-0.83 ± 0.32	0.51	111
[Ar/H]	0.91 ± 0.01	-1.45 ± 0.20	0.73	118

b Elemental abundance versus [Cl/H]

[Cl/H] vs. [X/H]	Slope	y-Intercept	r^2	# of PNe
[S/H]	0.70 ± 0.01	0.30 ± 0.14	0.60	113
[Ar/H]	0.66 ± 0.01	0.50 ± 0.16	0.65	114
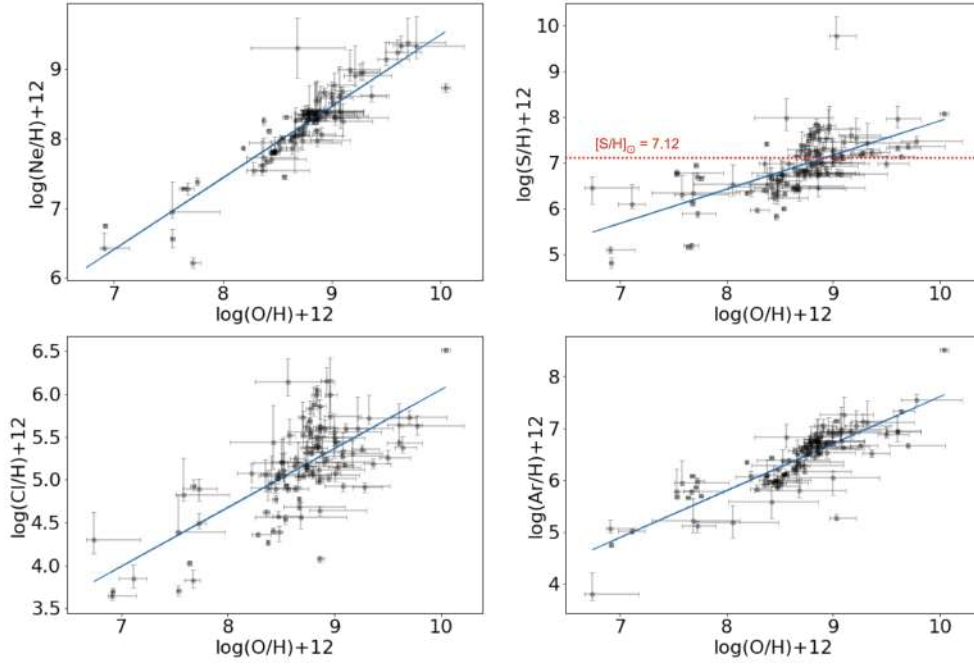
Figure 4.18: Starting with the upper left panel and proceeding in a clockwise manner, [Ne/H], [S/H], [Ar/H] and [Cl/H], are plotted against [O/H], where values are presented in 12+log(X/H) form. Error bars are from the measurement uncertainties. The blue solid line in each panel is the least-squares fit to the PN data. Table. 4.4a displays the regression parameters and uncertainties. Red dotted horizontal line on the log(S/H)+12 v.s. log(O/H)+12 indicates sulfur abundance of the Sun.

4.3.5   N and He abundances

Nitrogen and helium are elements that are produced in more massive PN progenitors. The histogram of the nitrogen enrichment, [N/O] is shown in the left panel of Fig.4.20 where the [O/H] is used as the metallicity indicator. The derived values of [N/O] range from −2.12 to 1.28 with the median value is −0.45 and 25th and 75th percentile values are −0.96 and −0.06 respectively. Both extremely low ([N/O] < −2) and high ([N/O] > 1) [N/O] abundance ratios were obtained in our results, which were not seen in previous works of bulge PNe including CGS09 and Cuisinier et al (1999). These extreme ratios correspond to either compact high-excitation PNe in which the low excitation [O III] lines are weak relative to Hβ lines or very high excitation PNe in which the low excitation [N II] lines are weak or were absent in previous spectroscopic observations. For this, our GBPNe sample is more representative of the underlying Bulge PNe population.

As it was argued in Wesson et al. (2018), the determination of N/O ratios could suffer from large systematic uncertainties for two reasons: first, the recombination contribution to [O III] λ4363 and [O II] $\lambda\lambda$3727, 3729 would result in an overestimation of temperature and the O$^+$ abundance; and second, using of different ICFs could result in a difference up to 20% in [N/H] values. Thus, the first reason would be more important for the extreme [N/O] ratios measured, however, the measurement of weak lines is challenging, and this would contribute more to the uncertainties. The [N/O] will be used only quantitatively in this work, such uncertainties would
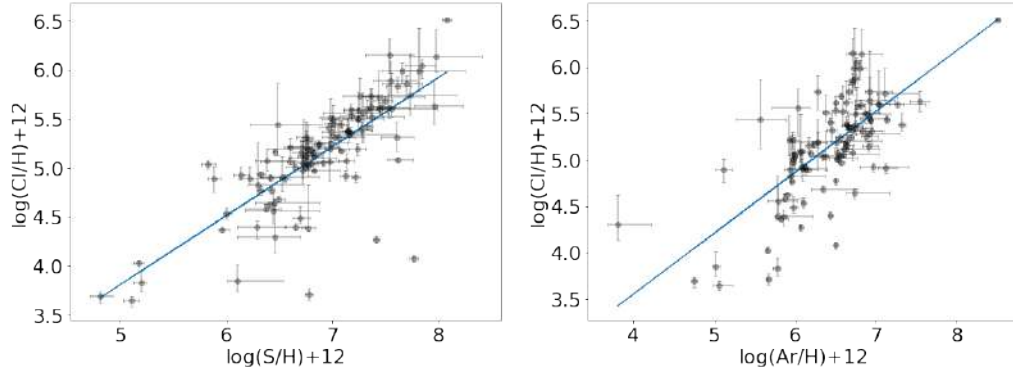
Figure 4.19: In the left and the right panel, Cl/H is plotted against S/H and Ar/H respectively in the same manner as in Fig.4.18.

not influence any of our analysis or results. The left panel in Fig.4.21 shows [N/O] vs. [O/H]. Our data indicate a weak anti-correlation between [N/O] and [O/H], with P=-0.36. In the plot, there is generally a wide spread of [N/O] values especially for [O/H] between 8.7 and 9.0, there are more scatters toward the higher [N/O] values.

The right panel in Fig.4.20 shows the histogram of [He/H] abundance values. 100 out of 118 PNe have [He/H] measured > 10.93, the solar abundance, and the [He/H] value is less than 10.78 ($> 3\sigma$ lower) for only 11 PNe. The [N/O], i.e. the N enrichment, is plotted versus [He/H] in the right panel in Fig.4.21. The pattern is similar to the [N/O] vs. [O/H] plot as helium abundance usually varies moderately with the [O/H] as seen in Fig.1 in Henry et al. (2018). A tight correlation of He and N enrichment in *wels* PNe and normal PNe is seen Fig.19 in GCS09 as far as the objects with [N/O] > −1 and [He/H] > 10.93 (solar) are concerned. For comparison, the region of object selection is shaded in the right panel in Fig.4.21 and objects of different CS spectral types are labelled based on the catalogue of spectral classification of CSPNe in Weidmann et al. (2020). The scattering of data is large and no correlation is found between N enrichment and [He/H] in the parent stars of either *wels* or normal PNe.
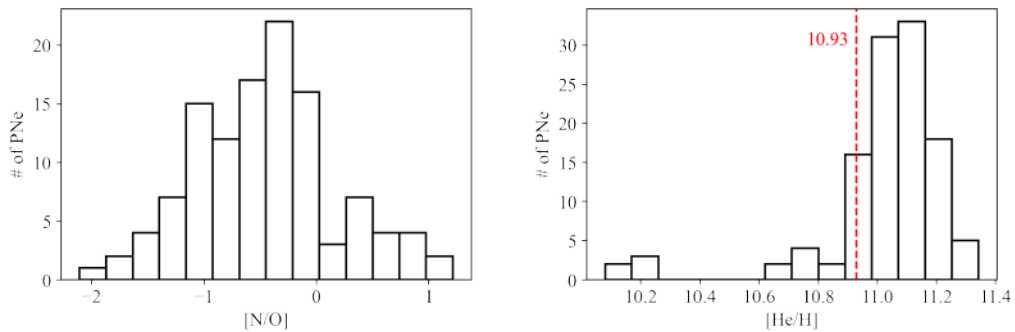
Figure 4.20: Left panel: Distribution of N enrichment in a log scale of 116 PNe in this sample where the ratio is available. Right panel: Distribution of available He/H abundance ratio of 117 PNe in this sample. Red dashed line indicates the solar helium abundance, [He/H]$_\odot$ = 10.93.
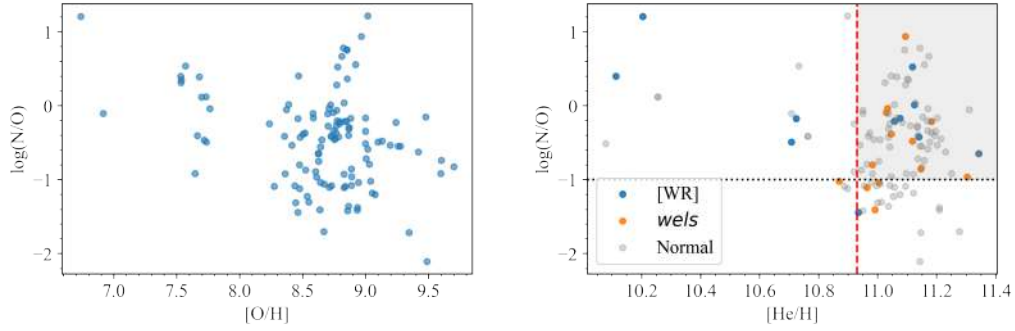
Figure 4.21: Left panel: [N/O] versus [O/H] for 116 Galactic bulge PNe in this sample. Right panel: [N/O] versus [He/H] for 116 PNe in this sample where the measurements are available. Red dashed line indicates the solar helium abundance, [He/H]$_\odot$ = 10.93. Data points are color-coded according to their central star spectral types. The shaded region represents the selection criteria under which a strong correlation between [N/O] and [He/H] is seen for PNe with *wels* or normal central stars. However, no correlation is seen in our data.

4.3.6   Objects with peculiar abundances

In previous discussion about the elemental abundance results, a few objects distinguished themselves by their low ([O/H] < 7.5) and high [O/H] values ([O/H] > 9.5), the ionic, elemental oxygen abundances and the literature values of [O/H] are listed in Table.4.5.

For the three PNe measured with [O/H] > 9.5, PNG 000.7-07.4 was measured as high-metallicity (twice the solar metallicity) in the literature, however, the value of [O/H] is 4 times higher in our results which results from the high O^+/H ratios with an uncertainty of 0.12 dex. It has a bipolar morphology and small angular size from Rees (2011). The deviation from the literature values could be due to the different regions being traced. The high O^+ abundances are also the reason for the high [O/H] measured for PNG 352.0-04.6 and PNG 356.1-03.3. Both are compact PNe with morphologies of Eaps and Bas, the variation in O^+/H could result from internal structures and point-symmetric features as discussed before.

For PNG 004.0-03.0 and PNG 357.1-04.7, [O/H] are measured less than 7. Both PNe are compact with a bright central stars. The emission line fluxes are then greatly influenced by the stellar continuum. PNG 004.0-03.0 is measured with the highest [O III] temperature allowed in NEAT (35,000 K), the same was obtained in Smith et al. (2017). The determination of [O/H] for the VLE bipolar PN, PNG 357.1-04.7, in Escudero et al. (2004) included [O III] λ5007 line. [O III] λ4959 was not observed and the extinction coefficient is 0 in their work. In our spectra of this objects, [O III] lines are not seen and the extinction is 0.6 and the measured N$_e$([S II]) is the highest among the sample (17, 500 cm^{-3}). Thus, the accurate determination is difficult for these two complex objects.

Table 4.5: The ionic and elemental abundances of oxygen for 5 PNe with either low (<7.5) or high values (>9.5) [O/H] results.

PNG	$O^+/H \times 10^4$	$O^{2+}/H \times 10^4$	ICF(O)	$[O/H]_{T.W.}$	[O/H] lit	Ref.
000.7-07.4	36.8	3.56	1.07	9.63	9.04	(1)
004.0-03.0	0.01	0.07	1.00	6.91	7.47	(1)
352.0-04.6	30.0	5.12	1.10	9.60	8.74	(2)
356.1-03.3	40.0	4.37	1.06	9.70	8.34	(3)
357.1-04.7	0.06	0.00	1.00	6.75	8.84	(4)

(1) Ratag et al. (1997);

(2) CGS09;

(3) Stasinska et al. (1998);

(4) Escudero et al. (2004);

4.3.7 Conclusion on the abundance ratios

In §4.3.5, element-versus-element plots of alpha elements were formed to explore the lockstep behaviour using PNe in their sample. Strong linear correlations between [Ne/H] and [O/H] and between [Ar/H] and [O/H] expected from the theory are seen and the lockstep variation is proved as the slopes of least-square fits are close to unity. More importantly, larger amount of scatters seen the same analysis using PNe in the literature in Kwitter & Henry (2022) are not seen in our data, this could be demonstrated by higher r^2 values in our results: in this work, r^2 values are 0.81 for [Ne/H] vs. [O/H] and 0.73 for [Ar/H] vs. [O/H], in Kwitter & Henry (2022) r^2 values are 0.72 and 0.66 respectively. The strict lockstep allows using of [Ne/H], [Ar/H] and [O/H] as a metallicity indicator in PNe. The metallicity studies in this work used oxygen as in previous studies. For sulfur, the 'depleted' S abundances compared to [O/H] noticed in previous studies are also obvious in our data. The strong correlations expected for [Cl/H] versus [O/H], [S/H] or [Ar/H] are not seen in the results. The same is seen for [Cl/H] versus [O/H] in Kwitter & Henry (2022). This could be due to large uncertainties in [Cl/H] calculation as discussed in §4.3.3.

Compared with CGS09, [N/O] ratios have a wider range in this study. As more weak emission lines were detected and used in our abundance calculation, the results should better represent the Bulge PN population. A correlation between [He/H] and [N/O] was noticed in GCS09 for *wels* and normal PNe, however, our results did not show that. This is related to a systematical shift in [He/H] between GCS09 and this work. The [He/H] results are expected to be more accurate as discussed in §4.3.3. Such correlation is to be confirmed with more high-resolution spectroscopic observations of bulge PNe. In addition, five compact PNe stand out because their [O/H] values are either lower than 7.5 or higher than 9.5. The extreme values are related to either their complex morphology or excitation states. Although, more accurate information about their distances is required to identify whether they are foreground contaminants.

4.4   The alpha-element abundance distribution in the Galactic bulge

The existence of a metallicity gradient was explored along both the minor axis from b = $-4°$ to $-12°$ and the $b = 0°$ axis. In particular, the vertical metallicity gradient was measured in the previous studies of different stellar populations in the Galactic bulge, e.g. measured using bulge field stars in Zoccali et al. (2008), through RGB stars in Gonzalez et al. (2013). The metallicity gradient was first recognised as a signature of dissipative processes in the formation of a classical bulge because for a boxy/peanut bulge, bulge stars are with a disk origin and any pre-existing metallicity gradient would be flattened out during the bar buckling event. However, in Martinez-Valpuesta & Gerhard (2013), a metallicity gradient was reproduced with a boxy bulge provided that the disk has an initial radial metallicity gradient. Later, as a composite nature of the Galactic bulge was indicated in the ARGOS results (Freeman et al. 2013), the metallicity gradient is considered out of the mixing of components at different latitudes.

In Fig.4.22, the distributions of elemental abundances of oxygen, neon and argon against the Galactic longitude and latitudes are presented. A kernel density estimate (KDE) plot in the middle gives a rough indication of the number density distribution of our PN sample which is patchy because of the lack of high-extinction observations at lower latitudes.

The upper panel shows the results plotted against Galactic longitude and the dotted red line indicates the solar abundance. An error-weighted least-square straight line fitting was performed which gives a slope of -0.0002 ± 0.0054 dex/deg and an intercept of -0.012 ± 0.035 dex. Thus, along the major axis, there is no evidence for a metallicity gradient from this Bulge PNe sample. The distribution of argon abundances follows that of the oxygen while the neon abundances at different longitudes are generally super-solar, especially at lower longitudes. This is because, firstly, [Ne/H] is not available for 20% objects in this sample, secondly, Ne^{2+}/H from [Ne III] $\lambda3868$ is usually the only ionic abundance available, thus, objects with no [Ne/H] are those with [Ne III] $\lambda3868$ lines that are too weak to detect, therefore, low [Ne/H] values are usually not measured in previous PN studies and this work.

4.4.1   Oxygen abundance along the Galactic longitude

In the metallicity map of the southern bulge obtained from RGB stars in Gonzalez et al. (2013), the variations in metallicity along the Galactic longitude seen in the $|b| < 4°$ and the $|b| > 4°$ regions are different, as shown in their Fig.2. The observations in this work were split into the inner ($|b|<4°$) and the outer ($4° < |b| < 10°$) region to make a comparison. [O/H] of individual PNe versus their l coordinates and the mean [O/H] of PNe in an internal of $2.5°$ along the l in the inner and the outer regions are presented in Fig.4.23.

Due to the limitation of sample size, a 2D metallicity mapping could not be obtained for bins smaller than $1°\times1°$ as used in Gonzalez et al. (2013), instead, the PN [O/H] values were averaged in Galactic longitude bins to make a comparison. The tight relation between [O/Fe] and stellar
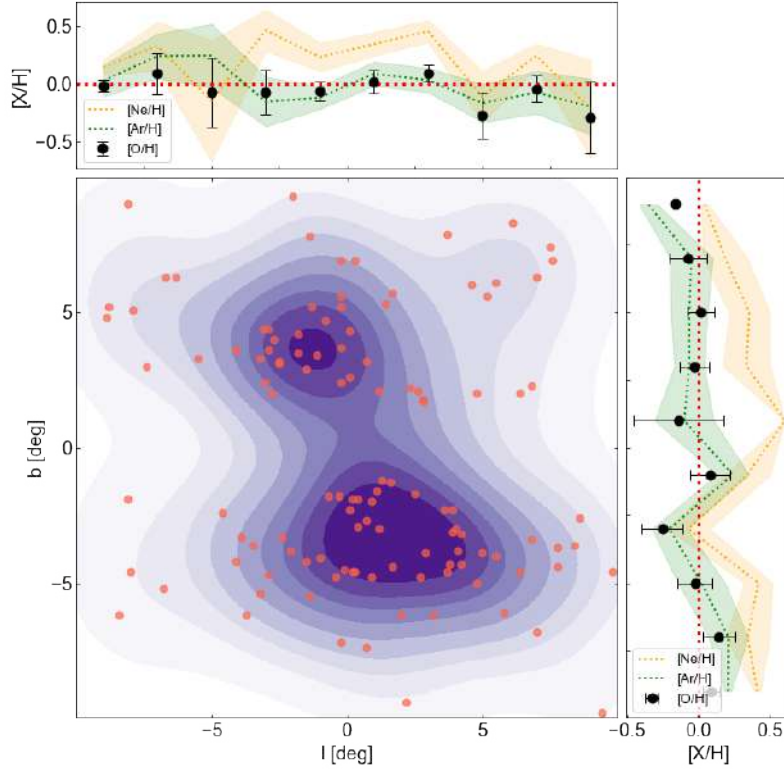
Figure 4.22: The middle panel shows distribution of PNe in a Galactic latitude versus Galactic longitude diagram in this sample. The purple contours show the density map of this PN sample derived using the KDE technique. In the upper panel, black dots show the mean [O/H] values along the Galactic longitude, l, in an interval of $2.5°$. Error bars are from the measured uncertainties. The green and the orange dashed lines show the mean value of [Ar/H] and [Ne/H] in the same Galactic longitude bins. The shaded regions are enclosed by the upper and the lower uncertainties from our measurements. The right panel: The mean [O/H], [Ar/H] and [Ne/H] values along the Galactic latitude, b, in a interval of $2.5°$. The symbols used have the same indication as in the upper panel.

metallicity was found for the bulge RGB population in Jönsson et al. (2016) and Zasowski et al. (2019). In Zasowski et al. (2019), the [O/Fe] decreases with [Fe/H] for $-0.5 <$ [Fe/H] < 0.1, which contains the range of values measured in Gonzalez et al. (2013). The oxygen enhancement tends to constant values for the rest of low- and high-metallicity. Therefore, the metallicity could be a representation of the [O/H] distribution, at least in terms of statistics.

In the lower-left panel of Fig.4.23, the mean [O/H] of PNe in the inner region as a function of Galactic longitude was explored. At positive longitude, the mean oxygen abundance is showing a slight decrease, where [O/H] is higher towards the GC. The mean value of [O/H] then becomes lower around $l \sim 1°$. The elemental abundance of oxygen for individual objects versus Galactic longitude is shown in the upper left panel of Fig.4.23. A linear fit performed for the [O/H] values at positive longitude gives a slope of -0.06 ± 0.01 dex/deg for an error-weighted fitting and the uncertainty in slope is sensitive to the binning. The turning point around the GC at which the mean [O/H] starts to decrease inwards was investigated by deriving the rate of change
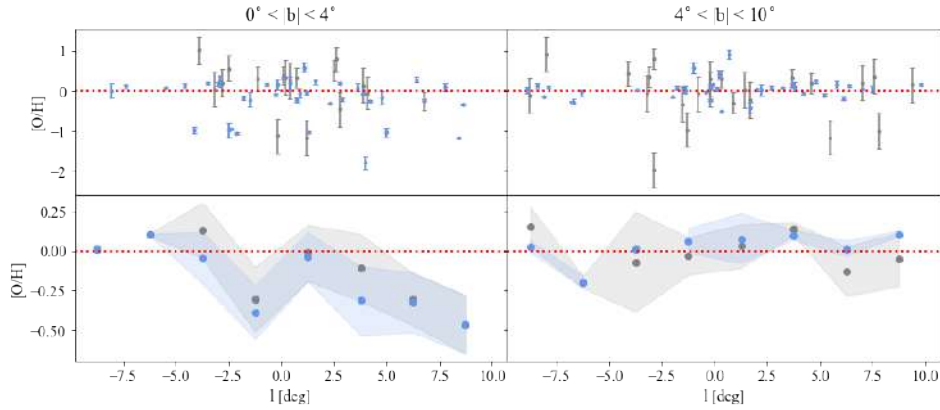
Figure 4.23: The upper panels: [O/H] is plotted versus the Galactic longitude, l. [O/H] is expressed in a log scale such that $[O/H]_\odot = 0$. Blue points represent data with a precision better than 0.3 dex while grey points are less-accurate data with an uncertainty larger than 0.3 dex. The upper left panel is for the inner bulge region defined as $|b|<4°$ while the upper right panel shows data in the outer region in which $4° < |b| < 10°$. The lower panels: mean value of [O/H] versus l in an interval of $2.5°$. The dots show the mean values of [O/H] while shaded regions are enclosed by the upper and lower uncertainties from the measurement. Results from data with a precision better than 0.3 dex are plotted in blue while less-accurate data with an uncertainty greater than 0.3 are plotted in grey. The lower left panel shows the results in the inner bulge region while the lower right panel shows the outer. The red dashed lines indicate the solar abundance.

for each $2°$ longitude bin. This indicates that the minimum in [O/H] happens in the range $2°<l < 4°$. At negative longitude, the PNe within the range $-5°< l < 0°$ show a slight symmetrical trend as for the positive lower longitude. However, for $l < -5°$, each bin contains one object only, therefore, no standard deviation was calculated.

A similar trend at positive longitude in the inner bulge region was also seen for metallicity of the RGB sample in Gonzalez et al. as shown in the left panel of Fig.4.24, the right panel shows our results derived from the bulge PNe sample for comparison. The plot was made by averaging over the mean values in 2D bins in the Galactic plane for each longitude interval instead of individual metallicity and data was accessed from their BEAM (Bulge Extinction And Metallicity) code II. A decrease of metallicity when moving from the GC to higher longitude is seen, however, moderately. A decrease in metallicity near the GC is also noticed, using the same method as before but investigated in bins of $1°$, the minimum is found around $3° < l < 3°$. The metallicity of RGB stars levels off around $l = 1°$, increases at low negative longitude then decreases as move to the higher longitude, following a similar pattern as for the positive longitude. One thing to notice is that the metallicity is derived systemically lower at negative longitude. This is because, as explained in Gonzalez et al. following the discussion in Saito et al. (2011), stars at the far side of the bar are at larger vertical distances from the plane due to the bar-viewing angle.

For PNe in the outer bulge region, as shown in the lower right panel of Fig.4.23 which include the PNe with $b < -4°$ and $4° < b < 5°$ only to match the RGB sample in Gonzalez et al. (2013). The decrease is also seen at higher positive longitude. The number of objects at

positive longitude is close to that in the inner region, however, the derived standard deviations are relatively smaller for $-2° < l < 6°$. This is not due to a selection effect as the extinction in the outer region is lower than the inner as seen in the bulge extinction map in Gonzalez et al. (2012) and the distance to bulge samples sees slight variation, the selection bias on stellar luminosity and density would not lead to such regional difference. The little variation in oxygen abundance in this region could signal a population with solar to slightly super-solar metallicity. Sub-solar [O/H] values are seen at $l \sim 10°$. The RGB population in the outer region show a larger variation in metallicity compared with that in the inner region which is mainly due to the increase in sample size. There is an overall increase in metallicity in moving from negative longitude to positive longitude. However, a slight similar trend is exhibited in the results from the PNe, except for the high negative Galactic longitude.
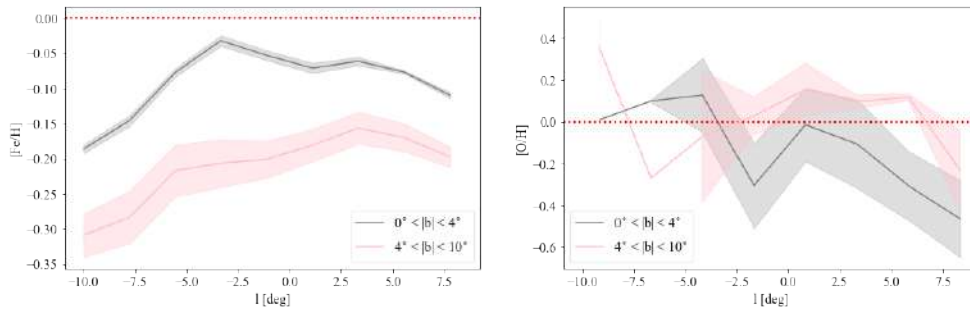
Figure 4.24: The left panel: variation in the mean metallicity, [Fe/H], with the Galactic longitude, l for the inner bulge region ($b < -4°$, grey line) and the outer region ($4° < b < 5°$, pink line) of the RGB sample in Gonzalez et al. (2013). Shaded regions show the variance in the mean metallicity. The red dotted line represents solar metallicity. The bin size is $2.5°$. The right panel: mean oxygen abundance versus l for the bulge PNe sample in this work. The same plot indications are used in the left panel. The red dotted line shows the solar oxygen abundance.

Interpretation of the variation in [O/H] along l

The comparison between RGB star and PNe is not straightforward to interpret. Stars that are currently in the RGB phase are younger than the CSPNe with the same progenitor mass, however, the stellar rotation, mass-loss processes, and the visibility time of PNe would bring complications. The bulge PNe observed were either born earlier in the Galaxy, with low-mass progenitors or ejected from more young massive stars as they are already in the PN phase. However, we would expect the differences in both age and progenitor masses are small as the bulge is dominated by a very old population formed on a short timescale (Ortolani et al. 1995, Zoccali et al. 2006). The same pattern observed in the bulge for [Fe/H] versus l of the RGB stars and for [O/H] versus l of our PN sample includes a metallicity/abundance gradient and a 'dip' near the GC is also consistent with the APOGEE DR13 data in Fragkoudi et al. (2017), and reproduced by a model with an initially co-spatial thin and thick disc. The simulation shows that stars in the inner metal-poor region were formed from a well-mixed and turbulent ISM with a flat radial metallicity gradient. The 'dip' could then be reproduced through the bar mapping stars in the thin and thick inner disc into a B/P bulge.

In addition, according to observed characteristics (Ness et al. 2013b), the thick disk is massive, metal-poor, α-enriched while the MW thin disk has a metal-rich, α-poor and young star population. In the right panel of Fig.4.24, for the inner bulge region, the mean [O/H] of the bulge PNe at the dip around the GC is lower than the two peak values by around 0.4 dex while the difference in [Fe/H] values for the RGB sample is smaller. The central region is, therefore, less α-enhanced and dominated by the thin disk which supports a thicker boxy, B/P bulge formed close to the GC (Bensby et al. (2017).

4.4.2   [O/H] along the Galactic latitude

The distribution of PN oxygen abundance along the Galactic latitude is shown in Fig.4.25. The bulge PN population is found in three distinct abundance groups: a slightly sub-solar to super-solar abundance group (-0.5 < [O/H] < 1 dex) spreading across the bulge, a sub-solar metallicity group ([O/H] < −0.8 dex) distributed in the inner bulge (|b| < 6.1°) and two PNe with significantly sub-solar metallicity ([O/H] < −1.5 dex) that locate in a slightly more inner region (|b| < 5°), which is clearly seen in the histogram plotted along the [O/H] axis. The differentiation, as well as the distribution of oxygen abundances, are not affected if only the high-quality measurements (Δ[O/H] < 0.2 dex, colour-coded blue) were considered. The sizes of these three abundance groups take up 88%, 10% and 2% among the sample respectively.
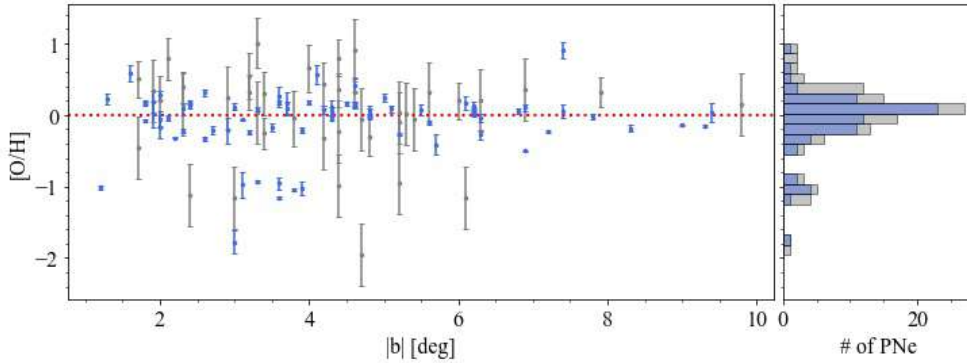
Figure 4.25: The left panel: [O/H] distribution of the Galactic bulge PNe along the Galactic latitude, b. Error bars of the scatters are from the measurement uncertainties. The blue points are data with a precision better than 0.3 dex while the grey points are the less precious measurement with an error greater than 0.3 dex. The values are expressed in the [O/H]-[O/H]$_{\odot}$ scale. The red dashed line indicates the solar abundance. The right panel: the histogram of [O/H] of the bulge PNe sample. Different colours have the same indication as the left panel.

The existence of low oxygen abundance object results in a gentle decrease in [O/H] values towards the midplane, thus, we segregate each oxygen abundance group to investigate whether the vertical metallicity gradient seen clearly in bulge RGB stars is present in our PNe sample. [O/H] of individual PN is plotted against the Galactic latitude in Fig. 4.26. The error-weighted least squares fitting was performed for high and the low oxygen abundance groups at negative and positive b respectively, the slope and the Pearson's correlation coefficient are shown on the plot. All bar one of the slopes agree with a flat but noisy gradient. For the high metallicity PNe

at positive latitude, the oxygen metallicity gradient is negative at the 2.4σ level. However, none of the correlation coefficients is greater than 0.2, indicating no or very weak correlations.

We also consider the sample of PNe with a bipolar morphology which is thought as a direct consequence of the higher masses and angular momenta of their progenitor stars. (Peimbert et al. 1983, García-Segura et al. 1999). Therefore, they correspond to a younger population among PNe. The same calculations were applied to bipolar PNe only and the results are seen in Fig.4.27. No significant correlation or slope was measured for bipolar PNe at negative b, while a high correlation is measured for bipolar objects at positive b with a gradient of -0.051 ± 0.011 dex/deg obtained.
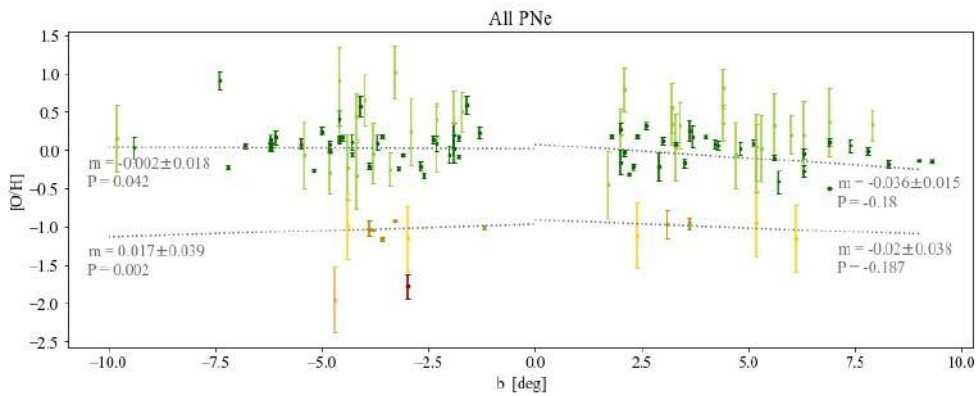
Figure 4.26: [O/H] is plotted versus the Galactic latitude, b for the bulge PNe. The data are colour-coded according to their abundance groups: green - the super-solar abundance group; yellow - the sub-solar metallicity group; red - the strongly sub-solar metallicity group. The dark colour in each group represents data with an uncertainty of less than 0.3 dex. The dashed lines are the results of error-weighted least squares fitting. The fitting was performed for positive b and negative b respectively. The slope, m and Pearson's r coefficient are shown next to the best fit. As there are two data points only for the strongly sub-solar metallicity group, no fitting was performed.
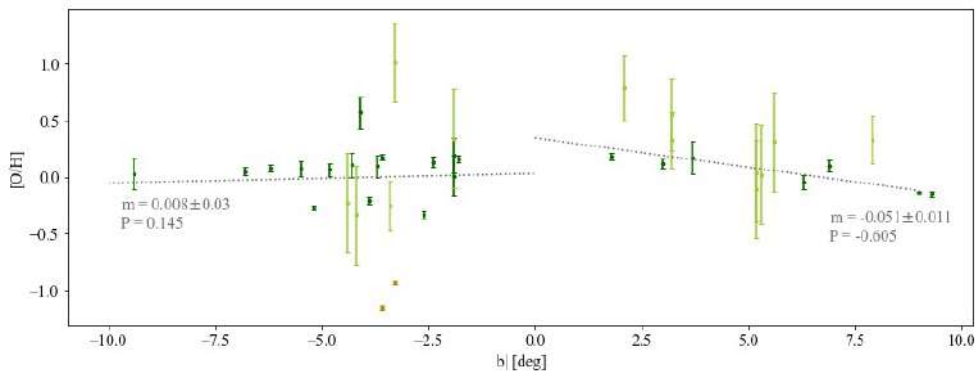
Figure 4.27: The plot is constructed in the same manner as Fig. 4.26 for the bulge bipolar PNe only.

Interpretation of the variation in [O/H] along *b*

The bipolar sample generally shows a super-solar oxygen abundance as seen in Fig. 4.27, which matches with the expectation for a younger population, and exhibits an abundance gradient with a moderate correlation for b>0°. As the correlation is weak when we consider the whole sample, instead of a classical bulge, bipolar PNe may be a representative of the young thin disk population in which the metallicity is strong while the rest of PNe are of the thick disk with a nearly flat metallicity distribution.

4.4.3   Conclusion on the abundance gradient

With the bulge PN sample in this work, we find an abundance gradient along the Galactic Plane. The gradient is negative from the GC outwards while a dip in [O/H] is seen which is consistent with previous studies of the metallicity of stars. This pattern was reproduced in a model of a co-spatial thin and thick disk with no classical bulge component. We noticed the mean [O/H] value at the dip is less α-enhanced compared with other data points and using the RGB results as a reference. This is consistent with a B/P bulge formed near the Galactic centre.

A composite distribution of [O/H] is seen. We isolated the bipolar PNe which are considered with a younger and massive progenitor. The vertical abundance gradient was measured with a moderate correlation with the bipolar PNe while the correlation between [O/H] and *b* is weak for the whole sample. This is considered to be the result of mixing the metal-rich thin disk and metal-poor thick disk when forming the B/P bulge.

4.5   Chemical evolution in the bulge and the PN dating methods

Dividing PNe into different groups according to the ages of their progenitors is essential to pinpoint the chemical evolution in the Galactic bulge at a certain time or during a time interval. However, such a process is not straightforward. The physical properties of AGB stars are not as well-known as normal stars, the traditional method using theoretical isochrones is, therefore, less effective. Alternative methods using nebular properties were put forward instead as discussed in Maciel et al. (2010).

4.5.1   Classification based on models of AGB evolution

A differentiation scheme between young ($t_\star$ < 0.5-1 Gyr) and old populations ($t_\star$ > 7.5 Gyr) was introduced in Stanghellini & Haywood (2018). The theoretical yields from evolutionary models of AGB star in Ventura et al. (2016) show that the young and old PNe occupy distinct loci on the N/H versus C/H plane in their Fig. 2, allowing this to be used for the classification. It was summarised in Stanghellini & Haywood (2018) that the AGB stars with C/H > N/H have gone through the carbon star phase, therefore, have a low-mass progenitor while the AGB stars with [N/H] > 0.57 × [C/H] + 3.67 line (obtained by a linear fit on the right plot in Fig. 2 in Ventura et

al. 2016) have gone through the HBB and have a mass $> 3M_\odot$ and an age < 0.5-1 Gyr. A similar criterion was obtained for oxygen abundance instead of carbon from the left panel in Fig. 2 in Ventura et al. (2016). This could be used when only optical observations of PNe are available. PNe with young progenitor should comply with the equation $[N/H] > 0.6 \times [O/H] + 3.3$. PNe with older progenitors (OPPNe) are defined as those with $[N/H] < 0.8 \times [O/H] + 1.4$ as such stars have gone through the carbon star phase.

The concordance between this PN dating scheme and the one from the morphological aspect discussed before is evaluated. The distributions of PN morphologies among the young and the old groups are shown in Fig.4.28. The number density distribution of main morphological classifiers is shown in the left panel, 44% of YPPNe and 28% of OPPNe have a bipolar morphology and 44% of the bipolar PNe are classified as YPPN while the ratio is 31% for elliptical PNe. Therefore, using bipolar morphology as an indicator of PN age is showing a certain consistency with the scheme based on AGB models. The distribution of the number of PNe with a certain sub-classifier is shown in the right panel. From the plot, none of these morphological substructures shows an indication of the PN age differentiation under the above-mentioned scheme.
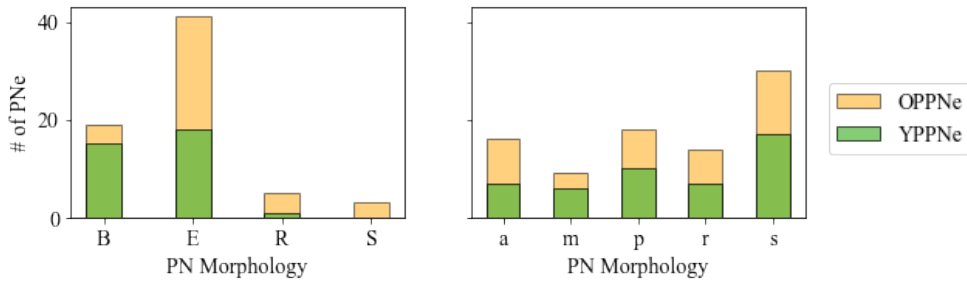
Figure 4.28: PN morphology distribution of the YPPNe (green) and OPPNe (orange) groups. The left panel shows the distribution of main classifiers while the right presents the distribution of sub-classifiers.

The spatial distribution of the young and old populations of PNe are shown in Fig.4.29, together with the number density distributions along both the Galactic longitude and the latitude. It could be seen from the PN density distribution plot along l that PNe of the young population spread across the Galactic longitude. The Kuiper's variant of the well-known Kolmogorov-Smirnov test implemented by `astropy.stats.kuiper` was used to check the randomness of the PNe distribution. In the null hypothesis, H_0, is that the spatial coordinates are uniformly distributed. The inner 2 degrees of the bulge were excluded from the range of the uniform cumulative distribution function. The p-value returned is therefore an estimation of the probability that the distribution is drawn from a uniform distribution. The field of the Bulge in this work was split into north and south, and east and west of the Galactic Centre (GC). The p-values obtained together with the sizes of the whole sample as well as of each subsample are listed in Table.4.6.

The stringent threshold for significance: $p < 0.003$ (approximately $3\ \sigma$) was considered to

confidently reject the null hypothesis. Then, the longitude of YPPNe cannot be rejected from a uniform distribution as p-values in the first columns are all greater than 0.003. This is also true for the YPPNe b coordinate in all subfields, but for the complete field (p-value is 2.4E-03). This might be due to the lack of observations in the outer northern-west bulge region. Significant differences that could be declared from a uniform distribution are seen for OPPNe along l and b in the whole field and most of the subfields. For the 13 young PNe on the northern sky, the p-value is 0.93, their distribution along l is, thus, close to a random distribution. For the old population of PNe, their distributions along l for the complete field, the north, the south and the west are distinguished from a uniform distribution. Although no observations are available in the high-extinction strips in which b is within $2°$, the number density of OPPNe is exhibiting a certain north-south asymmetry in terms of number density and excessive OPPNe are observed at $b = -4°$ strip. This is consistent with systematically higher counts at $b < 0°$ found in the stellar density distribution of the MW bulge in Valenti et al. (2016). An over-density at $l \sim 7°$ is observed for OPPNe which is also seen in the same bulge stellar density profile.
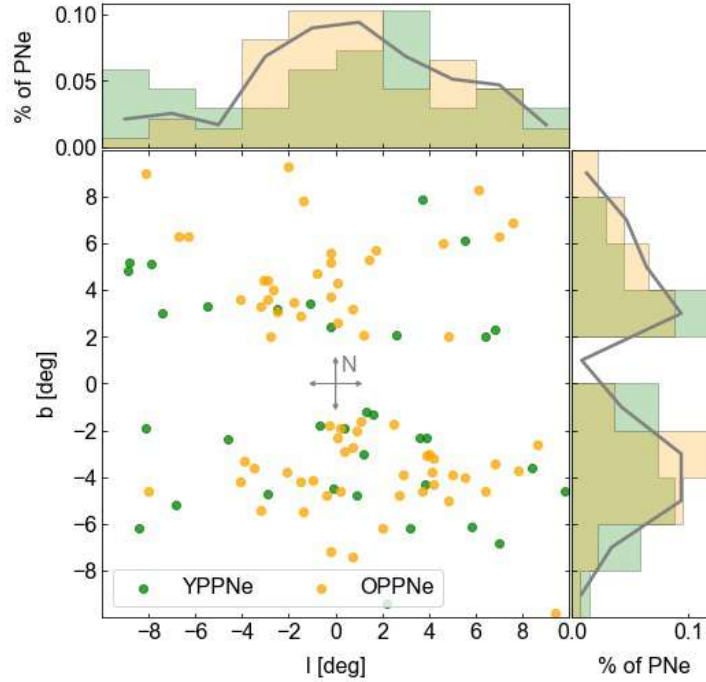
Figure 4.29: The middle panel: Distribution of our bulge sample in a Galactic latitude versus Galactic longitude diagram. "Incomplete" stripe along the Galactic plane due to high extinction. Orange dots are the OPPNe classified according to the AGB models while green dots are the YPPNe. The upper panel presents the density distribution histograms along the Galactic plane of both the OPPNe (in orange) and the YPPNe (in green) sample. The grey line connects the density histogram of the whole sample. The right panel shows the vertical density distribution of the OPPNe and the YPPNe samples, the colours and symbols have the same meaning as the upper panel.

Thus, the YPPNe and the OPPNe are showing distinct distributions in terms of number densities. YPPNe are located at low longitudes and strongly sub-solar oxygen abundances are found in the

	l_{YPPNe}	b_{YPPNe}	l_{OPPNe}	b_{OPPNe}
All	3.5E-01 (34)	**2.4E-03** (34)	**1.3E-06** (68)	**7.1E-07** (68)
N (b>0°)	9.3E-01 (13)	2.3E-02 (13)	**8.3E-05** (30)	8.9E-03 (30)
S (b<0°)	9.2E-02 (21)	7.6E-02 (21)	**1.0E-03** (38)	**1.8E-06** (38)
E (l>0°)	4.1E-01 (19)	3.1E-01 (19)	7.5E-02 (37)	**5.3E-04** (37)
W (l<0°)	4.7E-01 (15)	3.3E-02 (15)	**1.2E-05** (31)	**1.1E-04** (31)

Table 4.6: The p-values of the Kuiper's test for the OPPNe and YPPNe samples, as well as their area subsamples. The null hypothesis (H_0) for the test is that the distribution of the Galactic coordinate l or b is uniform. East (E), west (W), north (N) and south (S) are with respect to Galactic coordinates on either side of $0°$ longitude and latitude. P-values less than 0.003 are in bold which leads us to reject H0 for those single samples.
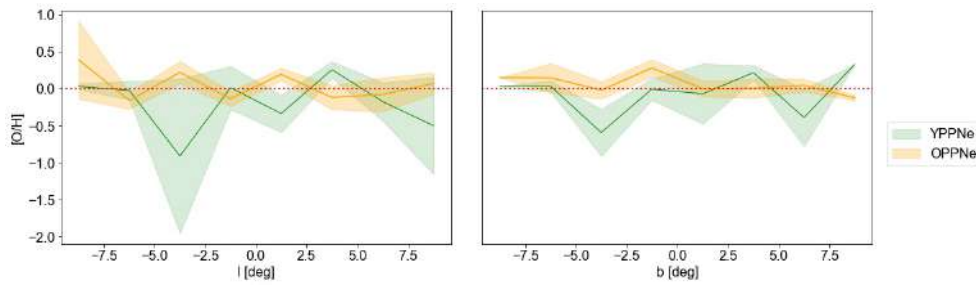
Figure 4.30: The left and the right panels show variations in the mean [O/H], with l and b, respectively, for the OPPNe (in orange) and the YPPNe (in green). Shaded regions show statistical uncertainties. The red dotted line represents solar oxygen abundance. The bin size is $2.5°$.

inner region while the OPPNe has an over-density at $b \sim -4°$ and their oxygen abundances are showing an east-west asymmetry.

The oxygen abundance distributions along each of the Galactic coordinates of both the YPPNe and the OPPNe are shown in Fig.4.30. The variation in [O/H] of the YPPNe along both l and b are more evident compared with the OPPNe, as the presence of low-[O/H] objects, which might come from the thin disk in the MW. The mean values of bins at $b \sim -7.5°$ and $b \sim 7.5°$ are not good references as they contain only 1 object. The mean [O/H] values of YPPNe along the l and b are fluctuating between super-solar and sub-solar. For the OPPNe, the [O/H] distribution along l is fluctuating moderately around the solar oxygen abundance. At $l \sim 0°$ and $l \sim -4°$, the results are super-solar. Along the Galactic latitude, b, the mean [O/H] of the OPPNe agree well with the solar abundance within the statistical uncertainties except for one measurement, at $b \sim -1°$, mean [O/H] is super-solar.

While the fluctuation is seen, the [O/H] distribution of YPPNe along l is showing two peaks of [O/H] values at low negative and positive l respectively as well as a dip around the GC, which is similar to the trend observed from the whole sample of PNe and the RGB stars in the inner bulge region. The [O/H] distribution for the OPPNe is generally flat and less noisy. Besides, from the left panel in Fig.4.30, a certain anti-correlation between mean [O/H] values of YPPNe and of OPPNe along l is seen. The bi-variate Kolmogorov–Smirnov tests were performed in

each Galactic longitude bin to compare the metallicity distributions along l of the PNe. The null hypothesis, H_0 is that the [O/H] values for the young and the old PNe have the same distribution along l. For the bin $0° < l < 2.5°$ and $2.5° < l < 5°$, the p-values are 0.05 and 0.02 respectively, which allow us to reject the null hypothesis if we are working on at the 0.05 significance level. In this case, the metallicities of the young and the old populations should come from the same population. This is also true if we compare bipolar PNe in the YPPNe and non-bipolar PNe in the OPPNe only. However, because of the small sample size (< 10) and this is not statistically significant.

In previous studies of the chemical evolution in the bulge, stellar populations originated from different components have a metallicity distribution peaked at different values of [Fe/H]. A metallicity distribution function of stars (MDF), which shows the proportion of stars that have a particular metallicity, was used to infer different components and estimate the contribution of each component. In Bensby et al. (2011), a doubly-peaked metallicity distribution was derived from a sample of microlensed dwarf, turn-off and sub-giant stars, indicating a bimodal metallicity distribution. This was confirmed in subsequent studies, e.g. in Rojas-Arriagada et al. (2014) using stars, in Nandakumar et al. (2018) using M giants in the inner bulge, together with multiple-peak features in the MDF. These raised the question of how many components of stars are there in the bulge was then concerned.

In Ness et al. (2013a), five populations were noticed. The nature of each main component and the corresponding mean metallicity are shown in their Fig. 1 and summarised as the following:

- Component A: a metal-rich population with a mean [Fe/H] of 0.15 in a relatively thin boxy/peanut-bulge structure concentrated close to the Galactic plane, which is likely to be the younger chemically evolved thin disk in the inner region.

- Component B: is a more metal-poor population (mean [Fe/H] = −0.25) with a thick boxy/peanut-bulge structure, spread across $b = -5°$ to $-10°$. They might be formed out of the thin disc at early times.

- Component C: a population with a mean [Fe/H] of −0.61 and is associated with the old thick disk.

- Components D & E: populations with low mean metallicity and are interpreted as metal-poor stars in the metal-weak thick disc and the inner Galactic halo.

Bensby et al. (2017) investigated the probability distribution of stellar age for stellar populations at different peaks in the MDF. The results show that component A is composed of stars either younger than 3 Gyr or with an age of 4 to 8 Gyr, component B is of stars with an age of 3 to 6 Gyr or older than 10 Gyr and components C are old stars with an average age of 10 Gyr. Stars of components D & E have a spread-out age distribution with a peak value at around 10 Gyr in Bensby et al. (2017).
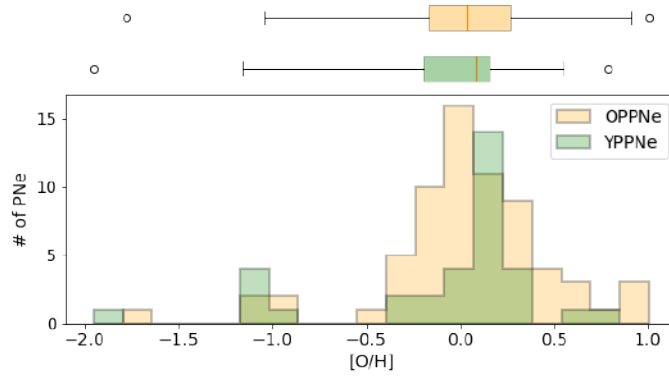
Figure 4.31: The [O/H] distributions of the OPPNe (orange) and the YPPNe (green). The top panel shows the corresponding box plots extend from the 25th to 75th percentiles, breaking by a red vertical line indicating the median. Whiskers extends to the 1st and 99th percentiles.

We then consider an oxygen abundance distribution function as an analogue of the metallicity distribution function in the bulge star studies to investigate the age-[O/H] relation with our bulge PN sample. A histogram together with a box plot of the oxygen abundance of both the YPPNe and OPPNe is presented as Fig.4.31. Both the YPPNe and the OPPNe show a wide range of oxygen abundance and are present in the three metallicities groups discussed before. Median [O/H] values of the OPPNe and the YPPNe are 0.04 and 0.09 respectively, the YPPNe have a higher oxygen abundance as expected for a younger population. To study the peak structures in our oxygen abundance distribution function, the 10, 000 data points of each object generated in `NEAT` with the Monte-Carlo method were adopted. This gives a smoother oxygen abundance distribution function as shown in Fig.4.32. The `scipy.signal.find_peaks_cwt` method was applied to identify the number of peaks.
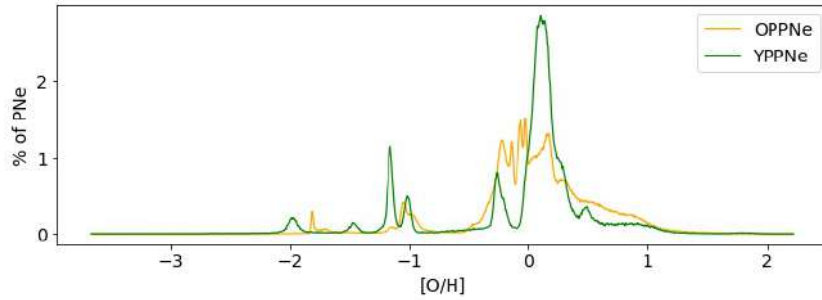
Figure 4.32: Oxygen abundance distribution function of this bulge PN sample with a Monte-Carlo realisation. The orange and the green show data of the OPPNe and the YPPNe respectively.

For the OPPNe, three peaks could be found for the high metallicity population at [O/H] = -0.25(C), -0.07(B), and 0.17(A) respectively, which is qualitatively consistent with the results in Bensby et al. (2017) and Ness et al. (2013a). There are also two peaks at [O/H] = -1.02 and -1.79 corresponding to stars in the metal-weak thick disc metal-poor and the inner Galactic halo respectively with a mean age around 10 Gyr in Bensby et al. (2017).

For the YPPNe, peaks of the high-metallicity group are found at [O/H] = −0.25 dex, 0.11 dex and 0.47 dex respectively. The two peaks with super-solar [O/H] values are consistent with the age distribution of components A in Bensby et al. (2017) and are related to the younger chemically evolved thin disc in connection with the Galactic bar and accommodate a large proportion of stars that are younger than ∼ 1 Gyr in the bulge. The peak at sub-solar oxygen abundance is also seen in Bensby et al. (2017) and is explained by the overlap of think and thick disk stars.

4.5.2 Age distribution through the statistical age-N/O mass relation for CSPN

For the CSPN ages, we have also used another method, Method 3 in Maciel et al. (2010), based on the statistical age-N/O mass relation in CSPNe. With this method, the mass of a CSPN, m_{CS}, is first estimated in the unit of $m_\odot$ using the [N/O] ratio through

$$m_{CS} = \begin{cases} 0.7242 + 0.1742 \, [\text{N/O}] & \text{if} - 1.20 < [\text{N/O}] < -0.26 \\ 0.825 + 0.936 \, [\text{N/O}] + 1.439 \, ([\text{N/O}])^2 & \text{if} - 0.26 < [\text{N/O}] < 0.20 \end{cases}$$

The initial-final mass relation from Macial et al. (2003) was then adopted to estimate the main sequence progenitor stellar masses, m_{MS} which is of the form

$$m_{CS} = a + bm_{MS} + c \left(m_{MS}\right)^2$$

where a = 0.47778, b = 0.09028 and c = 0. The mass-age relation

$$\log t = d + e \log m_{MS} + f \left(\log m_{MS}\right)^2$$

was applied to estimate the main sequence lifetime, The two cases in Maciel et al. (2010) were considered. The values of parameters adopted are d = 1.0, e = −2.0 and f = 0.0 for Case A and d = 1.0, e = −3.6 and f = 1.0 for Case B that are taken from Bahcall & Piran (1983).

The derived ages of CSPNe are shown in Fig.4.33 in rank order and the objects that were classified as YPPNe or OPPNe are colour-coded blue and orange respectively in the plot. The results for the complete sample are present Fig.4.33(a) in which it could be seen that the young population determined from the scheme in Stanghellini & Haywood (2018) are all with the age of CSPN derived lower than 1.0 Gyr as suggested, the classification scheme in Stanghellini & Haywood (2018) then agrees with this age determination method well for the young population PNe. For PNe that were defined as OPPNe, all bar one of the objects have their CSPN ages calculated ≳ 1 Gyr, but not as the suggested old range (t > 7.5 Gyr). In Fig.4.33(b), the ages calculated for 53 objects with well-determined abundances (Δ([N/O]) < 0.2 dex) are presented, the exception is ruled out for objects with more reliable measurements. The discrepancy between the age suggested for the OPPNe and that derived could result from large uncertainties in the age determination of FKG stars in Ramírez et al. (2013) which was used to indicate CSPN age in Stanghellini & Haywood (2018). In addition, the initial-final mass relation used to derive the

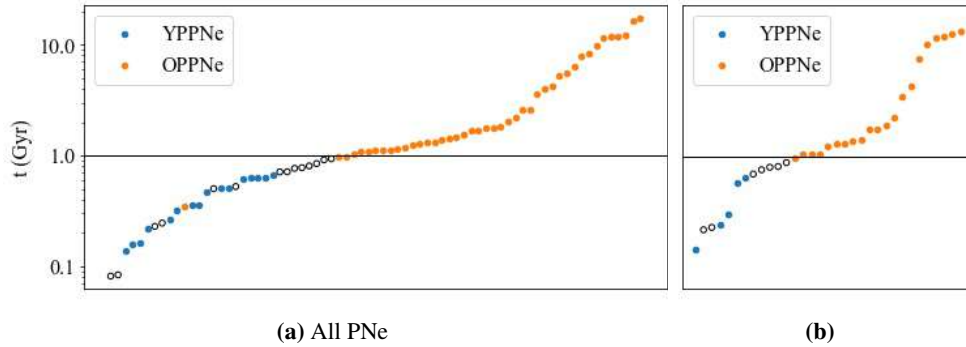main-sequence stellar mass brings extra uncertainties.

(a) All PNe   **(b)**

Figure 4.33: A comparison of CSPN ages derived from two schemes. The ages derived through the statistical age-N/O mass relation are presented in ranked order. **(a)** shows the results for all PNe in this sample while **(b)** shows the results for PNe with an uncertainty less than 0.2 dex in abundances. The vertical axis shows the ages of CSPNe derived on a log scale. The orange and the blue dots show the YPPNe and the OPPNe determined based on the AGB models. The black solid line represents an age of 1 Gyr which is the maximum age considered as a YPPN.

The age distribution of the CSPNe is shown in Fig.4.34 in which the histograms in white show the data of the highest quality, i.e. [O/H] with an uncertainty less than 0.2 dex and a median uncertainty is present. Using parameters for Case A, the age distribution of CSPNe shows a maximum at around 3 Gyr (3 Gyr for the high-quality data as well), the youngest and the oldest objects are calculated up to about 0.4 and 13.6 Gyr which are systematically lower than the range of ages derived spectroscopically from microlensed bulge dwarfs in Bensby et al. (2013) by ~1 Gyr. For Case B, the lifetime decreases more rapidly for massive stars resulting in a narrower distribution. the sharp maximum is around 1-2 Gyr (the same result for objects with high-quality measurement only), and the ages obtained range from 0.1 to approximately the age of the universe. When considering the PNe with the highest-quality abundance measurement, except for the maximums at the younger ages, there is another maximum located at around 11 Gyr for Case A and 12 Gyr for Case B, containing one-eighth of this sample.

Compared with the bulge PN age distribution obtained in Gesicki et al. (2014), an extended distribution including an older as well as a younger population is derived from both cases, the fraction of younger PNe is large. This results from low-[O/H] samples in our data set.

4.6 The sulfur anomaly

Possible reasons for this sulfur anomaly were suggested by Henry et al. (2012). For either oxygen or chlorine, in the slightly sub-solar to the super-solar range that accommodates most of the data points (8.5, 9) for [O/H] and (5, 5.7) for [Cl/H]), the sulfur abundance varies from its minimum value to the maximum, extending over 7 orders of magnitude. The same also applied to neon and argon as the correlation is seen between [Ne/H], [Ar/H] and [O/H]. Therefore, the amount of sulfur deficit or depletion is independent of these elemental abundances. The correlation
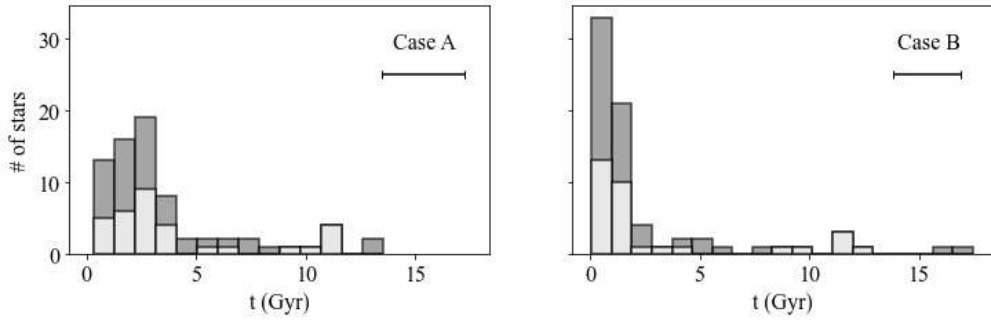
Figure 4.34: Age distribution of the central stars of planetary nebulae using a statistical [N/O]-mass relation. The left panel shows the results obtained with parameters for Case A and the right panel shows that for Case B. A typical age uncertainty estimated is shown in the upper right corner. The highlighted histograms show the location of the high-quality data namely that have uncertainty in abundances less than 0.2 dex.

between the observed sulfur anomaly and a variety of PN parameters was tested by Henry et al. (2012), who also defined the difference between the abundance observed from Galactic and extragalactic H II regions and the actual observed [S/H] from PNe as a sulfur deficit to quantify such an anomaly. The sulfur deficit, SD, is given by

$$ \mathrm{SD} \equiv \epsilon(S_{\mathrm{exp}}) - \epsilon(S_{\mathrm{icf}}) $$

where $\epsilon(S_{\mathrm{exp}})$ is the expected [S/H], i.e., the abundance that a PN of a given [O/H] would have if its [S/H] placed it on the track of H II regions, and is given by

$$ \epsilon(S_{\mathrm{exp}}) = 1.053 \times [\mathrm{O/H}] - 1.994 $$

while $\epsilon(S_{\mathrm{obs}})$ is the observed [S/H] of a PN calculated with the use of an ICF. Sulfur deficit shows no correlation with these parameters, thus, few possibilities are left and the corresponding follow-up studies are:

(1) The conventional ICF is used to uncover the unobserved S^{3+} ions (including KB94). However, with the new improved ICF computed from a large grid of photoionization models in their work, and later in Delgado-Inglada et al. (2014), and direct measurements of S^{3+} abundance from infrared observations, the sulfur anomaly still exists.

(2) The uncertainties in AGB nucleosynthesis models. Luke et al. (2013) explored whether the neutron capture process in AGB modelling could lead to the observed sulfur abundance, but systematically high sulfur abundance values are still predicted in their results.

(3) The depletion of sulfur due to dust or molecule formation. Such formation is required to happen in a carbon-rich nebula, otherwise, the sulfides will be oxidized and released back to the gas phase. Since no strong correlation is seen between [C/O] and the sulfur deficit, they conclude that the sulfur depletion to dust is unlikely.

Further questions could be asked on the these arguments are:

(a) Can H II regions accurately represent the expected sulfur or other α elemental abundances? Although stronger relationship between [Ne/H] or [Ar/H] and [O/H], the data points are still suffering from scatters unlike the good linear relationship measured with H II regions. The determination of sulfur deficit depends largely on the accurate expected value and the calculated deficit has a small variation from -0.5 to 0.5, thus, if the expected value differs by only 0.1 dex, the deficit can change by a large percentage. Theoretically, H II regions in which star formation is taking place represent a younger stellar population than the PNe and usually have an age of a few million years.

(b) Can [C/O] ratio reflect the actual chemical environment in the PNe? Using CELs could give an overview of the abundance of a PN, but it was noticed that two distinct gas phases are existing in a PN, this results in large abundance variations known as the abundance discrepancy problem, therefore, an accurate determination of [C/O] is difficult.

Thus, the numerical value of sulfur deficit might not quantify this problem well. One thing to notice from the integral-field spectroscopy of three PNe from the VLT/MUSE in García-Rojas et al. (2022) is that the dominant line in sulfur abundance determination, [S II] $\lambda6731$ depend largely on the PN morphology and the regions of overdensities contribution the most to the emission which is also true for [O II] $\lambda7330$. Thus, the flux measurement of such lines would be affected a lot by the slit size, position of the slit and the internal morphological features of the PNe. Meanwhile, the uncertainties in [O/H] and [S/H] could also make a difference. For these three PNe, the integrated abundances could vary from the literature values by up to 0.5 dex. The dispersion between multiple measurements could, therefore, reflect the non-spherical and homogeneous density distributions within the PNe.

The PN morphological features measured in the previous chapter were tested for any correlation with the sulfur deficit. For both the main morphological classifiers and the sub-classifiers the distribution of the sulfur deficit values show essentially no difference.

It is worth comparing the sulfur anomaly seen in the YPPNe and the OPPNe to investigate whether this discrepancy between the sample of H II regions and PNe resulted from the difference in ages of the stellar population. The calculated sulfur deficit for the two PNe populations, using the definition in Henry et al. (2012), together with a box plot is shown in Fig.4.35. The objects with accurate abundances measurement, i.e. with uncertainty less than 0.2 dex, are emphasised. A distinction in sulfur anomaly between the young and the old PNe is seen: young PNe, having a mean sulfur deficit of -0.08 ± 0.10 dex, are showing certain fluctuation around 0 (no deficit) and half of the YPPNe has [S/H] measured higher than the expected value, while for OPPNe the mean deficit is 0.51 ± 0.06 dex with only two out of 30 OPPNe are measured with no deficit. This distinction is also present if the whole PNe sample is considered. A Kolmogorov–Smirnov test was performed in which the null hypothesis, H_0, is that the sulfur deficits of these two PNe populations are from the same distribution. The p-value is 1.5E-06 for the high-precision measurement and 3.0E-11 for the whole PN sample. Thus, the null hypothesis is rejected and the PNe of the two age populations have a different distribution of sulfur deficit. The correlation between the age derived in the previous analysis and the sulfur deficit was tested

and only a slight positive correlation is seen for the PNe younger than 1 Gyr with the Case B age determination and the Pearson's r is 0.48.

The conclusion that could be drawn from this study about the sulfur anomaly is that this problem is related to the different ages between H II regions and the PNe population. PNe from an older stellar population are the main reason for such systematically lower sulfur abundance measurements. This indicates that previous suspects on the reliability of ICF, the chemical processes within the PNe might not be the reason for the sulfur anomaly. In Lucertini et al. (2021), the sulfur abundance in the bulge was investigated with dwarf and sub-giant stars and compared with stellar metallicity as well as oxygen abundance. Their results show that [S/Fe] decreases with [Fe/H] as expected for other α-elements. However, in their Fig. 9, [S/O] decreases with [Fe/H] which is not seen when comparing sulfur with other α-elements. This was attributed to departures from LTE and granulation effects but has not been quantified. Therefore, explanations for the sulfur anomaly include either the results from stars come out of uncertainties and there is a certain depletion in OPPNe or sulfur was enriched as the evolution of the GB. Therefore, high-resolution observations of PNe in the disk are expected to be compared with this sample.
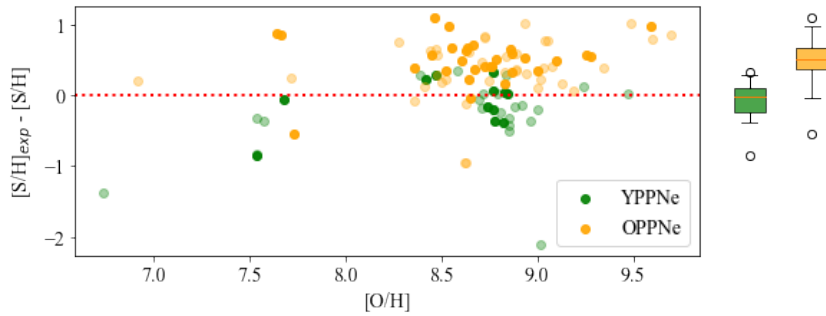

Figure 4.35: The left panel: The sulfur deficit is plotted versus the oxygen abundance. Solid data points are those with uncertainty in abundances less than 0.2 dex. The right panel: box plots summarising the sulfur deficits measured in this work with the boxes extend from the 25th to 75th percentiles, breaking by a vertical line indicating the median. Whiskers extends to the 1st and 99th percentiles.

4.7   Conclusion

In this Chapter, the chemical abundance of this PN sample in the bulge was first derived by spectroscopic data reduction, correcting for the interstellar extinction, calculating electron temperatures and densities and summing up ionic abundances and multiplying ICFs to account for unobserved ions. The derived logarithmic extinction as well the chemical abundances were compared with literature results. Then, by considering oxygen abundance as the metallicity indicator, this sample of PNe was used to probe the chemical evolution in the Galactic bulge.

The interstellar extinction values derived are generally consistent with the literature values, but overall lower. This was largely attributed to the better spectroscopic data quality of our data,

however, the data reduction methodology and the observation strategies could also influence results. The individual fluxes show a good agreement with high-resolution spectroscopic data in the literature, however, the number of objects that allow such a comparison is limited. The individual ionic abundances of objects were compared with homogeneous results in the literature. All bar one of the results shows small deviation that are related to the use of atomic data and line lists. The O^+ abundance derived in this work uses the [O II] $\lambda\lambda7320,7330$ doublet and this could vary largely with the internal structures, physical conditions and line ratio measurement, thus few measurements show large differences to the literature value. Considering the lower S/N, the significant increase in the number of emission lines detected in our VLT/FORS2 spectra, compared to previous literature values mean that data in this work are the current largest and the most accurate data set of the planetary nebulae in the Galactic bulge.

The spatial variations of oxygen abundance in the Galactic bulge were investigated with this PN sample. A similar increase of metallicity along $b = 0°$ towards the GC in the inner bulge was seen in our sample and the literature results from RGB stars, showing a certain consistency with the simulation results assuming a boxy bulge. However, along the minor axis, the vertical metallicity gradient observed in RGB stars is not seen in our results even when the age of PNe was taken into consideration. However, the age of PNe is likely to be a solution to the problem of the sulfur anomaly as no mean sulfur deficit was measured for our YPPN sample.

Two different PN dating schemes were employed and cross-compared. The one from the morphological point of view is indicative but limited to the statistical purpose. The two schemes based on AGB models and an age-N/O mass relation of CSPN show good consistency in terms of the young population PNe. The spatial distributions of the YPPNe and the OPPNe are consistent with the model of a thin disc and a peanut/boxy bulge. For the metallicity distributions of these two groups, a number of peaks are seen and the peak values agree with the study using stars and dwarfs when different alpha enhancement was considered. This adds another independent line of evidence to the existence of a B/P bulge and our results also show some bulge asymmetries.

Chapter 5

The Abundance Discrepancy Factor in the bulge PNe

5.1   Introduction

The determination of chemical abundances of the elements heavier than He in PNe uses usually and traditionally the collisionally excited lines (CELs), which is the case in Chapter 4. It was not until faint optical recombination lines (ORLs) were detected in spectroscopic observations of PNe, that the ORLs were used to derive the ionic abundances. With spectrograms measured from photographic plates and the primitive atomic data in Wyse (1942), a discrepancy between the oxygen abundances determined from emission lines formed by recombination and collisional excitations was noticed. ORLs measured a higher abundance of oxygen than CELs in PNe NGC 7009 and NGC 7027. Later in Torres-Peimbert & Peimbert (1977), with the 0.91 m and 1.5 m telescopes at CTIO and KPNO, carbon abundances in PNe were determined with the weak C II λ4267 measurement and exceeded the results obtained from the CELs of the same ion in ultra-violet observations. The discrepancy could be as large as an order of magnitude. Both the observing facilities and the atomic data has had large improvements in subsequent decades and this discrepancy was confirmed in several studies, e.g. Tsamis et al. (2004) and Wesson, Liu & Barlow (2005).

The discrepancy is generally parameterised by the abundance discrepancy factor (ADF) in Liu et al. (2001)

$$ADF(X^{+i}) = \frac{(X^{+i}/H^+)_{ORLs}}{X^{+i}/H^+)_{CELs}}.$$

There is no break in seeking the mechanism for such an abundance discrepancy. Emissivities of CELs depend exponentially on electron temperature while ORLs have a much weaker (inverse power-law) dependence. The temperature fluctuations within a homogeneous plasma and the existence of cold and hydrogen deficit clumps in the extended nebulae were suggested for the solution. The former could not explain in the cases of high ADFs while a 3D model considering chemical inhomogeneities successfully reproduced the observed intensities of CELs and ORLs simultaneously in Yuan et al. (2011). The H-deficit regions, constitute less than 2% of the total nebula mass, resulting in the majority of emission lines of heavy elements in the model.

The emissivity of ORLs is affected by both the amount of metals and the mass contribution of the H-poor and metal-rich components. Later, a grid of photoionization models considering the two metallicity components within a PN was built in Gómez-Llanos & Morisset (2018), which could be used to determine the mass of metals, however, the contribution of the metal-rich region could be isolated because the H I intensity used for the ionic abundance determination is measured from the whole nebula instead of the small regions. The chemical inhomogeneities were confirmed by observational pieces of evidence in García-Rojas et al. (2016): ORLs O II λ 4649, 51 are mainly from the central part of the nebula in the narrow-band images, and recently, in García-Rojas et al. (2022), with the VLT/MUSE seep integral-field unit (IFU) spectroscopic observations of 3 high-ADF PNe, by obtaining 2D maps of ADF.

The mechanism for the existence of two gas phases is not well-understood. The abundance discrepancy is universal in photoionised nebulae and was also measured in H II regions. In Tsamis et al. (2011), with the VLT/FLAMES IFU observations, the ADF in Orion nebulae is largely related to the protoplanetary disc LV 2. One would consider whether the solid body deconstructions during the formation of PNe could lead to a similar pocket of cool and metal-rich gas. This has been investigated in Henney & Stasinska (2010). To reproduce the ADFs measured in PNe, which are typically an order of magnitude higher than H II regions, sublimation of volatile bodies with a mass comparable to the most massive debris disk around solar-like stars as well as an inefficient mixing of metal-rich gas is required. The current most promising hint to resolve this problem is the binarity in CSPNe, which was uncovered by the statistical analysis of literature ADFs measured in PNe in Wesson et al. (2018). ADFs were seen to correlate with binarity and electron density only and high ADFs are related to the short binary periods.

In this chapter, the ADFs were measured with this Bulge PNe sample. With this high-resolution observational data, the physical conditions, chemical abundances, and PN morphological features were investigated to see whether they are linked to the measured ADFs. Additionally, with the discovery of new binary stars in *Gaia* DR2, detailed configurations of binary CSPNe were considered. The log of observation and the data reduction procedure was described in the previous Chapter.

5.2 Physical conditions from ORLs

Recombination lines in the PN spectra were measured with `ALFA`, of which the methodologies and algorithm details were discussed in Chapter 4. For 105 PNe, `ALFA` detected recombination lines for more than 1 multiplet and the number of ORLs detected ranges from 2 to 27.

The physical conditions, including the electron temperatures and densities, were derived from He I line ratios and from O II recombination lines ratio in `NEAT` apart from using CELs in Chapter 4. The Balmer jump, i.e. I(λ3643) - I(λ3681), however, could not be used for temperature determination for our spectra as they are out of the wavelength coverage. For the O II recombination line temperatures, the recombination coefficients in Storey et al. (2017) were adopted in `NEAT`

which was derived for nebular conditions. `NEAT` also performs a number of plasma diagnostics from recombination lines. Electron densities and temperature were obtained through Lagrange interpolation with fraction intensities of O^{2+} recombination lines measured from the spectra. In `NEAT`, temperatures estimated from helium line ratios are calculated using equations derived through fitting the tabulated values of $\lambda 5876/\lambda 4471$ and $\lambda 6678/\lambda 4471$. The electron density is fixed to be 5000 cm^{-3} in `NEAT`.

5.3 Measurement of Abundance and ADF with ORLs

`NEAT` was employed to derive the ionic abundances from ORL fluxes with the atomic data listed in Table.1 in Wesson et al. (2018). The electron temperatures and densities derived from CELs in Chapter 4 were used for the determination. `NEAT` first calculates the ionic abundance from each RL intensity measurement. Then, intensities of RLs belonging to the same multiplet were co-added to give the ionic abundance measurement from this multiplet. The final ionic abundance measured from RLs adopts the weighted-average abundances derived from each multiplet. Because of the faintness of recombination lines, contamination of background and sky subtraction residuals, as well as the stellar continuum, could result in large uncertainties in their intensities. The multiplet abundance for each multiplet was weighted by the co-added intensity as default `NEAT`. Although, according to Wesson et al. (2018), the V5 multiplet of O^{2+} usually gives higher abundances, however, no object has the V5 multiplet detected in our data.

The ionic abundance would be flagged as unreliable in `NEAT` and not used in subsequent ADF calculations if the following is true

1. The object's emission list contains only one multiplet

2. Among abundance derived from different multiplets, the highest measurement is greater than three times the lowest measurement

3. For O^{2+}, both the V1 and V10 multiplets, which are usually the most strong, are not detected but other multiplets

With these criteria, the reliable heavy element recombination line emission was detected in spectra of 13 PNe in this sample. The spectra in the 4650 Å region where multiple recombination lines are concentrated of these objects are shown in Fig.5.1, together with the `ALFA` fitting as well as the residuals. The derived physics conditions for these 13 PNe from both CELs and ORLs are present in Table.5.1. It was noticed that T$_e$(He I 7281/6678) is extremely high in 7 PNe. This could be due to flux calibration at the red end as the temperature determination is sensitive to the line ratios. Thus, T$_e$(He I 7281/6678) is considered as unreliable in this study.

Table 5.1: Electron densities and temperatures of 13 objects with an ADF measured, together with uncertainties derived in NEAT. Temperatures are in units of Kelvin and densities in cm^{-3}. For most of the cases when T_e(He I 7281/667) is extremely high, the measurements are considered as unreliable.

PN G	T_e([NII])	T_e([OIII])	T_e(He I 5876/4471)	T_e(He I 6678/4471)	T_e(He I 7281/6678)	T_e(O II)	n_e([O III])	n_e([S II])	n_e([ArIV])	n_e(O II)
000.9-02.0	9380^{+780}_{-620}	9240^{+350}_{-380}	-	-	19500^{+2700}_{-3200}	-	-	5700^{+2680}_{-5700}	2620^{+1350}_{-1450}	-
001.3-01.2	6540^{+100}_{-90}	-	4240^{+1370}_{-1390}	3220^{+1110}_{-1680}	22300^{+1900}_{-2000}	-	-	4310^{+1030}_{-1590}	-	-
004.1-03.8	10800 ± 300	11300 ± 100	-	9780^{+4540}_{-3710}	23400^{+2800}_{-3400}	-	-	1900^{+630}_{-1090}	504^{+218}_{-224}	-
351.9+09.0	-	12700 ± 100	2650^{+460}_{-560}	1810^{+380}_{-450}	1450^{+240}_{-250}	-	-	423^{+356}_{-423}	941^{+305}_{-310}	-
353.2-05.2	8100 ± 50	9260 ± 90	3870^{+1370}_{-1520}	3010^{+920}_{-1320}	-	-	321^{+305}_{-406}	103^{+76}_{-71}	1 ± 0	-
353.7+06.3	7450 ± 110	7120 ± 80	-	3150^{+1280}_{-2140}	14500^{+1300}_{-1400}	-	905^{+198}_{-253}	910^{+335}_{-493}	-	-
356.5-03.6	7940 ± 110	8750 ± 120	1000^{+560}_{-650}	2680^{+1140}_{-2180}	7100 ± 350	-	-	2620^{+320}_{-370}	3720^{+330}_{-360}	-
357.2+02.0	10400^{+400}_{-300}	10000 ± 100	-	3970^{+1960}_{-3970}	18000^{+2300}_{-2700}	-	-	3590^{+1110}_{-2240}	2820 ± 400	-
357.5+03.2	8570^{+200}_{-210}	8660 ± 1180	262^{+262}_{-262}	620^{+620}_{-620}	-	-	-	1110^{+390}_{-610}	133^{+132}_{-1448}	-
357.9-03.8	21200^{+1200}_{-1300}	20900 ± 400	-	-	-	-	-	2000^{+640}_{-1040}	1 ± 0	-
358.2+04.2	9580^{+350}_{-310}	7940 ± 60	3070^{+1160}_{-1570}	5000^{+2720}_{-5000}	19300^{+2400}_{-3000}	-	2050^{+1200}_{-2050}	10700^{+2500}_{-4900}	3360^{+380}_{-430}	-
359.0-04.1	8540 ± 70	8890 ± 70	-	4320^{+1480}_{-2470}	14000^{+1000}_{-1100}	-	-	952^{+167}_{-202}	499^{+305}_{-330}	-
359.7-01.8	9320 ± 220	12100 ± 200	3140^{+3140}_{-2030}	-	-	-	-	1650^{+440}_{-610}	1590^{+390}_{-400}	-

The ionic and elemental abundances derived using both the CELs and RLs are presented in Table.5.2 and Table.5.3 respectively. The abundance discrepancy factors of O^{2+}/H^+ and O/H are shown in Table. Other than the oxygen abundance discrepancy, a discrepancy in N/H was measured for 3 objects among the whole sample, in which the derivation of N/H using CELs is from N^+/H^+ measured while using RLs lines could only obtain N/H from N^{2+} ionic abundance. Thus, there are large uncertainties as discussed in Wesson et al. (2018), especially when N II, and N III recombination lines at the red end were used. In addition, extremely high ADFs in Ne/H were measured for 4 objects. These are related to the RL abundance derived from Ne II $\lambda 3709.62$ line at which the noisy spectrophotometric table could result in large uncertainties in flux measurement. Therefore, the ADFs in O^{2+}/H^+ and O/H are considered in this work.
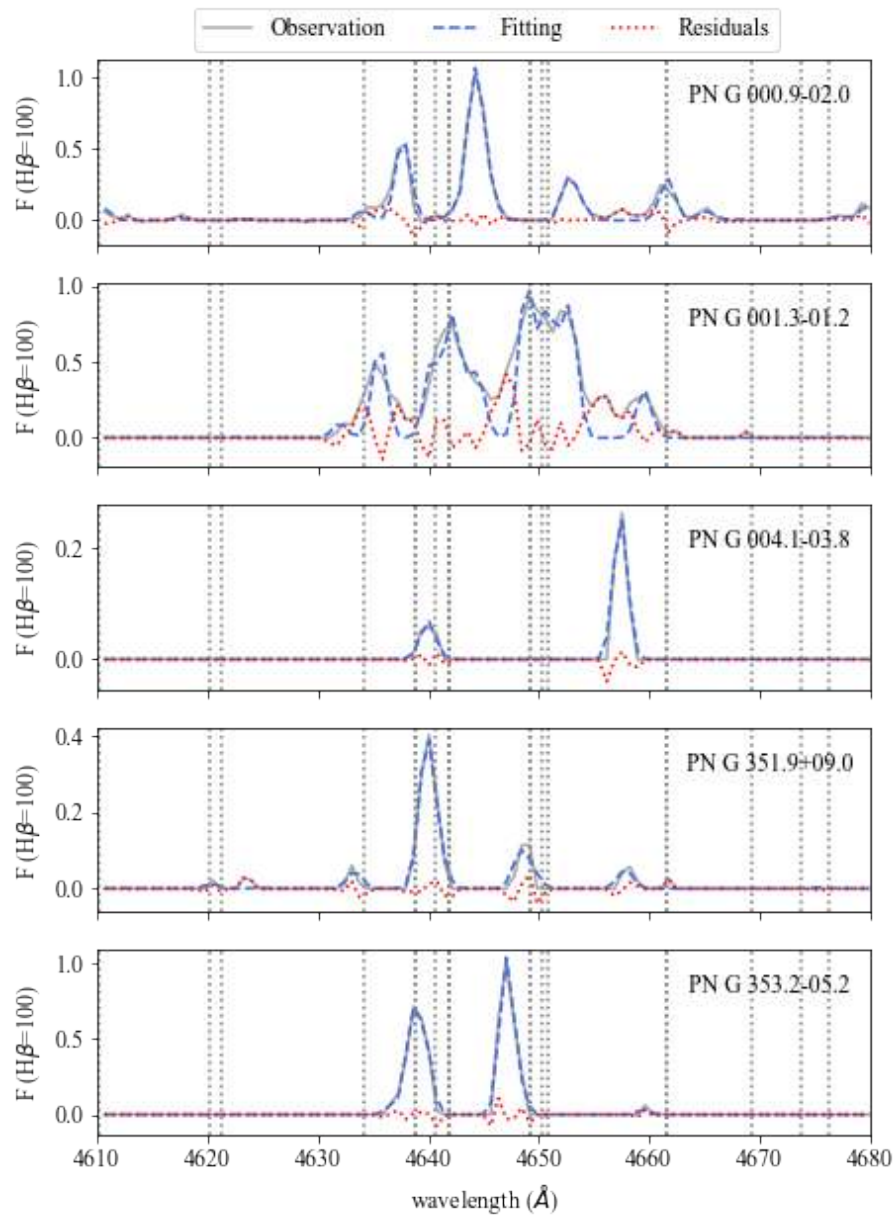
Figure 5.1: Spectra of the 13 objects with ADFs measured in the sample, covering the region from 4610 Å to 4680 Å. which contains recombination lines due to O II, N II, and C III. The vertical axis shows the intensity of the emission lines , i.e. F(Hβ)=100. Some of the recombination lines are indicated as the vertical lines on the plot.
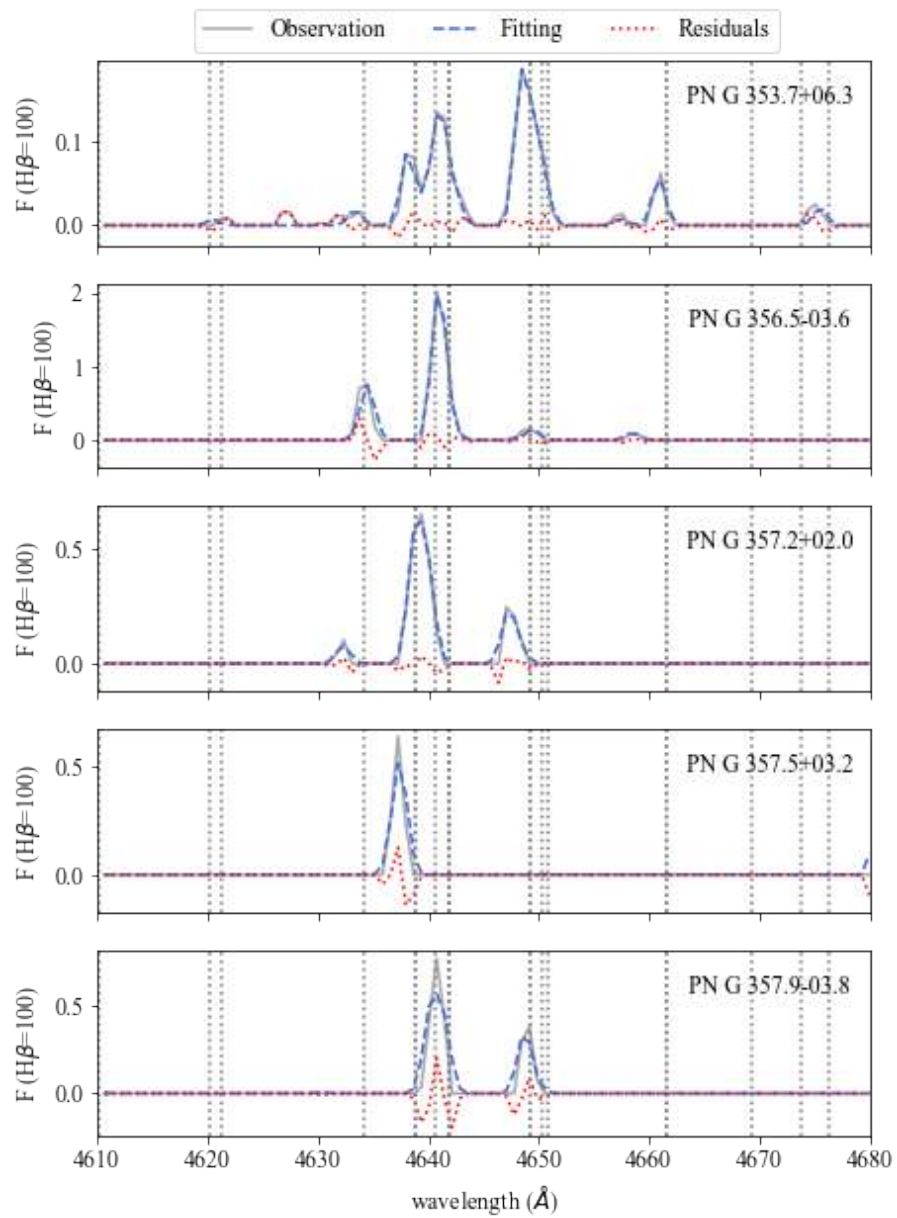
Figure 5.1: (continued):
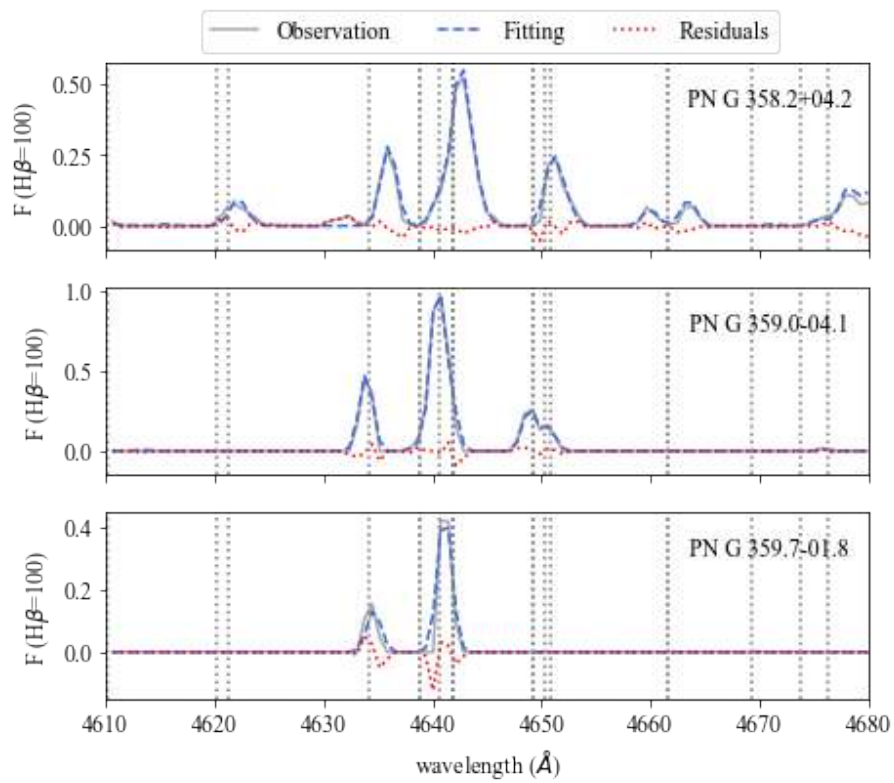
Figure 5.1: (continued):

Table 5.2: Ionic and total abundances derived from collisional excited lines for the 13 objects with ADFs measured. Abundances are given on a scale where log(H)=12.

PN G	000.9-02.0	001.3-01.2	004.1-03.8	351.9+09.0	353.2-05.2	353.7+06.3	356.5-03.6	357.2+02.0	357.5+03.2	357.9-03.8	358.2+04.2	359.0-04.1	359.7-01.8
CEL Abundance													
N+/H	$6.71^{+0.10}_{-0.13}$	7.75 ± 0.02	$7.31^{+0.15}_{-0.28}$	5.20 ± 0.04	$7.26^{+0.01}_{-0.03}$	$7.54^{+0.07}_{-0.09}$	7.80 ± 0.04	$7.33^{+0.20}_{-0.36}$	$7.94^{+0.06}_{-0.07}$	5.34 ± 0.02	$7.12^{+0.18}_{-0.43}$	$8.58^{+0.07}_{-0.08}$	$6.17^{+0.04}_{-0.05}$
icf(N)	$9.40^{+2.40}_{-3.22}$	$2.07^{+0.12}_{-0.14}$	$1.85^{+0.53}_{-1.01}$	$114.00^{+24.00}_{-31.00}$	$38.30^{+6.50}_{-5.60}$	$3.52^{+0.80}_{-1.03}$	$4.66^{+0.47}_{-0.52}$	$4.02^{+2.18}_{-4.02}$	$11.90^{+4.00}_{-9.80}$	$24.10^{+3.10}_{-3.80}$	$23.60^{+17.20}_{-23.60}$	$1.34^{+0.08}_{-0.12}$	$34.50^{+5.10}_{-5.90}$
N/H	$7.66^{+0.11}_{-0.20}$	$8.07^{+0.03}_{-0.04}$	$7.60^{+0.04}_{-0.08}$	$7.25^{+0.10}_{-0.13}$	8.85 ± 0.06	8.09 ± 0.05	8.47 ± 0.03	$7.93^{+0.06}_{-0.19}$	$9.01^{+0.13}_{-0.34}$	$6.72^{+0.06}_{-0.07}$	$8.49^{+0.19}_{-0.28}$	$8.71^{+0.04}_{-0.05}$	$7.71^{+0.05}_{-0.06}$
O+/H	$7.66^{+0.15}_{-0.24}$	7.36 ± 0.05	$8.37^{+0.24}_{-0.43}$	$6.49^{+0.10}_{-0.12}$	$6.84^{+0.05}_{-0.08}$	$8.10^{+0.12}_{-0.19}$	$8.20^{+0.06}_{-0.07}$	$8.28^{+0.30}_{-0.43}$	$8.17^{+0.10}_{-0.13}$	6.26 ± 0.07	$7.39^{+0.28}_{-0.43}$	$9.13^{+0.13}_{-0.18}$	$7.07^{+0.07}_{-0.09}$
O2+/H	$8.58^{+0.09}_{-0.11}$	7.38 ± 0.01	8.30 ± 0.03	8.28 ± 0.01	8.35 ± 0.02	8.50 ± 0.04	$8.63^{+0.02}_{-0.03}$	8.72 ± 0.02	$8.87^{+0.15}_{-0.37}$	7.42 ± 0.02	8.73 ± 0.02	8.55 ± 0.01	8.45 ± 0.02
icf(O)	1.00 ± 0.01	1.01 ± 0.01	1.00 ± 0.00	$1.85^{+0.02}_{-0.02}$	1.13 ± 0.01	1.00 ± 0.01	$1.26^{+0.01}_{-0.01}$	1.09 ± 0.01	$1.94^{+0.10}_{-0.11}$	$1.56^{+0.01}_{-0.01}$	1.01 ± 0.01	$1.06^{+0.01}_{-0.01}$	$1.35^{+0.01}_{-0.01}$
O/H	$8.63^{+0.09}_{-0.11}$	7.68 ± 0.03	$8.64^{+0.13}_{-0.39}$	8.55 ± 0.01	8.42 ± 0.02	$8.65^{+0.05}_{-0.06}$	8.87 ± 0.03	$8.89^{+0.09}_{-0.35}$	$9.24^{+0.12}_{-0.32}$	7.64 ± 0.02	$8.77^{+0.03}_{-0.06}$	$9.26^{+0.11}_{-0.14}$	8.60 ± 0.02
Ne2+/H	$8.02^{+0.07}_{-0.08}$	-	7.69 ± 0.02	7.74 ± 0.01	8.03 ± 0.03	$7.73^{+0.08}_{-0.09}$	7.84 ± 0.04	8.15 ± 0.02	$8.57^{+0.17}_{-0.43}$	7.07 ± 0.02	8.23 ± 0.02	8.24 ± 0.02	7.30 ± 0.03
icf(Ne)	$1.12^{+0.03}_{-0.05}$	1.00 ± 0.00	$2.17^{+0.64}_{-1.93}$	$1.88^{+0.02}_{-0.03}$	$1.17^{+0.01}_{-0.01}$	$1.40^{+0.12}_{-0.18}$	$1.73^{+0.06}_{-0.06}$	$1.49^{+0.28}_{-1.15}$	$2.31^{+0.19}_{-0.27}$	1.66 ± 0.02	$1.06^{+0.03}_{-0.14}$	$5.07^{+1.20}_{-1.57}$	$1.41^{+0.01}_{-0.01}$
Ne/H	$8.07^{+0.07}_{-0.09}$	-	$8.03^{+0.13}_{-0.38}$	8.01 ± 0.01	8.10 ± 0.03	$7.88^{+0.09}_{-0.10}$	8.08 ± 0.04	$8.32^{+0.08}_{-0.33}$	$8.93^{+0.14}_{-0.42}$	7.29 ± 0.02	$8.26^{+0.02}_{-0.06}$	$8.94^{+0.10}_{-0.13}$	7.45 ± 0.03
Ar2+/H	$6.68^{+0.09}_{-0.11}$	6.08 ± 0.02	$5.92^{+0.03}_{-0.04}$	5.55 ± 0.01	6.36 ± 0.02	$6.40^{+0.03}_{-0.04}$	6.47 ± 0.04	6.20 ± 0.05	$6.56^{+0.11}_{-0.24}$	5.45 ± 0.02	$6.54^{+0.04}_{-0.05}$	6.60 ± 0.02	$5.75^{+0.04}_{-0.05}$
Ar3+/H	$5.91^{+0.07}_{-0.08}$	-	5.14 ± 0.02	5.96 ± 0.02	$5.49^{+0.02}_{-0.03}$	3.84 ± 0.14	6.23 ± 0.03	5.93 ± 0.02	$6.72^{+0.14}_{-0.37}$	4.11 ± 0.03	5.75 ± 0.01	5.79 ± 0.02	5.84 ± 0.02
icf(Ar)	$1.12^{+0.04}_{-0.05}$	1.00 ± 0.00	$2.17^{+0.64}_{-1.93}$	1.01 ± 0.01	$1.03^{+0.00}_{-0.01}$	$1.40^{+0.12}_{-0.18}$	$1.28^{+0.04}_{-0.04}$	$1.30^{+0.23}_{-0.82}$	$1.09^{+0.04}_{-0.05}$	1.04 ± 0.01	$1.04^{+0.03}_{-0.14}$	1.00 ± 0.00	1.03 ± 0.00
Ar/H	$6.80^{+0.09}_{-0.11}$	6.08 ± 0.02	$6.33^{+0.14}_{-0.39}$	6.12 ± 0.01	6.43 ± 0.02	$6.56^{+0.04}_{-0.06}$	$6.77^{+0.03}_{-0.04}$	$6.51^{+0.10}_{-0.30}$	$7.06^{+0.11}_{-0.27}$	5.66 ± 0.02	$6.63^{+0.04}_{-0.07}$	6.67 ± 0.02	6.16 ± 0.03
S+/H	$5.30^{+0.12}_{-0.31}$	$5.71^{+0.04}_{-0.06}$	$5.75^{+0.15}_{-0.31}$	$3.46^{+0.05}_{-0.06}$	$5.59^{+0.02}_{-0.04}$	$5.99^{+0.08}_{-0.10}$	6.19 ± 0.04	$5.94^{+0.19}_{-0.43}$	$6.31^{+0.06}_{-0.07}$	$4.10^{+0.03}_{-0.04}$	$5.45^{+0.19}_{-0.43}$	$6.89^{+0.07}_{-0.09}$	$5.01^{+0.05}_{-0.06}$
S2+/H	$7.01^{+0.10}_{-0.13}$	5.90 ± 0.11	$6.36^{+0.04}_{-0.05}$	5.81 ± 0.02	6.18 ± 0.13	$6.75^{+0.07}_{-0.08}$	$6.83^{+0.05}_{-0.06}$	$6.58^{+0.05}_{-0.06}$	$7.36^{+0.17}_{-0.43}$	4.78 ± 0.05	$6.79^{+0.09}_{-0.10}$	6.85 ± 0.05	6.19 ± 0.06
icf(S)	$1.52^{+0.13}_{-0.14}$	$1.05^{+0.01}_{-0.01}$	$1.03^{+0.03}_{-0.08}$	$3.37^{+0.25}_{-0.28}$	$2.36^{+0.14}_{-0.11}$	$1.16^{+0.06}_{-0.08}$	$1.25^{+0.03}_{-0.03}$	$1.20^{+0.17}_{-0.38}$	$1.63^{+0.19}_{-0.34}$	$2.03^{+0.09}_{-0.10}$	$2.02^{+0.66}_{-0.80}$	$1.00^{+0.00}_{-0.00}$	$2.28^{+0.11}_{-0.12}$
S/H	$7.20^{+0.09}_{-0.11}$	6.14 ± 0.07	$6.49^{+0.04}_{-0.06}$	6.34 ± 0.04	$6.64^{+0.10}_{-0.11}$	$6.89^{+0.06}_{-0.07}$	7.01 ± 0.05	$6.78^{+0.05}_{-0.08}$	$7.61^{+0.18}_{-0.43}$	5.17 ± 0.05	$7.11^{+0.13}_{-0.19}$	7.18 ± 0.05	6.58 ± 0.05

Table 5.3: Ionic and total abundances derived from recombination lines for the 13 objects with ADFs measured. Abundances are given on a scale where log(H)=12.

PN G	000.9-02.0	001.3-01.2	004.1-03.8	351.9+09.0	353.2-05.2	353.7+06.3	356.5-03.6	357.2+02.0	357.5+03.2	357.9-03.8	358.2+04.2	359.0-04.1	359.7-01.8
RL Abundance													
He+/H	11.47 ± 0.04	11.06 ± 0.01	10.98 ± 0.01	10.61 ± 0.01	11.15 ± 0.01	11.04 ± 0.01	10.99 ± 0.01	10.99 ± 0.02	10.65 ± 0.03	10.96 ± 0.00	11.10 ± 0.01	11.11 ± 0.01	10.72 ± 0.02
He2+/H	$9.16^{+0.04}_{-0.05}$	9.25 ± 0.08	-	10.79 ± 0.00	10.46 ± 0.00	7.57 ± 0.06	10.60 ± 0.01	10.12 ± 0.00	$10.88^{+0.04}_{-0.05}$	10.94 ± 0.00	9.38 ± 0.07	10.05 ± 0.01	10.48 ± 0.01
He/H	11.47 ± 0.04	11.06 ± 0.01	10.98 ± 0.01	11.01 ± 0.00	11.23 ± 0.01	11.04 ± 0.01	11.14 ± 0.01	11.05 ± 0.02	11.08 ± 0.03	11.25 ± 0.00	$11.11^{+0.01}_{-0.02}$	11.15 ± 0.01	10.92 ± 0.01
C2+/H	$9.43^{+0.08}_{-0.09}$	-	7.93 ± 0.03	$8.40^{+0.03}_{-0.04}$	9.25 ± 0.02	8.94 ± 0.01	8.96 ± 0.03	$8.30^{+0.06}_{-0.07}$	10.26 ± 0.02	8.88 ± 0.04	8.81 ± 0.01	9.04 ± 0.02	-
C3+/H	-	9.09 ± 0.08	6.92 ± 0.06	-	8.20 ± 0.10	8.08 ± 0.03	-	7.76 ± 0.12	-	-	-	-	-
icf(C)	1.00 ± 0.00	1.00 ± 0.00	1.00 ± 0.00	1.00 ± 0.00	1.00 ± 0.00	1.00 ± 0.00	1.00 ± 0.00	1.00 ± 0.00	1.00 ± 0.00	1.00 ± 0.00	1.00 ± 0.00	1.00 ± 0.00	1.00 ± 0.00
C/H	$9.43^{+0.08}_{-0.09}$	9.09 ± 0.08	7.97 ± 0.02	$8.40^{+0.03}_{-0.04}$	9.29 ± 0.02	9.00 ± 0.01	8.96 ± 0.03	$8.40^{+0.05}_{-0.06}$	10.26 ± 0.02	8.88 ± 0.04	8.81 ± 0.01	9.04 ± 0.02	-
N2+/H	10.15 ± 0.06	$10.28^{+0.05}_{-0.07}$	10.03 ± 0.02	10.38 ± 0.01	10.67 ± 0.02	10.72 ± 0.03	$8.98^{+0.06}_{-0.07}$	10.40 ± 0.02	8.68 ± 0.15	$10.04^{+0.08}_{-0.12}$	10.46 ± 0.03	10.51 ± 0.01	9.58 ± 0.07
N3+/H	8.37 ± 0.04	8.44 ± 0.10	7.32 ± 0.03	8.21 ± 0.01	8.36 ± 0.02	7.00 ± 0.08	8.86 ± 0.01	8.27 ± 0.02	$8.24^{+0.06}_{-0.07}$	8.20 ± 0.08	8.24 ± 0.01	8.49 ± 0.01	8.21 ± 0.02
icf(N)	$1.12^{+0.03}_{-0.05}$	$1.93^{+0.11}_{-0.12}$	$2.17^{+0.64}_{-1.93}$	1.01 ± 0.01	$1.03^{+0.00}_{-0.01}$	$1.40^{+0.12}_{-0.18}$	$1.28^{+0.04}_{-0.04}$	$1.33^{+0.23}_{-0.85}$	$1.09^{+0.04}_{-0.05}$	1.04 ± 0.01	$1.04^{+0.03}_{-0.14}$	$3.96^{+0.75}_{-0.93}$	1.03 ± 0.00
N/H	$10.20^{+0.05}_{-0.08}$	10.58 ± 0.06	$10.36^{+0.13}_{-0.38}$	10.39 ± 0.01	10.68 ± 0.02	$10.86^{+0.04}_{-0.06}$	$9.33^{+0.04}_{-0.05}$	$10.52^{+0.07}_{-0.28}$	$8.86^{+0.11}_{-0.12}$	10.04 ± 0.12	$10.49^{+0.03}_{-0.06}$	$11.10^{+0.08}_{-0.10}$	9.61 ± 0.06
O2+/H	9.04 ± 0.09	9.80 ± 0.05	$8.84^{+0.08}_{-0.10}$	$8.88^{+0.06}_{-0.07}$	9.57 ± 0.02	8.96 ± 0.03	9.18 ± 0.05	9.34 ± 0.02	$9.60^{+0.22}_{-0.11}$	9.57 ± 0.04	9.14 ± 0.02	9.27 ± 0.03	$9.08^{+0.08}_{-0.09}$
icf(O)	$1.12^{+0.03}_{-0.05}$	$1.97^{+0.11}_{-0.12}$	$2.17^{+0.64}_{-1.93}$	$1.88^{+0.02}_{-0.03}$	$1.17^{+0.01}_{-0.01}$	$1.40^{+0.12}_{-0.18}$	$1.73^{+0.06}_{-0.06}$	$1.49^{+0.28}_{-1.15}$	$2.31^{+0.19}_{-0.27}$	1.66 ± 0.02	$1.06^{+0.03}_{-0.14}$	$5.07^{1.20}_{-1.57}$	$1.41^{+0.01}_{-0.01}$
O/H	9.09 ± 0.09	$10.08^{+0.04}_{-0.07}$	$9.19^{+0.14}_{-0.39}$	$9.16^{+0.06}_{-0.07}$	9.63 ± 0.02	$9.11^{+0.04}_{-0.06}$	9.41 ± 0.05	$9.51^{+0.08}_{-0.33}$	$10.00^{+0.09}_{-0.13}$	$9.79^{+0.04}_{-0.05}$	$9.17^{+0.03}_{-0.06}$	$9.95^{+0.10}_{-0.14}$	$9.23^{+0.08}_{-0.09}$
Ne2+/H	-	-	-	-	-	-	-	-	-	-	-	-	-
icf(Ne)	$1.12^{+0.03}_{-0.05}$	$1.97^{+0.11}_{-0.12}$	$2.17^{+0.64}_{-1.93}$	$1.88^{+0.02}_{-0.03}$	$1.17^{+0.01}_{-0.01}$	$1.40^{+0.12}_{-0.18}$	$1.73^{+0.06}_{-0.06}$	$1.49^{+0.28}_{-1.15}$	$2.31^{+0.19}_{-0.27}$	1.66 ± 0.02	$1.06^{+0.03}_{-0.14}$	$5.07^{1.20}_{-1.57}$	$1.41^{+0.01}_{-0.01}$
Ne/H	-	-	-	-	-	-	-	-	-	-	-	-	-

5.4 Results

The measured values of ADFs for these 13 PNe are plotted in Fig. 5.2, together with updated literature values of ADFs measured from PNe in Roger's Astronomy page. The PN known with close binary central stars are indicated in the plot as well as the median and 80th percentile values of the literature values.
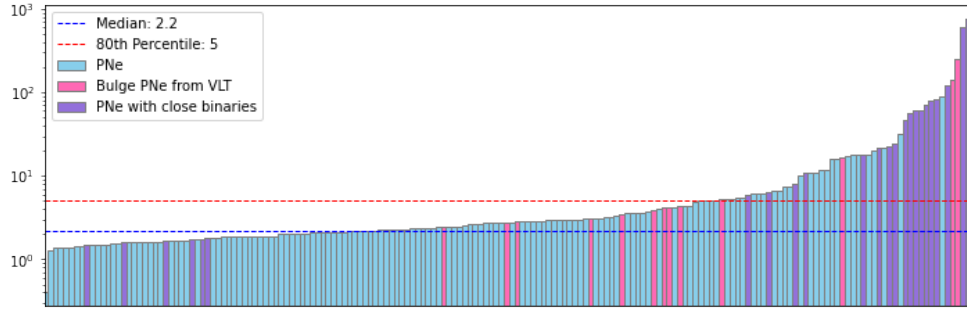
Figure 5.2: The PN ADF values in literature in combination with our PN measurements in ranked order. The literature ADF values of individual PN used was obtained from `https://www.nebulousresearch.org/adfs` on 30/06/2022.

The number of PNe possessing a close binary central star increased since Wesson et al. (2018) in which the link between binary CSPNe and ADFs was confirmed. In this ranked order plot, more PNe with high ADFs have their binary CSPNe identified with observations from *Kepler/K2*, *TESS*, *Chandra*, *Gaia* and other photometric and spectroscopic surveys, e.g. in Jacoby et al. (2021), Aller et al. (2020), Jones et al. (2020) and Chornay et al. (2021), which adds evidence of the link. In addition, 6 out of 26 PNe with a close binary CSPN have an ADF measured below the median values and range from 1.49 to 1.8. These CSPNe have a binary period longer than 1.15 days, according to Wesson et al. (2018).

The pink bars in the plot are new ADF measurements from Bulge PNe of this sample, none of these was measured in previous research. The 13 ADFs measured are between 2.44 and 256, all greater than the median literature value. With the descriptions in Wesson et al. (2018), 9 were measured with 'normal' ADFs (< 5), 1 has an 'elevated' ADF and 3 PNe in our sample had an 'extreme' ADF (> 10). It is worth noting that the ADFs of two PNe, PN G 357.9-03.8 and PN G 001.3-01.2, are 140 and 256 respectively, giving the current 3rd and 4th highest ADF measurements.

5.5 Discussion of individual results

The image, ADF, recombination line list, O^{2+} ionic abundance and previous studies in the literature of each individual object are discussed in the following.

5.5.1 PN G 000.9-02.0

The imaging data of PN G 000.9-02.0 is not available in the VLT observations, the de-convolved image obtained from NTT in Rees (2011) is presented in Fig. 5.3. This has a resolved elliptical morphology and is classified as Ea. The Galactic position angle was measured as 79±2° in Rees & Zijlstra (2013). Its central star was classified as *wels* according to the catalogue of CSPN spectral classification given in Weidmann & Gamen (2011) and its excitation class is 3. The CSPN was identified in *Gaia* DR2 in Chornay et al. (2021). The chemical abundances of PN G 000.9-02.0 are available in CGS09 in which both T_e([NII]) and n_e([SII]) are not available. The extinction, c(Hβ) agrees with the literature well. Compared with CGS09, T_e([OIII]) measured from our spectra is 2σ higher while the oxygen abundance in our results is 1.4σ lower ($\sim$ 0.14 dex).
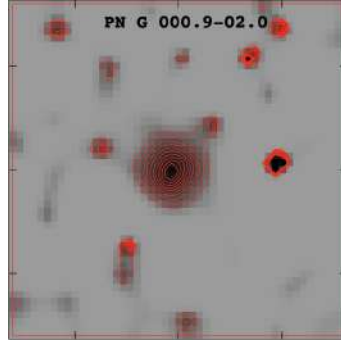
Figure 5.3: The de-convolved image of the PNe PNG 000.9-02.0 observed using the NTT in Rees (2011). The brightness is plotted in negative form and overlaid with its contour plot.

The detected O^{2+} recombination lines are listed in Table.5.4. RL abundance was derived from the V1 multiplet. He I 7281/6678 line ratio yields an extremely high temperature of 19500^{+2700}_{-3200}. Meanwhile, the line intensity ratios of 5876/4471 and 6678/4471 are below the lowest limit for temperature determination. This could be due to uncertainties in flux calibration and extinction at the red end of the spectra. Only the ADFs of O^{2+}/H and O/H were measured with this object (ADF(O^{2+}) = 2.79±0.83). The blue spectrum has an exposure time of 1000s and was not saturated, therefore, more weak recombination lines might have not been detected. In addition, the scaling factor (discussed in §4.3.2) applied to the red spectrum is 1.84, which also contributes to the high line ratios.

Multiplet	λ_0	I(λ)	O^{2+}/H ($\times 10^{-4}$)
V36	4189.79	$0.149^{+0.038}_{-0.039}$	-
V15	4590.97	$0.009^{+0.003}_{-0.003}$	-
V1	4649.13	$0.357^{+0.070}_{-0.071}$	$11.20^{+2.30}_{-2.60}$
V1	4676.24	$0.109^{+0.024}_{-0.024}$	-

Table 5.4: Detected O^{2+} recombination lines of PN G 000.9-02.0 and the ionic abundance derived.

5.5.2 PN G 001.3-01.2

PN G 001.3-01.2 is compact with an elliptical morphology and classified as Em. It is not resolved in the VLT image. The central star of this PN has a proper motion measured as μ_α=−8.0 mas yr^{-1} and μ_δ=−38 mas yr^{-1} in Kerber et al. (2008), however, large deviation among literature values. GPA of this PN measured in Rees (2011) is 116±2° while no measurement is available in this work as this object is compact and fuzzy in the VLT image.
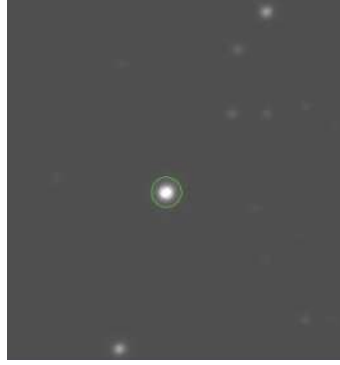
Figure 5.4: Hα image of PN G 001.3-01.2 from the VLT

Chemical abundances of this PN are not availble in previous studies. In this work, high interstellar extinction, c(Hβ)=2.79$^{+0.4}_{-0.17}$ was measured. The T$_e$([NII]) and n$_e$([SII]) obtained are 6540$^{+100}_{-90}$K K and 4310$^{+1030}_{-1590}cm^{-3}$ respectively. No T$_e$([OIII]) measured because of the low excitation. Besides, n$_e$([ClIII]) = 15000$^{+1900}_{-2200}$K was adopted for both medium and high ionization temperatures. The derived [O/H] is 7.68±0.03 dex, which is extremely sub-solar.

Multiplet	λ	I(λ)	O^{2+}/H ($\times 10^{-4}$)
V50b	4048.21	0.569$^{+0.111}_{-0.115}$	-
V48c	4087.15	0.640$^{+0.192}_{-0.194}$	190.00$^{+60.00}_{-60.00}$
V48a	4089.29	0.491$^{+0.114}_{-0.117}$	50.00$^{+10.00}_{-10.00}$
V67a	4275.55	0.552$^{+0.036}_{-0.039}$	98.00$^{+6.50}_{-6.90}$
V1	4638.86	0.994$^{+0.315}_{-0.318}$	90.00$^{+30.00}_{-30.00}$
V1	4649.13	1.435$^{+0.441}_{-0.450}$	30.00$^{+10.00}_{-10.00}$

Table 5.5: Detected O^{2+} recombination lines of PN G 001.3-01.2 and the ionic abundance derived.

Strong oxygen recombination line emissions were detected in PN G 001.3-01.2 as seen in Fig. 5.1. T$_e$(He I 5876/4471) and T$_e$(HeI 6678/4471) are 4240$^{+1370}_{-1390}$ K and 3220$^{+1110}_{-1680}$ K respectively, which are in a good agreement.

The O^{2+} recombination line intensities and ionic abundances obtained are shown in Table.5.5. The final O^{2+}/H adopted is 0.006, resulting in an ADF = 256$^{+34}_{-33}$. The 3d-4f multiplets give high

ionic abundance, however, their line flux measurements are suffering from larger uncertainties. If we consider only the V1 multiplet measurement here, the O^{2+}/H is 0.005, reducing the ADF to 208^{+42}_{-48}. The ADF is still the 3rd highest among all previous ADF measurements in PNe.

5.5.3   PN G 004.1-03.8

From the *HST* image, PN G 004.1-03.8 is exhibiting a bipolar feature with multiple shells, therefore, a Bm morphological classifier. The Galactic position angle measured in Rees (2011) is $65\pm2°$ and in this work is $21\pm2°$. The difference mainly comes from the resolved outer lobes in the *HST* image. Its central star was identified in *Gaia* DR2 in Chornay et al. (2020).

Figure 5.5: Hα image of PN G 004.1-03.8 from the *HST*

The chemical abundances of PN G 004.1-03.8 are available in CGS09, and with these data, a photoionisation models was built in Gesicki et al. (2014). Compared with CGS09, our T_e([O III]) and n_e([S II]) results agree within uncertainties. T_e([NII]) = 10800 ± 300K measured in this work agree with T_e([O III]), however, 2.1σ lower than T_e([NII]) = 13580^{+706}_{-1309}K in CGS09. The oxygen abundance measured in CGS09 is 8.39 and in this work is 8.64, nearly doubled. This could be due to the slit position relative to the object because of its outer shells.

Multiplet	λ	I(λ)	O^{2+}/H ($\times 10^{-4}$)
V10	4069.62	$0.141^{+0.031}_{-0.030}$	$6.82^{+1.54}_{-1.58}$
V20	4110.78	$0.009^{+0.002}_{-0.002}$	-
V20	4120.28	$0.009^{+0.003}_{-0.003}$	$1230.00^{+400.00}_{-430.00}$
V65a	4303.61	$0.003^{+0.001}_{-0.001}$	$9.20^{+2.11}_{-2.13}$
V92	4621.25	$0.002^{+0.001}_{-0.001}$	$14.30^{+4.00}_{-4.10}$
V1	4676.24	$0.002^{+0.001}_{-0.001}$	-
V28	4890.86	$0.008^{+0.002}_{-0.001}$	$7.02^{+1.39}_{-1.41}$

Table 5.6: Detected O^{2+} recombination lines of PN G 004.1-03.8 and the ionic abundance derived. The extremely high ionic abundance derived from the V20 multiplet was not carried forward for the calculation.

Table. 5.6 gives the detected O^{2+} recombination lines. The derived T_e(He I 6678/4471) is 9780^{+4540}_{-3710}. Ionic abundances of O^{2+} adopted is 0.0007, this excludes the extreme high and low

values derived from the multiplets V20 and 3d-4f. The ADF in O^{2+}/H and O/H measured is 3.48±0.73.

5.5.4 PN G 351.9+09.0

The VLT imaging data provide currently the best-resolved image of PN G 351.9+09.0, seen in Fig.5.6. This PNe has an Emps morphology with a faint outer shell and a resolved CSPN. The GPA measured from the VLT image is 101±3∘ which is consistent with 105±6° in Rees (2011). The central star was also identified in *Gaia* DR2 in Chornay et al. (2020).
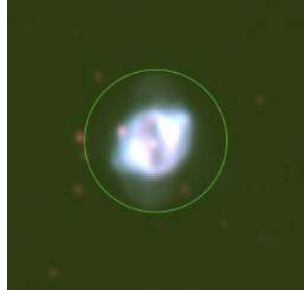
Figure 5.6: Composite color image of Hα and [OIII] observations of PN G 351.9+09.0 from the VLT

PN G 351.9+09.0 is a compact and high excitation PN. Its chemical abundances have not been reported in previous studies. The VLT data contain both 30s and 1000s exposure blue spectra for this object, but no significant difference in image quality between these two observations as it is faint. Electron temperature derived from [O III] lines is 12700±100K while [N II] lines are too faint to be accurately measured. The electron densities measured from [S II] lines and [Ar IV] lines agree approximately within 1σ. He I 5876/4471, He I 6678/4471 and He I 7281/6678 yield electron temperatures of 2650^{+460}_{-560}K, 1810^{+380}_{-450}K and 1450^{+240}_{-250}K respectively, agreeing with each other with 2σ.

Multiplet	λ	I(λ)	O^{2+}/H ($\times 10^{-4}$)
V48a	4071.23	$0.257^{+0.058}_{-0.060}$	-
V10	4072.16	$0.505^{+0.059}_{-0.060}$	-
V48b	4097.25	$1.196^{+0.308}_{-0.309}$	-
V101	4253.86	$0.004^{+0.001}_{-0.001}$	-
V1	4641.81	$0.183^{+0.037}_{-0.038}$	$6.34^{+1.28}_{-1.34}$
V1	4649.13	$0.221^{+0.034}_{-0.035}$	$9.36^{+1.94}_{-2.45}$
V28	4890.86	$0.004^{+0.001}_{-0.001}$	$3.85^{+0.90}_{-0.92}$

Table 5.7: Detected O^{2+} recombination lines of PN G 351.9+09.0 and the ionic abundance derived.

Table.5.7 presents the detected recombination lines of O^{2+}. The final $O^{2+}/H=0.0008$ combines measurements using the V1 and V28 multiplets, giving an ADF of $3.95^{+0.64}_{-0.70}$ in O^{2+}/H.

5.5.5   PN G 353.2-05.2

This VLT imaging data provides currently the best-resolved observation of PN G 353.2-05.2 in which its bipolar morphology, the multiple shells, the internal ring structure and overdensities in brightness are seen, shown in Fig.5.7, therefore, a Bmrs PN. The GPAs measured in Rees (2011) and in this work agree with each other and are $105\pm6°$ and $103\pm2°$ respectively.

As a faint source, the chemical abundance of this object is not available in previous PN studies. In our data, the 1000s-exposure blue spectra are not saturated. Electron densities derived from [O II], [S II] and [Ar IV] line ratios all indicate a low density. Te([O III]) and Te([N II]) derived are 8100 ± 50 K and 9260 ± 90 K respectively (T_e([N II]) > T_e([O III])). The spectra include the blue doublet of [O II], however, noisy. [O/H] measured is 8.42 ± 0.02, which is subsolar.

10 recombination lines detected in PN G 353.2-05.2 are shown in Table.5.8. He I
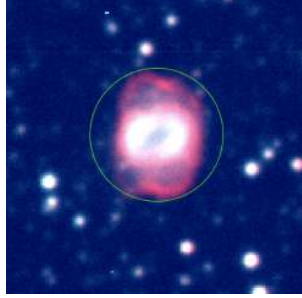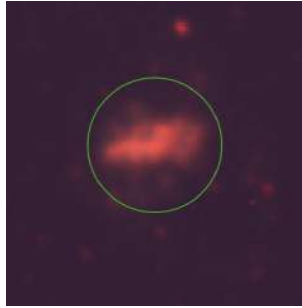

Figure 5.7: Composite color image of Hα and [OIII] observations of PN G 353.2-05.2 from the VLT

Multiplet	λ	I(λ)	O^{2+}/H ($\times10^{-4}$)
V50b	4048.21	$0.012^{+0.005}_{-0.005}$	-
V10	4069.62	$1.104^{+0.147}_{-0.142}$	$31.40^{+4.20}_{-4.00}$
V10	4072.16	$0.557^{+0.144}_{-0.143}$	-
V10	4075.86	$0.847^{+0.086}_{-0.096}$	$97.80^{+9.90}_{-11.00}$
V48b	4097.25	$1.561^{+0.403}_{-0.408}$	-
V1	4638.86	$0.135^{+0.031}_{-0.032}$	$5.71^{+1.33}_{-1.35}$
V1	4641.81	$0.746^{+0.082}_{-0.081}$	$33.80^{+3.70}_{-3.70}$
V1	4649.13	$1.678^{+0.060}_{-0.060}$	128.00 ± 5.00
V1	4661.63	$0.078^{+0.013}_{-0.013}$	$2.95^{+0.49}_{-0.50}$
V89b	4669.27	$0.015^{+0.005}_{-0.006}$	-

Table 5.8: Detected O^{2+} recombination lines of PN G 353.2-05.2 and the ionic abundance derived.

5876/4417 and He I 6678/4471 give temperatures of 3870^{+1370}_{-1520}K and 3010^{+920}_{-1320}K respectively, showing consistency with each other within 1σ.

There is a large deviation between the values of O^{2+}/H derived from individual recombination line, however, when co-adding individual line measurements from the V1 and the V10 multiplets respectively, the values agree within 25%, giving the final O^{2+}/H = 0.004. The ADF in O^{2+}/H is $16.39^{+1.00}_{-1.06}$, which is extreme and the 3rd highest among our results.

5.5.6 PN G 353.7+06.3

PN G 353.7+06.3 is an elliptical PN with an internal ring structure. Internal filaments could be discerned as well as the central star. Therefore, an Ers PN. The CSPN was detected in *Gaia* DR2 in Chornay et al. (2020). Its kinematics were studies in Richer et al.(2010). GPA measured in this work is 56±2°, which agrees with 53±2° in Rees (2011) within 1.5σ. According to Weidmann (2020), the CSPN is of an O-type.
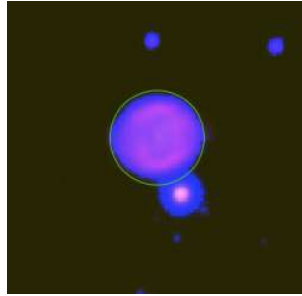
Figure 5.8: Composite color image of Hα and [OIII] observations of PN G 353.2-05.2 from the VLT

The chemical abundances of this object are available in Escudero et al. (2004). c(Hβ) measured in the literature is 1.0, and in this work is 0.64±0.39. The derived n_e([S II]) and T_e([N II]) agree with the literature. T_e([O III]) in our measurement is 7120±80 K, which is, however, slight lower than T_e([N II]). The blue [O II] doublet is available in our spectra and it gives a consistent electron density with n_e([S II]). For chemical abundances, [O/H]=$8.65^{+0.05}_{-0.06}$ from the VLT, which is 0.09 dex lower than the literature result.

Strong recombination lines are seen in PNG 353.7+06.3 and the detected O^{2+} RLs are listed in Table.5.9. He I 6678/4471 line ratio yields an electron temperature of 3150^{+1280}_{-2140} K. The O^{2+}/H values adopted combine measurement from the V1, the V2 and the 3d-4f multiplets. However, the V2 and the 3d-4f give higher ionic abundance than the V1. The ADF in O^{2+}/H is 2.88±0.32.

5.5.7 PN G 356.5-03.6

PNG 356.5-03.6 exhibits a clear bipolar feature with two outer shells perpendicular to each other and has a Bmprs morphology. GPA measured in this work is 117±3° and is equal to the result

Multiplet	λ	I(λ)	O^{2+}/H ($\times 10^{-4}$)
V10	4072.16	$0.306^{+0.077}_{-0.079}$	-
V48a	4089.29	$0.149^{+0.043}_{-0.043}$	$28.80^{+8.20}_{-8.40}$
V101	4253.86	$0.004^{+0.001}_{-0.001}$	-
V67a	4275.55	$0.031^{+0.008}_{-0.008}$	$12.10^{+3.00}_{-3.00}$
V53b	4294.78	0.013 ± 0.004	$5.54^{+1.64}_{-1.62}$
V65a	4303.61	$0.002^{+0.001}_{-0.001}$	$5.00^{+1.68}_{-1.68}$
V2	4317.14	$0.086^{+0.012}_{-0.014}$	$7.98^{+1.12}_{-1.31}$
V2	4349.43	$0.102^{+0.020}_{-0.021}$	$10.90^{+2.10}_{-2.20}$
V92b	4602.13	$0.029^{+0.008}_{-0.008}$	$12.60^{+3.40}_{-3.50}$
V92a	4609.44	$0.022^{+0.007}_{-0.007}$	$4.09^{+1.34}_{-1.30}$
V1	4638.86	$0.164^{+0.011}_{-0.011}$	$7.02^{+0.48}_{-0.51}$
V1	4641.81	$0.229^{+0.012}_{-0.012}$	$9.90^{+0.54}_{-0.54}$
V1	4649.13	0.294 ± 0.012	$20.10^{+0.80}_{-0.80}$
V1	4650.84	$0.051^{+0.010}_{-0.011}$	$1.56^{+0.32}_{-0.34}$
V1	4661.63	0.118 ± 0.004	4.51 ± 0.18
V1	4676.24	$0.052^{+0.008}_{-0.008}$	-
V1	4696.35	$0.015^{+0.002}_{-0.002}$	$7.89^{+0.96}_{-0.96}$

Table 5.9: Detected O^{2+} recombination lines of PN G 353.2-05.2 and the ionic abundance derived.

in Rees (2011).
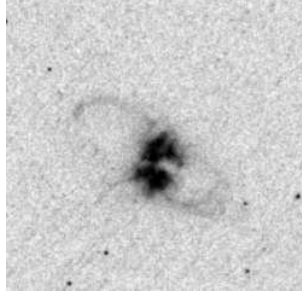
Figure 5.9: Hα image of PN G 356.5-03.6 from the *HST*

1D and 3D photoionisation models of this object are in Gesicki et al. (2014) and Gesicki et al. (2016) respectively. No previous chemical abundances were obtained because of the low brightness. In this work, T_e([N II])=7940±110 K, T_e([O III])=8750±120 K and n_e([N II])=2620^{+320}_{-370} K were measured as well as a super-solar [O/H] = 8.87±0.03. Temperatures determined from He I 5876/4471 and 6678/4471 are 1000^{560}_{650} and 2680^{1140}_{2180} respectively, suffering from large uncertainties. He I 7281/6678 yields a more precious temperature of 7100±350 which is lower than the CEL temperatures. Table.5.10 presents the Rls of O^{2+} measured in PN G 356.5-03.6. Final O^{2+}/H=0.0015 was derived from the V1, the V28 and the 3d-4f multiplets, giving an ADF of $3.09^{+3.09}_{-0.62}$.

Multiplet	λ	I(λ)	O^{2+}/H ($\times 10^{-4}$)
V48b	4083.90	$0.093^{+0.018}_{-0.017}$	$21.60^{+4.00}_{-3.90}$
V76b	4371.62	0.029 ± 0.011	-
V92	4621.25	$0.029^{+0.008}_{-0.008}$	150.00 ± 40.00
V1	4649.13	$0.347^{+0.050}_{-0.052}$	$9.84^{+1.43}_{-1.46}$
V28	4890.86	0.028 ± 0.006	$24.20^{+4.90}_{-4.80}$

Table 5.10: Detected O^{2+} recombination lines of PN G 356.5-03.6 and the ionic abundance derived.

5.5.8   PN G 357.2+02.0

PN G 357.2+02.0 has a perfect round ring structure in Hα image from the *HST* and is classified as Rar because of slight overdensities in the SE direction. GAP measurement is therefore not applicable. It has a velocity profile in [O III] from the photoionisation model in Gesicki et al. (2014). No previous spectroscopic observations, and thereby, no chemical abundances available in previous studies. The CSPN was identified as binary in Hlabathe (2015) and later, in Jacoby et al. (2021) from *Kepler/K2*. The variable period measured from the *Kepler/K2* is 0.89 days and the companion is a main-sequence star. ()

The electron temperatures derived from [N II] and [O III] lines are 10400^{+400}_{-300} K and 10000 ± 100 K respectively (T$_e$([O III]) < T$_e$([N II])). Electron densities derived from [S II] line ratio is 3590^{+1110}_{-2240} cm^{-3}, which is largely uncertain but agree with the [Ar IV] measurement.
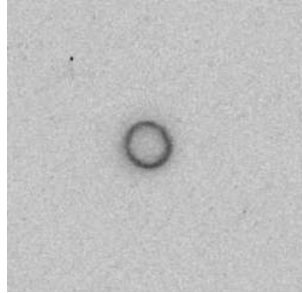
Figure 5.10: Hα image of PN G 357.2+02.0 from the *HST*

He I 6678/4471 line ratio gives a temperature of $3970.0^{+1960.0}_{-3970.0}$ K, which is highly uncertain. The detected O^{2+} RLs are summarized in Table. 5.11. Only the V1 and the V20 multiplets were used for O^{2+}/H derivation and the final result is 0.003, resulting in a moderate ADF of $4.20^{+0.34}_{-0.35}$.

5.5.9   PN G 357.5+03.2

PNG 357.5+03.2 is a bipolar PN and its internal overdensities are resolved in the VLT observation. No information about its central star is available. GPA measured in Rees (2011) is $83 \pm 5°$ and in this work is $82 \pm 5°$, showing a good consistency. The uncertainty in GPA is largely due to

Multiplet	λ	$I(\lambda)$	O^{2+}/H ($\times 10^{-4}$)
V97	4060.60	$0.254^{+0.058}_{-0.059}$	-
V20	4120.28	$0.032^{+0.007}_{-0.006}$	$5770.00^{+1220.00}_{-1290.00}$
V1	4641.81	$0.819^{+0.056}_{-0.060}$	$28.60^{+2.00}_{-2.10}$
V1	4649.13	0.461 ± 0.028	$15.40^{+1.20}_{-1.30}$
V28	4890.86	0.014 ± 0.002	$12.10^{+2.20}_{-2.20}$

Table 5.11: Detected O^{2+} recombination lines of PN G 357.2+02.0 and the ionic abundance derived. The extremely high ionic abundance derived from the V20 multiplet was not carried forward for the calculation.

the fuzzy boundary of its outer envelope. The kinematics of the object were studied by Richer et al. (2008) and Richer et al.(2009). In Jacoby et al. (2021), a variability was found in its CSPN, therefore it possesses a binary star at its centre with a variable period of 0.32 days.

Chemical abundances of this object were studied in CGS09, in which T_e([N II])=9312 K, T_e([O III])=10862 and n_e([S II])=1300 respectively. In our results, both electron temperatures were measured lower: T_e([N II])=$8570.0^{+200.0}_{-210.0}$ K and T_e([O III])= $8660.0^{+1180.0}_{-1180.0}$ K respectively, but the electron density agrees well. [O/H] obtained in this study is $9.24^{+0.12}_{-0.3}$ and in CGS09 is 8.83 dex, all strongly super-solar.

Figure 5.11: Composite color image of Hα and [OIII] observations of PN G 357.5+03.2 from the VLT

Multiplet	λ	$I(\lambda)$	O^{2+}/H ($\times 10^{-4}$)
V10	4075.86	$0.586^{+0.114}_{-0.115}$	$50.00^{+20.00}_{-20.00}$
V20	4120.28	$0.038^{+0.013}_{-0.013}$	$2750.00^{+1110.00}_{-3640.00}$
V19	4132.80	$0.185^{+0.055}_{-0.057}$	$22.00^{+6.60}_{-7.20}$
V28	4890.86	$0.037^{+0.010}_{-0.010}$	$40.00^{+10.00}_{-20.00}$

Table 5.12: Detected O^{2+} recombination lines of PN G 357.5+03.2 and the ionic abundance derived. The extremely high ionic abundance derived from the V20 multiplet was not carried forward for the calculation.

He I 5876/4471 and He I 6678/4471 line ratios yield extremely low temperatures of $262.0^{+262.0}_{-262.0}$ K and $620.0^{+620.0}_{-620.0}$ K respectively. Table.5.12 lists O^{2+} RLs detected in this PN. $O^{2+}/H = 0.01$ are derived from the V10, the V19 and the V28 multiplets, the extremely high value derived from the V20 multiplet was ignored. The final ADF in O^{2+}/H is $4.29^{+4.29}_{-2.28}$.

5.5.10 PN G 357.9-03.8

The Hα image of PN G 357.9-03.8 is shown in Fig.5.12. Its angular dimension measured in Tylenda et al. (2003) is 13 arcsec $\times$ 13 arcsec. The CSPN is seen in the VLT image, which has not been catalogued before. The elliptical appearance, the clear ting structure and the resolved flux distribution give it an Ers classifier. GPAs measured in this work and Rees (2011) agree with each other and are $125\pm2°$ and $126\pm2°$ respectively.

This is a faint object in a crowded region as its spectra is crossed by the continua of many nearby stars. No literature chemical abundance is availble. The physical parameters derived indicate a high temperature and low density environment: $T_e([N\ II])=21200.0^{+1200.0}_{-1300.0}$ K, $T_e([O\ III])=20900.0^{+400.0}_{-400.0}$ K and $n_e([S\ II])=2000.0^{+640.0}_{-1040.0}$ cm^{-3}. The oxygen abundance is 7.64 ± 0.02, which is strongly sub-solar. The O^{2+} RL measurements are presented in Table.5.13. No
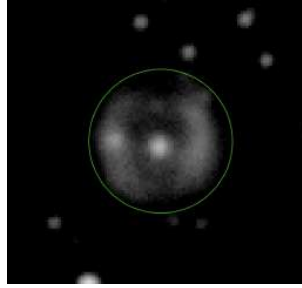
Figure 5.12: Hα image of PN G 357.9-03.8 from the VLT

Multiplet	λ	I(λ)	O^{2+}/H ($times10^{-4}$)
V10	4069.62	$1.027^{+0.016}_{-0.016}$	$27.90^{+0.40}_{-0.40}$
V48c	4087.15	$0.122^{+0.018}_{-0.021}$	$46.10^{+6.80}_{-7.90}$
V67a	4275.55	$0.041^{+0.008}_{-0.008}$	$29.50^{+5.90}_{-5.90}$
V15	4595.96	$0.025^{+0.006}_{-0.006}$	-
V1	4641.81	$0.712^{+0.182}_{-0.178}$	$32.00^{+8.30}_{-8.20}$
V1	4649.13	0.721 ± 0.051	$64.90^{+4.60}_{-4.90}$

Table 5.13: Detected O^{2+} recombination lines of PN G 351.9+09.0 and the ionic abundance derived.

temperature was derived from RLs. O^{2+}/H derived from V1 is consistent with that from 3d-4f and is 50% higher than the V10 result. The final O^{2+}/H adopted is 0.00003, giving an ADF of $140.0^{+11.0}_{-11.0}$, which is the second highest among our sample.

5.5.11 PN G 358.2+04.2

The VLT image of PN G 358.2+04.2 is not well-resolved in which only an elliptical/round shape is seen as shown in Fig.5.13. Because of this, a deviation in GPA measurements is present. In Rees (2011), the GPA of this object is 66±2° which is 24° larger than our measurement (42±2∘). This object is showing a certain 'boxy' structure, therefore, it is likely to have a bipolar morphology in better-resolved observations. Its CSPN was identified in *Gaia* DR2 (Chornay et al., 2020), however, not discernable in the VLT image.

The chemical abundances of this object were studied in Cuisinier et al. (2000), in which physical parameters derived are T_e([N II])=10105 K and n_e([S II])=5410 K. Temperatures in our results are relatively lower: T_e([N II])= $9580.0^{+350.0}_{-310.0}$ K and T_e([O III])=$7940.0^{+60.0}_{-60.0}$ K (T_e([O III]) < T_e([N II])). Highly uncertain n_e([S II]) = $10700.0^{+2500.0}_{-4900.0}$ cm^{-3} was derived in our result, however, electron density measured from [Cl III] and [Ar IV] lines agree with each other well and are $4230.0^{+330.0}_{-360.0}$ cm^{-3} and $3360.0^{+380.0}_{-430.0}$ cm^{-3} respectively. [O/H] is 8.38 (sub-solar) in Cuisinier et al. (2000) and is $8.77^{+0.03}_{-0.06}$ (doubled the literature result, super-solar) in this work. The difference mainly comes from measured O^{2+}/H using CELs.
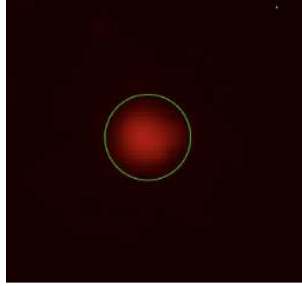
Figure 5.13: Composite color image of Hα and [OIII] observations of PN G 358.2+04.2 from the VLT

Table.5.14 gives the detected O^{2+} RLs. Strong recombination line features are seen in this object and 6 multiplets were identified. The V20 multiplet gives an extremely high O^{2+}/H, which is largely due to noises and was excluded in the final ionic abundance determination. The final O^{2+}/H adopted is 0.0014 and the result from the V1 multiplet contribute the most. The ADF in O^{2+}/H is $2.44^{+2.44}_{-0.26}$.

5.5.12 PN G 359.0-04.1

The composite-color image of PN G 359.0-04.1 from the VLT is shown in Fig.5.14. This object is exhibiting a bipolar morphology, a point symmetry, therefore classified as Bp. The CSPN was identified in *Gaia* DR2 in Chornay et al. (2020). The diameter of this PN is 5.4 arcsec × 4.4 arcsec in Tylenda et al.(2003), which is compact. GPA is measured as 100 ± 2° which is equal to the result in this study.

Chemical abundances of this object are available in Exter et al.(2004) and Gorny et al.(2009).

Multiplet	λ	$I(\lambda)$	O^{2+}/H ($\times 10^{-4}$)
V48b	4097.25	$1.099^{+0.229}_{-0.230}$	-
V20	4120.28	0.359 ± 0.023	$81980.00^{+5460.00}_{-5850.00}$
V19	4132.80	$0.066^{+0.006}_{-0.007}$	$9.41^{+0.90}_{-1.00}$
V19	4156.53	0.024 ± 0.004	$17.50^{+2.60}_{-2.70}$
V36	4189.79	0.030 ± 0.008	-
V65a	4303.61	$0.016^{+0.005}_{-0.004}$	$28.00^{+8.20}_{-7.90}$
V2	4349.43	$0.155^{+0.040}_{-0.039}$	$15.50^{+4.00}_{-3.90}$
V1	4638.86	0.196 ± 0.030	$15.10^{+2.40}_{-2.30}$
V1	4641.81	0.438 ± 0.025	16.20 ± 0.90
V1	4649.13	0.475 ± 0.027	$13.20^{+0.80}_{-0.80}$
V1	4650.84	$0.138^{+0.027}_{-0.026}$	$10.20^{+2.00}_{-1.90}$
V1	4661.63	$0.176^{+0.014}_{-0.015}$	$12.10^{+0.90}_{-1.00}$

Table 5.14: Detected O^{2+} recombination lines of PN G 358.2+04.2 and the ionic abundance derived. The extremely high ionic abundance derived from the V20 multiplet was not carried forward for the calculation.

In Exter et al.(2004), physical parameters derived are T_e([N II])=7900 K and n_e =631 cm^{-3}, no T_e([O III]) is availble. In Gorny et al.(2009), T_e([N II])=9266^{+358}_{-487}K, T_e([O III])=8884^{+277}_{-767} K and n_e =521^{+2069}_{-453} cm^{-3} were calculated. T_e([O III]) in our results agrees with Gorny et al.(2009), while T_e([N II])=$8540.0^{+70.0}_{-70.0}$ K is lower than that in Gorny et al.(2009) but higher than the result in Exter et al.(2004). We have a more precise n_e measurement, $952.0^{+167.0}_{-202.0}$ cm^{-3}, which is higher than the literature value in Exter et al.(2004) by 51% and lies within the 1σ of the result in Gorny et al.(2009).
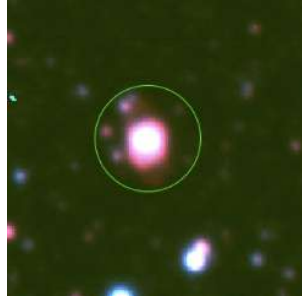
Figure 5.14: Composite color image of Hα and [OIII] observations of PN G 359.0-04.1 from the VLT

He I 6678/4471 yields a temperature of $4320.0^{+1480.0}_{-2470.0}$ K. The detected O^{2+} RLs are listed in Table. 5.15. The multiplets V1 and V10 were used to derive O^{2+}/H. The final O^{2+}/H is equal to 0.0019, resulting in an 'elevated' ADF of $5.23^{+0.34}_{-0.44}$.

Multiplet	λ	I(λ)	O^{2+}/H ($\times 10^{-4}$)
V10	4069.62	$0.518^{+0.123}_{-0.127}$	$17.30^{+4.30}_{-5.10}$
V48b	4097.25	$1.580^{+0.439}_{-0.421}$	-
V20	4110.78	0.027 ± 0.007	-
V106	4146.00	$0.042^{+0.011}_{-0.010}$	-
V1	4641.81	0.607 ± 0.042	$23.80^{+2.30}_{-3.10}$
V1	4649.13	0.497 ± 0.024	$30.80^{+4.50}_{-5.70}$
V1	4650.84	$0.241^{+0.019}_{-0.021}$	$8.54^{+1.20}_{-1.37}$
V1	4696.35	$0.017^{+0.004}_{-0.004}$	$9.28^{+2.16}_{-2.29}$

Table 5.15: Detected O^{2+} recombination lines of PN G 359.0-04.1 and the ionic abundance derived.

5.5.13   PN G 359.7-01.8

PN G 359.7-01.8 has a round shape, and an inner envelope, an outer envelope and a certain ring structure could be seen in the VLT image in Fig.5.15 (Rmr). GPA measured in Rees (2011) is 8±2°, while we failed to measure the GPA. The CSPN was identified in *Gaia* DR2 in Chornay et al. (2020), however, not discernible in our image. Kinematics of this PN were studied by Richer et al. (2009).

Figure 5.15: Composite color image of Hα and [OIII] observations of PN G 359.7-01.8 from the VLT

Chemical abundances of PN G 359.7-01.8 are availble in Exter et al. (2004), in which T_e([O III])=14191 K and n_e([S II])=1030 cm^{-3}. We measured a lower electron temperature from [O III] lines while a higher electron density: T_e([O III]) = $12100.0^{+200.0}_{-200.0}$ K and n_e([S II])=$1650.0^{+440.0}_{-610.0}$ cm^{-3}. In addition, T_e([N II]) = $9320.0^{+220.0}_{-220.0}$ K from our data.

The 4 O^{2+} RLs detected in PN G 359.7-01.8 are listed in Table.5.16. He I 5876/4471 line ratio gives a temperature of $3140.0^{+3140.0}_{-2030.0}$ K, which is highly uncertain. O^{2+}/H was derived by co-adding the results from the V10 and the V28 multiplets and is equal to 0.0012. The ADF in O^{2+}/H is $5.23^{+0.34}_{-0.44}$, which is 'elevated'.

Multiplet	λ	$I(\lambda)$	O^{2+}/H ($\times 10^{-4}$)
V10	4069.62	$0.191^{+0.042}_{-0.044}$	$8.67^{+1.99}_{-2.18}$
V10	4078.84	$0.181^{+0.053}_{-0.051}$	$22.30^{+6.60}_{-6.50}$
V1	4676.24	$0.021^{+0.007}_{-0.007}$	-
V28	4890.86	0.014 ± 0.002	$13.10^{+2.40}_{-2.40}$

Table 5.16: Detected O^{2+} recombination lines of PN G 359.7-01.8 and the ionic abundance derived.

5.6   Discussion

A few preliminary statistical inferences made in Wesson et al. (2018) will be tested in this section with the ADF measurements in this study. These include both the central star properties and nebular properties. The catalogued spectral type, the known central star binarity and the electron densities derived in this work of 13 PNe with ADFs measured are summarised in Table.5.17 and will be discussed in the following subsections.

PNG	Main Name	ADF	Electron density	O/H	N/H	CS info.
000.9-02.0	Bl 3-13	$2.8^{+0.84}_{-1.01}$	5680^{+2600}_{-5680}	$8.63^{+0.09}_{-0.11}$	$7.66^{+0.11}_{-0.20}$	*wels*[1]
001.3-01.2	Bl M	$256.0^{+34.0}_{-33.0}$	4310^{+1030}_{-1590}	$7.68^{+0.03}_{-0.03}$	$8.07^{+0.03}_{-0.04}$	
004.1-03.8	KFL 11	$3.48^{+0.73}_{-0.77}$	1900^{+630}_{-1090}	$8.64^{+0.13}_{-0.39}$	$7.60^{+0.04}_{-0.08}$	
351.9+09.0	PC 13	$3.95^{+0.7}_{-0.64}$	423^{+356}_{-423}	$8.55^{+0.01}_{-0.01}$	$7.25^{+0.1}_{-0.13}$	
353.2-05.2	H 1-38	$16.39^{+0.99}_{-1.06}$	155^{+75}_{-143}	$8.42^{+0.02}_{-0.02}$	$8.85^{+0.06}_{-0.06}$	
353.7+06.3	M 2-7	$3.04^{+0.32}_{-0.36}$	931^{+203}_{-254}	$8.64^{+0.05}_{-0.06}$	$8.09^{+0.05}_{-0.05}$	$O^{[2]}$
356.5-03.6	H 2-27	$3.09^{+3.09}_{-0.62}$	2620^{+320}_{-370}	$8.87^{+0.03}_{-0.03}$	$8.47^{+0.03}_{-0.03}$	
357.2+02.0	H 2-13	$4.2^{+0.34}_{-0.35}$	3590^{+1110}_{-2240}	$8.89^{+0.09}_{-0.35}$	$7.93^{+0.06}_{-0.19}$	Binary CS[3]
357.5+03.2	M 3-42	$4.29^{+4.29}_{-2.28}$	1110^{+390}_{-610}	$9.24^{+0.12}_{-0.32}$	$9.01^{+0.13}_{-0.34}$	Binary CS[3]
357.9-03.8	H 2-30	$140.0^{+11.0}_{-11.0}$	2000^{+640}_{-1040}	$7.64^{+0.02}_{-0.02}$	$6.72^{+0.06}_{-0.07}$	
358.2+04.2	M 3-8	$2.44^{+2.44}_{-0.26}$	6670^{+1410}_{-2940}	$8.77^{+0.03}_{-0.06}$	$8.49^{+0.19}_{-0.28}$	
359.0-04.1	M 3-48	$5.23^{+0.34}_{-0.44}$	952^{+167}_{-202}	$9.26^{+0.11}_{-0.14}$	$8.71^{+0.04}_{-0.05}$	
359.7-01.8	M 3-45	$4.17^{+0.79}_{-0.87}$	1650^{+440}_{-610}	$8.60^{+0.02}_{-0.02}$	$7.71^{+0.05}_{-0.06}$	

[1] Gorny et al. (2004); [2] Weidmann et al. (2018); [3] Jacoby et al. (2021)

Table 5.17: Electron density and central star information of PNe with ADFs measured.

5.6.1   ADF with the central star binarity

Combining ADFs of 13 PNe measured in this work and the literature PN ADF measurements summarised in `nebulousresearch.org` by Roger Wesson, there are 175 PN ADF values available with a mean value of 18.04±76.72. The median, 25th percentile and 75th percentile values are 2.8, 1.9, and 5.4 respectively. Compare with the corresponding values 2.5, 1.7, and 7.3 derived from the samples at the time of Wesson et al. (2018), more normal or 'elevated' ADFs have been measured in subsequent studies. For 150 PNe with currently no binary CS detected

at their centres, the mean ADF is 7.27±24.61. The median, 25th percentile and 75th percentile values are 2.58, 1.90 and 4.13 respectively. For 25 PNe with known binary CS, the mean ADF is 46.02±90.82 if ADFs measured in 3 knots of the PN Abell 30 were averaged or 58.26±148.58 if the highest value was taken. The association between extreme discrepancies (ADF > 10) and close binarity in PNe is reflected in the mean value and also in Fig. 5.2. However, compared with Wesson et al. (2018), 4 more PNe with a binary CS have an ADF measured below 2.2 (mean value among all H II region and PN measurements) plus 2 PNe in this work are measured with normal ADFs (ADF < 5).

Low ADFs measured in PNe with a binary CS were explained by the binary period in Wesson et al. (2018). 15 PNe with known binary central stars in their sample show that extreme ADFs (> 10) are measured in objects with a binary period less than 1.15 days only. The low ADFs are therefore measured in objects with a longer period. The relationship between the binary period and the ADF in the combined sample is shown in Fig. 5.16. It was noticed from the plot that new ADF measurements since Wesson et al. (2018) generally hold the statement, however, two counter-examples were pointed out. One is the PN Sp 3, the period of its CS is 4.81 days which was measured in Miszalski et al. (2019), however, it has an extreme ADF of 24.0. A possible triple nature of the CS was also suggested in this work, the mechanism that causes its ADF might be related to the tertiary component. However, this is to be confirmed with more observations of PNe with more than two components at their centres. The other 'outlier' comes from the results in this work. For PNG 357.2+02.0 (H 2-13), the period of its binary CS measured in Jacoby et al. (2021) is 0.89 while ADF in O^{2+} is $4.20^{+0.35}_{-0.34}$. This might be related to electron densities in the nebula and to be discussed in the following section.
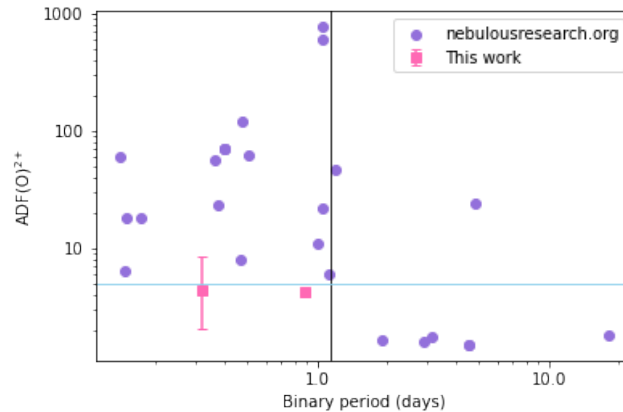
Figure 5.16: The relationship between the abundance discrepancy factor for O^{2+} and the binary period for in the combined sample of 25 PNe. Purple dots show values taken from `https://nebulousresearch.org/adfs` running by Roger Wesson on 30/06/2022 while pink squares are the measurements in this study. The 'threshold' period, 1.15 days, which is the longest period of objects with extreme ADFs in Wesson et al. (2018) is indicated by a vertical black line while the blue horizontal line indicates an ADF of 5.0, i.e. the lowest value for an ADF to be considered as extreme.
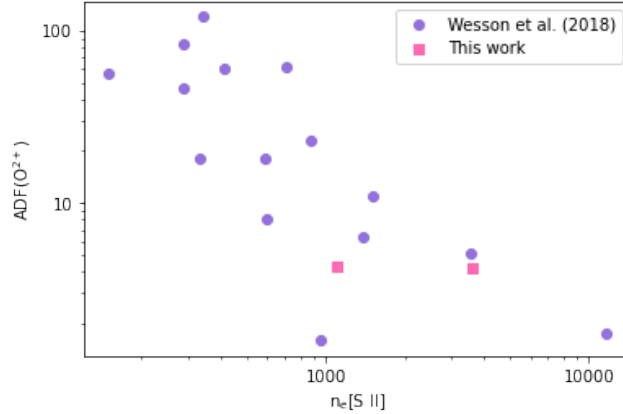
Figure 5.17: The relationship between ADF(O^{2+}) and n^e([S II]) in the sample combining 15 PNe in Wesson et al. (2018) and 2 PNe in this work. Both axes are in log scale.

5.6.2 ADFs with nebular properties

Electron density

In Wesson et al. (2018), one PN with a binary CS, Hen 2-283, has a period of 1.15 days and a moderate ADF of 5.1±0.5 while it was noticed that this PN has an electron density of $3200 cm^{-3}$ which is 4.3 times and 7.8σ higher than the mean, 750±316 cm³, of the rest. And generally in their sample, electron densities higher than 1000 cm^{-3} are only seen in objects with ADFs less than 12, except for the PN A 46. Consider the outlying PN with a close binary CS in our sample, PNG 357.2+02.0 (H 2-13), the ADF measured is $4.2^{+0.34}_{-0.35}$ while the electron density is 3590^{+1110}_{-2240} cm^{-3} which is higher than 1000 cm^{-3} within 1.2σ. Another PN with short-period binary CS in our sample, PNG 357.5+03.2, has an electron density of 1110^{+390}_{+610} cm^{-3}, which is also higher than 1000 cm^{-3} and has a moderate ADF of $4.29^{+4.29}_{-2.28}$. Thus, the correlation between moderate ADF in objects with short-period binary CSs and the high electron density is also present in our data.

This relationship between electron densities and the abundance discrepancies was further quantified by Wesson et al. (2018), who found that PNe with n_e([O II])/n_e([S II]) > 1 are all measured with and an ADF(O^{2+}) > 10. Moreover, there is a positive correlation between n_e([S II]) and ADF(O^{2+}). For two PNe with close binary CS in this work, neither allows an n_e([O II]) determination because of the wavelength coverage of our spectra. We present here the relationship between ADF(O^{2+}) and n_e([S II]) in Fig. 5.17 for the combined data set of objects with a close binary CS. The Pearson correlation coefficient between log(ADF(O^{2+})) and log(n_e([S II])) for 15 PNe in Wesson et al. (2018) is −0.76 which becomes −0.78 when two objects in this work were added.

In Fig. 5.18, the ADFs measured in this work as a function of electron density derived from [O II], [S II], [Cl III] and [Ar IV] line ratios respectively are plotted, together with the lines indicating the maximum limit of ADFs derived in Wesson et al. (2018). When all ADF measurements in

PNe and HII regions were combined in Wesson et al. (2018), it was noticed that, except for few scatters, all ADFs are less than $1.2 \times 10^4 n_e^{-0.8}$. From Fig. 5.18, this is generally true irrespective to the lines used. Two outliers are seen in terms of $n^e([S\ II])$, which are the two PNe with the highest two ADFs measured in our data set, PNG 001.3-01.2 and PNG 357.9-03.8. They exceed the maximum value by 0.61 dex and 1.21 dex respectively. The ADF in PNG 001.3-01.2 is also 1.67 dex higher than this limit when $n^e([Cl\ III])$ is considered as seen in the lower left panel.
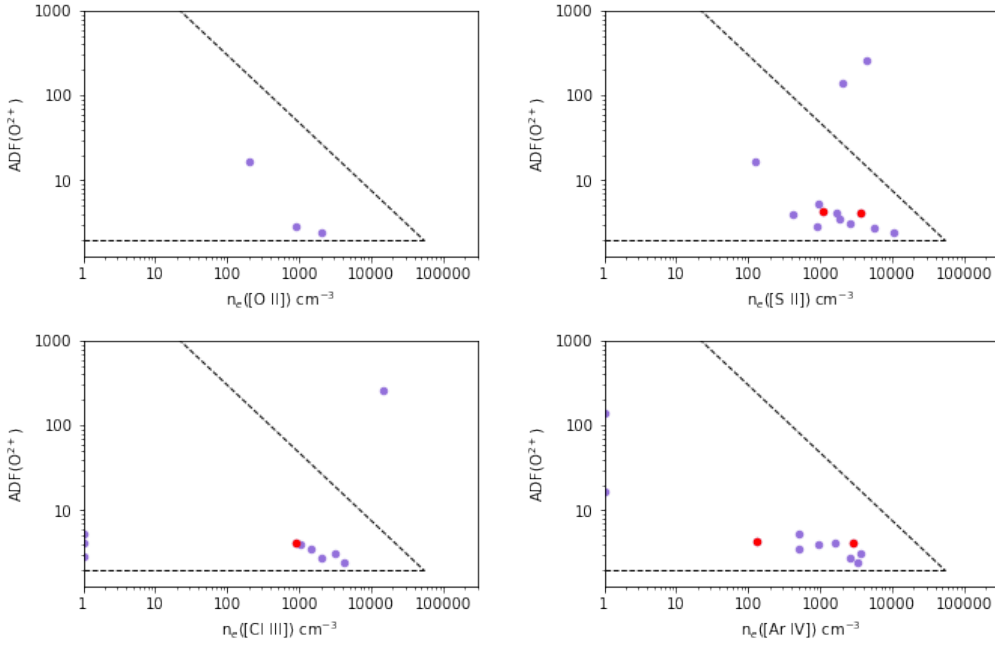
Figure 5.18: ADF values against electron density estimated from [O II] (upper left), [S II] (upper right), [Cl III] (lower left), and [Ar IV] (lower right) line ratios in this work and plotted in the same manner as Fig. 16 in Wesson et al. (2018). PNe with binary central stars are indicated with red dots, other PNe with are shown with purple dots. The dotted lines indicate the ADF = 1 and ADF = $1.2 \times 10^4 n_e^{-0.8}$ (suggested as the upper limit of ADFs in Wesson et al. (2018)) respectively.

Thus, the relationship between electron densities and ADFs explored in Wesson et al. (2018) includes the relationship between low electron densities and extreme ADFs, the positive correlation between $n_e([S\ II])$ and the ADFs and the upper limit of ADFs in objects derived from electron densities generally applies to results in this work. Two PNe with close binaries but normal ADFs adds a piece of evidence that low-density nebulae show the most extreme ADFs. The correlation between $n^e([S\ II])$ and the ADF measured in PNe with binary central stars, together with Fig. 16 in Wesson et al. (2018), suggest that the ADFs measured in PNe with binary central stars are caused differently than the other normal or 'elevated' abundance discrepancies in H II regions which show no correlation with the electron densities. In addition, our measurements are lower than the empirically maximum ADF determined from the electron densities except for

two outliers with the highest ADFs.

Chemical abundances

The correlation between the chemical abundances in PNe and the abundance discrepancies was studied by Wesson et al. (2018), they noticed that ADFs in post-CE PNe exhibit a negative correlation with oxygen and nitrogen abundances. In Fig. 5.19, we include the 15 PNe discovered as post-CE summarised in Wesson et al. (2018) that are either from previous studies, including Corradi et al. (2015), Jones et al. (2015), Garcia-Rojas et al. (2013), Sowicka et al. (2017) and Jones et al. (2016), or their work, 4 high-density PNe with an ADF measured in Ruiz-Escobedo et al. (2022) and 13 PNe in this work to investigate the relationship between [O/H] or [N/H] and the abundance discrepancy.

For chemical abundances, when adding our and Ruiz-Escobedo et al. (2022) results to the post-CE samples in Wesson et al. (2018), more data points with slightly sub-solar to super-solar abundances are seen while they are all with low ADFs. For [O/H], the Pearson r coefficient measured in the combined sample is −0.64 with a p-value of 6.8E-05, indicating a strong anti-correlation. If the PN NGC 6326 at the far right in the plot is excluded, the r and p-value become −0.73 and 3.68E-06 respectively. It was also noticed that, for [O/H] > 8.60, no 'elevated' ADF > 5 is seen. Besides, With the PN NGC 6326 and two PNe with the highest ADF values in our results, an increase in ADF as the increase of [O/H] is seen at extremely sub-solar oxygen abundance ([O/H] < 7.5) followed by a decrease till approximately the solar abundance. However, more measurements are required to confirm this trend. The Pearson correlation coefficient is −0.35, with a p-value of 0.05 for [N/H], indicating a weak anti-correlation. If we exclude PNG 001.3-01.2 at (8.07, 256), the r and p-value become −0.59 and 5.1E-04 respectively, the correlation is then less likely seen by chance. In this combined sample, PNe with [N/H] > 7.87 ([N/H]$_\odot$ = 7.77) are all measured with an ADF less than 20, except for one outlier.

One argument about post-common envelope PN in De Marco (2009) is that the CE evolution could shuttle down the Hydrogen-bottom burning, in which carbon is burned into nitrogen, and leave the surface abundance an arbitrary C/O or N/O ratio compared with common PNe. The carbon abundances are not available in our data, therefore, we consider N/O ratios here. In Fig. 5.19(c), ADF is plotted against nitrogen-to-oxygen ratio of this combined sample and the mean N/O ratios of a large sample of normal PNe in KB94 are indicated in the plot. The Pearson r and p-values are 0.2 and 0.33 respectively, indicating a less reliable positive correlation. Even if the point at (0.39, 256) is excluded, the r and p-value are −0.18 and 0.33 respectively. From this plot, for PNe with an extreme [N/O] (> -0.23 or < -1.13), 7 out of 10 objects are of the post-CE sample, this could indicate that the other 3 PNe, PNG 351.9+09.0 at (-1.3, 3.95), PNG 001.3-01.2 at (0.39, 256) and PNG 353.2-05.2 (0.43, 16.39) respectively, in our sample possibly have a binary CS at their centre and are post-CE PNe.

In summary, the anti-correlation between oxygen and nitrogen abundances and the abundance discrepancy in O^{2+} in PNe still present if we include both the post-CE and the normal PNe.

Compared with the literature results, a weaker Pearson r coefficient was measured but a higher p-value because of the increase in the number of data points. For [O/H], PNe with [O/H] less than 8.6 are measured with moderate or normal ADFs only. [N/O] ratios in PNe were investigated in this combined sample. A much weaker correlation is seen between [N/O] and ADFs which is expected because unlike normal PNe, [N/O] ratios spread a wide range in post-CS PNe. A certain indication of extreme [N/O] and post-CE is seen and with this, three PNe with ADFs measured in this work could be post-CE PNe.
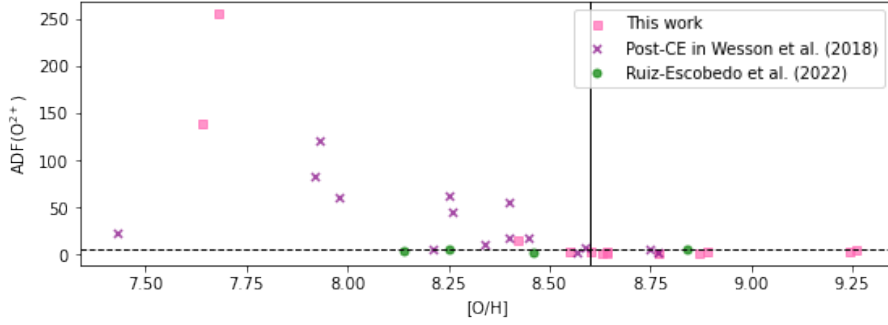
(a) The relationship between [O/H] and ADF(O^{2+}). [O/H] was determined from CELs and is in the scale such than hydrogen abundance is equal to 12. The combined sample includes 32 PNe in total. The Pearson r value is -0.64 and p-value is 6.8E-5. The black dashed horizontal line indicates the threshold value of an extreme ADF (ADF = 5) and the vertical solid line indicates an oxygen abundance of 8.60.
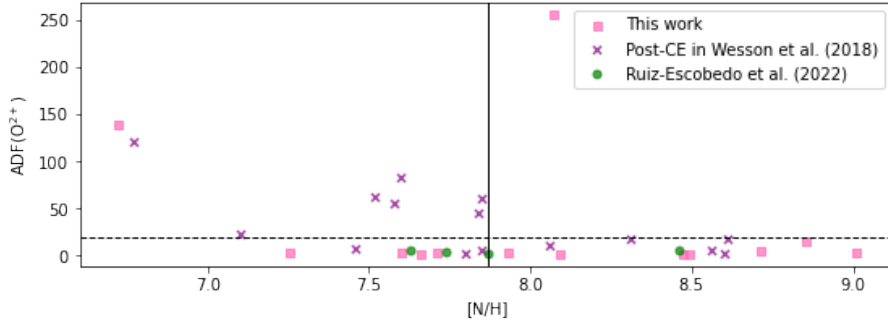
(b) The relationship between [N/H] and ADF(O^{2+}). Similarly, [N/H] was determined from CELs and is in the scale such than hydrogen abundance is equal to 12. The Pearson r value is -0.37 and p-value is 0.04. The black dashed horizontal line indicate an ADF of 20 and the vertical solid line indicates an oxygen abundance of 7.87.
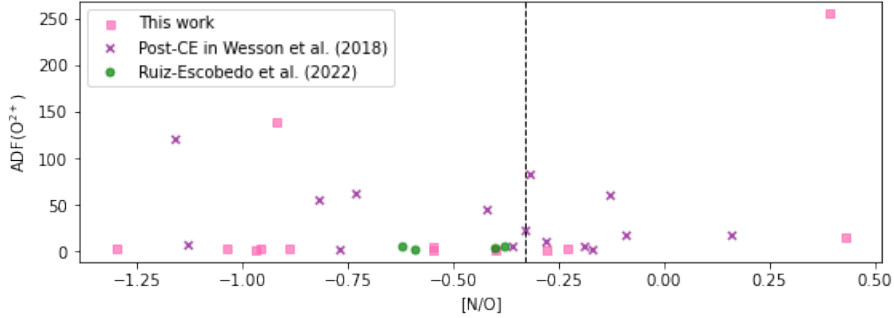
(c) The relationship between [N/O] and ADF(O^{2+}). The Pearson r value is 0.20 and p-value is 0.33. The black dashed vertical line indicates the average [N/O] value for the sample of PNe in KB94.

Figure 5.19: The relationship between the abundance discrepancies in 13 planetary nebulae and their oxygen or nitrogen abundances.

Nebular morphology

The morphologies, position angle, central star visibilities as well as the telescopes used of 13 PNe with ADFs measured in this work in Table.5.18. 7 out of 13 objects (58%) are bipolar PNe in which 6 show clear bipolar lopes or central bars and the image of 1 is not well-resolved. 4 PNe

(31%) are elliptical in which PNG 000.9-02.0 and 001.3-01.2 have an image of a fuzzy elliptical nebulosity only and morphologies are very uncertain. 2 PNe (15%) have a round structure, at least for the VLT images of PNG 359.7-01.8 and the *HST* images of PNG 357.2+02.0, they are perfectly round with ring structures.

Obj	ADF	GPA (± 2°)	Morph	Morph comments	CS visible?	Telescope
000.9-02.0	2.79	79	Ea	Image not resolved		VLT
001.3-01.2	256	116	Em	Image not resolved		VLT
004.1-03.8	3.48	67	Bm			*HST*
351.9+09.0	3.95	105	Emps		Yes	VLT
353.2-05.2	16.39	105	Brs			VLT
353.7+06.3	2.88	56	Baps			VLT
356.5-03.6	3.09	117	Bs			*HST*
357.2+02.0	4.20	147	Rmrs			*HST*
357.5+03.2	4.29	8	Bs			VLT
357.9-03.8	140	125	Ers		Yes	VLT
358.2+04.2	2.44	42	B	Image not resolved		VLT
359.0-04.1	5.23	100	Bps			VLT
359.7-01.8	4.17	8	Rmr			VLT

Table 5.18: The galactic position angle, morphologies, central star visibilities and the telescopes used of 13 planetary nebulae with abundance discrepancies in O^{2+} measured in this work.

The ADF in O^{2+} peaks at the centre of the objects according to the spatially resolved analysis using long slit observations in Wesson et al. (2018). In García-Rojas et al. (2022), the VLT/MUSE IFU observations were performed for 3 PNe with high ADFs, NGC6778, M 1-42 and Hf 2-2. The corresponding morphologies are Bs, Bamprs and Rmr respectively. The derived 2D maps of ADFs and fraction errors adopted from García-Rojas et al. (2022) are shown in Fig. 5.20. The ADF(O^{2+}) centrally peaks for 3 PNe which confirmed the trend found in Wesson et al. (2018) and the existence of a central low-temperature and metal-right components in the inner regions of PNe. For NGC 6678, the region is the clumps within its two-component central bar structure. For M 1-42, high ADF is seen within its innermost arc structure and showing on the top and the bottom of this region. For Hf 2-2, ADF gradually increases from its outer ring structure. Wesson et al. (2018) provide extra high-resolution images for 4 PNe with high ADFs, NGC 6326, NGC 6337, Pe 1-9 and Fg 1. NGC 6326 and Pe 1-9 have clear arc structures, NGC 6337 is an Rrs PNe and Fg 1 is a bipolar PN with a similar two-component bar to NGC 6678. High ADFs in their spatially resolved studies were found at the centre of NGC 6326 NGC 6337, but the value fluctuation within the long-slit observation for Fg 1.

For morphologies of 13 PNe in our results, among 7 bipolar PNe, PNG 353.2-05.2, PNG 353.7+06.3, show a clear point-symmetrical arc structure, this might also be the case for PNG 004.1-03.8, its faint *HST* image is showing certain arc-shape overdensities. PNG 358.2+04.2 and PNG 359.0-04.1 are also classified bipolar, however, their internal structures are not resolved,

PNG 356.5-03.6 is showing a two-component central bar structure in the *HST* image while PNG 357.5+03.2 is possibly a bipolar or irregular PN, a better imaging data is required for a further confirmation. Among 4 elliptical PNe, PNG 351.9+09.0, PNG 357.9-03.8, have two arc structures in the inner region while PNG 000.9-02.0 and PNG 001.3-01.2 are not resolved. PNG 357.2+02.0 and PNG 359.7-01.8 are all round PNe with a ring structure. If we consider PNe exhibiting a clear morphology only, PNe with ADFs are seen with either of these features:

1. A symmetrical or point-symmetrical structure in an elliptical or bipolar PNe

2. A two-component bar structure at the centre of a bipolar PN

3. A ring structure enclosing a round PN

This is expected to be confirmed by more high-resolution images of PNe with ADFs measured. If this indeed applies, the mechanism that causes the abundance discrepancy in PNe might be related to the formation of these structures around the CSPNe and further studies on the more detailed morphological features are needed.

Can magnetic field cause the abundance discrepancy? This question is asked based on a few studies: a. in Tang et al. (2018), through a study of starless molecular cloud in NGC 6334, a decoupling between ions and neutrals was noticed and interpreted the decoupling of the neutral turbulence from magnetic fields in a partially ionized medium, the magnetic field in the interstellar medium could, therefore, potentially lead to a variation in local chemical abundances; b. in Rees et al. (2018), an alignment of bipolar PNe with the Galactic magnetic field was noticed, if the Galactic magnetic field could influence the orientation of the entire PN, the magnetic field of either the PN itself or the nearby sources and background might also have some effects on its internal angular momentum distribution and other processes when the PN forms; c. a magnetic field in a few PNe, oxygen-rich AGB and post-AGB stars in Greaves et al. (2002) and Sabin et al. (2007).

We test the distribution of GPAs here to see whether the angular momentum of the PNe with ADFs measured exhibit any alignment the bipolar sample in Rees & Zijlstra (2013). The spatial distribution of GPAs of these 13 PNe is shown in the left panel of Fig.5.21, the bipolar sample in Rees & Zijlstra (2013) is also plotted in the right panel as a reference. Form the rose plot of the doubled GPA is shown in Fig. 5.22, the distribution of GPAs in 13 PNe are slightly unbalanced. The Rayleigh test was employed to check the uniformity of their GPA distribution which gives p-values of 0.3 for PNe with an ADF measured and 8E-04 for the bipolar sample in Rees et al. (2018). Therefore, a preferred orientation of PNe with ADFs measured is not seen in our data, however, the results suffer from a small-sample statistics. This question is to be better qualified with more GPA measurements of PNe with high ADFs and better knowledge of the Galactic magnetic field.

The relationship between the background magnetic field in the Galactic bulge and the abundance discrepancy in PNe was considered. The 21 cm radio continuum polarisation in Testori et al. (2008) was used to infer the Galactic magnetic field. The polarised intensity and polarisation angle were accessed via http://www.mpifr-bonn.mpg.de/survey.html. We consider the

angle made between the external field and the angular momentum vector of the PN. The angle, θ, made between the GPA of a PN and the local polarisation angle are plotted v.s. the polarised intensity, I in a unit of mkT_B in Fig. 5.23. As the polarised intensities measured at the positions of two PNe are negative while one PN has no GPA measurement in our results, these three PNe were excluded from the plot. The bipolar PN sample in Rees & Zijlstra (2013) is also shown in the plot for comparison. A positive correlation between θ and I is found with a Pearson r coefficient of -0.77. This makes sense if the time scale for the alignment of the angular momentum in a PN with the external field is longer than the duration of the PN phase and the magnetic field of the central star is weak. Such a correlation is not seen in the bipolar bulge PN sample. The abundance discrepancy is related to the external magnetic field if such a correlation is confirmed. However, as the p-value is 0.01, this correlation is less statistically significant. The viewing angle of PNe would cause large uncertainty in θ and thereby, in the results. If the external magnetic field is the mechanism leading to the abundance discrepancy, the exact values of ADFs would be influenced by the strength of the magnetic field in the PN, the mass of the central star, the ionises masses, the mass-loss rate of the PN and the chemical abundance in PN. More measurements are required for further investigations.

5.7 Conclusion

With the observation of 118 PNe in the Galactic bulge from the VLT, 13 PNe were measured with ADFs. Most of the ADF values are moderate (< 5), but the ADFs of PNe in this sample are currently the third and the fourth highest among all PN ADF literature results. Another two out of the 13 are PNe with newly discovered short-period binary CSs.

When combining new measurements since Wesson et al. (2018) together, the link between close binary objects and extreme ADFs is still seen. A PN with a long-period triple nuclei CS in a recent literature was also measured with extreme ADF. Extremely high ADFs might be related to the extra components at its centre. One of the two PNe with close binary central stars in our sample has merely a moderate ADF and this was explained by its high electron densities. In the log-log scale, the positive correlation between electron densities derived from [S II] lines and the ADFs became stronger when new measurements in this study were added.

PNe with measured ADFs in several previous studies and this work were combined to investigate the relationship between ADFs and the nebular chemical abundances. The anti-correlation between [O/H] or [N/H] and ADFs stills holds for the combined data set, however, few outliers coming from our measurement are present. When [N/O] ratios were considered, the outliers are those with a [N/O] largely differing from an average value measured in normal PNe. Thus, we consider three of them might be post-CE PNe and the common-envelope evolution halts the change in [N/O] ratios.

The high-resolution images of 15 PNe with ADFs measured in previous studies and this work were used to give an accurate morphological description of each object. It was noticed that these

PNe could be divided into three morphological groups: arc structure elliptical/bipolar, bipolar with a two-component central bar and round with outer ring structures. Previous studies show that the ADFs measured are strongly related to these substructures. The understanding of the formation of these substructures is therefore important for the study of abundance discrepancy.

(a) NGC 6778

(b) M 1-42

(c) Hf 2-2
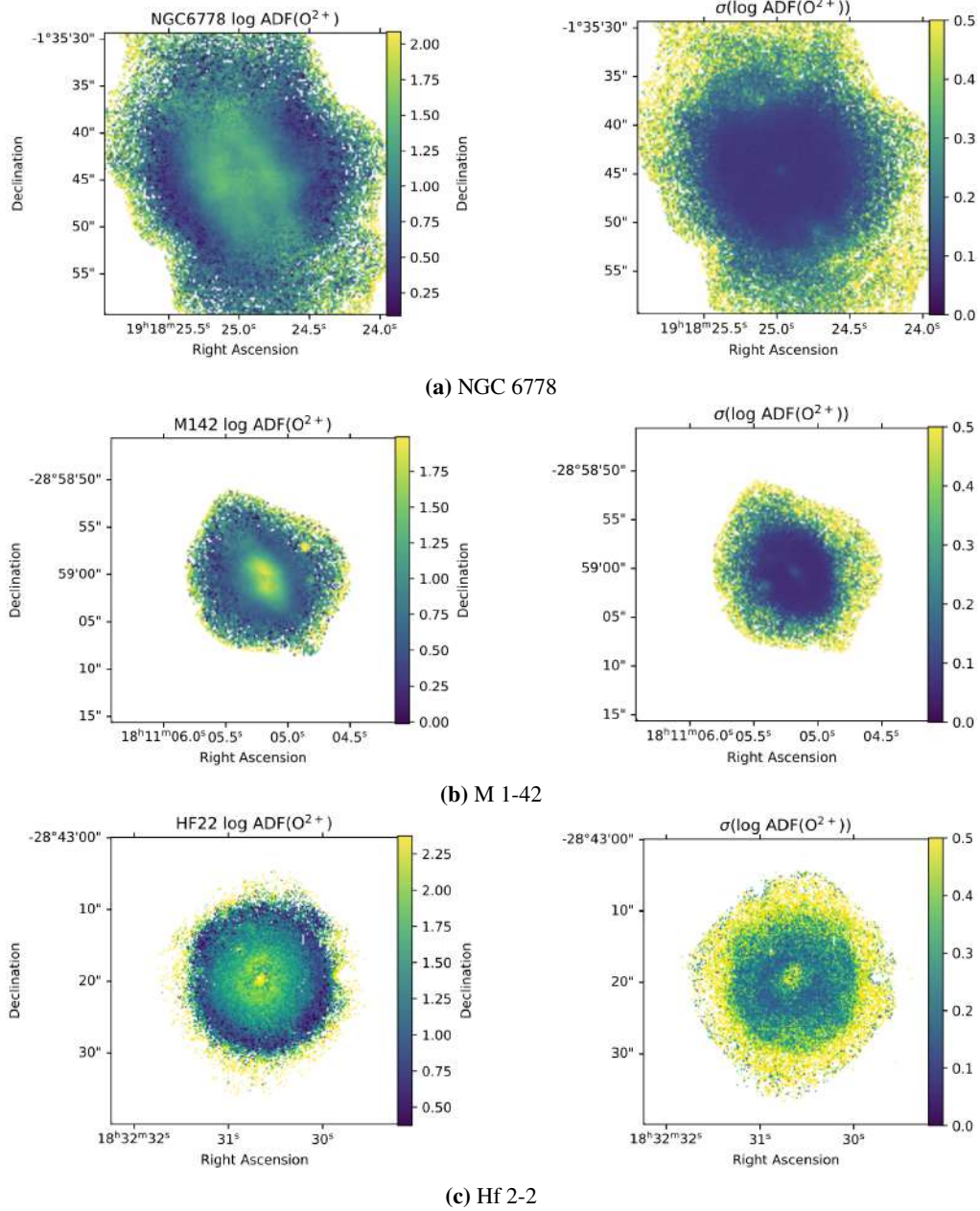
Figure 5.20: Spatial distributions of log [ADF(O^{2+})] in NGC 6778, M 1-42 and Hf 2-2 and the corresponding fractional error (ADF error/ADF ratio) maps in García-Rojas et al. (2022).
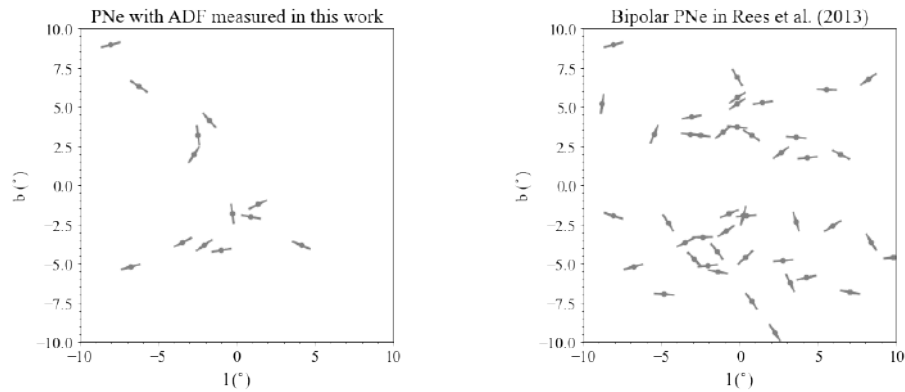
Figure 5.21: The distribution of Galactic position angle in the Galactic plane. Left panel: the sample of 13 PNe with an ADF measured. Right panel: 44 bipolar PNe in Rees & Zijlstra (2013).
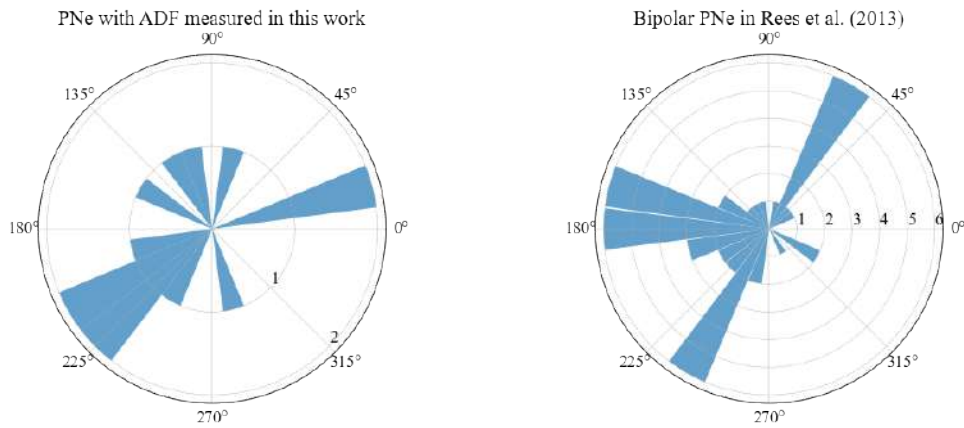
Figure 5.22: The rose plots of the doubled GPA for 13 PNe with ADFs measured in this work (left panel) and the bipolar PNe in Rees & Zijlstra (2013) (right panel). The radial scale indicates the number of objects.
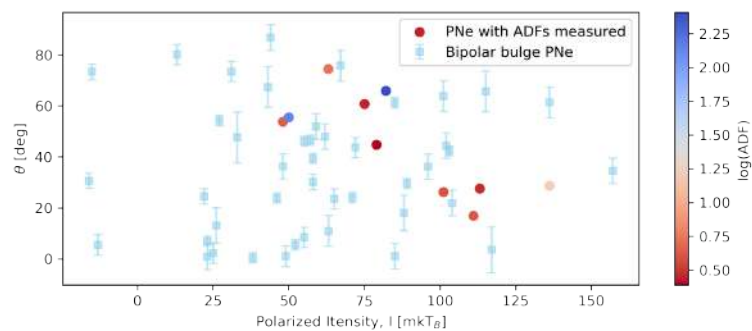
Figure 5.23: Relationship between the angle, θ, made between the 21 cm radio continuum polarisation angle and the Galactic position angle of PN and the polarised intensity, I. The polarisation angles are with respect to the Galactic North Pole Blue squares are the bipolar bulge PN sample in Rees & Zijlstra (2013) with error bars from the measurement uncertainties. Dots are the PNe with ADFs measured in this work and colour-coded according to log(ADF).

Chapter 6

Conclusion

The research in this thesis is briefly summarised in this chapter and findings in each study as well as future works are highlighted in the following.

In Chapter 3, the morphological classifications, central star detection and position angles of this sample of bulge PNe were reviewed with the VLT imagery. The *HST* observations are available for 36 out of 111 PNe in our sample and were combined with the VLT data for the analysis. This reveals morphologies for 19 PNe which were fuzzy nebulosity in previous observations and resolved the internal structures and features for 28 PNe. These more accurate morphological classifications are important for the study of PN internal density distribution, mass-loss processes, formation mechanism and other topics in nebulae sciences. Other than that, 43 central stars of PNe were seen from the image for the first time and have not been catalogued. These CSPN coordinates are to be included in the future *Gaia* studies to give a better estimation of the PN distance as well as a check for central star binarity. The VLT images also allow us to measure the position angles of PNe which works as a supplementary study to the alignment of bipolar PNe. The results first-time revealed bipolar features of a number of PNe that were classified as elliptical, round or point-like in the catalogue.

In Chapter 4, the physical conditions and chemical abundances of this bulge PN sample were calculated. When comparing with the literature results, our data show better accuracy and are more representative of the bulge PN population. This is exemplified by the clear lockstep behaviour of α elements which also allows us to use oxygen abundance as an indicator of metallicity in PNe. To study the origin of the bulge, an oxygen abundance gradient along the major axis and the Galactic plane was investigated. A gradient along l was noticed in the inner bulge region which is consistent with a thick disk after a disk instability event, therefore, a pseudo-bulge. Besides, only when the young bipolar PNe were taken into account, a vertical gradient could be found. This adds another line of evidence. One extra evidence comes from the uniform distribution of a young population of PNe in the Galactic plane. The PN dating employed one method based on the AGB models and another method based on a [N/O]-mass relation. Both methods show consistency in the young population less than 1 Gyr. By studying the oxygen abundance distribution function for the old and young populations, the peaks in the distribution functions are consistent with previous studies in which a large fraction of PNe from young

progenitors with super-solar oxygen abundances are in the thin disk. This also suggests a B/P bulge. Re-observing the saturated objects is important to complete our conclusion as most of them are faint and metal-poor objects observed with long exposure time. Further investigation could combine with radio data or observations of [Zn IV] lines to better estimate the extinction or construct a more accurate substitute for metallicity.

The famous abundance discrepancy problem in nebular science was investigated in Chapter 5 with the sample of bulge PNe. 13 objects have ORLs observed with good reliability which allows the first-time determination of their ADFs. Among these, 3 PNe were measured with extremely high ADFs. Moreover, two of them have current the third and the fourth largest ADFs measured in PNe. We carried out investigations of different properties that could be linked to the ADF. One is the central star binarity, the central stars of two PNe with moderate ADF were newly identified as binary. The correlation between the magnitude of ADF and their electron densities follows a positive correlation as suggested in the previous studies. Besides, an anti-correlation between [O/H] and ADFs found for the PNe with central star binarity and an ADF also holds if we consider all the 13 PNe. This may indicate that this relationship might be universal or these central stars are in a binary system but have not been identified yet. We failed to find any link between the ADFs and the PN morphologies, however, we noticed the distribution of PN GPAs is slightly less balanced which might suggest a relationship with the background magnetic field, however, more GPA measurements of PNe with ADFs measured are required to confirm this link.

Appendix A

Source and coordinate list

Table A.1: Source and coordinate list

PN G	Name	RAJ2000	DECJ2000
000.1-02.3	Bl 3-10	17:55:20.5	-29:57:36.14
000.1+02.6	Al 2-J	17:35:35.4	-27:24:04.97
000.1+04.3	H 1-16	17:29:23.4	-26:26:04.38
000.2-01.9	M 2-19	17:53:45.6	-29:43:46.34
000.2-04.6	Wray 16-363	18:04:44.1	-31:02:48.16
000.3-04.6	M 2-28	18:05:02.7	-30:58:17.40
000.3+06.9	Terz N 41	17:20:22.0	-24:51:52.24
000.4-01.9	M 2-20	17:54:25.4	-29:36:08.78
000.4-02.9	M 3-19	17:58:19.3	-30:00:39.31
000.7-02.7	M 2-21	17:58:09.6	-29:44:20.08
000.7-03.7	M 3-22	18:02:19.2	-30:14:25.37
000.7-07.4	M 2-35	18:17:37.2	-31:56:46.86
000.7+03.2	M 4-5	17:34:54.7	-26:35:56.90
000.9-02.0	Bl 3-13	17:56:02.8	-29:11:16.22
000.9-04.8	M 3-23	18:07:06.1	-30:34:16.97
001.1-01.6	Sa 3-92	17:54:52.1	-28:48:55.33
001.2-03.0	H 1-47	18:00:37.6	-29:21:50.22
001.2+02.1	Hen 2-262	17:40:12.8	-26:44:21.37
001.3-01.2	Bl M	17:53:47.2	-28:27:18.0
001.4+05.3	H 1-15	17:28:37.6	-24:51:06.59
001.6-01.3	Bl Q	17:54:34.9	-28:12:43.06
001.7-04.4	H 1-55	18:07:14.552	-29:41:24.424

Table A.1 Continued: Source and coordinate list

PN G	Name	RAJ2000	DECJ2000
001.7+05.7	H 1-14	17:28:01.8	-24:25:23.02
002.0-06.2	M 2-33	18:15:06.5	-30:15:32.90
002.1-02.2	M 3-20	17:59:19.3	-28:13:48.04
002.1-04.2	H 1-54	18:07:07.2	-29:13:06.35
002.2-09.4	Cn 1-5	18:29:11.65	-31:29:59.2
002.3-03.4	H 2-37	18:04:28.8	-28:37:38.28
002.3+02.2	K 5-11	17:42:30.0	-25:45:27.07
002.5-01.7	Pe 2-11	17:58:31.2	-27:37:05.38
002.6+02.1	Terz N 1580	17:43:39.4	-25:36:42.52
002.7-04.8	M 1-42	18:11:05.0	-28:58:59.34
002.8+01.7	H 2-20	17:45:39.8	-25:40:00.05
002.8+01.8	Terz N 1567	17:45:28.3	-25:38:12.48
002.9-03.9	H 2-39	18:08:05.77	-28:26:10.8
003.1+03.4	H 2-17	17:40:07.4	-24:25:42.56
003.2-06.2	M 2-36	18:17:41.4	-29:08:19.57
003.6-02.3	M 2-26	18:03:11.8	-26:58:30.22
003.6+03.1	M 2-14	17:41:57.3	-24:11:15.65
003.7-04.6	M 2-30	18:12:34.4	-27:58:10.63
003.7+07.9	H 2-8	17:24:45.5	-21:33:35.24
003.8-04.3	H 1-59	18:11:29.3	-27:46:15.67
003.9-02.3	M 1-35	18:03:39.31	-26:43:33.7
003.9-03.1	KFL 7	18:06:50.0	-27:06:19.51
003.9+01.6	Terz N 2111	17:48:28.4	-24:41:23.93
004.0-03.0	M 2-29	18:06:40.9	-26:54:55.94
004.1-03.8	KFL 11	18:10:12.2	-27:16:35.00
004.2-03.2	KFL 10	18:08:01.3	-26:54:01.51
004.2-04.3	H 1-60	18:12:25.2	-27:29:12.95
004.2-05.9	M 2-37	18:18:38.3	-28:07:58.55
004.3+01.8	H 2-24	17:48:36.5	-24:16:34.25
004.3+01.8a	PHR J1748-2417	17:48:33.0	-24:17:36.02
004.6+06.0	H 1-24	17:33:37.6	-21:46:24.78
004.8-05.0	M 3-26	18:16:11.4	-27:14:57.44

Table A.1 Continued: Source and coordinate list

PN G	Name	RAJ2000	DECJ2000
004.8+02.0	H 2-25	17:49:00.5	-23:42:54.58
005.0-03.9	H 2-42	18:12:23.0	-26:32:54.38
005.2+05.6	M 3-12	17:36:22.6	-21:31:12.22
005.5-04.0	H 2-44	18:13:40.6	-26:08:38.72
005.5+06.1	M 3-11	17:35:21.4	-20:57:23.00
005.8-06.1	NGC 6620	18:22:54.2	-26:49:17.00
005.9-02.6	MaC 1-10	18:09:12.4	-25:04:34.50
006.1+08.3	M 1-20	17:28:57.6	-19:15:53.82
006.3+03.3	H 2-22	17:47:33.9	-21:47:23.10
006.3+04.4	H 2-18	17:43:28.7	-21:09:51.30
006.4-04.6	Pe 2-13	18:18:13.4	-25:38:08.92
006.4+02.0	M 1-31	17:52:41.4	-22:21:56.84
006.8-03.4	H 2-45	18:14:28.7	-24:43:37.96
006.8+02.3	Th 4-7	17:52:22.62	-21:51:13.7
007.0-06.8	Vy 2-1	18:27:59.6	-26:06:48.28
007.0+06.3	M 1-24	17:38:11.6	-19:37:37.63
007.5+04.3	Th 4-1	17:46:20.8	-20:13:48.07
007.5+07.4	M 1-22	17:35:10.2	-18:34:20.42
007.6+06.9	M 1-23	17:37:22.0	-18:46:41.88
007.8-03.7	M 2-34	18:17:15.9	-23:58:54.52
007.8-04.4	H 1-65	18:20:08.8	-24:15:05.08
008.2+06.8	Hen 2-260	17:38:57.4	-18:17:35.77
008.4-03.6	H 1-64	18:18:23.9	-23:24:57.13
008.6-02.6	MaC 1-11	18:14:50.9	-22:43:55.42
009.4-09.8	M 3-32	18:44:43.1	-25:21:33.84
009.8-04.6	H 1-67	18:25:05.0	-22:34:52.64
350.5-05.0	H 1-28	17:42:54.1	-39:36:24.05
351.1+04.8	M 1-19	17:03:46.8	-33:29:44.41
351.2+05.2	M 2-5	17:02:19.1	-33:10:05.02
351.6-06.2	H 1-37	17:50:44.6	-39:17:25.98
351.9-01.9	Wray 16-286	17:33:00.7	-36:43:52.54
351.9+09.0	PC 13	16:50:17.1	-30:19:55.49

Table A.1 Continued: Source and coordinate list

PN G	Name	RAJ2000	DECJ2000
352.0-04.6	H 1-30	17:45:06.8	-38:08:49.49
352.1+05.1	M 2-8	17:05:30.7	-32:32:08.30
352.6+03.0	H 1-8	17:14:42.9	-33:24:47.20
353.2-05.2	H 1-38	17:50:45.2	-37:23:53.09
353.3+06.3	M 2-6	17:04:18.3	-30:53:28.72
353.7+06.3	M 2-7	17:05:13.9	-30:32:19.68
354.5+03.3	Th 3-4	17:18:51.9	-31:39:06.34
354.9+03.5	Th 3-6	17:19:20.2	-31:12:40.50
355.1-06.9	M 3-21	18:02:32.3	-36:39:10.94
355.4-02.4	M 3-14	17:44:20.6	-34:06:40.57
355.6-02.7	H 1-32	17:46:06.3	-34:03:45.54
355.9-04.2	M 1-30	17:52:58.9	-34:38:22.99
355.9+03.6	H 1-9	17:21:31.9	-30:20:48.34
356.1-03.3	H 2-26	17:49:50.8	-34:00:31.14
356.3-06.2	M 3-49	18:02:32.0	-35:13:13.69
356.5-03.6	H 2-27	17:51:50.6	-33:47:35.59
356.8-05.4	H 2-35	18:00:18.2	-34:27:39.60
356.8+03.3	Th 3-12	17:25:06.1	-29:45:16.88
356.9+04.4	M 3-38	17:21:04.5	-29:02:59.21
357.0+02.4	M 4-4	17:28:50.3	-30:07:44.47
357.1-04.7	H 1-43	17:58:14.4	-33:47:37.50
357.1+03.6	M 3-7	17:24:34.4	-29:24:19.48
357.1+04.4	Terz N 18	17:21:38.0	-28:55:14.34
357.2+02.0	H 2-13	17:31:08.1	-30:10:27.98
357.3+04.0	H 2-7	17:23:24.9	-28:59:06.04
357.5+03.1	Th 3-16	17:27:24.4	-29:21:14.00
357.5+03.2	M 3-42	17:26:59.8	-29:15:31.86
357.6-03.3	H 2-29	17:53:16.8	-32:40:38.57
357.9-03.8	H 2-30	17:56:13.9	-32:37:22.08
357.9-05.1	M 1-34	18:01:22.2	-33:17:43.08
358.0+09.3	Th 3-1	17:05:44.5	-25:25:01.74
358.2+03.5	H 2-10	17:27:32.8	-28:31:06.89

Continued on next page:

Table A.1 Continued: Source and coordinate list

PN G	Name	RAJ2000	DECJ2000
358.2+04.2	M 3-8	17:24:52.1	-28:05:54.60
358.5-04.2	H 1-46	17:59:02.5	-32:21:43.42
358.5+02.9	Al 2-F	17:30:30.4	-28:35:54.89
358.6-05.5	M 3-51	18:04:56.2	-32:54:01.22
358.6+07.8	M 3-36	17:12:39.2	-25:43:37.38
358.7+05.2	M 3-40	17:22:28.3	-27:08:42.40
358.8+03.0	Th 3-26	17:31:09.3	-28:14:50.42
358.9+03.4	H 1-19	17:30:02.5	-27:59:17.56
359.0-04.1	M 3-48	17:59:56.8	-31:54:27.72
359.1-02.9	M 3-46	17:55:05.7	-31:12:16.85
359.2+04.7	Th 3-14	17:25:44.1	-26:57:47.70
359.3-01.8	M 3-44	17:51:18.9	-30:23:52.98
359.6-04.8	H 2-36	18:04:07.7	-31:39:10.66
359.7-01.8	M 3-45	17:52:05.9	-30:05:13.81
359.8-07.2	M 2-32	18:14:50.6	-32:36:55.22
359.8+02.4	Th 3-33	17:35:48.1	-27:43:20.39
359.8+03.7	Th 3-25	17:30:46.7	-27:05:59.14
359.8+05.2	Terz N 19	17:25:23.6	-26:11:53.02
359.8+05.6	M 2-12	17:24:01.4	-25:59:23.17
359.8+06.9	M 3-37	17:19:13.4	-25:17:17.56
359.9-04.5	M 2-27	18:03:52.6	-31:17:46.54

Appendix B

The VLT Observing log

Table B.1: Observing log.

PN	Position Angle	Grism	T_{EXP}	Modified Julian Date	Airmass
PNG 000.1+02.6	−78	1200B	30	57129.295	1.07
PNG 000.1+02.6	−78	600RI	1000	57129.310	1.02
PNG 000.1+02.6	−78	1200B	1000	57129.296	1.04
PNG 000.1+02.6	−78	600RI	30	57129.309	1.04
PNG 000.1+04.3	−105	600RI	1000	57130.294	1.04
PNG 000.1+04.3	−105	1200B	30	57130.279	1.09
PNG 000.1+04.3	−105	600RI	30	57130.293	1.06
PNG 000.1+04.3	−105	1200B	1000	57130.280	1.06
PNG 000.1−02.3	−152	600RI	1000	57129.342	1.01
PNG 000.1−02.3	−152	1200B	1000	57129.329	1.02
PNG 000.2−01.9	−105	600RI	1000	57129.375	1.01
PNG 000.2−01.9	−105	1200B	1000	57129.361	1.00
PNG 000.2−01.9	−105	600RI	30	57129.374	1.00
PNG 000.2−04.6	−53	1200B	1000	57129.391	1.01
PNG 000.2−04.6	−53	600RI	1000	57129.403	1.03
PNG 000.3+06.9	−132	600RI	1000	57131.228	1.20
PNG 000.3+06.9	−132	1200B	30	57131.214	1.35
PNG 000.3+06.9	−132	600RI	30	57131.227	1.26
PNG 000.3+06.9	−132	1200B	1000	57131.215	1.27
PNG 000.3−04.6	−71	600RI	30	57130.343	1.02
PNG 000.3−04.6	−71	600RI	1000	57130.344	1.01
PNG 000.3−04.6	−71	1200B	1000	57130.330	1.03

PN	Position Angle	Grism	T$_{EXP}$	Modified Julian Date	Airmass
PNG 000.4−01.9	−39	1200B	1000	57130.362	1.00
PNG 000.4−01.9	−39	600RI	1000	57130.376	1.01
PNG 000.4−01.9	−39	1200B	30	57130.361	1.00
PNG 000.4−01.9	−39	600RI	30	57130.375	1.00
PNG 000.4−02.9	−174	1200B	1000	57131.245	1.24
PNG 000.4−02.9	−174	600RI	1000	57131.258	1.18
PNG 000.7+03.2	−179	1200B	1000	57131.276	1.07
PNG 000.7+03.2	−179	600RI	1000	57131.289	1.05
PNG 000.7−02.7	−133	1200B	1000	57131.327	1.02
PNG 000.7−02.7	−133	600RI	1000	57131.341	1.01
PNG 000.7−02.7	−133	600RI	30	57131.340	1.02
PNG 000.7−02.7	−133	1200B	30	57131.326	1.03
PNG 000.7−03.7	−75	600RI	1000	57161.371	1.15
PNG 000.7−03.7	−75	1200B	1000	57161.358	1.11
PNG 000.7−07.4	−152	600RI	30	57161.401	1.18
PNG 000.7−07.4	−152	600RI	1000	57161.402	1.24
PNG 000.7−07.4	−152	1200B	1000	57161.388	1.18
PNG 000.9−02.0	−19	600RI	1000	57169.358	1.21
PNG 000.9−02.0	−19	1200B	1000	57169.340	1.14
PNG 000.9−02.0	−19	600RI	105	57169.353	1.15
PNG 000.9−04.8	−141	1200B	1000	57183.092	1.34
PNG 000.9−04.8	−141	1200B	1000	57195.122	1.08
PNG 000.9−04.8	−141	600RI	1000	57183.104	1.27
PNG 000.9−04.8	−141	600RI	1000	57195.135	1.05
PNG 001.1−01.6	−45	1200B	1500	57191.253	1.08
PNG 001.1−01.6	−45	600RI	100	57191.290	1.14
PNG 001.1−01.6	−45	600RI	1500	57191.271	1.13
PNG 001.2+02.1	−12	600RI	30	57169.225	1.01
PNG 001.2+02.1	−12	1200B	1000	57169.212	1.01
PNG 001.2+02.1	−12	600RI	1000	57169.225	1.00
PNG 001.2−03.0	−155	1200B	1000	57191.321	1.31
PNG 001.2−03.0	−155	600RI	30	57191.334	1.32
PNG 001.2−03.0	−155	1200B	30	57191.348	1.42

PN	Position Angle	Grism	T_{EXP}	Modified Julian Date	Airmass
PNG 001.2−03.0	−155	600RI	1000	57191.335	1.40
PNG 001.3−01.2	−136	600RI	1000	57215.081	1.03
PNG 001.3−01.2	−136	600RI	1000	57183.068	1.45
PNG 001.3−01.2	−136	1200B	1000	57215.068	1.06
PNG 001.3−01.2	−136	1200B	1000	57183.056	1.57
PNG 001.4+05.3	−41	1200B	1000	57165.277	1.02
PNG 001.4+05.3	−41	600RI	30	57165.289	1.02
PNG 001.4+05.3	−41	600RI	1000	57165.290	1.03
PNG 001.4+05.3	−41	600RI	123	57165.303	1.04
PNG 001.6−01.3	−81	600RI	1000	57193.242	1.05
PNG 001.6−01.3	−81	1200B	1000	57193.229	1.03
PNG 001.7+05.7	−116	600RI	1000	57169.274	1.03
PNG 001.7+05.7	−116	1200B	1000	57169.262	1.01
PNG 001.7−04.4	−84	1200B	1000	57194.278	1.13
PNG 001.7−04.4	−84	600RI	30	57194.291	1.14
PNG 001.7−04.4	−84	600RI	1000	57194.292	1.18
PNG 002.0−06.2	−145	1200B	30	57215.101	1.05
PNG 002.0−06.2	−145	1200B	30	57191.205	1.01
PNG 002.0−06.2	−145	1200B	1000	57215.102	1.03
PNG 002.0−06.2	−145	600RI	1500	57191.220	1.01
PNG 002.0−06.2	−145	1200B	1000	57191.206	1.00
PNG 002.0−06.2	−145	600RI	1000	57215.116	1.01
PNG 002.0−06.2	−145	600RI	30	57191.219	1.00
PNG 002.0−06.2	−145	600RI	30	57215.115	1.03
PNG 002.1−02.2	−117	600RI	1000	57195.168	1.01
PNG 002.1−02.2	−117	1200B	30	57195.154	1.03
PNG 002.1−02.2	−117	1200B	1000	57195.155	1.02
PNG 002.1−02.2	−117	600RI	30	57195.167	1.01
PNG 002.1−04.2	−167	1200B	30	57195.187	1.01
PNG 002.1−04.2	−167	600RI	16	57195.200	1.00
PNG 002.1−04.2	−167	600RI	1000	57195.201	1.00
PNG 002.1−04.2	−167	1200B	1000	57195.188	1.00
PNG 002.2−09.4	−149	1200B	30	57191.353	1.31

Continued on next page:

PN	Position Angle	Grism	T_{EXP}	Modified Julian Date	Airmass
PNG 002.2−09.4	−149	600RI	15	57191.384	1.55
PNG 002.2−09.4	−149	1200B	1000	57191.354	1.39
PNG 002.2−09.4	−149	600RI	30	57191.381	1.52
PNG 002.2−09.4	−149	600RI	1000	57191.367	1.50
PNG 002.3+02.2	−143	1200B	1000	57215.168	1.04
PNG 002.3+02.2	−143	1200B	1000	57173.158	1.10
PNG 002.3+02.2	−143	600RI	1000	57215.181	1.07
PNG 002.3+02.2	−143	600RI	1000	57173.171	1.06
PNG 002.3−03.4	−72	600RI	1000	57215.150	1.01
PNG 002.3−03.4	−72	1200B	1000	57215.137	1.00
PNG 002.5−01.7	−90	1200B	1000	57215.203	1.09
PNG 002.5−01.7	−90	600RI	1000	57215.215	1.13
PNG 002.6+02.1	−70	600RI	1000	57216.018	1.18
PNG 002.6+02.1	−70	1200B	1000	57216.005	1.24
PNG 002.7−04.8	−33	600RI	1000	57215.986	1.48
PNG 002.7−04.8	−33	1200B	1000	57215.973	1.62
PNG 002.7−04.8	−33	600RI	30	57215.985	1.60
PNG 002.8+01.7	−9	1200B	1000	57216.041	1.10
PNG 002.8+01.7	−9	600RI	1000	57216.055	1.07
PNG 002.8+01.7	−9	600RI	30	57216.054	1.10
PNG 002.8+01.8	−43	600RI	1000	57216.088	1.01
PNG 002.8+01.8	−43	1200B	1000	57216.075	1.03
PNG 002.9−03.9	−15	600RI	1000	57216.120	1.00
PNG 002.9−03.9	−15	1200B	1000	57216.107	1.01
PNG 003.1+03.4	−157	1200B	1000	57216.170	1.05
PNG 003.1+03.4	−157	600RI	1000	57216.182	1.08
PNG 003.2−06.2	−144	1200B	24	57216.200	1.04
PNG 003.2−06.2	−144	1200B	1000	57216.201	1.06
PNG 003.2−06.2	−144	600RI	15	57216.213	1.07
PNG 003.2−06.2	−144	600RI	1000	57216.214	1.10
PNG 003.6+03.1	−27	600RI	1000	57216.278	1.67
PNG 003.6+03.1	−27	600RI	30	57216.277	1.54
PNG 003.6+03.1	−27	1200B	1000	57216.265	1.52

Continued on next page:

PN	Position Angle	Grism	T$_{\mathrm{EXP}}$	Modified Julian Date	Airmass
PNG 003.6−02.3	−136	600RI	1000	57216.310	1.88
PNG 003.6−02.3	−136	1200B	1000	57216.296	1.68
PNG 003.6−02.3	−136	600RI	30	57216.309	1.70
PNG 003.7+07.9	−90	1200B	1000	57166.104	1.41
PNG 003.7+07.9	−90	600RI	1000	57166.118	1.31
PNG 003.7+07.9	−90	600RI	30	57166.117	1.39
PNG 003.7−04.6	−34	600RI	1000	57610.244	1.98
PNG 003.7−04.6	−34	1200B	1000	57610.230	1.76
PNG 003.7−04.6	−34	600RI	30	57610.243	1.78
PNG 003.7−04.6	−34	1200B	30	57610.229	1.61
PNG 003.8−04.3	−71	600RI	30	57227.265	1.49
PNG 003.8−04.3	−71	600RI	1000	57227.266	1.61
PNG 003.8−04.3	−71	1200B	30	57227.251	1.38
PNG 003.8−04.3	−71	1200B	1000	57227.252	1.48
PNG 003.9+01.6	−59	1200B	30	57228.239	1.44
PNG 003.9+01.6	−59	600RI	30	57228.252	1.56
PNG 003.9+01.6	−59	600RI	1000	57228.253	1.71
PNG 003.9+01.6	−59	1200B	1000	57228.239	1.55
PNG 003.9−02.3	−138	600RI	1000	57229.239	1.46
PNG 003.9−02.3	−138	600RI	30	57229.238	1.37
PNG 003.9−02.3	−138	1200B	1000	57229.226	1.36
PNG 003.9−03.1	−35	1200B	897	57239.109	1.03
PNG 003.9−03.1	−35	1200B	1000	57245.212	1.60
PNG 003.9−03.1	−35	600RI	1000	57245.225	1.75
PNG 004.0−03.0	−176	600RI	15	57242.068	1.00
PNG 004.0−03.0	−176	1200B	30	57242.038	1.02
PNG 004.0−03.0	−176	1200B	1000	57242.040	1.01
PNG 004.0−03.0	−176	600RI	30	57242.053	1.01
PNG 004.0−03.0	−176	600RI	1000	57242.054	1.00
PNG 004.1−03.8	−6	1200B	30	57242.113	1.02
PNG 004.1−03.8	−6	600RI	1000	57242.127	1.07
PNG 004.1−03.8	−6	1200B	1000	57242.114	1.04
PNG 004.1−03.8	−6	600RI	30	57242.126	1.05

Continued on next page:

PN	Position Angle	Grism	T$_{EXP}$	Modified Julian Date	Airmass
PNG 004.2−03.2	−51	600RI	20	57252.216	1.73
PNG 004.2−03.2	−51	600RI	1000	57250.188	1.49
PNG 004.2−03.2	−51	1200B	20	57252.215	1.72
PNG 004.2−03.2	−51	1200B	1000	57250.175	1.38
PNG 004.2−03.2	−51	1200B	1000	57252.189	1.55
PNG 004.2−03.2	−51	600RI	1000	57252.202	1.69
PNG 004.2−04.3	−114	600RI	30	57242.160	1.12
PNG 004.2−04.3	−114	1200B	1000	57242.147	1.12
PNG 004.2−04.3	−114	600RI	1000	57242.161	1.17
PNG 004.2−05.9	−40	1200B	1000	57216.138	1.00
PNG 004.2−05.9	−40	600RI	1000	57216.151	1.00
PNG 004.3+01.8	−36	1200B	1000	57223.223	1.31
PNG 004.3+01.8	−36	600RI	1000	57223.237	1.40
PNG 004.3+01.8	−36	600RI	30	57223.236	1.32
PNG 004.6+06.0	−71	600RI	1000	57224.147	1.06
PNG 004.6+06.0	−71	1200B	1000	57224.133	1.04
PNG 004.6+06.0	−71	600RI	30	57224.146	1.04
PNG 004.8+02.0	−35	1200B	1000	57224.168	1.09
PNG 004.8+02.0	−35	600RI	30	57224.180	1.09
PNG 004.8+02.0	−35	600RI	1000	57224.181	1.13
PNG 004.8−05.0	0	600RI	30	57224.213	1.13
PNG 004.8−05.0	0	1200B	1000	57224.200	1.12
PNG 004.8−05.0	0	600RI	1000	57224.214	1.17
PNG 005.0−03.9	−70	600RI	30	58310.190	1.02
PNG 005.0−03.9	−70	1200B	30	58310.176	1.01
PNG 005.0−03.9	−70	1200B	1000	58310.177	1.02
PNG 005.0−03.9	−70	600RI	1000	58310.191	1.04
PNG 005.2+05.6	−166	1200B	1000	57224.234	1.49
PNG 005.2+05.6	−166	600RI	30	57224.247	1.51
PNG 005.2+05.6	−166	600RI	1000	57224.248	1.64
PNG 005.5+06.1	−31	600RI	1000	57228.116	1.03
PNG 005.5+06.1	−31	1200B	1000	57228.104	1.01
PNG 005.5−04.0	−90	600RI	1000	58303.023	1.40

Continued on next page:

PN	Position Angle	Grism	T_{EXP}	Modified Julian Date	Airmass
PNG 005.5−04.0	−90	1200B	30	58303.008	1.65
PNG 005.5−04.0	−90	1200B	1000	58303.009	1.52
PNG 005.5−04.0	−90	600RI	30	58303.022	1.51
PNG 005.8−06.1	−63	1200B	1000	57927.364	1.70
PNG 005.8−06.1	−63	1200B	10	57927.390	1.92
PNG 005.8−06.1	−63	600RI	1000	57927.378	1.90
PNG 005.8−06.1	−63	1200B	30	57593.290	1.70
PNG 005.8−06.1	−63	600RI	30	57593.304	1.90
PNG 005.8−06.1	−63	1200B	1000	57593.291	1.88
PNG 005.8−06.1	−63	600RI	1000	57593.305	2.13
PNG 005.8−06.1	−63	600RI	30	57927.377	1.72
PNG 005.8−06.1	−63	1200B	30	57927.363	1.56
PNG 005.9−02.6	−63	600RI	1000	57228.152	1.04
PNG 005.9−02.6	−63	1200B	1000	57228.138	1.02
PNG 005.9−02.6	−63	1200B	30	57228.137	1.01
PNG 005.9−02.6	−63	600RI	30	57228.151	1.02
PNG 006.1+08.3	−90	1200B	30	57228.173	1.16
PNG 006.1+08.3	−90	600RI	1000	57228.187	1.28
PNG 006.1+08.3	−90	600RI	30	57228.186	1.21
PNG 006.1+08.3	−90	1200B	1000	57228.174	1.21
PNG 006.3+03.3	−32	600RI	1000	57228.220	1.40
PNG 006.3+03.3	−32	1200B	1000	57228.207	1.31
PNG 006.3+04.4	−116	600RI	1000	57245.182	1.50
PNG 006.3+04.4	−116	1200B	1000	57245.169	1.39
PNG 006.4+02.0	−3	600RI	26	57250.122	1.12
PNG 006.4+02.0	−3	1200B	30	57250.109	1.08
PNG 006.4+02.0	−3	1200B	30	57252.123	1.14
PNG 006.4+02.0	−3	1200B	1000	57252.124	1.19
PNG 006.4+02.0	−3	600RI	1000	57252.137	1.26
PNG 006.4+02.0	−3	600RI	26	57252.136	1.20
PNG 006.4+02.0	−3	600RI	1000	57250.123	1.17
PNG 006.4+02.0	−3	1200B	1000	57250.110	1.12
PNG 006.4−04.6	−75	600RI	30	58303.060	1.26

PN	Position Angle	Grism	T_{EXP}	Modified Julian Date	Airmass
PNG 006.4−04.6	−75	600RI	1000	58303.061	1.20
PNG 006.4−04.6	−75	1200B	30	58303.046	1.34
PNG 006.4−04.6	−75	1200B	1000	58303.047	1.27
PNG 006.8+02.3	−69	1200B	1000	57252.155	1.38
PNG 006.8+02.3	−69	1200B	1000	57250.142	1.26
PNG 006.8+02.3	−69	600RI	1000	57250.156	1.34
PNG 006.8+02.3	−69	600RI	1000	57252.169	1.49
PNG 006.8+02.3	−69	1200B	20	57252.182	1.51
PNG 006.8+02.3	−69	600RI	30	57252.168	1.39
PNG 006.8+02.3	−69	600RI	30	57250.155	1.27
PNG 006.8−03.4	−171	1200B	1000	58310.215	1.09
PNG 006.8−03.4	−171	1200B	30	58310.214	1.06
PNG 006.8−03.4	−171	600RI	30	58310.228	1.10
PNG 006.8−03.4	−171	600RI	1000	58310.228	1.14
PNG 007.0+06.3	−39	1200B	20	57252.118	1.17
PNG 007.0+06.3	−39	600RI	1000	57252.103	1.16
PNG 007.0+06.3	−39	1200B	1000	57250.075	1.06
PNG 007.0+06.3	−39	600RI	1000	57250.088	1.09
PNG 007.0+06.3	−39	600RI	30	57250.087	1.06
PNG 007.0+06.3	−39	600RI	30	57252.102	1.11
PNG 007.0+06.3	−39	600RI	20	57250.104	1.10
PNG 007.0+06.3	−39	1200B	1000	57252.089	1.11
PNG 007.0−06.8	−20	600RI	5	58309.145	1.01
PNG 007.0−06.8	−20	600RI	20	58309.130	1.02
PNG 007.0−06.8	−20	1200B	30	58309.115	1.04
PNG 007.0−06.8	−20	600RI	1000	58309.130	1.01
PNG 007.0−06.8	−20	1200B	5	58309.143	1.01
PNG 007.0−06.8	−20	1200B	1000	58309.116	1.02
PNG 007.0−06.8	−20	1200B	20	58309.128	1.02
PNG 007.5+04.3	−119	600RI	1000	58026.075	1.88
PNG 007.5+04.3	−119	1200B	29	58309.194	1.06
PNG 007.5+04.3	−119	1200B	1000	58309.195	1.09
PNG 007.5+04.3	−119	600RI	2	58026.074	1.69

PN	Position Angle	Grism	T_{EXP}	Modified Julian Date	Airmass
PNG 007.5+04.3	−119	600RI	1000	58309.209	1.13
PNG 007.5+04.3	−119	1200B	1000	58026.061	1.68
PNG 007.5+04.3	−119	600RI	2	58309.208	1.10
PNG 007.5+04.3	−119	1200B	29	58026.060	1.53
PNG 007.5+07.4	−90	600RI	1000	57551.190	1.01
PNG 007.5+07.4	−90	600RI	30	57551.188	1.01
PNG 007.5+07.4	−90	1200B	1000	57551.176	1.01
PNG 007.6+06.9	−150	1200B	1000	57952.163	1.09
PNG 007.6+06.9	−150	1200B	30	57952.162	1.06
PNG 007.6+06.9	−150	600RI	1000	57952.177	1.13
PNG 007.6+06.9	−150	600RI	30	57952.176	1.09
PNG 007.8−03.7	−171	1200B	30	57952.216	1.12
PNG 007.8−03.7	−171	1200B	1000	57952.217	1.16
PNG 007.8−03.7	−171	600RI	1000	57952.231	1.22
PNG 007.8−03.7	−171	600RI	30	57952.230	1.17
PNG 007.8−04.4	−111	1200B	1000	57576.270	1.26
PNG 007.8−04.4	−111	1200B	30	57576.269	1.20
PNG 007.8−04.4	−111	600RI	1000	57576.284	1.34
PNG 007.8−04.4	−111	600RI	14	57576.283	1.27
PNG 008.2+06.8	−68	600RI	1000	57963.029	1.03
PNG 008.2+06.8	−68	1200B	30	57963.015	1.08
PNG 008.2+06.8	−68	1200B	1000	57963.016	1.05
PNG 008.2+06.8	−68	600RI	8	57963.028	1.05
PNG 008.4−03.6	−149	1200B	1000	57952.258	1.38
PNG 008.4−03.6	−149	1200B	30	57952.257	1.30
PNG 008.4−03.6	−149	600RI	1000	57952.272	1.50
PNG 008.4−03.6	−149	600RI	30	57952.271	1.39
PNG 008.6−02.6	−162	1200B	1000	57522.187	1.25
PNG 008.6−02.6	−162	600RI	30	57522.228	1.12
PNG 008.6−02.6	−162	1200B	30	57522.214	1.18
PNG 008.6−02.6	−162	1200B	30	57522.186	1.32
PNG 008.6−02.6	−162	600RI	1000	57522.201	1.18
PNG 008.6−02.6	−162	600RI	30	57522.200	1.24

Continued on next page:

PN	Position Angle	Grism	T_{EXP}	Modified Julian Date	Airmass
PNG 008.6−02.6	−162	600RI	1000	57522.229	1.09
PNG 008.6−02.6	−162	1200B	1000	57522.215	1.13
PNG 009.4−09.8	−86	600RI	1000	57550.301	1.06
PNG 009.4−09.8	−86	1200B	1000	57550.287	1.03
PNG 009.4−09.8	−86	600RI	30	57550.300	1.03
PNG 009.4−09.8	−86	1200B	30	57550.286	1.02
PNG 009.8−04.6	−33	1200B	1000	57550.093	1.41
PNG 009.8−04.6	−33	1200B	30	57550.092	1.52
PNG 009.8−04.6	−33	600RI	1000	57550.107	1.31
PNG 009.8−04.6	−33	600RI	30	57550.106	1.40
PNG 350.5−05.0	−48	600RI	1000	57520.218	1.10
PNG 350.5−05.0	−48	1200B	30	57520.204	1.17
PNG 350.5−05.0	−48	1200B	1000	57520.205	1.13
PNG 351.1+04.8	−159	600RI	20	57520.269	1.01
PNG 351.1+04.8	−159	600RI	1000	57520.257	1.01
PNG 351.1+04.8	−159	600RI	30	57520.256	1.01
PNG 351.1+04.8	−159	1200B	1000	57520.243	1.01
PNG 351.1+04.8	−159	1200B	30	57520.242	1.02
PNG 351.2+05.2	−120	1200B	30	57548.027	1.60
PNG 351.2+05.2	−120	1200B	1000	57548.028	1.49
PNG 351.2+05.2	−120	600RI	1000	57548.041	1.38
PNG 351.2+05.2	−120	600RI	30	57548.040	1.47
PNG 351.6−06.2	−47	1200B	1000	57543.261	1.05
PNG 351.6−06.2	−47	1200B	30	57543.261	1.04
PNG 351.6−06.2	−47	600RI	1000	57543.275	1.07
PNG 351.6−06.2	−47	600RI	30	57543.274	1.05
PNG 351.9+09.0	−54	600RI	30	57550.030	1.46
PNG 351.9+09.0	−54	600RI	1000	57550.031	1.36
PNG 351.9+09.0	−54	1200B	30	57550.015	1.59
PNG 351.9+09.0	−54	1200B	1000	57550.017	1.47
PNG 351.9−01.9	−15	1200B	1000	57575.113	1.02
PNG 351.9−01.9	−15	600RI	30	57575.126	1.02
PNG 351.9−01.9	−15	1200B	30	57575.112	1.03

PN	Position Angle	Grism	T$_{EXP}$	Modified Julian Date	Airmass
PNG 351.9−01.9	−15	600RI	1000	57575.127	1.02
PNG 352.0−04.6	−155	1200B	30	57571.302	1.45
PNG 352.0−04.6	−155	600RI	30	57571.316	1.56
PNG 352.0−04.6	−155	1200B	1000	57571.303	1.55
PNG 352.0−04.6	−155	600RI	1000	57571.317	1.68
PNG 352.1+05.1	−131	600RI	1000	57575.294	1.94
PNG 352.1+05.1	−131	1200B	30	57575.280	1.60
PNG 352.1+05.1	−131	1200B	1000	57575.281	1.74
PNG 352.1+05.1	−131	600RI	30	57575.293	1.76
PNG 352.6+03.0	−76	600RI	1000	57576.066	1.04
PNG 352.6+03.0	−76	600RI	30	57576.066	1.06
PNG 352.6+03.0	−76	1200B	1000	57576.053	1.06
PNG 352.6+03.0	−76	1200B	30	57576.052	1.09
PNG 353.2−05.2	−46	1200B	30	57577.989	1.49
PNG 353.2−05.2	−46	1200B	1000	57577.990	1.40
PNG 353.2−05.2	−46	600RI	1000	57578.003	1.32
PNG 353.3+06.3	−33	600RI	1000	57957.185	1.31
PNG 353.3+06.3	−33	600RI	10	57957.197	1.31
PNG 353.3+06.3	−33	1200B	1000	57957.172	1.24
PNG 353.3+06.3	−33	1200B	30	57957.170	1.18
PNG 353.3+06.3	−33	600RI	25	57957.184	1.24
PNG 353.7+06.3	−90	600RI	1000	57579.995	1.18
PNG 353.7+06.3	−90	1200B	30	57579.980	1.30
PNG 353.7+06.3	−90	1200B	1000	57579.981	1.24
PNG 353.7+06.3	−90	600RI	30	57579.994	1.23
PNG 354.5+03.3	−102	600RI	1000	57583.260	1.65
PNG 354.5+03.3	−102	600RI	16	57583.259	1.52
PNG 354.5+03.3	−102	1200B	1000	57583.247	1.51
PNG 354.5+03.3	−102	1200B	30	57583.246	1.41
PNG 354.9+03.5	−8	1200B	30	57608.011	1.02
PNG 354.9+03.5	−8	600RI	1000	57608.025	1.01
PNG 354.9+03.5	−8	1200B	1000	57608.012	1.01
PNG 355.1−06.9	−25	1200B	1000	57583.283	1.55

PN	Position Angle	Grism	T_{EXP}	Modified Julian Date	Airmass
PNG 355.1−06.9	−25	1200B	9	57583.282	1.45
PNG 355.1−06.9	−25	600RI	5	57583.295	1.56
PNG 355.1−06.9	−25	600RI	1000	57583.296	1.69
PNG 355.4−02.4	−154	1200B	1000	57643.101	1.50
PNG 355.4−02.4	−154	600RI	30	57643.113	1.52
PNG 355.4−02.4	−154	600RI	1000	57643.114	1.64
PNG 355.4−02.4	−154	1200B	30	57643.100	1.41
PNG 355.6−02.7	−90	1200B	30	57958.011	1.14
PNG 355.6−02.7	−90	600RI	1000	57958.026	1.07
PNG 355.6−02.7	−90	1200B	1000	57958.012	1.10
PNG 355.6−02.7	−90	600RI	30	57958.025	1.10
PNG 355.9+03.6	−77	600RI	2	57958.071	1.01
PNG 355.9+03.6	−77	600RI	1000	57958.072	1.00
PNG 355.9+03.6	−77	1200B	25	57958.058	1.01
PNG 355.9+03.6	−77	1200B	1000	57958.059	1.01
PNG 355.9−04.2	−106	1200B	30	58284.118	1.16
PNG 355.9−04.2	−106	600RI	30	57958.107	1.02
PNG 355.9−04.2	−106	1200B	30	57958.093	1.02
PNG 355.9−04.2	−106	600RI	30	58284.132	1.11
PNG 355.9−04.2	−106	600RI	1000	58284.133	1.08
PNG 355.9−04.2	−106	600RI	1000	57958.108	1.02
PNG 355.9−04.2	−106	1200B	1000	57958.094	1.02
PNG 355.9−04.2	−106	1200B	1000	58284.119	1.12
PNG 356.1−03.3	−138	600RI	30	57963.073	1.02
PNG 356.1−03.3	−138	1200B	1000	57963.060	1.02
PNG 356.1−03.3	−138	600RI	1000	57963.074	1.01
PNG 356.1−03.3	−138	1200B	30	57963.059	1.02
PNG 356.3−06.2	−153	1200B	30	57965.054	1.04
PNG 356.3−06.2	−153	600RI	1000	57965.069	1.02
PNG 356.3−06.2	−153	1200B	1000	57965.055	1.02
PNG 356.3−06.2	−153	600RI	30	57965.068	1.02
PNG 356.5−03.6	−57	600RI	30	57965.107	1.02
PNG 356.5−03.6	−57	600RI	1000	57965.108	1.03

Continued on next page:

PN	Position Angle	Grism	T$_{EXP}$	Modified Julian Date	Airmass
PNG 356.5−03.6	−57	1200B	30	57965.094	1.01
PNG 356.5−03.6	−57	1200B	1000	57965.095	1.02
PNG 356.8+03.3	−28	1200B	1000	58285.152	1.01
PNG 356.8+03.3	−28	600RI	1000	58285.167	1.00
PNG 356.8+03.3	−28	600RI	30	58285.166	1.01
PNG 356.8+03.3	−28	1200B	30	58285.151	1.02
PNG 356.8−05.4	−80	600RI	30	57965.236	1.46
PNG 356.8−05.4	−80	1200B	30	57965.222	1.36
PNG 356.8−05.4	−80	1200B	1000	57965.223	1.45
PNG 356.8−05.4	−80	600RI	1000	57965.237	1.57
PNG 356.9+04.4	−45	1200B	26	58287.182	1.00
PNG 356.9+04.4	−45	1200B	1000	58287.183	1.01
PNG 356.9+04.4	−45	600RI	1000	58287.197	1.02
PNG 356.9+04.4	−45	600RI	13	58287.196	1.01
PNG 357.0+02.4	−50	1200B	30	57966.112	1.04
PNG 357.0+02.4	−50	600RI	1000	57966.126	1.10
PNG 357.0+02.4	−50	600RI	30	57966.125	1.07
PNG 357.0+02.4	−50	1200B	1000	57966.113	1.06
PNG 357.1+03.6	−40	1200B	30	58247.326	1.02
PNG 357.1+03.6	−40	600RI	1000	58247.341	1.07
PNG 357.1+03.6	−40	1200B	1000	58247.327	1.04
PNG 357.1+03.6	−40	600RI	30	58247.340	1.04
PNG 357.1+04.4	0	600RI	30	58247.383	1.16
PNG 357.1+04.4	0	1200B	1000	58247.371	1.16
PNG 357.1+04.4	0	1200B	30	58247.370	1.12
PNG 357.1+04.4	0	600RI	1000	58247.385	1.21
PNG 357.1−04.7	−164	1200B	30	58007.065	1.16
PNG 357.1−04.7	−164	600RI	1000	58007.079	1.27
PNG 357.1−04.7	−164	600RI	15	58007.079	1.21
PNG 357.1−04.7	−164	1200B	1000	58007.066	1.21
PNG 357.2+02.0	−90	600RI	30	57567.283	1.31
PNG 357.2+02.0	−90	1200B	30	57567.270	1.24
PNG 357.2+02.0	−90	600RI	1000	57567.284	1.39

PN	Position Angle	Grism	T$_{EXP}$	Modified Julian Date	Airmass
PNG 357.2+02.0	−90	1200B	1000	57567.270	1.30
PNG 357.3+04.0	−68	1200B	30	57522.147	1.33
PNG 357.3+04.0	−68	600RI	30	58249.330	1.04
PNG 357.3+04.0	−68	600RI	1000	58249.331	1.06
PNG 357.3+04.0	−68	1200B	1000	57522.148	1.26
PNG 357.3+04.0	−68	1200B	1000	58249.318	1.03
PNG 357.3+04.0	−68	1200B	30	58249.317	1.02
PNG 357.3+04.0	−68	600RI	1000	57522.161	1.19
PNG 357.3+04.0	−68	600RI	30	57522.161	1.25
PNG 357.5+03.1	−70	1200B	1000	57545.073	1.35
PNG 357.5+03.1	−70	600RI	30	57545.085	1.34
PNG 357.5+03.1	−70	600RI	1000	57545.086	1.26
PNG 357.5+03.1	−70	1200B	30	57545.072	1.44
PNG 357.5+03.2	−26	600RI	30	57550.065	1.38
PNG 357.5+03.2	−26	1200B	1000	57550.053	1.39
PNG 357.5+03.2	−26	1200B	30	57550.052	1.49
PNG 357.5+03.2	−26	600RI	1000	57550.066	1.30
PNG 357.6−03.3	−32	600RI	1000	57550.262	1.06
PNG 357.6−03.3	−32	1200B	30	57550.249	1.02
PNG 357.6−03.3	−32	1200B	1000	57550.250	1.04
PNG 357.9−03.8	−65	600RI	30	57567.320	1.44
PNG 357.9−03.8	−65	600RI	1000	57567.320	1.55
PNG 357.9−03.8	−65	1200B	1000	57567.307	1.43
PNG 357.9−03.8	−65	1200B	30	57567.306	1.34
PNG 357.9−05.1	−35	1200B	1000	57554.286	1.13
PNG 357.9−05.1	−35	600RI	1000	57554.299	1.17
PNG 357.9−05.1	−35	1200B	30	57554.285	1.09
PNG 358.0+09.3	−16	600RI	30	57571.279	1.51
PNG 358.0+09.3	−16	600RI	1000	57571.280	1.64
PNG 358.0+09.3	−16	1200B	1000	57571.266	1.50
PNG 358.0+09.3	−16	1200B	30	57571.265	1.40
PNG 358.2+03.5	−69	600RI	1000	57575.162	1.03
PNG 358.2+03.5	−69	1200B	30	57575.147	1.00

PN	Position Angle	Grism	T$_{\text{EXP}}$	Modified Julian Date	Airmass
PNG 358.2+03.5	−69	1200B	1000	57575.148	1.01
PNG 358.2+03.5	−69	600RI	30	57575.161	1.01
PNG 358.2+04.2	−150	1200B	1000	57575.240	1.28
PNG 358.2+04.2	−150	600RI	30	57575.253	1.29
PNG 358.2+04.2	−150	1200B	30	57575.239	1.22
PNG 358.2+04.2	−150	600RI	1000	57575.254	1.37
PNG 358.5+02.9	−120	600RI	30	57576.028	1.20
PNG 358.5+02.9	−120	600RI	1000	57576.029	1.15
PNG 358.5+02.9	−120	1200B	30	57576.014	1.27
PNG 358.5+02.9	−120	1200B	1000	57576.015	1.21
PNG 358.5−04.2	−157	1200B	20	57576.088	1.08
PNG 358.5−04.2	−157	600RI	4	57576.102	1.05
PNG 358.5−04.2	−157	1200B	1000	57576.089	1.05
PNG 358.5−04.2	−157	600RI	1000	57576.102	1.03
PNG 358.6+07.8	−127	600RI	1000	57578.076	1.01
PNG 358.6+07.8	−127	600RI	30	57578.075	1.03
PNG 358.6+07.8	−127	1200B	1000	57578.062	1.03
PNG 358.6+07.8	−127	1200B	30	57578.062	1.05
PNG 358.6−05.5	−10	1200B	1000	57578.267	1.32
PNG 358.6−05.5	−10	1200B	30	57578.266	1.25
PNG 358.6−05.5	−10	600RI	1000	57578.280	1.41
PNG 358.6−05.5	−10	600RI	30	57578.279	1.33
PNG 358.7+05.2	−175	600RI	30	57580.030	1.13
PNG 358.7+05.2	−175	1200B	1000	57580.017	1.14
PNG 358.7+05.2	−175	1200B	30	57580.016	1.18
PNG 358.7+05.2	−175	600RI	1000	57580.031	1.09
PNG 358.8+03.0	−16	600RI	1000	57597.243	1.84
PNG 358.8+03.0	−16	1200B	30	57597.229	1.54
PNG 358.8+03.0	−16	1200B	1000	57597.230	1.67
PNG 358.9+03.4	−73	600RI	30	57608.125	1.11
PNG 358.9+03.4	−73	1200B	30	57608.111	1.08
PNG 358.9+03.4	−73	1200B	1000	58279.233	1.02
PNG 358.9+03.4	−73	600RI	1000	57608.126	1.16

PN	Position Angle	Grism	T_{EXP}	Modified Julian Date	Airmass
PNG 358.9+03.4	−73	1200B	30	58279.232	1.01
PNG 358.9+03.4	−73	600RI	1000	58279.246	1.04
PNG 358.9+03.4	−73	600RI	30	58279.245	1.03
PNG 358.9+03.4	−73	1200B	1000	57608.112	1.11
PNG 359.0−04.1	−40	1200B	1000	57608.208	1.52
PNG 359.0−04.1	−40	1200B	30	57608.208	1.42
PNG 359.0−04.1	−40	600RI	1000	57608.221	1.66
PNG 359.1−02.9	−63	600RI	1000	57658.090	1.77
PNG 359.1−02.9	−63	1200B	30	57658.076	1.49
PNG 359.1−02.9	−63	1200B	1000	57658.077	1.61
PNG 359.2+04.7	−88	1200B	1000	57643.007	1.09
PNG 359.2+04.7	−88	1200B	30	57643.006	1.06
PNG 359.2+04.7	−88	600RI	30	57643.019	1.09
PNG 359.2+04.7	−88	600RI	1000	57643.020	1.13
PNG 359.3−01.8	−54	600RI	30	58279.285	1.07
PNG 359.3−01.8	−54	1200B	30	58279.271	1.04
PNG 359.3−01.8	−54	600RI	1000	58279.286	1.10
PNG 359.3−01.8	−54	1200B	1000	58279.272	1.07
PNG 359.6−04.8	−153	1200B	30	58247.250	1.08
PNG 359.6−04.8	−153	600RI	1000	58247.265	1.04
PNG 359.6−04.8	−153	1200B	1000	58247.251	1.06
PNG 359.6−04.8	−153	600RI	30	58247.264	1.06
PNG 359.7−01.8	−129	600RI	1000	58279.335	1.30
PNG 359.7−01.8	−129	1200B	1000	58279.321	1.23
PNG 359.7−01.8	−129	1200B	30	58279.320	1.17
PNG 359.7−01.8	−129	600RI	30	58279.334	1.23
PNG 359.8+02.4	−9	1200B	156	58281.039	1.66
PNG 359.8+02.4	−9	1200B	1000	58281.048	1.47
PNG 359.8+02.4	−9	1200B	30	58281.047	1.58
PNG 359.8+02.4	−9	1200B	30	58281.038	1.69
PNG 359.8+02.4	−9	600RI	30	58281.061	1.45
PNG 359.8+02.4	−9	600RI	1000	58281.062	1.36
PNG 359.8+03.7	−27	600RI	30	58285.250	1.06
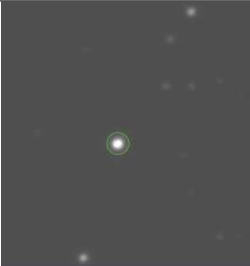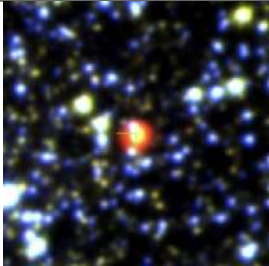
PN	Position Angle	Grism	T_{EXP}	Modified Julian Date	Airmass
PNG 359.8+03.7	−27	1200B	30	58285.236	1.03
PNG 359.8+03.7	−27	600RI	1000	58285.251	1.09
PNG 359.8+03.7	−27	1200B	1000	58285.237	1.05
PNG 359.8+05.2	−68	600RI	30	58286.293	1.22
PNG 359.8+05.2	−68	600RI	1000	58286.294	1.28
PNG 359.8+05.2	−68	1200B	30	58286.279	1.16
PNG 359.8+05.2	−68	1200B	1000	58286.280	1.21
PNG 359.8+05.6	−68	1200B	1000	58287.217	1.04
PNG 359.8+05.6	−68	600RI	30	58287.230	1.04
PNG 359.8+05.6	−68	1200B	30	58310.138	1.01
PNG 359.8+05.6	−68	600RI	5	58310.166	1.04
PNG 359.8+05.6	−68	600RI	1000	58287.231	1.06
PNG 359.8+05.6	−68	600RI	30	58310.152	1.02
PNG 359.8+05.6	−68	1200B	30	58287.217	1.02
PNG 359.8+05.6	−68	1200B	1000	58310.139	1.02
PNG 359.8+05.6	−68	600RI	1000	58310.153	1.03
PNG 359.8+06.9	−156	600RI	30	58309.170	1.05
PNG 359.8+06.9	−156	1200B	30	58309.156	1.02
PNG 359.8+06.9	−156	1200B	1000	58309.157	1.04
PNG 359.8+06.9	−156	600RI	1000	58309.171	1.07
PNG 359.8−07.2	−124	1200B	1000	58247.290	1.02
PNG 359.8−07.2	−124	1200B	30	58247.289	1.03
PNG 359.8−07.2	−124	600RI	30	58247.302	1.02
PNG 359.8−07.2	−124	600RI	1000	58247.303	1.01
PNG 359.9−04.5	−56	600RI	1000	58279.373	1.52
PNG 359.9−04.5	−56	1200B	30	58279.359	1.33
PNG 359.9−04.5	−56	600RI	30	58279.373	1.42
PNG 359.9−04.5	−56	1200B	1000	58279.360	1.41

Appendix C
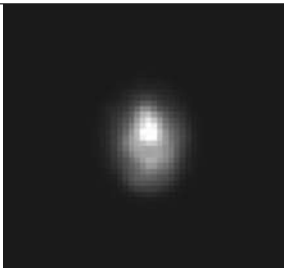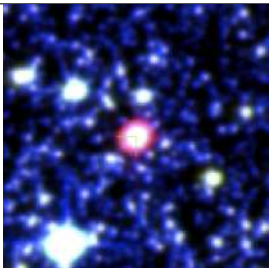
Individual Objects

Note: The VLT images are cut as the best to show the PN morphologies in the telescope coordinate system.
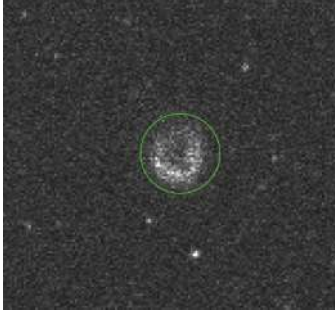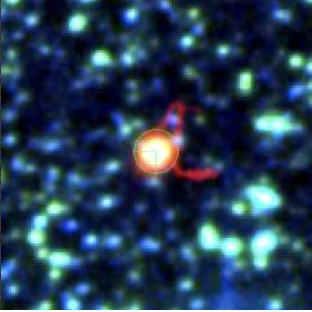
C.1 PN G 001.3-01.2

Catalogue	ESO-VLT	HASH
Image		
Centroid Coord.	17:53:47.7 -28:27:10.3	17:53:47.2 -28:27:18.0
Morph.	E	Em
Central Star Coord.	N/A	N/A
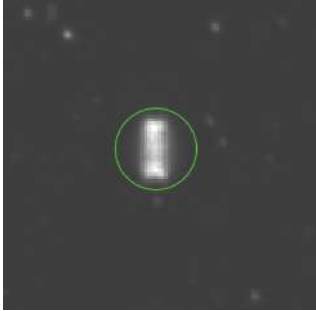
C.2 PN G 002.0-06.2

Catalogue	ESO-VLT	HASH
Image		
Centroid Coord.	18:15:07.2 -30:15:26.5	18:15:06.5 -30:15:32.90
Morph.	Es	Em
Central Star Coord.	N/A	N/A
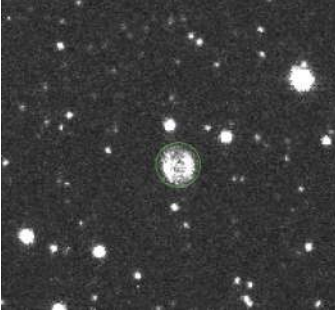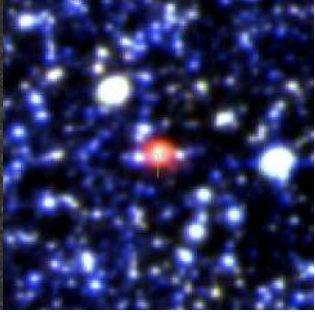
C.3   PN G 002.3+02.2

Catalogue	ESO-VLT	HASH
Image		
Centroid Coord.	17:42:30.6 -25:45:19.1	17:42:30.0 -25:45:27.07
Morph.	Rars	Ear
Central Star Coord.	N/A	N/A
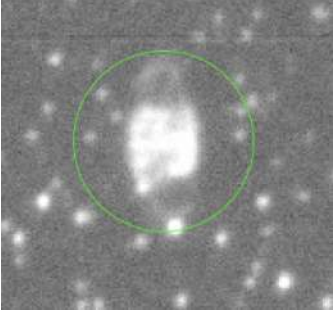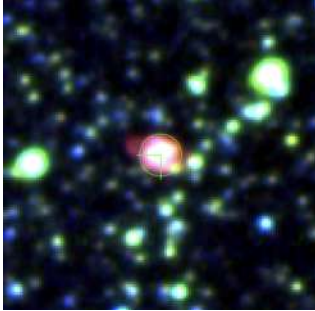
C.4   PN G 002.3-03.4

Catalogue	ESO-VLT	HASH
Image		
Centroid Coord.	18:04:28.3 -28:37:26.3	18:04:28.8 -28:37:38.28
Morph.	Bps	Bmprs
Central Star Coord.	N/A	N/A
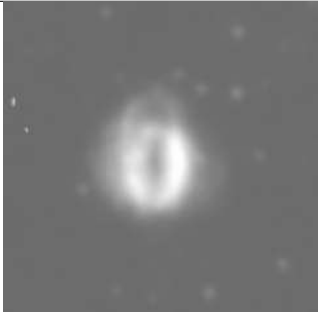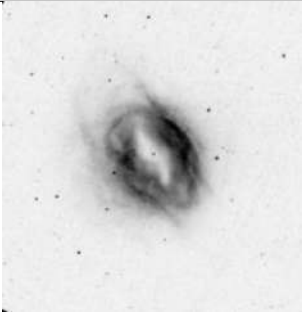
C.5   PN G 002.5-01.7

Catalogue	ESO-VLT	HASH
Image		
Centroid Coord.	17:58:31.1 -27:36:55.0	17:58:31.2 -27:37:05.38
Morph.	Rps	Rps
Central Star Coord.	N/A	N/A
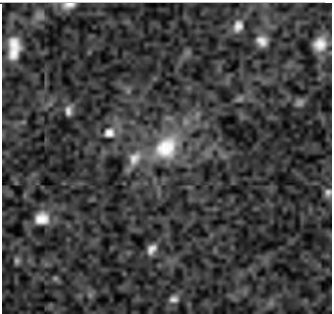
C.6   PN G 002.6+02.1

Catalogue	ESO-VLT	HASH
Image		
Centroid Coord.	17:43:39.4 -25:36:42.5	17:43:39.4 -25:36:42.52
Morph.	Baps	Bms
Central Star Coord.	N/A	N/A
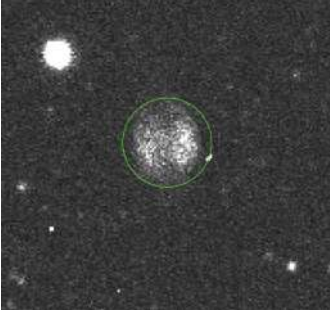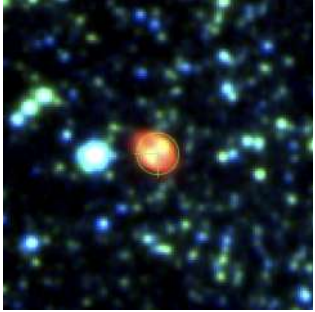
C.7   PN G 002.7-04.8

Catalogue	ESO-VLT	HASH
Image		
Centroid Coord.	18:11:04.2 -28:58:53.0	18:11:05.0 -28:58:59.34
Morph.	Bamprs	Bamprs
Central Star Coord.	N/A	N/A
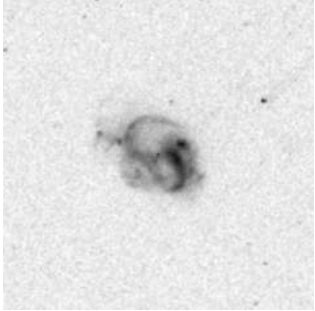
C.8   PN G 002.8+01.7

Catalogue	ESO-VLT	HASH
Image		
Centroid Coord.	17:45:38.9 -25:39:58.7	17:45:39.8 -25:40:00.05
Morph.	E	Bars
Central Star Coord.	N/A	N/A
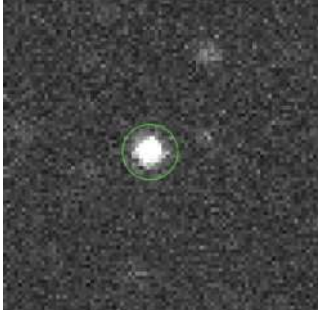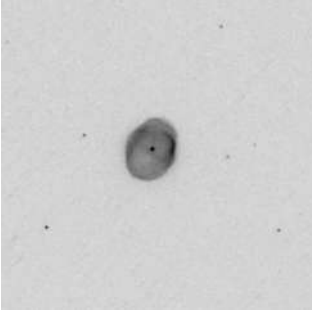
C.9 PN G 002.8+01.8

Catalogue	ESO-VLT	HASH
Image		
Centroid Coord.	17:45:27.7 -25:38:05.1	17:45:28.3 -25:38:12.48
Morph.	Bas	Bs
Central Star Coord.	N/A	N/A
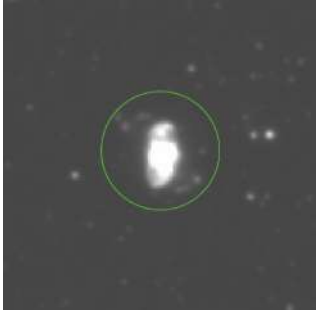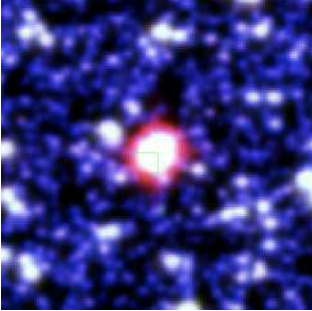
C.10 PN G 002.9-03.9

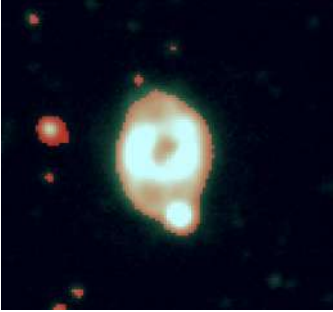| Catalogue	ESO-VLT	HASH
Image		
Centroid Coord.	18:08:04.9 -28:26:09.5	18:08:05.77 -28:26:10.8
Morph.	Baps	Bams
Central Star Coord.	N/A	N/A
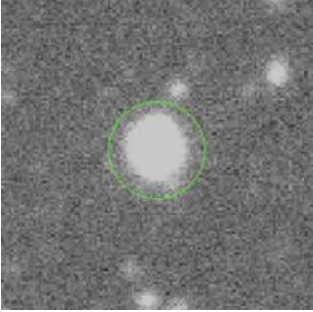
C.11   PN G 003.1+03.4

Catalogue	ESO-VLT	HASH
Image		
Centroid Coord.	17:40:08.1 -24:25:36.4	17:40:07.4 -24:25:42.56
Morph.	Ea	Eamrs
Central Star Coord.	N/A	N/A
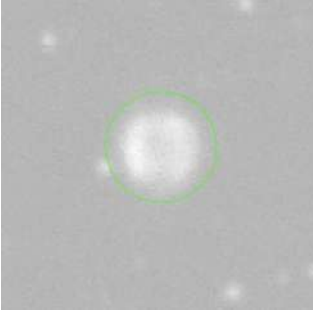
C.12   PN G 003.2-06.2

Catalogue	ESO-VLT	HASH
Image		
Centroid Coord.	18:17:42.0 -29:08:12.4	18:17:41.4 -29:08:19.57
Morph.	Bmps	Bmp
Central Star Coord.	N/A	N/A
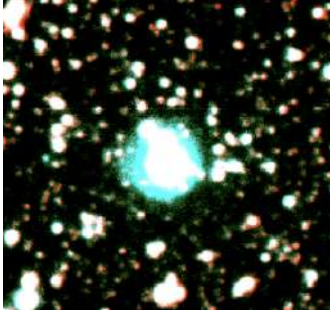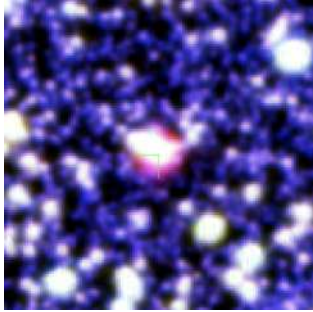
C.13   PN G 003.6+03.1

Catalogue	ESO-VLT	HASH
Image		
Centroid Coord.	17:41:56.4 -24:11:12.4	17:41:57.3 -24:11:15.65
Morph.	E	Baps
Central Star Coord.	N/A	N/A
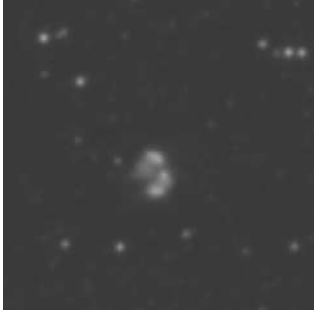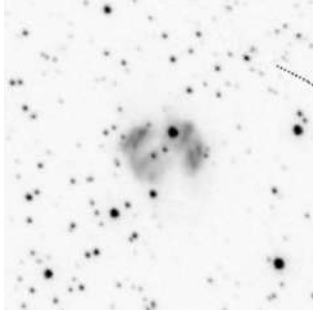
C.14   PN G 003.6-02.3

Catalogue	ESO-VLT	HASH
Image		
Centroid Coord.	18:03:12.4 -26:58:21.4	18:03:11.8 -26:58:30.22
Morph.	Ear	Eaps
Central Star Coord.	N/A	N/A
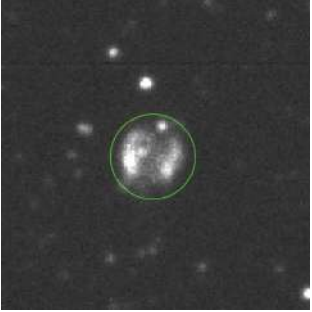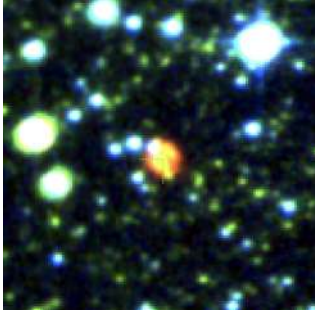
C.15 PN G 003.7-04.6

Catalogue	ESO-VLT	HASH
Image		
Centroid Coord.	18:12:33.7 -27:58:05.9	18:12:34.4 -27:58:10.63
Morph.	Ea	E
Central Star Coord.	N/A	N/A
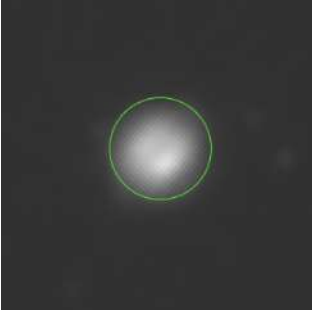
C.16 PN G 003.8-04.3

Catalogue	ESO-VLT	HASH
Image		
Centroid Coord.	18:11:28.9 -27:46:05.8	18:11:29.3 -27:46:15.67
Morph.	Bps	Bps
Central Star Coord.	N/A	N/A
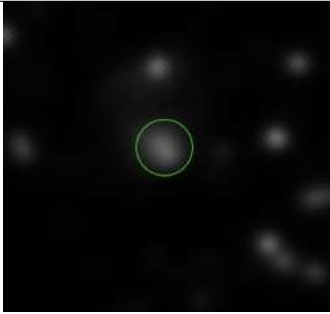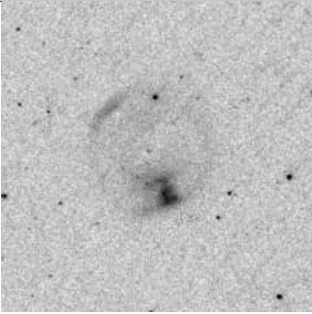
C.17 PN G 003.9+01.6

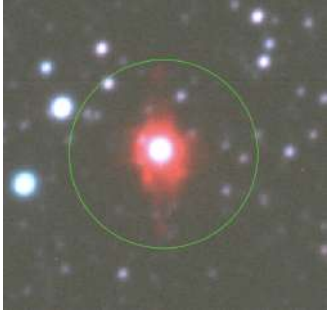| Catalogue	ESO-VLT	HASH
Image		
Centroid Coord.	17:48:27.9 -24:41:14.7	17:48:28.4 -24:41:23.93
Morph.	Eas	Ea
Central Star Coord.	N/A	N/A
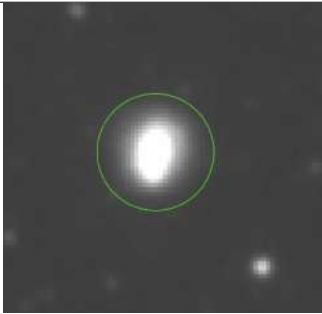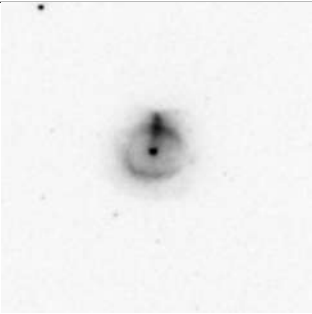
C.18 PN G 003.9-02.3

Catalogue	ESO-VLT	HASH
Image		
Centroid Coord.	18:03:39.8 -26:43:26.0	18:03:39.31 -26:43:33.7
Morph.	Ea	E
Central Star Coord.	N/A	N/A
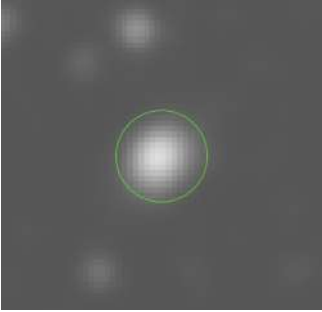
C.19 PN G 003.9-03.1

Catalogue	ESO-VLT	HASH
Image		
Centroid Coord.	18:06:49.1 -27:06:14.8	18:06:50.0 -27:06:19.51
Morph.	E	Ears
Central Star Coord.	N/A	N/A
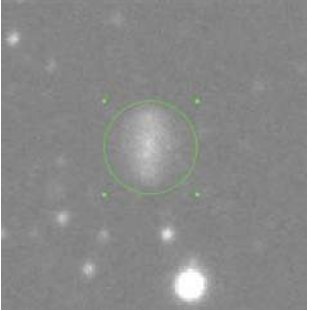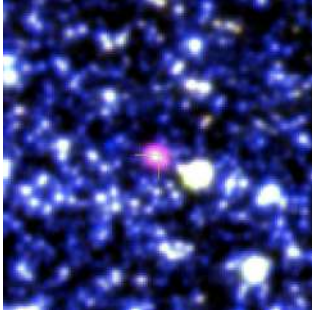
C.20 PN G 004.0-03.0

Catalogue	ESO-VLT	HASH
Image		
Centroid Coord.	18:06:41.8 -26:54:53.8	18:06:40.9 -26:54:55.94
Morph.	E	Eamr
Central Star Coord.	N/A	N/A
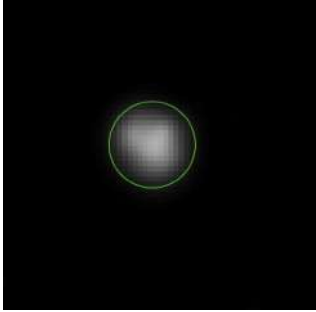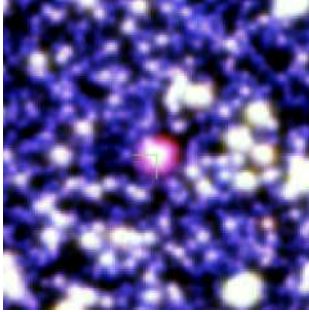
C.21   PN G 004.1-03.8

Catalogue	ESO-VLT	HASH
Image		
Centroid Coord.	18:10:11.3 -27:16:35.4	18:10:12.2 -27:16:35.00
Morph.	E	Bm
Central Star Coord.	N/A	N/A
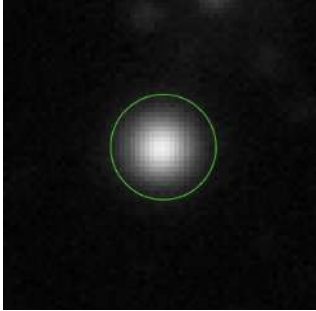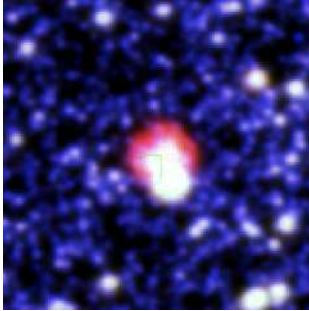
C.22   PN G 004.2-03.2

Catalogue	ESO-VLT	HASH
Image		
Centroid Coord.	18:08:00.7 -26:53:54.8	18:08:01.3 -26:54:01.51
Morph.	Bs	E
Central Star Coord.	N/A	N/A
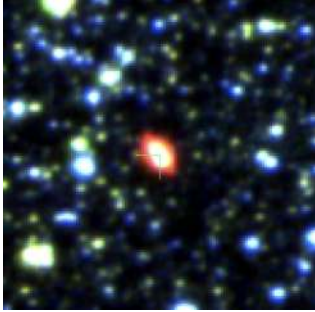
C.23   PN G 004.2-04.3

Catalogue	ESO-VLT	HASH
Image		
Centroid Coord.	18:12:25.3 -27:29:02.6	18:12:25.2 -27:29:12.95
Morph.	Es	E
Central Star Coord.	N/A	N/A
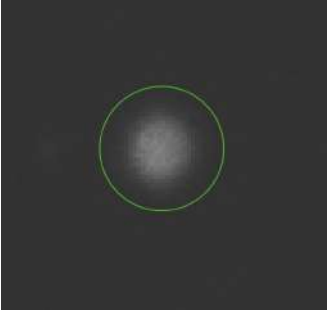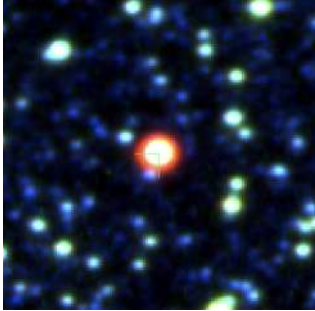
C.24   PN G 004.2-05.9

Catalogue	ESO-VLT	HASH
Image		
Centroid Coord.	18:18:37.6 -28:07:52.6	18:18:38.3 -28:07:58.55
Morph.	E	E
Central Star Coord.	N/A	N/A
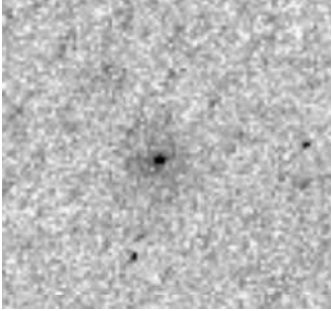
C.25 PN G 004.3+01.8

Catalogue	ESO-VLT	HASH
Image		
Centroid Coord.	17:48:35.8 -24:16:27.3	17:48:36.5 -24:16:34.25
Morph.	Bap	Ba
Central Star Coord.	N/A	N/A
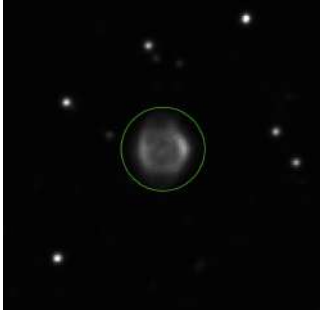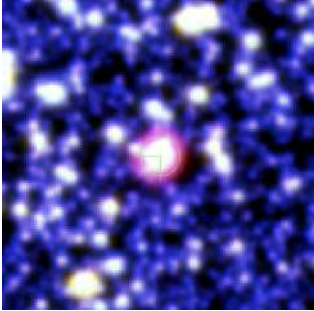
C.26 PN G 004.6+06.0

Catalogue	ESO-VLT	HASH
Image		
Centroid Coord.	17:33:37.2 -21:46:14.9	17:33:37.6 -21:46:24.78
Morph.	E	E
Central Star Coord.	N/A	N/A
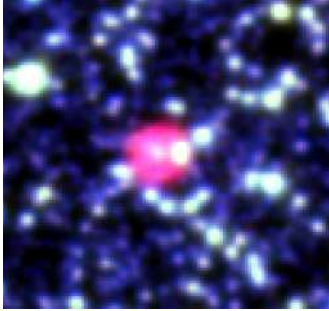
C.27   PN G 004.8+02.0

Catalogue	ESO-VLT	HASH
Image		
Centroid Coord.	17:48:59.8 -23:42:49.1	17:49:00.5 -23:42:54.58
Morph.	E	Eas
Central Star Coord.	N/A	N/A
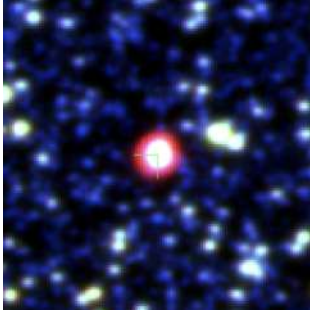
C.28   PN G 004.8-05.0

Catalogue	ESO-VLT	HASH
Image		
Centroid Coord.	18:16:10.5 -27:14:59.4	18:16:11.4 -27:14:57.44
Morph.	Ers	Emr
Central Star Coord.	N/A	N/A
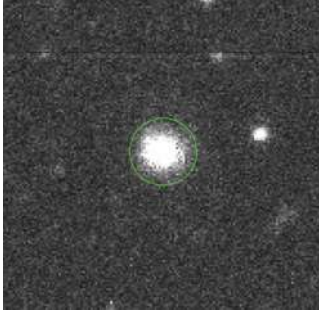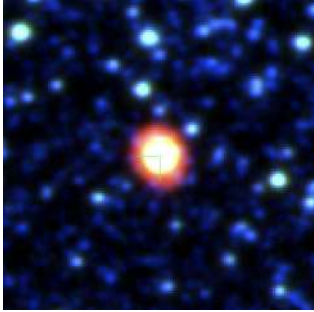
C.29 PN G 005.0-03.9

Catalogue	ESO-VLT	HASH
Image		
Centroid Coord.	18:12:22.6 -26:32:44.7	18:12:23.0 -26:32:54.38
Morph.	Eamrs	Rrs
Central Star Coord.	N/A	N/A
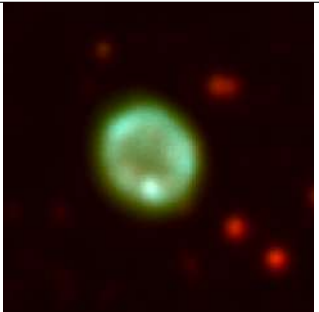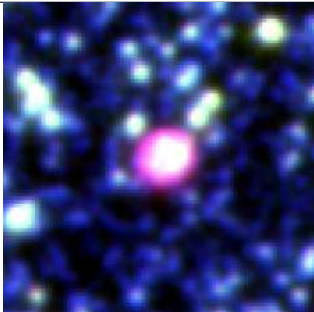
C.30 PN G 005.2+05.6

Catalogue	ESO-VLT	HASH
Image		
Centroid Coord.	17:36:23.4 -21:31:08.0	17:36:22.6 -21:31:12.22
Morph.	Ers	Er
Central Star Coord.	N/A	N/A
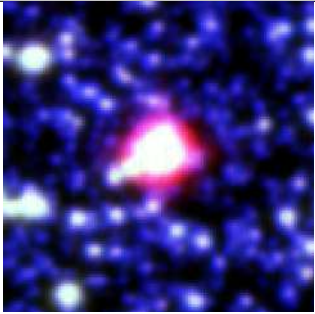
C.31   PN G 005.5+06.1

Catalogue	ESO-VLT	HASH
Image		
Centroid Coord.	17:35:20.6 -20:57:17.4	17:35:21.4 -20:57:23.00
Morph.	E	Bas
Central Star Coord.	N/A	N/A
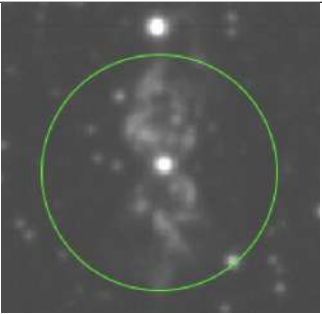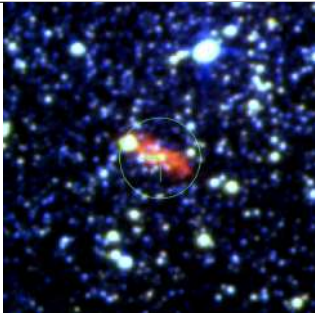
C.32   PN G 005.5-04.0

Catalogue	ESO-VLT	HASH
Image		
Centroid Coord.	18:13:40.5 -26:08:28.4	18:13:40.6 -26:08:38.72
Morph.	Ears	R
Central Star Coord.	N/A	N/A
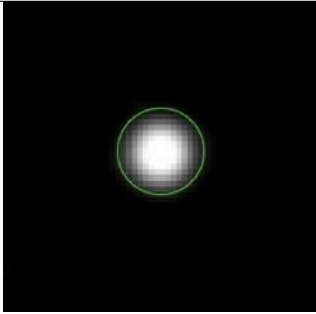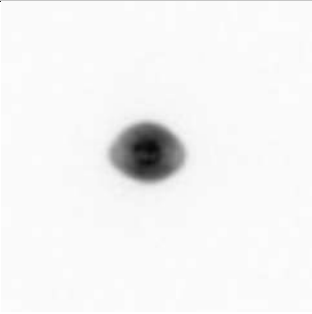
C.33 PN G 005.8-06.1

Catalogue	ESO-VLT	HASH
Image		
Centroid Coord.	18:22:54.1 -26:49:17.1	18:22:54.2 -26:49:17.00
Morph.	Emps	R
Central Star Coord.	N/A	N/A
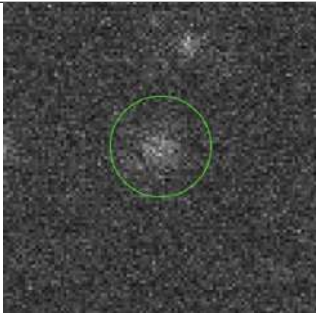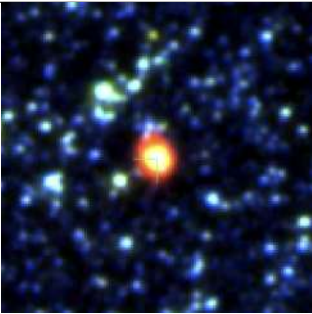
C.34 PN G 005.9-02.6

Catalogue	ESO-VLT	HASH
Image		
Centroid Coord.	18:09:12.4 -25:04:22.1	18:09:12.4 -25:04:34.50
Morph.	Bs	B
Central Star Coord.	N/A	N/A
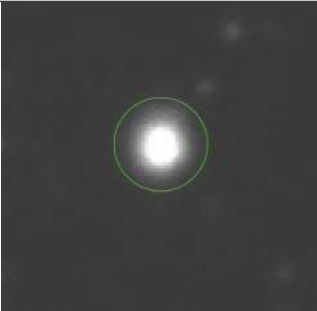
C.35   PN G 006.1+08.3

Catalogue	ESO-VLT	HASH
Image		
Centroid Coord.	17:28:57.5 -19:15:41.7	17:28:57.6 -19:15:53.82
Morph.	E	Ems
Central Star Coord.	N/A	N/A
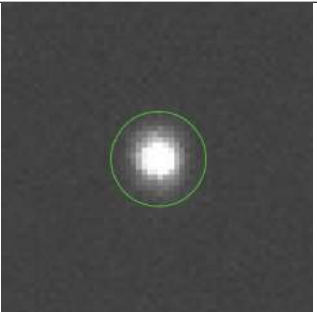
C.36   PN G 006.3+03.3

Catalogue	ESO-VLT	HASH
Image		
Centroid Coord.	17:47:33.2 -21:47:16.9	17:47:33.9 -21:47:23.10
Morph.	E	B
Central Star Coord.	N/A	N/A
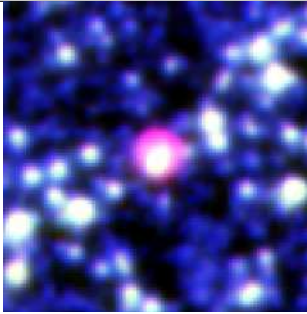
C.37   PN G 006.3+04.4

Catalogue	ESO-VLT	HASH
Image		
Centroid Coord.	17:43:29.1 -21:09:40.1	17:43:28.7 -21:09:51.30
Morph.	E	Bamps
Central Star Coord.	N/A	N/A
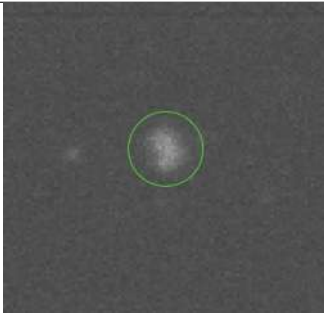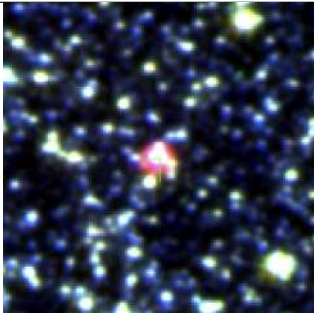
C.38   PN G 006.4+02.0

Catalogue	ESO-VLT	HASH
Image		
Centroid Coord.	17:52:40.5 -22:21:58.2	17:52:41.4 -22:21:56.84
Morph.	E	Bps
Central Star Coord.	N/A	N/A
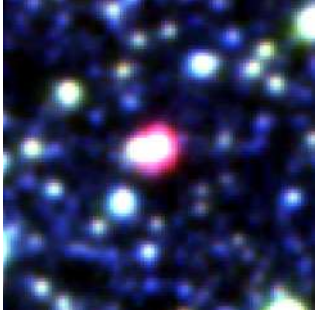
C.39 PN G 006.4-04.6

Catalogue	ESO-VLT	HASH
Image		
Centroid Coord.	18:18:12.9 -25:37:57.7	18:18:13.4 -25:38:08.92
Morph.	Eas	S
Central Star Coord.	N/A	N/A
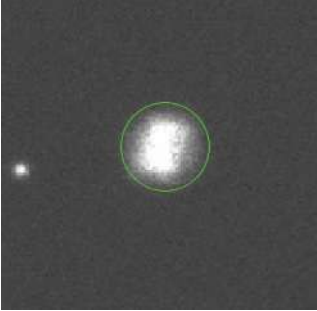
C.40 PN G 006.8+02.3

Catalogue	ESO-VLT	HASH
Image		
Centroid Coord.	17:52:22.2 -21:51:02.3	17:52:22.62 -21:51:13.7
Morph.	Es	B
Central Star Coord.	N/A	N/A
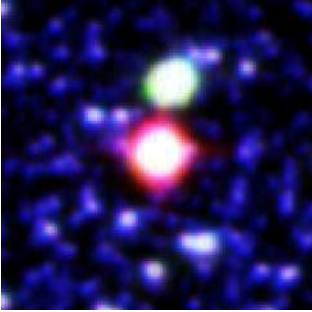
C.41 PN G 006.8-03.4

Catalogue	ESO-VLT	HASH
Image		
Centroid Coord.	18:14:29.6 -24:43:36.4	18:14:28.7 -24:43:37.96
Morph.	Bmps	R
Central Star Coord.	N/A	N/A
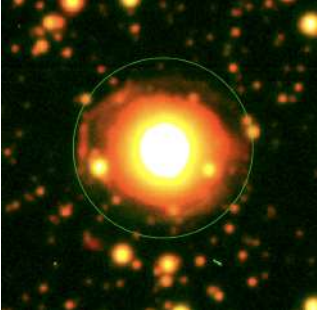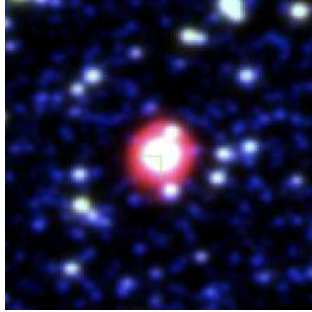
C.42 PN G 007.0+06.3

Catalogue	ESO-VLT	HASH
Image		
Centroid Coord.	17:38:10.8 -19:37:31.6	17:38:11.6 -19:37:37.63
Morph.	Bm	Bm
Central Star Coord.	N/A	N/A
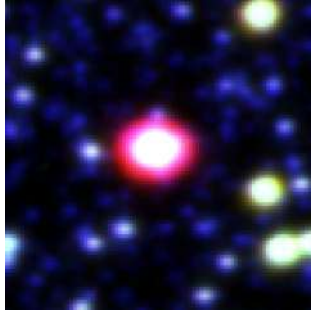
C.43   PN G 007.0-06.8

Catalogue	ESO-VLT	HASH
Image		
Centroid Coord.	18:27:58.7 -26:06:46.0	18:27:59.6 -26:06:48.28
Morph.	Bms	E
Central Star Coord.	N/A	N/A
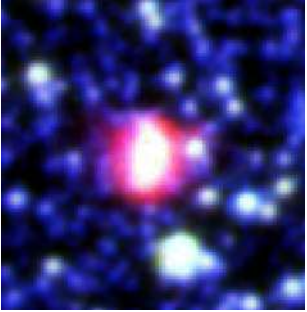
C.44 PN G 007.5+07.4

Catalogue	ESO-VLT	HASH
Image		
Centroid Coord.	17:35:10.2 -18:34:20.4	17:35:10.2 -18:34:20.42
Morph.	Ramr	Rar
Central Star Coord.	N/A	N/A
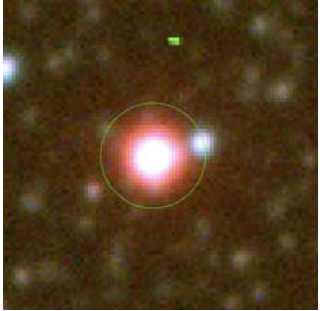
C.45 PN G 007.6+06.9

Catalogue	ESO-VLT	HASH
Image		
Centroid Coord.	17:37:22.6 -18:46:36.7	17:37:22.0 -18:46:41.88
Morph.	Bams	Bams
Central Star Coord.	N/A	N/A
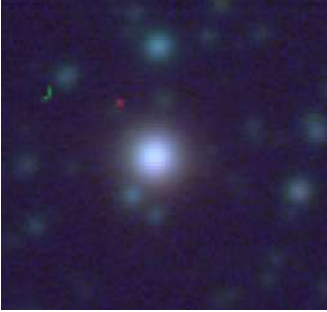
C.46   PN G 007.8-03.7

Catalogue	ESO-VLT	HASH
Image		
Centroid Coord.	18:17:15.9 -23:58:53.6	18:17:15.9 -23:58:54.52
Morph.	Baps	Em
Central Star Coord.	N/A	N/A
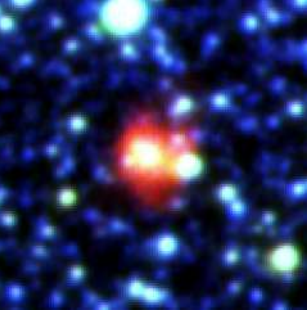
C.47   PN G 007.8-04.4

Catalogue	ESO-VLT	HASH
Image		
Centroid Coord.	18:20:08.8 -24:15:05.0	18:20:08.8 -24:15:05.08
Morph.	E	Eamrs
Central Star Coord.	N/A	N/A
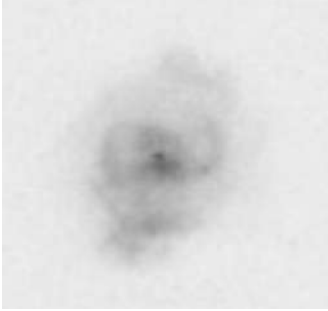
C.48   PN G 008.2+06.8

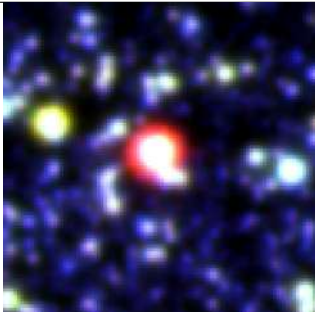| Catalogue	ESO-VLT	HASH
Image		
Centroid Coord.	17:38:56.9 -18:17:25.9	17:38:57.4 -18:17:35.77
Morph.	E	Bs
Central Star Coord.	N/A	N/A
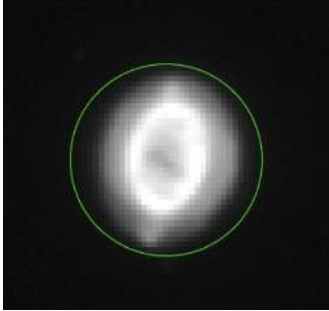
C.49   PN G 008.4-03.6

Catalogue	ESO-VLT	HASH
Image		
Centroid Coord.	18:18:24.7 -23:24:51.0	18:18:23.9 -23:24:57.13
Morph.	Eamps	Eamps
Central Star Coord.	N/A	N/A
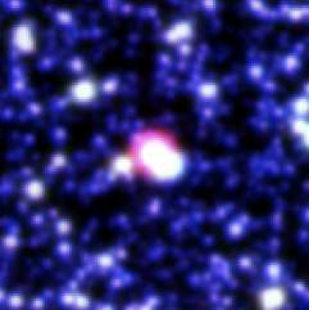
C.50   PN G 008.6-02.6

Catalogue	ESO-VLT	HASH
Image		
Centroid Coord.	18:14:51.7 -22:43:51.0	18:14:50.9 -22:43:55.42
Morph.	Bap	Bams
Central Star Coord.	N/A	N/A
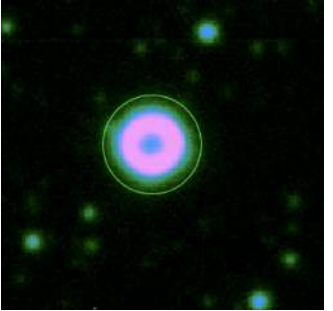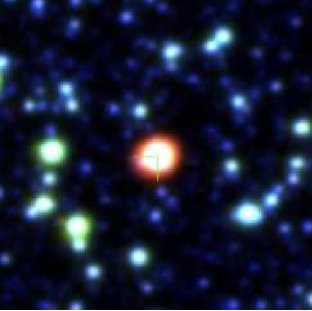
C.51   PN G 009.4-09.8

Catalogue	ESO-VLT	HASH
Image		
Centroid Coord.	18:44:43.0 -25:21:34.8	18:44:43.1 -25:21:33.84
Morph.	Emrs	Er
Central Star Coord.	N/A	N/A
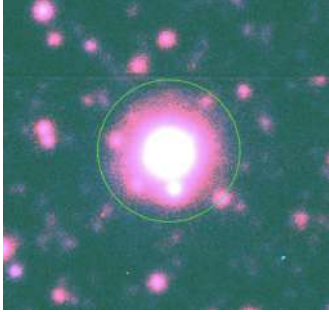
C.52   PN G 009.8-04.6

Catalogue	ESO-VLT	HASH
Image		
Centroid Coord.	18:25:04.9 -22:34:52.6	18:25:05.0 -22:34:52.64
Morph.	Ears	Ear
Central Star Coord.	N/A	N/A
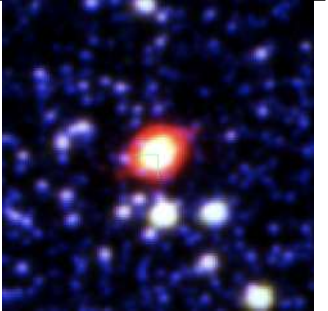
C.53   PN G 350.5-05.0

Catalogue	ESO-VLT	HASH
Image		
Centroid Coord.	17:42:53.3 -39:36:17.4	17:42:54.1 -39:36:24.05
Morph.	Er	Er
Central Star Coord.	N/A	N/A
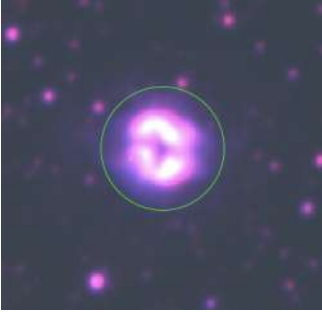
C.54 PN G 351.1+04.8

Catalogue	ESO-VLT	HASH
Image		
Centroid Coord.	17:03:47.7 -33:29:39.2	17:03:46.8 -33:29:44.41
Morph.	E	Emrs
Central Star Coord.	N/A	N/A
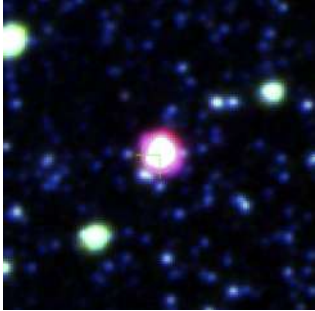
C.55 PN G 351.2+05.2

Catalogue	ESO-VLT	HASH
Image		
Centroid Coord.	17:02:19.0 -33:10:04.9	17:02:19.1 -33:10:05.02
Morph.	Bp	B
Central Star Coord.	N/A	N/A
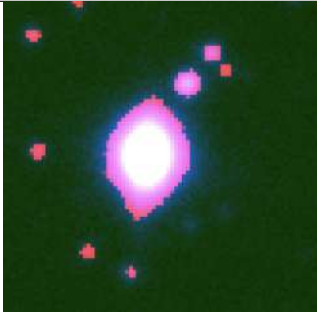
C.56 PN G 351.6-06.2

Catalogue	ESO-VLT	HASH
Image		
Centroid Coord.	17:50:44.5 -39:17:25.9	17:50:44.6 -39:17:25.98
Morph.	Eaps	Er
Central Star Coord.	N/A	N/A
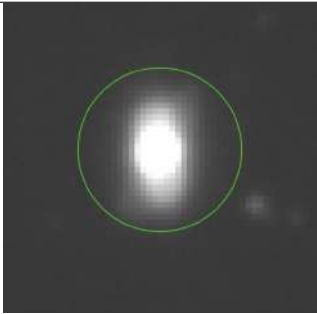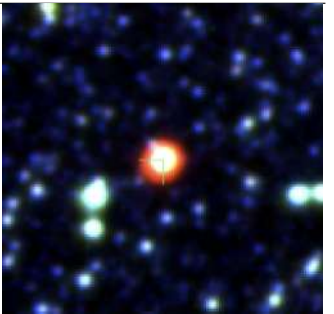
C.57 PN G 351.9+09.0

Catalogue	ESO-VLT	HASH
Image		
Centroid Coord.	16:50:17.1 -30:19:55.4	16:50:17.1 -30:19:55.49
Morph.	Emps	R
Central Star Coord.	N/A	N/A
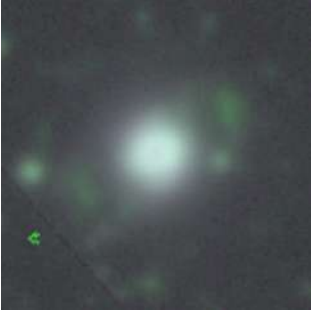
C.58   PN G 351.9-01.9

Catalogue	ESO-VLT	HASH
Image		
Centroid Coord.	17:32:59.6 -36:43:52.1	17:33:00.7 -36:43:52.54
Morph.	B	Bs
Central Star Coord.	N/A	N/A
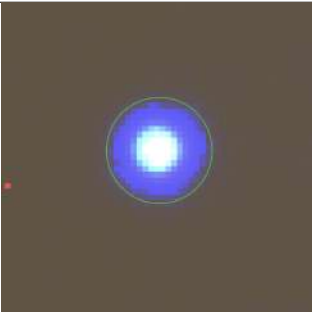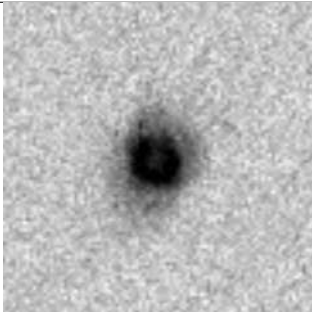
C.59   PN G 352.0-04.6

Catalogue	ESO-VLT	HASH
Image		
Centroid Coord.	17:45:07.6 -38:08:44.9	17:45:06.8 -38:08:49.49
Morph.	Bmps	E
Central Star Coord.	N/A	N/A
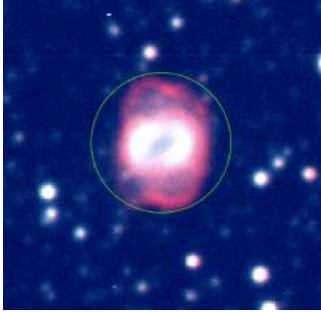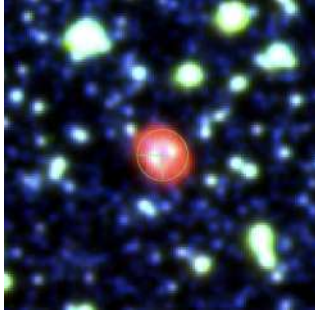
C.60 PN G 352.1+05.1

Catalogue	ESO-VLT	HASH
Image		
Centroid Coord.	17:05:31.1 -32:32:00.2	17:05:30.7 -32:32:08.30
Morph.	Bmrs	Em
Central Star Coord.	N/A	N/A
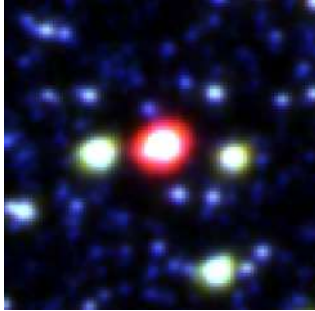
C.61 PN G 352.6+03.0

Catalogue	ESO-VLT	HASH
Image		
Centroid Coord.	17:14:42.5 -33:24:37.5	17:14:42.9 -33:24:47.20
Morph.	Bprs	Bamprs
Central Star Coord.	N/A	N/A
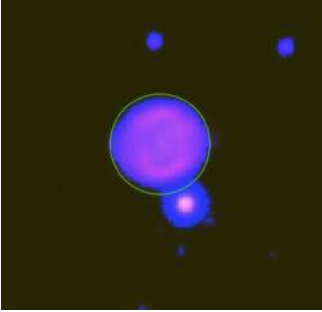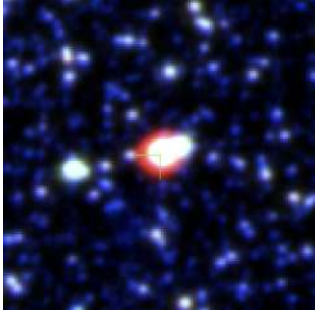
C.62   PN G 353.2-05.2

Catalogue	ESO-VLT	HASH
Image		
Centroid Coord.	17:50:44.6 -37:23:45.7	17:50:45.2 -37:23:53.09
Morph.	Bmprs	Brs
Central Star Coord.	N/A	N/A
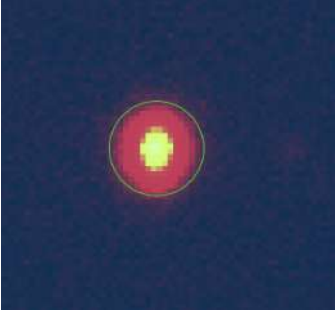
C.63   PN G 353.3+06.3

Catalogue	ESO-VLT	HASH
Image		
Centroid Coord.	17:04:18.3 -30:53:28.8	17:04:18.3 -30:53:28.72
Morph.	Bp	S
Central Star Coord.	N/A	N/A
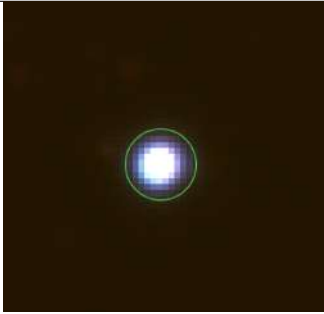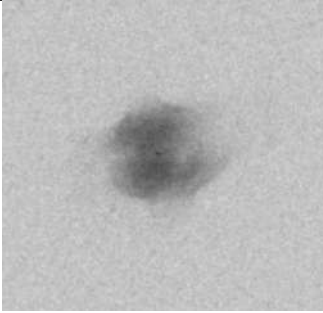
C.64 PN G 353.7+06.3

Catalogue	ESO-VLT	HASH
Image		
Centroid Coord.	17:05:13.9 -30:32:07.7	17:05:13.9 -30:32:19.68
Morph.	Earms	S
Central Star Coord.	N/A	N/A
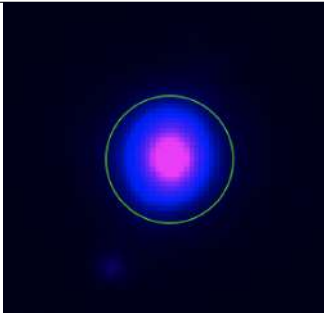
C.65 PN G 354.5+03.3

Catalogue	ESO-VLT	HASH
Image		
Centroid Coord.	17:18:52.1 -31:38:56.7	17:18:51.9 -31:39:06.34
Morph.	E	Bas
Central Star Coord.	N/A	N/A
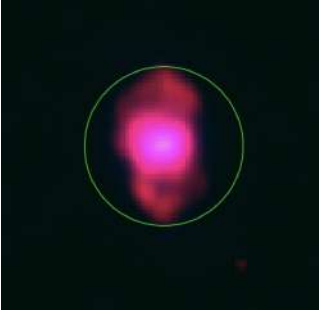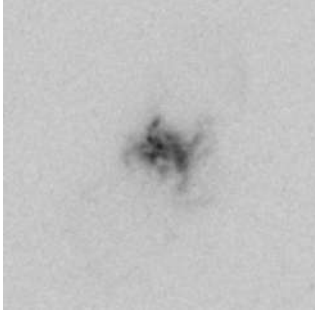
C.66   PN G 354.9+03.5

Catalogue	ESO-VLT	HASH
Image		
Centroid Coord.	17:19:19.2 -31:12:41.2	17:19:20.2 -31:12:40.50
Morph.	E	Bas
Central Star Coord.	N/A	N/A

C.67   PN G 355.1-06.9

Catalogue	ESO-VLT	HASH
Image		
Centroid Coord.	18:02:31.4 -36:39:08.8	18:02:32.3 -36:39:10.94
Morph.	R	Rm
Central Star Coord.	N/A	N/A
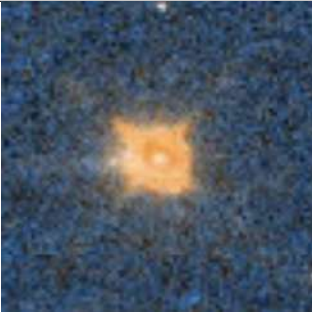
C.68   PN G 355.4-02.4

Catalogue	ESO-VLT	HASH
Image		
Centroid Coord.	17:44:21.3 -34:06:36.1	17:44:20.6 -34:06:40.57
Morph.	Bps	Bms
Central Star Coord.	N/A	N/A
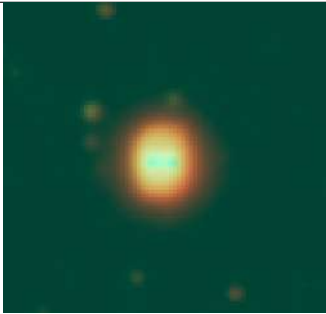
C.69   PN G 355.6-02.7

Catalogue	ESO-VLT	HASH
Image		
Centroid Coord.	17:46:06.3 -34:03:45.3	17:46:06.3 -34:03:45.54
Morph.	E	S
Central Star Coord.	N/A	N/A
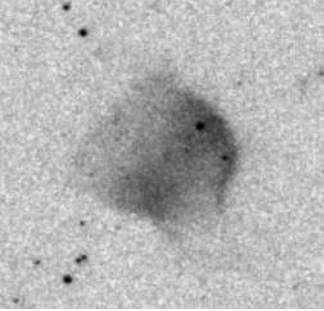
C.70   PN G 355.9+03.6

Catalogue	ESO-VLT	HASH
Image		
Centroid Coord.	17:21:31.5 -30:20:37.7	17:21:31.9 -30:20:48.34
Morph.	E	S
Central Star Coord.	N/A	N/A
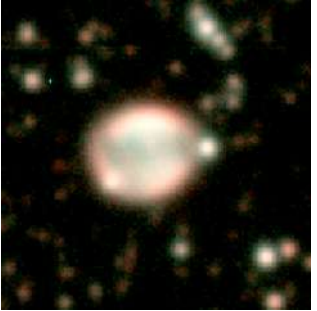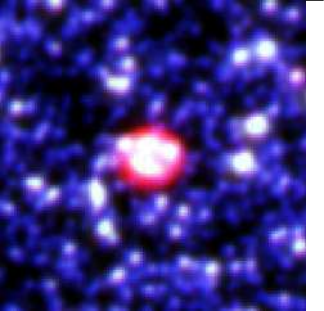
C.71   PN G 355.9-04.2

Catalogue	ESO-VLT	HASH
Image		
Centroid Coord.	17:52:58.9 -34:38:11.4	17:52:58.9 -34:38:22.99
Morph.	Eps	Bmps
Central Star Coord.	N/A	N/A
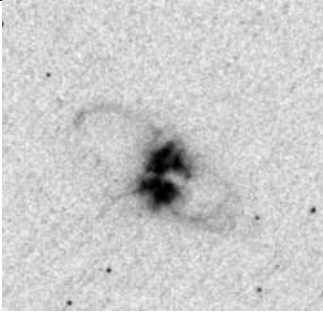
C.72 PN G 356.1-03.3

Catalogue	ESO-VLT	HASH
Image		
Centroid Coord.	17:49:51.4 -34:00:23.1	17:49:50.8 -34:00:31.14
Morph.	Bas	Bas
Central Star Coord.	N/A	N/A
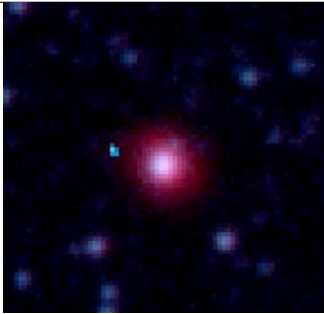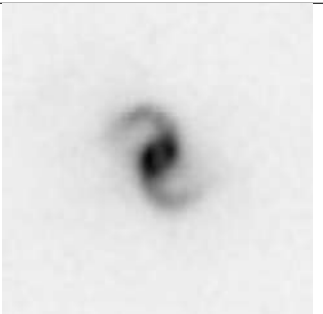
C.73 PN G 356.3-06.2

Catalogue	ESO-VLT	HASH
Image		
Centroid Coord.	18:02:32.7 -35:13:08.2	18:02:32.0 -35:13:13.69
Morph.	Eas	E
Central Star Coord.	N/A	N/A
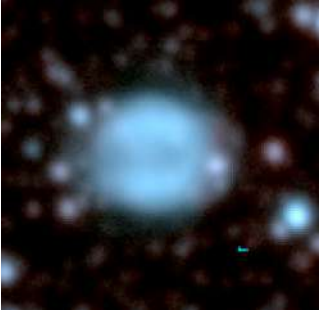
C.74 PN G 356.5-03.6

Catalogue	ESO-VLT	HASH
Image		
Centroid Coord.	17:51:50.0 -33:47:27.0	17:51:50.6 -33:47:35.59
Morph.	Bas	Bps
Central Star Coord.	N/A	N/A
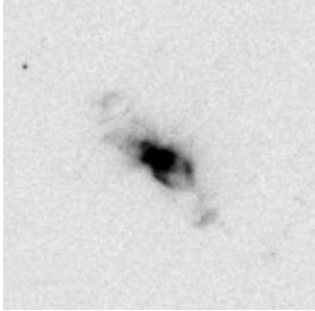
C.75 PN G 356.8+03.3

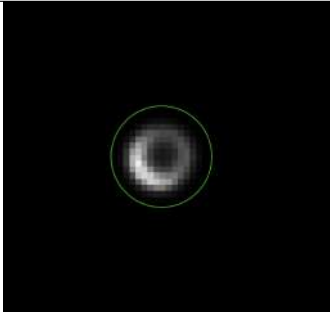| Catalogue	ESO-VLT	HASH
Image		
Centroid Coord.	17:25:05.1 -29:45:12.7	17:25:06.1 -29:45:16.88
Morph.	E	Bp
Central Star Coord.	N/A	N/A
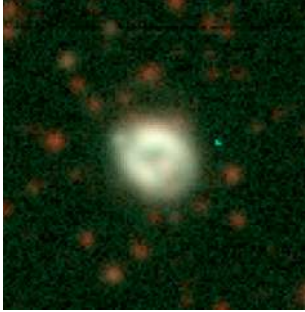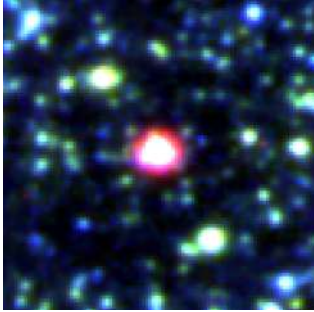
C.76 PN G 356.8-05.4

Catalogue	ESO-VLT	HASH
Image		
Centroid Coord.	18:00:18.0 -34:27:27.4	18:00:18.2 -34:27:39.60
Morph.	Ers	Er
Central Star Coord.	N/A	N/A

C.77 PN G 356.9+04.4

Catalogue	ESO-VLT	HASH
Image		
Centroid Coord.	17:21:03.8 -29:02:52.2	17:21:04.5 -29:02:59.21
Morph.	E	Bmps
Central Star Coord.	N/A	N/A
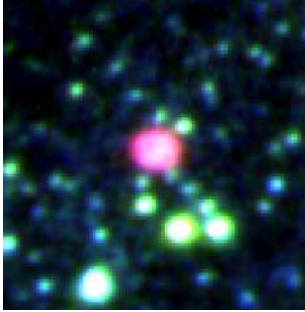
C.78 PN G 357.0+02.4

Catalogue	ESO-VLT	HASH
Image		
Centroid Coord.	17:28:49.7 -30:07:37.3	17:28:50.3 -30:07:44.47
Morph.	Ears	Ear
Central Star Coord.	N/A	N/A
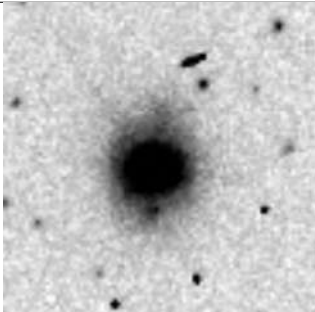
C.79 PN G 357.1+03.6

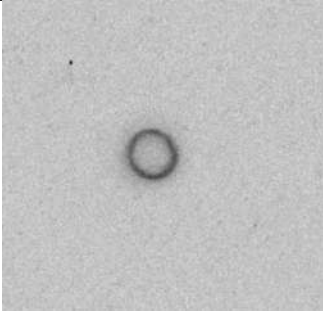| Catalogue	ESO-VLT	HASH
Image		
Centroid Coord.	17:24:33.6 -29:24:10.5	17:24:34.4 -29:24:19.48
Morph.	E	E
Central Star Coord.	N/A	N/A

C.80 PN G 357.1+04.4

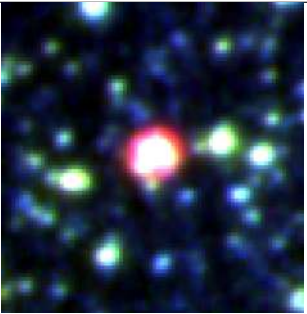| Catalogue	ESO-VLT	HASH
Image		
Centroid Coord.	17:21:37.0 -28:55:14.7	17:21:38.0 -28:55:14.34
Morph.	Ers	Er
Central Star Coord.	N/A	N/A
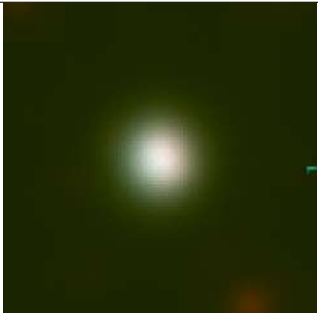
C.81 PN G 357.1-04.7

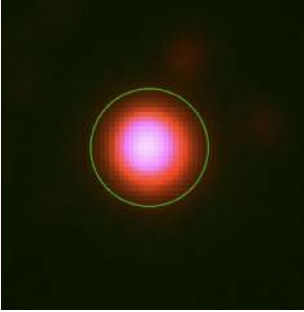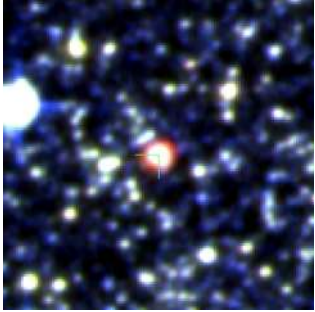| Catalogue	ESO-VLT	HASH
Image		
Centroid Coord.	17:58:15.3 -33:47:32.5	17:58:14.4 -33:47:37.50
Morph.	E	Bps
Central Star Coord.	N/A	N/A

C.82   PN G 357.2+02.0

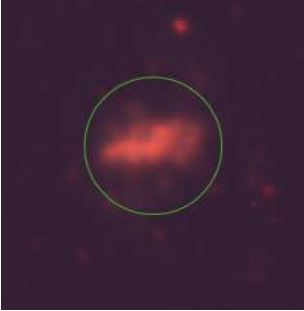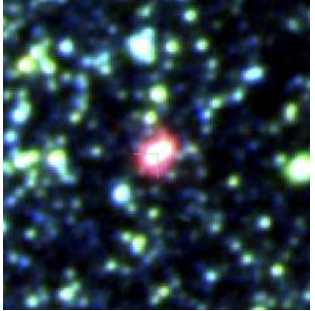| Catalogue	ESO-VLT	HASH
Image		
Centroid Coord.	17:31:08.0 -30:10:27.9	17:31:08.1 -30:10:27.98
Morph.	Rar	Rmrs
Central Star Coord.	N/A	N/A

C.83   PN G 357.3+04.0

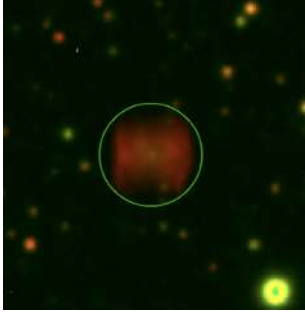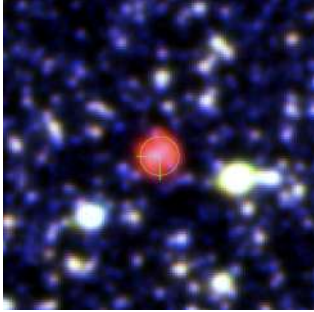| Catalogue	ESO-VLT	HASH
Image		
Centroid Coord.	17:23:24.5 -28:58:56.4	17:23:24.9 -28:59:06.04
Morph.	E	Rr
Central Star Coord.	N/A	N/A

C.84 PN G 357.5+03.1

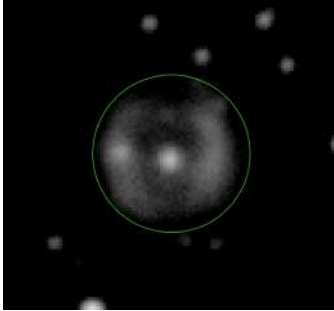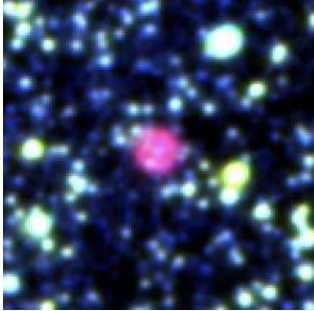| Catalogue	ESO-VLT	HASH
Image		
Centroid Coord.	17:27:24.3 -29:21:14.5	17:27:24.4 -29:21:14.00
Morph.	S	S
Central Star Coord.	N/A	N/A

C.85 PN G 357.5+03.2

Catalogue	ESO-VLT	HASH
Image		
Centroid Coord.	17:26:59.7 -29:15:31.8	17:26:59.8 -29:15:31.86
Morph.	Bs	B
Central Star Coord.	N/A	N/A
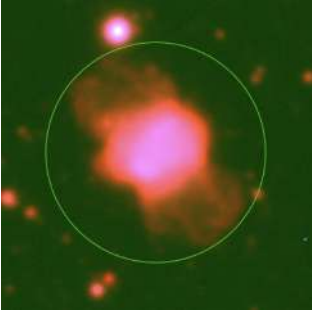
C.86   PN G 357.6-03.3

Catalogue	ESO-VLT	HASH
Image		
Centroid Coord.	17:53:16.7 -32:40:38.5	17:53:16.8 -32:40:38.57
Morph.	Bs	Ba
Central Star Coord.	N/A	N/A

C.87   PN G 357.9-03.8

Catalogue	ESO-VLT	HASH
Image		
Centroid Coord.	17:56:14.2 -32:37:19.4	17:56:13.9 -32:37:22.08
Morph.	Ers	Ers
Central Star Coord.	N/A	N/A

C.88 PN G 357.9-05.1

Catalogue	ESO-VLT	HASH
Image		
Centroid Coord.	18:01:21.2 -33:17:37.8	18:01:22.2 -33:17:43.08
Morph.	Bas	B
Central Star Coord.	N/A	N/A

C.89 PN G 358.0+09.3

Catalogue	ESO-VLT	HASH
Image		
Centroid Coord.	17:05:43.7 -25:24:59.9	17:05:44.5 -25:25:01.74
Morph.	Emps	Em
Central Star Coord.	N/A	N/A
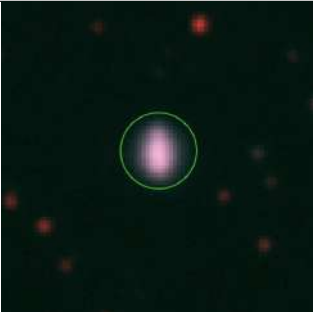
C.90   PN G 358.2+03.5

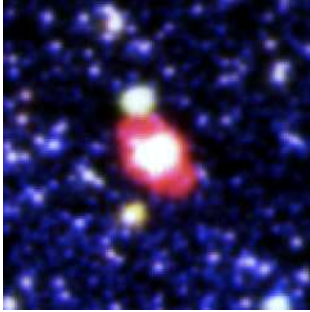| Catalogue	ESO-VLT	HASH
Image		
Centroid Coord.	17:27:32.5 -28:30:57.2	17:27:32.8 -28:31:06.89
Morph.	E	E
Central Star Coord.	N/A	N/A
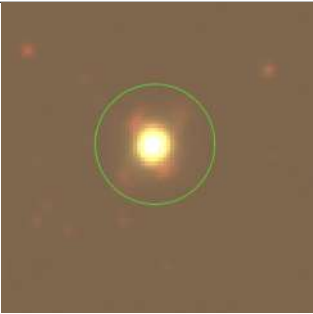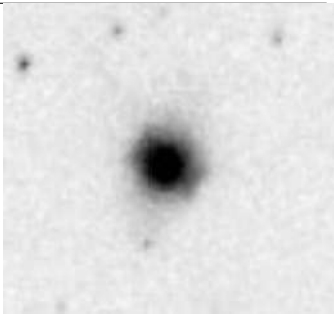
C.91   PN G 358.2+04.2

Catalogue	ESO-VLT	HASH
Image		
Centroid Coord.	17:24:52.1 -28:05:54.6	17:24:52.1 -28:05:54.60
Morph.	S	R
Central Star Coord.	N/A	N/A

C.92 PN G 358.5+02.9

Catalogue	ESO-VLT	HASH
Image		
Centroid Coord.	17:30:30.7 -28:35:45.1	17:30:30.4 -28:35:54.89
Morph.	E	Bas
Central Star Coord.	N/A	N/A

C.93 PN G 358.5-04.2

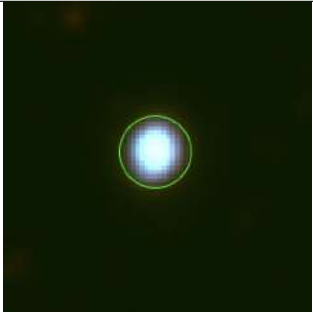| Catalogue	ESO-VLT	HASH
Image		
Centroid Coord.	17:59:03.2 -32:21:39.4	17:59:02.5 -32:21:43.42
Morph.	Bp	Bmps
Central Star Coord.	N/A	N/A

C.94　PN G 358.6+07.8

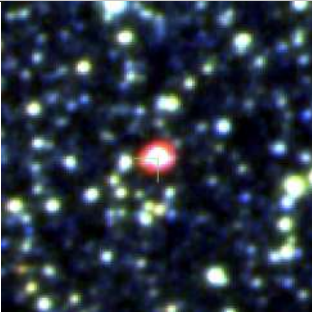| Catalogue	ESO-VLT	HASH
Image		
Centroid Coord.	17:12:39.6 -25:43:28.7	17:12:39.2 -25:43:37.38
Morph.	Es	S
Central Star Coord.	N/A	N/A

C.95　PN G 358.6-05.5

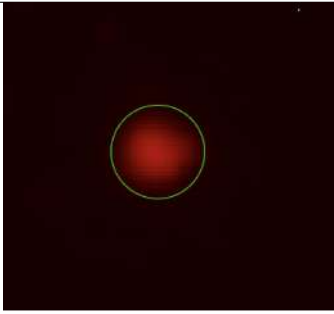| Catalogue	ESO-VLT	HASH
Image		
Centroid Coord.	18:04:55.4 -32:54:00.6	18:04:56.2 -32:54:01.22
Morph.	Bs	Bs
Central Star Coord.	N/A	N/A

C.96   PN G 358.7+05.2

Catalogue	ESO-VLT	HASH
Image		
Centroid Coord.	17:22:29.2 -27:08:40.5	17:22:28.3 -27:08:42.40
Morph.	Es	Emrs
Central Star Coord.	N/A	N/A
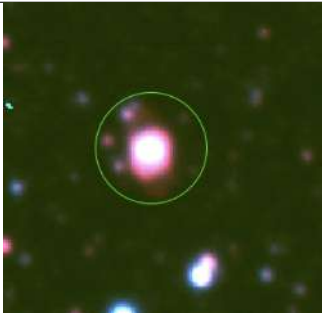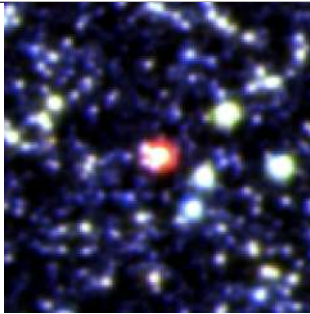
C.97   PN G 358.8+03.0

Catalogue	ESO-VLT	HASH
Image		
Centroid Coord.	17:31:08.3 -28:14:48.8	17:31:09.3 -28:14:50.42
Morph.	Ears	Ear
Central Star Coord.	N/A	N/A
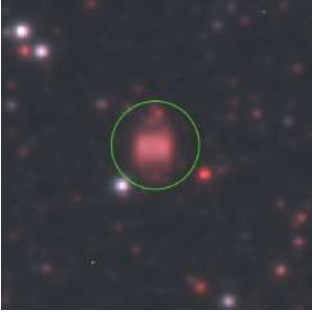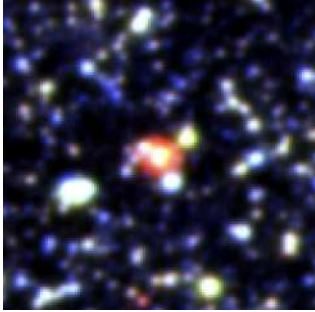
C.98   PN G 358.9+03.4

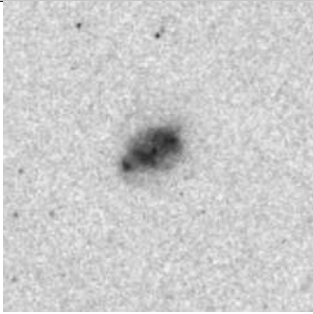| Catalogue	ESO-VLT	HASH
Image		
Centroid Coord.	17:30:02.2 -27:59:05.9	17:30:02.5 -27:59:17.56
Morph.	E	Bams
Central Star Coord.	N/A	N/A
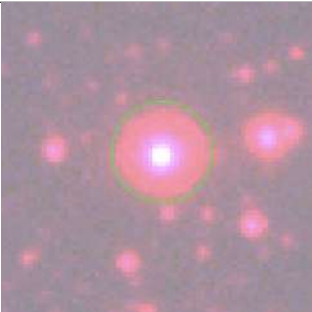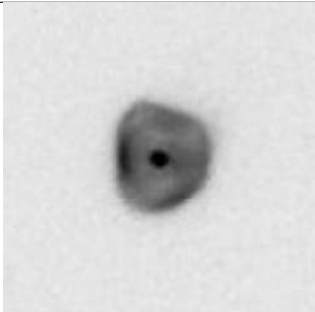
C.99   PN G 359.0-04.1

Catalogue	ESO-VLT	HASH
Image		
Centroid Coord.	17:59:55.9 -31:54:19.5	17:59:56.8 -31:54:27.72
Morph.	Bps	B
Central Star Coord.	N/A	N/A
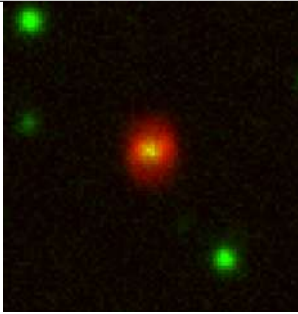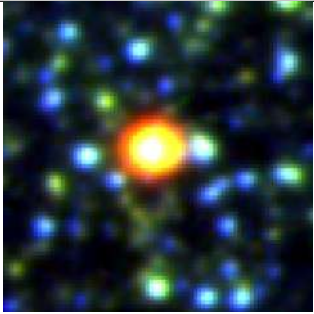
C.100   PN G 359.1-02.9

Catalogue	ESO-VLT	HASH
Image		
Centroid Coord.	17:55:05.1 -31:12:07.2	17:55:05.7 -31:12:16.85
Morph.	Bs	B
Central Star Coord.	N/A	N/A
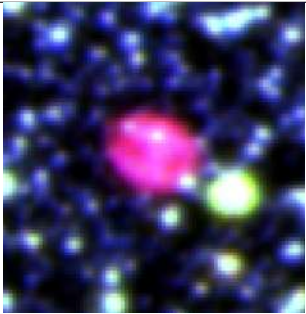
C.101   PN G 359.2+04.7

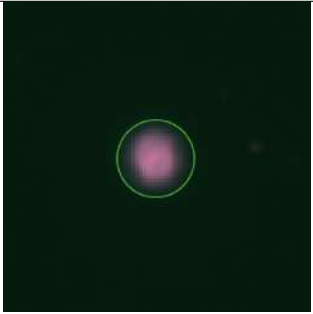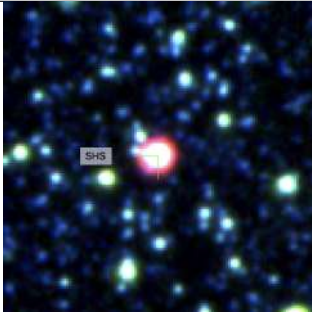| Catalogue	ESO-VLT	HASH
Image		
Centroid Coord.	17:25:44.0 -26:57:35.7	17:25:44.1 -26:57:47.70
Morph.	E	Ears
Central Star Coord.	N/A	N/A
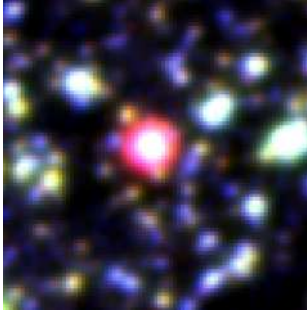
C.102   PN G 359.3-01.8

Catalogue	ESO-VLT	HASH
Image		
Centroid Coord.	17:51:18.3 -30:23:45.3	17:51:18.9 -30:23:52.98
Morph.	Bps	B
Central Star Coord.	N/A	N/A
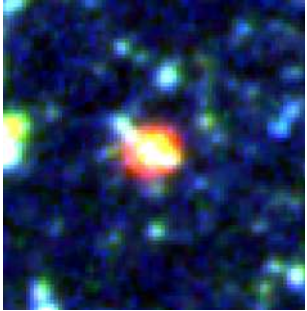
C.103   PN G 359.6-04.8

Catalogue	ESO-VLT	HASH
Image		
Centroid Coord.	18:04:08.6 -31:39:06.2	18:04:07.7 -31:39:10.66
Morph.	Bs	Bs
Central Star Coord.	N/A	N/A

C.104   PN G 359.7-01.8

Catalogue	ESO-VLT	HASH
Image		
Centroid Coord.	17:52:06.4 -30:05:05.2	17:52:05.9 -30:05:13.81
Morph.	Rmr	R
Central Star Coord.	N/A	N/A
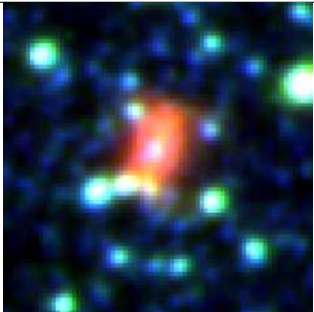
C.105   PN G 359.8+02.4

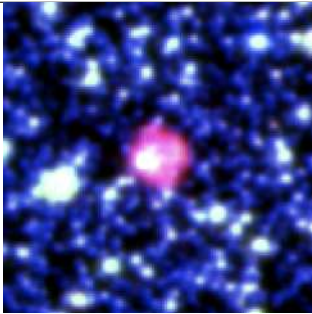| Catalogue	ESO-VLT	HASH
Image		
Centroid Coord.	17:35:47.2 -27:43:20.0	17:35:48.1 -27:43:20.39
Morph.	E	S
Central Star Coord.	N/A	N/A
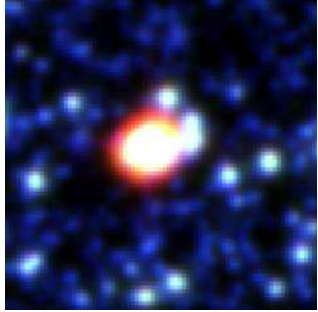
C.106 PN G 359.8+03.7

Catalogue	ESO-VLT	HASH
Image		
Centroid Coord.	17:30:45.9 -27:05:55.8	17:30:46.7 -27:05:59.14
Morph.	Bmps	E
Central Star Coord.	N/A	N/A
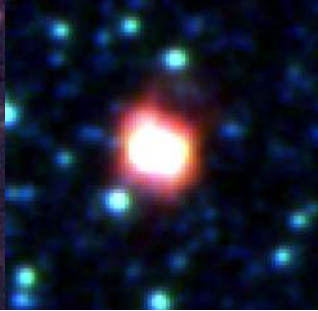
C.107 PN G 359.8+05.2

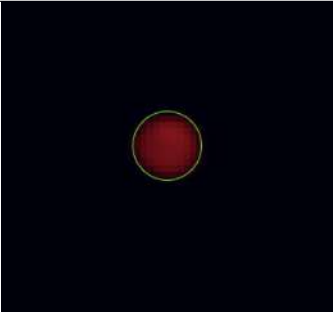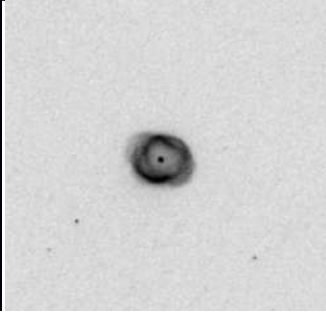| Catalogue	ESO-VLT	HASH
Image		
Centroid Coord.	17:25:23.2 -26:11:44.1	17:25:23.6 -26:11:53.02
Morph.	Bps	B
Central Star Coord.	N/A	N/A
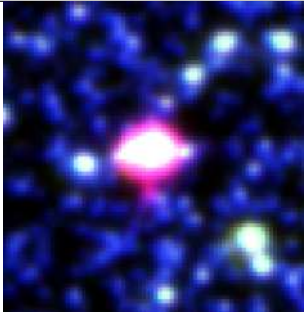
C.108   PN G 359.8+05.6

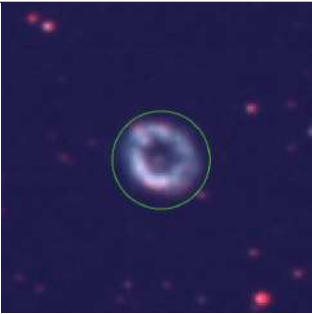| Catalogue	ESO-VLT	HASH
Image		
Centroid Coord.	17:24:01.0 -25:59:14.8	17:24:01.4 -25:59:23.17
Morph.	Bps	S
Central Star Coord.	N/A	N/A
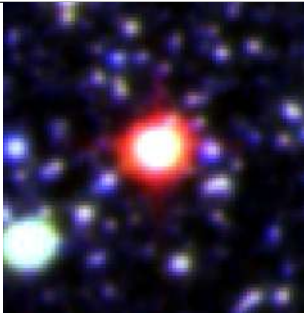
C.109   PN G 359.8+06.9

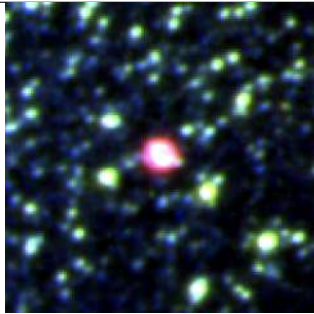| Catalogue	ESO-VLT	HASH
Image		
Centroid Coord.	17:19:14.0 -25:17:13.0	17:19:13.4 -25:17:17.56
Morph.	Bmps	Br
Central Star Coord.	N/A	N/A

C.110 PN G 359.8-07.2

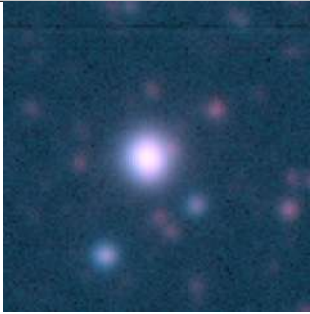| Catalogue	ESO-VLT	HASH
Image		
Centroid Coord.	18:14:51.1 -32:36:44.6	18:14:50.6 -32:36:55.22
Morph.	E	E
Central Star Coord.	N/A	N/A

C.111 PN G 359.9-04.5

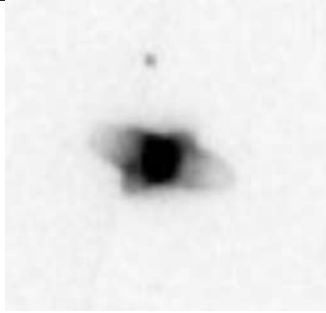| Catalogue	ESO-VLT	HASH
Image		
Centroid Coord.	18:03:52.0 -31:17:38.9	18:03:52.6 -31:17:46.54
Morph.	E	S
Central Star Coord.	N/A	N/A

Appendix D

Objects with inconsistent PA measurements

D.1 PNG007.8−04.4
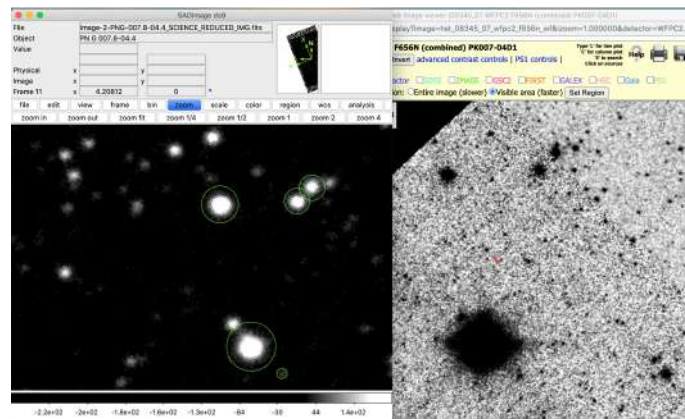
D.2 PNG351.1+04.8
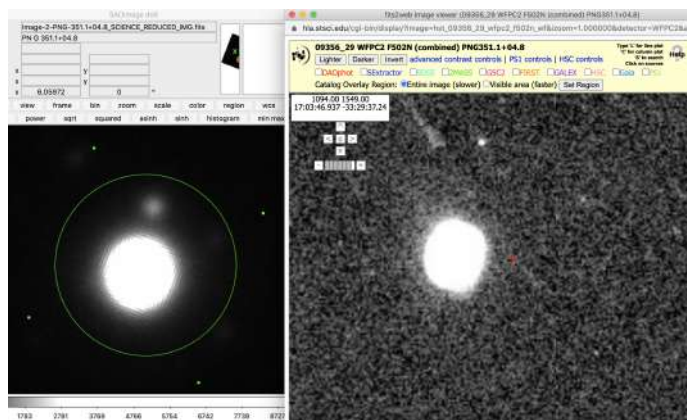
D.3 PNG352.6+03.0
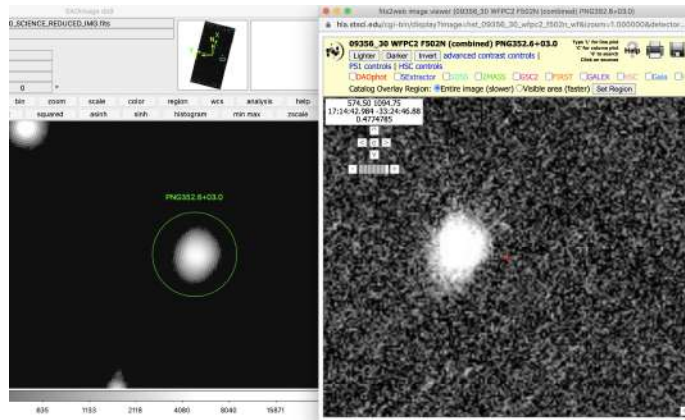
D.4 PNG355.9+03.6
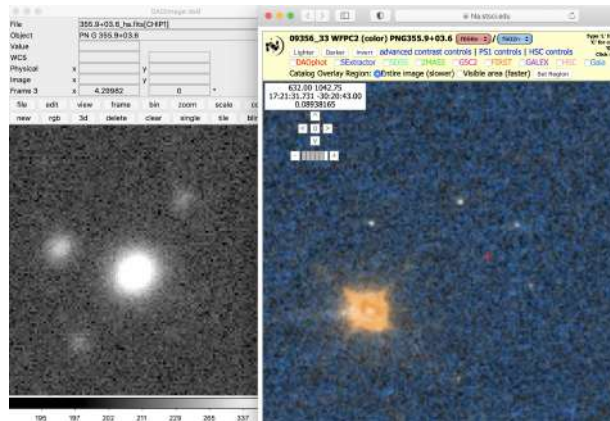
D.5 PNG356.8+03.3
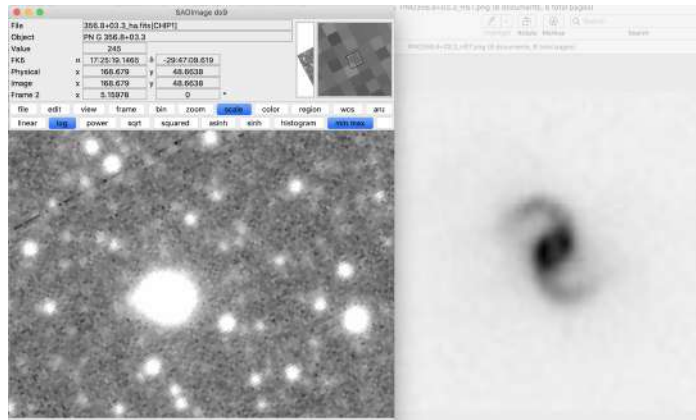
D.6 PNG357.1-04.7
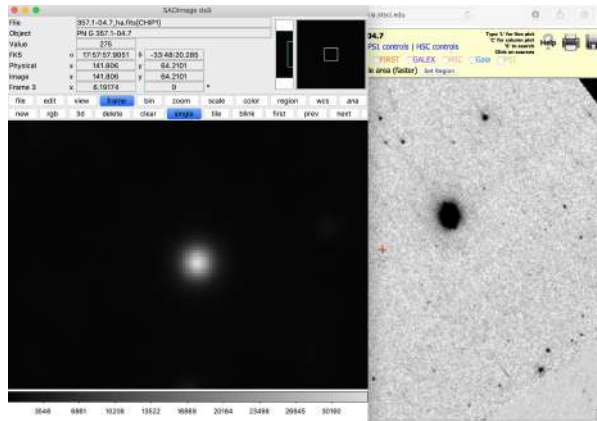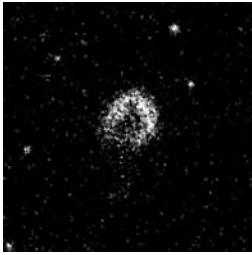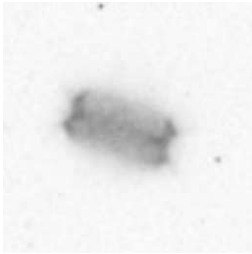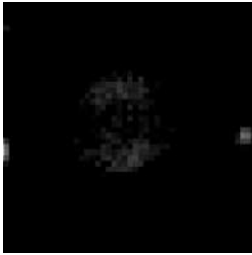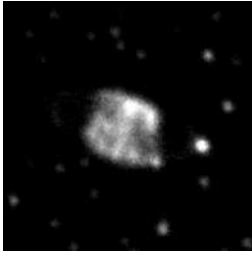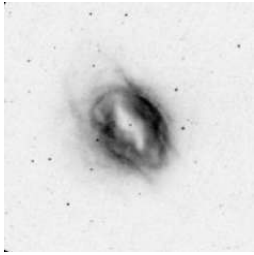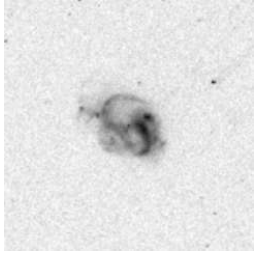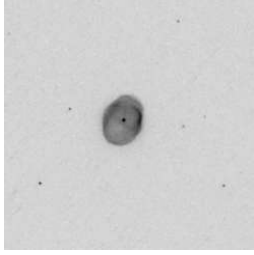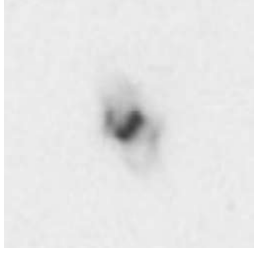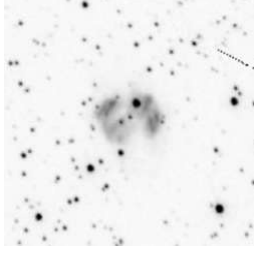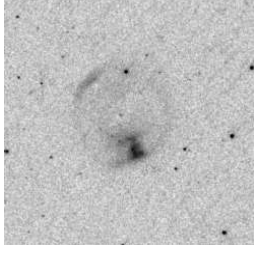
D.7 PNG358.5-04.2
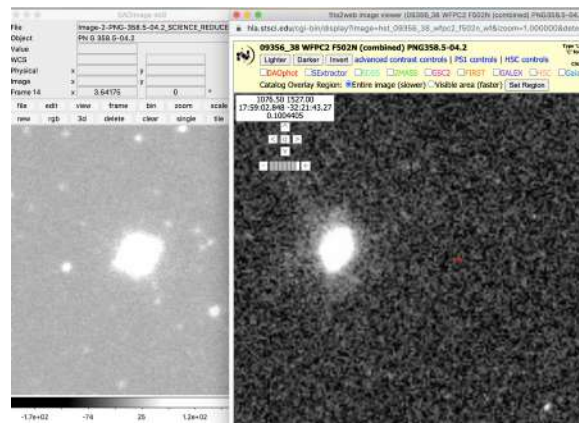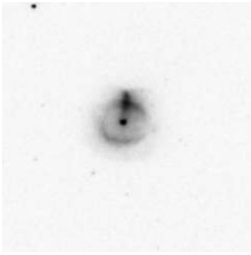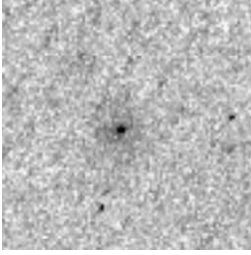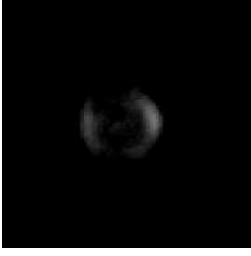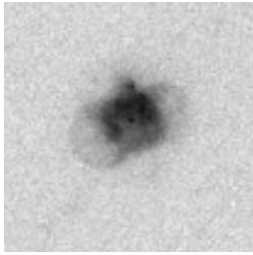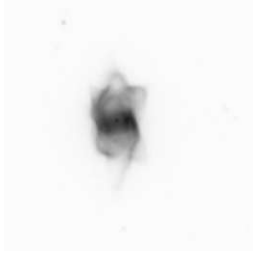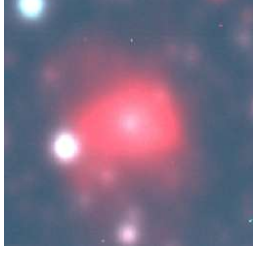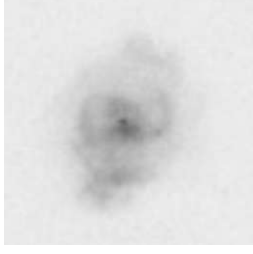
Appendix E
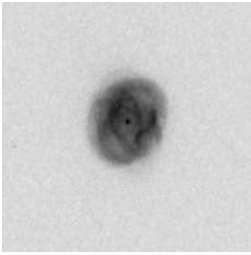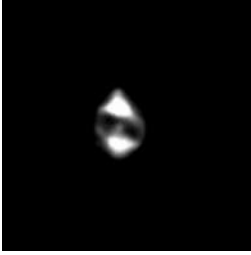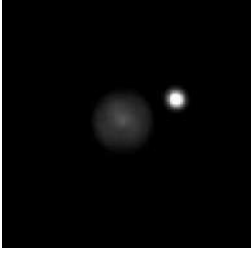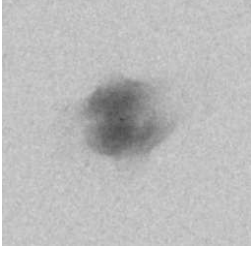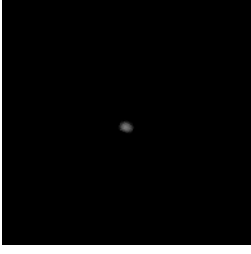
Central Star Observation from VLT and *HST*
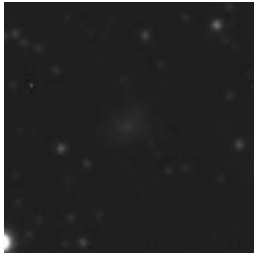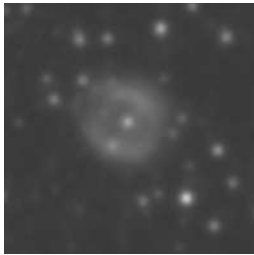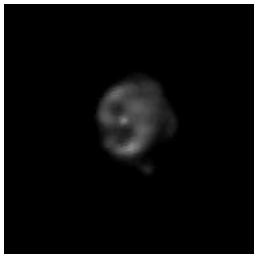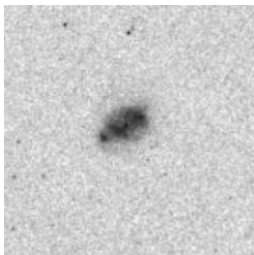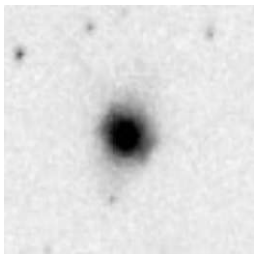
No.	PN G	Image	CSPN Coord.	Tele.	Catalogued ?
3	002.3+02.2		17:25:28.95 -26:15:24.93	VLT	No
4	002.3-03.4		17:25:28.95 -26:15:24.93	HST	No
5	002.5-01.7		17:25:28.95 -26:15:24.93	VLT	No
6	002.6+02.1		17:25:28.95 -26:15:24.93	VLT	No
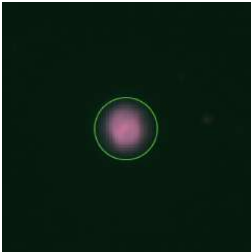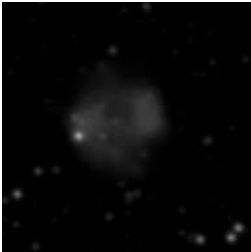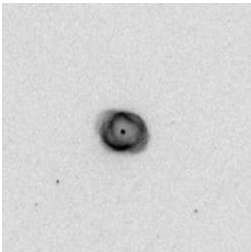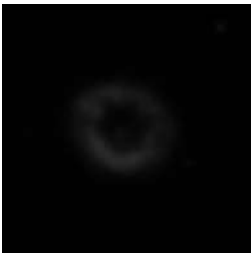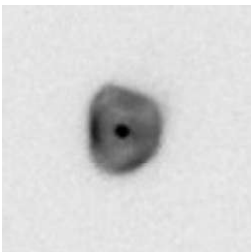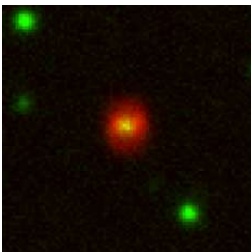
No.	PN G	Image	CSPN Coord.	Tele.	Catalogued ?
7	002.7-04.8		17:25:28.95 -26:15:24.93	HST	No
10	002.9-03.9		17:25:28.95 -26:15:24.93	HST	No
11	003.1+03.4		17:25:28.95 -26:15:24.93	HST	No
13	003.6+03.1		17:25:28.95 -26:15:24.93	HST	No
16	003.8-04.3		17:25:28.95 -26:15:24.93	HST	No
19	003.9-03.1		17:25:28.95 -26:15:24.93	HST	No
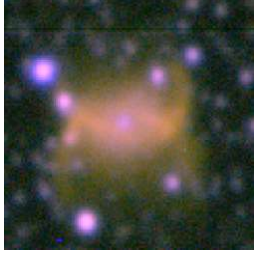
No.	PN G	Image	CSPN Coord.	Tele.	Catalogued ?
20	004.0-03.0		17:25:28.95 -26:15:24.93	HST	No
25	004.3+01.8		17:25:28.95 -26:15:24.93	VLT	No
27	004.8+02.0		17:25:28.95 -26:15:24.93	HST	No
28	004.8-05.0		17:25:28.95 -26:15:24.93	VLT	No
29	005.0-03.9		17:25:28.95 -26:15:24.93	VLT	No
34	005.9-02.6		17:25:28.95 -26:15:24.93	VLT	No

No.	PN G	Image	CSPN Coord.	Tele.	Catalogued ?
37	006.3+04.4		17:25:28.95 -26:15:24.93	HST	No
38	006.4+02.0		17:25:28.95 -26:15:24.93	HST	No
47	007.8-04.4		17:25:28.95 -26:15:24.93	HST	No
48	008.2+06.8		17:25:28.95 -26:15:24.93	HST	No
49	008.4-03.6		17:25:28.95 -26:15:24.93	VLT	No
50	008.6-02.6		17:25:28.95 -26:15:24.93	HST	No

No.	PN G	Image	CSPN Coord.	Tele.	Catalogued ?
54	351.1+04.8		17:25:28.95 -26:15:24.93	HST	No
57	351.9+09.0		17:25:28.95 -26:15:24.93	VLT	No
58	351.9-01.9		17:25:28.95 -26:15:24.93	HST	No
64	353.7+06.3		17:25:28.95 -26:15:24.93	VLT	No
66	354.9+03.5		17:25:28.95 -26:15:24.93	HST	No
68	355.4-02.4		17:25:28.95 -26:15:24.93	HST	No

No.	PN G	Image	CSPN Coord.	Tele.	Catalogued ?
71	355.9-04.2		17:25:28.95 -26:15:24.93	HST	No
86	357.6-03.3		17:25:28.95 -26:15:24.93	VLT	No
87	357.9-03.8		17:25:28.95 -26:15:24.93	VLT	No
89	358.0+09.3		17:25:28.95 -26:15:24.93	VLT	No
92	358.5+02.9		17:25:28.95 -26:15:24.93	HST	No
93	358.5-04.2		17:25:28.95 -26:15:24.93	HST	No

No. PN G	Image	CSPN Coord.	Tele.	Catalogued ?
94 358.6+07.8		17:25:28.95 -26:15:24.93	VLT	No
95 358.6-05.5		17:25:28.95 -26:15:24.93	VLT	No
96 358.7+05.2		17:25:28.95 -26:15:24.93	HST	No
97 358.8+03.0		17:25:28.95 -26:15:24.93	VLT	No
101 359.2+04.7		17:25:28.95 -26:15:24.93	HST	No
102 359.3-01.8		17:25:28.95 -26:15:24.93	VLT	No

No. PN G	Image	CSPN Coord.	Tele.	Catalogued ?
104359.7-01.8		17:25:28.95 -26:15:24.93	VLT	No
107359.8+05.2		17:25:28.95 -26:15:24.93	VLT	No

Appendix F

Physical Parameters and Chemical Abundances

Table F.1: Physical conditions and chemical abundances. The first, second and third rows give the parameters derived from the observational data, their upper and lower limits respectively. Column (1) gives the PNG number; Col. (3) electron density deduced from [S ii] $\lambda6731/6716$; Cols. (4) and (5) electron temperatures from [O iii] $\lambda4363/5007$ and [N ii] $\lambda5755/6584$ respectively. Columns (6) to (12) give the He/H, N/H, O/H, Ne/H, S/H, Ar/H, Cl/H ratios, respectively. Column (13) gives the logarithmic extinction C at Hβ derive from our spectra.

PN G	n_e(SII)	T_e(OIII)	T_e(NII)	He/H	N/H	O/H	Ne/H	S/H	Ar/H	Cl/H	ext.C
000.1+02.6	5.75E+02	9550	6690	1.36E-01	1.89E-04	1.01E-03	3.34E-04	1.34E-05	4.95E-06	1.16E-07	1.90E+00
	7.58E+02	9760	7470	1.38E-01	2.05E-04	1.10E-03	3.74E-04	1.54E-05	5.28E-06	1.35E-07	1.94E+00
	4.02E+02	9340	6270	1.34E-01	1.70E-04	9.30E-04	2.96E-04	1.14E-05	4.48E-06	9.70E-08	1.85E+00
000.1+04.3	9.67E+03	10700	12700	9.80E-02	2.03E-04	5.65E-04	1.42E-04	3.61E-04	2.57E-06	1.48E-07	2.35E+00
	1.44E+04	10900	17300	1.04E-01	2.82E-04	6.21E-04	1.62E-04	6.12E-04	2.91E-06	1.71E-07	2.50E+00
	0.00E+00	10300	11800	9.20E-02	0.00E+00	4.79E-04	1.23E-04	0.00E+00	2.25E-06	1.22E-07	2.20E+00
000.1-02.3	1.57E+03	10500	8170	1.19E-01	8.31E-05	1.18E-03	2.64E-04	1.15E-05	5.52E-06	2.21E-07	1.26E+00
	1.97E+03	11600	8310	1.21E-01	1.16E-04	1.46E-03	3.43E-04	1.60E-05	6.69E-06	2.62E-07	1.29E+00
	1.04E+03	9700	7990	1.18E-01	3.64E-05	7.10E-04	1.33E-04	4.40E-06	3.48E-06	1.45E-07	1.23E+00
000.2-01.9	2.34E+03	6630	6970	9.30E-02	1.86E-04	1.11E-03	2.04E-04	1.24E-05	3.19E-06	4.60E-08	1.50E+00
	3.57E+03	6760	7240	9.70E-02	2.21E-04	1.43E-03	2.65E-04	1.44E-05	3.47E-06	5.30E-08	1.54E+00
	0.00E+00	6530	6760	8.90E-02	1.45E-04	0.00E+00	1.00E-05	0.00E+00	2.76E-06	3.02E-08	1.45E+00
000.2-04.6	5.40E+02	8030	8120	1.50E-01	4.07E-04	1.28E-03	5.13E-04	1.26E-05	4.30E-06	1.50E-07	1.25E+00
	6.11E+02	8090	8170	1.52E-01	4.23E-04	1.55E-03	6.09E-04	1.37E-05	4.48E-06	1.58E-07	1.29E+00
	4.33E+02	7930	8060	1.48E-01	3.93E-04	1.05E-03	4.17E-04	1.17E-05	4.10E-06	1.42E-07	1.22E+00
000.3+06.9	1.08E+02	-	7360	1.51E-01	3.22E-04	5.25E-04	1.38E-04	3.21E-05	3.92E-06	2.16E-07	2.18E+00
	1.94E+02	-	7530	1.57E-01	3.42E-04	5.93E-04	1.60E-04	3.56E-05	4.27E-06	3.03E-07	2.23E+00

PN G	n_e(SII)	T_e(OIII)	T_e(NII)	He/H	N/H	O/H	Ne/H	S/H	Ar/H	Cl/H	ext.C
	5.70E+01	-	7130	1.46E-01	2.95E-04	4.50E-04	1.16E-04	2.73E-05	3.72E-06	1.60E-07	2.13E+00
000.3-04.6	1.53E+03	8840	5000	1.59E-01	4.55E-04	9.84E-04	4.78E-04	1.04E-05	3.73E-06	2.57E-07	1.43E+00
	1.66E+03	8960	5010	1.64E-01	4.89E-04	1.21E-03	5.99E-04	1.27E-05	4.07E-06	3.03E-07	1.51E+00
	1.35E+03	8710	4640	1.54E-01	0.00E+00	0.00E+00	0.00E+00	4.00E-07	3.33E-06	4.30E-08	1.37E+00
000.4-01.9	5.71E+03	7320	8580	1.18E-01	4.17E-04	8.08E-04	1.03E-04	1.70E-04	4.39E-06	2.02E-07	1.46E+00
	8.17E+03	7510	9280	1.24E-01	6.41E-04	9.86E-04	1.24E-04	3.15E-04	4.96E-06	2.24E-07	1.58E+00
	0.00E+00	7140	8190	1.12E-01	5.80E-05	1.87E-04	7.00E-06	0.00E+00	3.61E-06	1.71E-07	1.36E+00
000.4-02.9	1.95E+03	7980	9090	1.63E-01	3.46E-05	9.00E-04	3.04E-04	2.34E-06	6.78E-06	4.47E-08	9.26E-01
	2.96E+03	8110	9470	1.67E-01	4.24E-05	1.25E-03	4.19E-04	3.24E-06	9.27E-06	5.21E-08	9.66E-01
	0.00E+00	7860	8770	1.60E-01	1.97E-05	0.00E+00	0.00E+00	0.00E+00	0.00E+00	3.97E-08	8.84E-01
000.7+03.2	1.11E+03	8230	7610	1.47E-01	2.72E-04	1.08E-03	4.27E-04	2.04E-05	5.83E-06	3.08E-07	1.96E+00
	1.93E+03	8770	7930	1.55E-01	3.52E-04	1.36E-03	5.26E-04	2.74E-05	7.12E-06	3.74E-07	2.11E+00
	0.00E+00	7820	7230	1.36E-01	1.85E-04	5.60E-04	9.70E-05	5.30E-06	4.03E-06	2.07E-07	1.80E+00
000.7-02.7	7.61E+03	12300	11300	9.50E-02	4.29E-05	2.96E-04	6.44E-05	2.45E-05	7.30E-07	2.41E-08	9.89E-01
	9.84E+03	12500	13100	9.90E-02	5.95E-05	3.15E-04	6.86E-05	4.23E-05	8.17E-07	3.18E-08	1.03E+00
	9.80E+02	12100	9800	9.00E-02	0.00E+00	2.42E-04	5.40E-05	0.00E+00	6.30E-07	1.96E-08	9.37E-01
000.7-07.4	5.34E+02	8910	6310	1.25E-01	4.56E-04	3.92E-03	1.90E-03	1.81E-05	1.97E-05	8.10E-08	3.80E-01
	7.37E+02	8990	6500	1.28E-01	4.94E-04	4.62E-03	2.28E-03	2.02E-05	2.14E-05	8.51E-08	4.38E-01
	2.75E+02	8840	6160	1.22E-01	4.20E-04	3.02E-03	1.37E-03	1.50E-05	1.78E-05	7.74E-08	3.23E-01
000.9-02.0	4.86E+03	8260	8320	2.23E-01	3.76E-05	7.81E-04	1.07E-04	2.09E-05	8.70E-06	3.69E-07	6.93E-01
	6.71E+03	8550	9210	2.42E-01	4.74E-05	9.62E-04	1.27E-04	2.49E-05	1.05E-05	4.31E-07	8.03E-01
	0.00E+00	7970	7810	2.09E-01	1.57E-05	5.93E-04	8.70E-05	1.62E-05	7.28E-06	3.00E-07	5.31E-01
000.9-04.8	1.66E+03	13400	9190	1.14E-01	2.56E-04	2.77E-04	5.97E-05	3.75E-06	1.49E-06	9.05E-08	1.29E+00
	2.30E+03	13700	9350	1.19E-01	3.11E-04	4.00E-04	8.85E-05	5.60E-06	2.15E-06	1.23E-07	1.35E+00
	9.90E+02	13100	8960	1.10E-01	2.19E-04	1.01E-04	1.69E-05	1.19E-06	7.00E-07	5.64E-08	1.25E+00
001.1-01.6	1.24E+03	8220	8180	1.39E-01	5.46E-04	1.92E-03	8.98E-04	1.71E-05	1.39E-05	8.34E-08	1.97E+00
	1.40E+03	8230	8250	1.41E-01	5.75E-04	2.33E-03	1.09E-03	1.90E-05	1.65E-05	9.56E-08	2.00E+00
	1.04E+03	8210	8110	1.35E-01	5.08E-04	1.44E-03	7.01E-04	1.57E-05	1.02E-05	6.99E-08	1.94E+00
001.2+02.1	3.69E+03	8510	-	1.02E-01	1.64E-04	4.44E-04	1.05E-04	1.46E-05	1.65E-06	-	2.38E+00
	4.00E+03	8630	-	1.05E-01	2.14E-04	4.83E-04	1.10E-04	1.84E-05	1.84E-06	-	2.44E+00
	3.22E+03	8410	-	9.80E-02	1.06E-04	4.05E-04	9.70E-05	1.04E-05	1.48E-06	-	2.32E+00
001.2-03.0	4.84E+03	-	6030	1.28E-02	8.24E-05	3.36E-05	-	1.69E-06	1.47E-07	2.01E-08	1.51E+00
	6.44E+03	-	6320	1.37E-02	1.16E-04	6.12E-05	-	2.54E-06	2.17E-07	3.02E-08	1.67E+00

PN G	n_e(SII)	T_e(OIII)	T_e(NII)	He/H	N/H	O/H	Ne/H	S/H	Ar/H	Cl/H	ext.C
	3.10E+02	-	5910	1.17E-02	0.00E+00	0.00E+00	-	0.00E+00	0.00E+00	1.60E-09	1.38E+00
001.3-01.2	4.30E+03	-	6530	1.16E-01	9.97E-05	5.72E-05	-	1.36E-06	1.19E-06	8.09E-08	2.78E+00
	5.34E+03	-	6620	1.18E-01	1.04E-04	6.12E-05	-	1.59E-06	1.24E-06	8.85E-08	2.82E+00
	2.84E+03	-	6420	1.14E-01	9.19E-05	5.36E-05	-	1.18E-06	1.13E-06	6.44E-08	2.73E+00
001.4+05.3	1.91E+03	8050	9830	1.13E-01	3.95E-05	5.07E-04	1.00E-04	4.97E-06	2.73E-06	1.37E-07	2.12E+00
	2.60E+03	8210	10200	1.17E-01	4.43E-05	6.65E-04	1.31E-04	5.64E-06	3.01E-06	1.51E-07	2.17E+00
	3.50E+02	7870	9430	1.10E-01	2.62E-05	0.00E+00	0.00E+00	3.91E-06	2.45E-06	1.06E-07	2.06E+00
001.6-01.3	5.51E+03	8310	9810	1.44E-01	4.00E-03	8.54E-04	2.47E-04	3.28E-05	4.56E-06	1.44E-06	3.54E+00
	6.77E+03	8620	10000	1.47E-01	6.00E-03	9.78E-04	3.00E-04	4.50E-05	5.13E-06	1.99E-06	3.57E+00
	3.70E+03	7990	9500	1.40E-01	3.00E-03	7.27E-04	1.97E-04	1.60E-05	3.90E-06	9.70E-07	3.52E+00
001.7+05.7	8.04E+02	16000	12000	7.70E-02	1.65E-05	1.84E-04	3.47E-05	9.47E-07	6.35E-07	2.30E-08	1.50E+00
	9.31E+02	16300	12300	7.80E-02	2.13E-05	2.05E-04	3.83E-05	1.06E-06	6.89E-07	2.44E-08	1.53E+00
	5.91E+02	15800	11600	7.50E-02	9.30E-06	1.19E-04	2.23E-05	7.85E-07	4.71E-07	2.19E-08	1.48E+00
001.7-04.4	2.63E+03	-	6050	5.40E-02	1.92E-04	2.71E-04	-	5.78E-06	2.22E-06	1.01E-07	7.13E-01
	3.93E+03	-	6260	5.80E-02	2.83E-04	5.27E-04	-	7.54E-06	3.67E-06	1.73E-07	7.61E-01
	0.00E+00	-	5940	5.10E-02	6.70E-05	0.00E+00	-	2.70E-06	8.80E-07	3.00E-08	6.70E-01
002.0-06.2	2.80E+03	8160	9680	9.90E-02	4.43E-05	5.39E-04	1.18E-04	6.08E-06	1.67E-06	1.44E-07	2.95E-01
	3.78E+03	8270	10300	1.07E-01	5.54E-05	5.98E-04	1.25E-04	6.88E-06	1.94E-06	1.65E-07	4.28E-01
	3.90E+02	7990	9160	8.90E-02	3.24E-05	4.87E-04	1.12E-04	5.19E-06	1.33E-06	1.10E-07	1.63E-01
002.2-09.4	3.96E+03	8890	8980	1.34E-01	5.24E-04	5.14E-04	2.10E-04	9.76E-05	3.62E-06	1.50E-07	3.27E-01
	4.83E+03	9000	9300	1.42E-01	6.68E-04	5.65E-04	2.29E-04	1.55E-04	3.96E-06	1.63E-07	4.35E-01
	2.60E+03	8830	8720	1.29E-01	1.89E-04	3.45E-04	1.49E-04	0.00E+00	3.19E-06	1.36E-07	2.55E-01
002.3+02.2	6.36E+02	-	9670	2.03E-01	2.10E-04	2.35E-04	1.78E-04	2.53E-05	2.20E-06	1.86E-08	3.46E+00
	7.43E+02	-	9810	2.07E-01	2.18E-04	2.40E-04	2.01E-04	2.74E-05	2.26E-06	1.99E-08	3.48E+00
	5.09E+02	-	9490	1.99E-01	2.01E-04	2.31E-04	1.56E-04	2.32E-05	2.15E-06	1.74E-08	3.43E+00
002.5-01.7	1.02E+03	-	7510	1.60E-01	4.25E-04	1.49E-03	9.78E-04	3.88E-05	1.04E-05	1.94E-07	2.18E+00
	1.82E+03	-	8140	1.76E-01	5.19E-04	1.90E-03	1.28E-03	4.82E-05	1.28E-05	2.42E-07	2.41E+00
	0.00E+00	-	7090	1.43E-01	2.89E-04	6.80E-04	4.30E-04	2.16E-05	4.70E-06	1.14E-07	2.00E+00
002.6+02.1	4.43E+03	7380	8180	1.41E-01	5.69E-04	7.00E-03	4.00E-03	4.32E-05	1.64E-05	3.48E-07	2.36E+00
	7.62E+03	7930	10400	1.57E-01	7.66E-04	9.00E-03	6.00E-03	6.26E-05	2.25E-05	4.67E-07	2.78E+00
	0.00E+00	7010	7520	1.17E-01	1.75E-04	0.00E+00	0.00E+00	0.00E+00	2.70E-06	1.81E-07	2.03E+00
002.7-04.8	1.18E+03	8330	9370	1.63E-01	2.04E-04	5.71E-04	2.56E-04	2.31E-05	3.46E-06	1.42E-07	7.40E-01
	1.75E+03	8460	9560	1.69E-01	2.31E-04	6.29E-04	2.90E-04	3.02E-05	3.71E-06	1.52E-07	7.77E-01

PN G	n_e(SII)	T_e(OIII)	T_e(NII)	He/H	N/H	O/H	Ne/H	S/H	Ar/H	Cl/H	ext.C
	0.00E+00	8180	9160	1.57E-01	1.52E-04	4.94E-04	2.27E-04	1.02E-05	3.25E-06	1.32E-07	7.00E-01
002.8+01.7	1.00E+05	-	5960	8.10E-02	7.42E-05	1.65E-04	-	4.03E-06	7.23E-07	3.96E-08	2.40E+00
	1.86E+05	-	6130	8.60E-02	8.84E-05	1.82E-04	-	5.38E-06	8.60E-07	4.47E-08	2.55E+00
	9.90E+04	-	5020	7.40E-02	5.89E-05	1.48E-04	-	2.88E-06	4.55E-07	3.10E-08	2.28E+00
002.8+01.8	5.80E+02	-	8920	1.09E-01	3.25E-04	8.00E-04	3.70E-04	5.02E-05	3.23E-06	1.20E-08	2.22E+00
	6.51E+02	-	9040	1.11E-01	3.64E-04	8.61E-04	4.34E-04	6.01E-05	3.40E-06	1.33E-08	2.25E+00
	5.04E+02	-	8830	1.06E-01	2.85E-04	7.43E-04	3.03E-04	4.31E-05	3.12E-06	1.13E-08	2.19E+00
002.9-03.9	8.75E+03	13000	-	1.09E-01	4.31E-05	3.02E-04	6.82E-05	2.16E-06	1.51E-06	1.12E-07	9.08E-01
	1.31E+04	13100	-	1.11E-01	5.61E-05	3.25E-04	7.18E-05	2.59E-06	1.57E-06	1.18E-07	9.34E-01
	0.00E+00	12800	-	1.08E-01	0.00E+00	2.88E-04	6.58E-05	1.78E-06	1.45E-06	1.06E-07	8.87E-01
003.2-06.2	3.94E+03	8450	9150	1.25E-01	1.13E-03	5.87E-04	1.80E-04	2.00E-03	3.76E-06	1.84E-07	1.03E-01
	4.90E+03	8560	9520	1.29E-01	1.64E-03	6.13E-04	1.91E-04	3.00E-03	3.99E-06	1.98E-07	1.45E-01
	3.13E+03	8370	8850	1.22E-01	8.60E-04	5.25E-04	1.67E-04	1.00E-03	3.52E-06	1.65E-07	4.30E-02
003.6-02.3	8.70E+02	8430	8260	1.48E-01	3.05E-04	6.68E-04	2.21E-04	7.71E-06	4.42E-06	1.09E-07	1.18E+00
	1.05E+03	8590	8310	1.49E-01	3.41E-04	7.58E-04	2.56E-04	8.97E-06	4.90E-06	1.19E-07	1.20E+00
	7.73E+02	8270	8200	1.47E-01	2.41E-04	0.00E+00	0.00E+00	4.73E-06	0.00E+00	6.90E-08	1.16E+00
003.7+07.9	4.89E+02	13500	5070	8.02E-02	3.55E-03	1.30E-01	7.90E-02	2.27E-05	9.48E-07	-	2.75E+00
	5.60E+02	13700	5130	8.12E-02	3.87E-03	1.47E-01	9.50E-02	2.44E-05	9.98E-07	-	2.78E+00
	3.42E+02	13400	5030	7.87E-02	3.27E-03	1.03E-01	6.50E-02	2.03E-05	9.07E-07	-	2.71E+00
003.7-04.6	3.74E+03	10100	19200	9.10E-02	6.00E-05	6.62E-04	1.81E-04	6.18E-05	3.70E-06	2.44E-07	5.54E-01
	5.90E+03	10300	23500	9.80E-02	7.88E-05	7.21E-04	1.95E-04	9.45E-05	3.96E-06	2.74E-07	6.00E-01
	0.00E+00	9900	14000	8.50E-02	2.33E-05	6.00E-04	1.65E-04	0.00E+00	3.35E-06	2.13E-07	4.74E-01
003.8-04.3	2.07E+03	9760	10500	1.53E-01	3.72E-04	6.16E-04	2.65E-04	1.74E-05	6.17E-06	3.67E-07	1.74E+00
	2.83E+03	10000	10900	1.59E-01	5.26E-04	7.04E-04	3.00E-04	2.25E-05	6.82E-06	4.35E-07	1.88E+00
	9.40E+02	9550	10200	1.46E-01	1.17E-04	4.09E-04	2.08E-04	1.24E-05	4.45E-06	2.31E-07	1.63E+00
003.9-02.3	5.01E+03	8110	8630	1.50E-01	4.30E-04	7.25E-04	2.44E-04	1.06E-05	5.80E-06	3.32E-07	2.13E+00
	7.15E+03	8240	12300	1.58E-01	5.88E-04	8.93E-04	2.79E-04	1.36E-05	7.52E-06	3.97E-07	2.30E+00
	3.50E+02	7990	8250	1.37E-01	1.43E-04	0.00E+00	0.00E+00	7.40E-06	1.50E-07	2.24E-07	1.96E+00
003.9-03.1	2.55E+03	13400	-	1.01E-01	7.60E-05	4.20E-04	9.58E-05	2.23E-06	1.64E-06	1.46E-07	1.26E+00
	2.97E+03	13500	-	1.02E-01	8.23E-05	4.33E-04	9.85E-05	2.33E-06	1.68E-06	1.54E-07	1.29E+00
	1.90E+03	13300	-	1.00E-01	6.87E-05	4.09E-04	9.33E-05	2.10E-06	1.59E-06	1.36E-07	1.24E+00
004.0-03.0	3.58E+03	35000	11100	5.10E-02	6.31E-06	8.23E-06	2.65E-06	1.20E-07	9.43E-08	4.34E-09	7.28E-01
	4.86E+03	35100	11800	5.40E-02	8.23E-06	9.04E-06	2.85E-06	1.34E-07	9.93E-08	4.83E-09	7.91E-01

PN G	n_e(SII)	T_e(OIII)	T_e(NII)	He/H	N/H	O/H	Ne/H	S/H	Ar/H	Cl/H	ext.C
	6.40E+02	34900	10600	4.70E-02	3.51E-06	5.22E-06	1.63E-06	9.40E-08	8.74E-08	3.81E-09	6.87E-01
004.1-03.8	1.82E+03	11400	10800	9.50E-02	4.09E-05	4.24E-04	1.01E-04	3.08E-06	9.77E-07	4.76E-08	1.19E+00
	2.30E+03	11600	11200	9.80E-02	4.46E-05	5.29E-04	1.24E-04	3.38E-06	1.05E-06	5.08E-08	1.24E+00
	4.50E+02	11300	10400	9.20E-02	3.09E-05	0.00E+00	0.00E+00	2.62E-06	9.09E-07	4.36E-08	1.14E+00
004.2-03.2	1.65E+03	11400	12800	9.90E-02	1.41E-05	2.78E-04	6.20E-05	2.12E-06	8.80E-07	5.91E-08	1.40E+00
	2.09E+03	11600	13900	1.03E-01	1.61E-05	2.94E-04	6.49E-05	2.37E-06	9.49E-07	6.62E-08	1.54E+00
	9.50E+02	11200	11500	9.30E-02	1.21E-05	2.59E-04	5.96E-05	1.92E-06	8.12E-07	5.05E-08	1.31E+00
004.2-04.3	2.89E+03	9670	16900	9.80E-02	1.80E-05	4.30E-04	1.09E-04	2.63E-06	1.41E-06	8.07E-08	6.58E-01
	3.70E+03	9760	17900	1.01E-01	2.07E-05	4.56E-04	1.13E-04	3.04E-06	1.52E-06	8.96E-08	7.74E-01
	7.80E+02	9560	15900	9.40E-02	1.38E-05	4.05E-04	1.05E-04	2.16E-06	1.29E-06	7.22E-08	5.65E-01
004.6+06.0	2.97E+03	6660	9250	1.41E-01	1.01E-04	7.95E-04	2.63E-04	1.03E-05	6.91E-06	1.96E-07	1.41E+00
	4.39E+03	6800	9680	1.47E-01	1.21E-04	9.96E-04	3.32E-04	1.23E-05	8.50E-06	2.21E-07	1.46E+00
	8.00E+01	6550	8920	1.36E-01	2.10E-05	2.82E-04	9.60E-05	6.30E-06	1.46E-06	1.21E-07	1.37E+00
004.8+02.0	4.97E+03	7940	10500	8.80E-02	4.58E-05	3.35E-04	-	4.17E-06	9.42E-07	1.70E-07	3.18E+00
	6.18E+03	8250	10900	9.10E-02	5.10E-05	4.37E-04	-	4.93E-06	1.08E-06	1.95E-07	3.24E+00
	2.62E+03	7640	10100	8.50E-02	4.04E-05	2.26E-04	-	3.14E-06	8.00E-07	1.27E-07	3.12E+00
004.8-05.0	1.25E+03	7900	20700	1.61E-01	3.73E-05	8.64E-04	5.09E-04	6.30E-06	4.93E-06	1.76E-07	1.44E+00
	1.77E+03	8060	22100	1.64E-01	4.23E-05	9.42E-04	5.62E-04	6.97E-06	5.30E-06	1.87E-07	1.46E+00
	4.70E+02	7760	19400	1.59E-01	3.29E-05	7.45E-04	4.27E-04	5.74E-06	4.44E-06	1.65E-07	1.41E+00
005.0-03.9	4.13E+02	17500	17200	1.56E-01	1.07E-05	4.90E-05	1.96E-05	3.29E-06	6.04E-07	6.72E-09	1.03E+00
	5.91E+02	18400	17800	1.66E-01	1.16E-05	6.14E-05	2.47E-05	3.72E-06	7.00E-07	8.31E-09	1.10E+00
	2.35E+02	15800	16400	1.21E-01	9.50E-06	4.22E-05	1.60E-05	2.81E-06	5.28E-07	4.99E-09	9.27E-01
005.2+05.6	1.67E+03	8490	12600	1.58E-01	2.55E-04	3.85E-04	2.11E-04	1.00E-05	2.30E-06	3.45E-07	2.03E+00
	2.21E+03	8590	13000	1.62E-01	3.78E-04	4.15E-04	2.25E-04	1.32E-05	2.47E-06	4.65E-07	2.13E+00
	7.60E+02	8400	12200	1.51E-01	3.30E-05	3.59E-04	1.95E-04	5.30E-06	2.09E-06	1.91E-07	1.99E+00
005.5+06.1	7.07E+02	-	7110	1.27E-01	7.59E-05	3.47E-05	8.99E-06	5.70E-06	6.07E-07	2.50E-08	2.12E+00
	9.25E+02	-	7240	1.42E-01	8.19E-05	3.65E-05	1.04E-05	6.27E-06	6.28E-07	2.75E-08	2.16E+00
	4.83E+02	-	7000	1.25E-01	0.00E+00	0.00E+00	0.00E+00	4.55E-06	0.00E+00	0.00E+00	2.09E+00
005.5-04.0	1.07E+03	8050	-	1.41E-01	4.47E-05	2.12E-03	-	2.09E-05	1.32E-05	5.41E-07	8.20E-01
	1.24E+03	9310	-	1.44E-01	4.79E-05	2.67E-03	-	2.67E-05	1.62E-05	6.53E-07	8.68E-01
	9.00E+02	7510	-	1.39E-01	3.95E-05	0.00E+00	-	0.00E+00	0.00E+00	1.33E-07	7.67E-01
005.8-06.1	4.21E+03	9080	8540	1.25E-01	1.43E-03	7.31E-04	2.07E-04	3.00E-03	5.72E-06	2.39E-07	3.44E-01
	5.27E+03	9510	8830	1.29E-01	2.33E-03	8.24E-04	2.46E-04	6.00E-03	6.28E-06	2.66E-07	4.02E-01

PN G	n_e(SII)	T_e(OIII)	T_e(NII)	He/H	N/H	O/H	Ne/H	S/H	Ar/H	Cl/H	ext.C
	2.81E+03	8670	8340	1.20E-01	9.30E-04	5.49E-04	1.36E-04	2.00E-03	4.70E-06	2.01E-07	2.93E-01
006.1+08.3	6.39E+03	10200	12800	1.10E-01	1.37E-04	3.18E-04	8.78E-05	6.34E-06	8.26E-07	1.61E-07	1.87E+00
	8.53E+03	10400	13400	1.12E-01	2.03E-04	3.44E-04	9.53E-05	8.98E-06	8.72E-07	2.14E-07	1.89E+00
	3.41E+03	10000	12200	1.08E-01	2.90E-05	2.91E-04	7.89E-05	3.18E-06	7.80E-07	5.80E-08	1.85E+00
006.4+02.0	1.10E+04	7530	9480	1.24E-01	9.00E-03	9.24E-04	2.35E-04	1.40E-02	5.38E-06	2.02E-07	1.48E+00
	1.43E+04	7730	12400	1.27E-01	1.40E-02	1.05E-03	2.63E-04	2.40E-02	5.83E-06	2.31E-07	1.54E+00
	0.00E+00	7340	8900	1.21E-01	3.00E-03	7.42E-04	2.00E-04	0.00E+00	4.83E-06	1.44E-07	1.42E+00
006.4-04.6	1.01E+03	10600	11500	1.31E-01	8.01E-05	6.81E-04	-	8.84E-06	5.38E-06	2.36E-07	8.10E-01
	1.19E+03	10700	11800	1.33E-01	8.77E-05	7.33E-04	-	9.68E-06	5.76E-06	2.51E-07	9.04E-01
	7.50E+02	10400	11200	1.29E-01	7.10E-05	6.39E-04	-	8.06E-06	5.04E-06	2.20E-07	7.14E-01
006.8+02.3	3.00E+03	14000	11800	1.11E-01	7.44E-04	2.96E-04	6.61E-05	4.08E-06	7.98E-07	1.02E-07	1.94E+00
	3.62E+03	14200	12000	1.13E-01	9.81E-04	3.18E-04	6.90E-05	4.59E-06	8.40E-07	1.15E-07	1.98E+00
	1.91E+03	13800	11600	1.09E-01	4.25E-04	2.72E-04	6.12E-05	3.20E-06	7.56E-07	8.80E-08	1.90E+00
006.8-03.4	4.38E+03	11800	11400	9.00E-02	2.53E-05	2.68E-04	5.01E-05	1.75E-06	7.48E-07	8.28E-08	1.30E+00
	5.54E+03	12000	12400	9.40E-02	3.63E-05	2.93E-04	5.35E-05	2.19E-06	8.17E-07	9.68E-08	1.38E+00
	9.70E+02	11600	10600	8.60E-02	5.00E-06	1.40E-04	2.97E-05	1.10E-06	6.92E-07	5.90E-08	1.23E+00
007.0+06.3	3.57E+03	7470	8960	1.10E-01	6.28E-05	7.48E-04	2.09E-04	9.60E-06	2.94E-06	1.60E-07	1.45E+00
	4.62E+03	7570	9210	1.14E-01	7.39E-05	8.75E-04	2.44E-04	1.07E-05	3.20E-06	1.77E-07	1.52E+00
	5.60E+02	7390	8760	1.06E-01	4.09E-05	0.00E+00	0.00E+00	8.24E-06	2.66E-06	1.36E-07	1.39E+00
007.0-06.8	3.35E+03	8030	8690	1.07E-01	4.70E-04	5.56E-04	1.46E-04	2.35E-05	3.20E-06	4.16E-07	5.60E-01
	3.81E+03	8140	8960	1.11E-01	5.57E-04	6.07E-04	1.55E-04	2.77E-05	3.41E-06	4.90E-07	6.05E-01
	2.40E+03	7920	8440	1.04E-01	3.91E-04	5.15E-04	1.37E-04	1.91E-05	2.99E-06	3.61E-07	5.13E-01
007.5+04.3	2.50E+02	35000	-	7.50E-02	2.07E-06	8.31E-06	5.63E-06	5.84E-07	4.02E-08	4.76E-09	1.51E+00
	4.99E+02	35100	-	7.90E-02	2.60E-06	8.62E-06	6.05E-06	7.66E-07	4.21E-08	5.77E-09	1.60E+00
	0.00E+00	34900	-	7.00E-02	1.33E-06	8.04E-06	5.19E-06	9.60E-08	3.85E-08	4.01E-09	1.40E+00
007.5+07.4	8.90E+02	9350	8840	1.48E-01	2.06E-04	6.88E-04	2.82E-04	6.65E-06	5.41E-06	1.29E-07	7.04E-01
	9.92E+02	9440	8920	1.50E-01	2.14E-04	7.85E-04	3.19E-04	7.05E-06	6.12E-06	1.34E-07	7.35E-01
	7.88E+02	9250	8780	1.46E-01	1.98E-04	4.97E-04	2.00E-04	6.07E-06	4.24E-06	1.22E-07	6.70E-01
007.6+06.9	9.21E+02	9210	9700	1.31E-01	7.10E-05	1.08E-03	3.74E-04	5.86E-06	3.79E-06	1.90E-07	6.55E-01
	1.26E+03	9360	10000	1.34E-01	8.12E-05	1.60E-03	5.62E-04	6.65E-06	3.96E-06	2.02E-07	7.14E-01
	2.15E+02	9100	9390	1.28E-01	4.80E-05	0.00E+00	0.00E+00	4.82E-06	3.61E-06	1.76E-07	6.06E-01
007.8-03.7	6.82E+02	9020	8370	1.37E-01	2.32E-04	6.23E-04	2.02E-04	5.42E-06	3.17E-06	2.08E-07	7.74E-01
	8.04E+02	9060	8440	1.39E-01	2.42E-04	7.21E-04	2.29E-04	6.23E-06	3.26E-06	2.25E-07	8.05E-01

PN G	n_e(SII)	T_e(OIII)	T_e(NII)	He/H	N/H	O/H	Ne/H	S/H	Ar/H	Cl/H	ext.C
	5.14E+02	8980	8300	1.34E-01	2.17E-04	4.44E-04	1.45E-04	4.46E-06	3.09E-06	1.75E-07	7.51E-01
007.8-04.4	1.23E+04	-	5550	1.80E-02	6.04E-05	5.09E-05	-	3.72E-06	5.18E-08	-	9.12E-01
	1.67E+04	-	6100	2.00E-02	7.45E-05	8.02E-05	-	5.67E-06	6.90E-08	-	9.66E-01
	8.00E+02	-	5240	1.70E-02	0.00E+00	0.00E+00	-	2.19E-06	0.00E+00	-	8.75E-01
008.4-03.6	6.11E+02	-	5870	1.06E-01	6.91E-05	3.46E-05	3.61E-06	5.97E-06	4.72E-07	5.24E-09	1.13E+00
	7.38E+02	-	5920	1.09E-01	7.30E-05	3.65E-05	4.90E-06	6.64E-06	5.03E-07	5.79E-09	1.20E+00
	4.18E+02	-	5820	1.02E-01	6.52E-05	3.31E-05	2.69E-06	5.25E-06	4.37E-07	4.69E-09	1.05E+00
008.6-02.6	3.16E+03	11000	10400	9.60E-02	2.87E-05	2.27E-04	4.32E-05	2.54E-06	8.15E-07	4.14E-08	1.84E+00
	4.48E+03	11100	10700	1.00E-01	3.42E-05	2.41E-04	4.52E-05	2.77E-06	9.00E-07	4.50E-08	1.91E+00
	1.52E+03	10900	10100	9.30E-02	2.40E-05	2.13E-04	4.17E-05	2.17E-06	7.59E-07	3.66E-08	1.76E+00
009.4-09.8	2.22E+03	8550	10300	1.23E-01	5.65E-05	6.32E-04	2.31E-04	5.63E-06	2.72E-06	1.29E-07	4.00E-01
	3.24E+03	8810	10600	1.26E-01	6.87E-05	7.75E-04	2.95E-04	6.72E-06	3.06E-06	1.41E-07	4.46E-01
	7.40E+02	8350	10000	1.19E-01	2.47E-05	0.00E+00	0.00E+00	3.56E-06	2.38E-06	9.70E-08	3.75E-01
009.8-04.6	1.43E+03	9850	9160	1.14E-01	4.36E-04	6.97E-04	2.06E-04	1.64E-05	4.23E-06	2.41E-07	6.34E-01
	1.57E+03	9990	9350	1.15E-01	5.34E-04	7.42E-04	2.18E-04	1.83E-05	4.51E-06	2.69E-07	6.86E-01
	1.19E+03	9670	8970	1.13E-01	3.29E-04	6.58E-04	1.90E-04	1.32E-05	3.95E-06	2.00E-07	5.94E-01
351.1+04.8	4.78E+03	7700	8620	1.07E-01	4.95E-04	5.09E-04	1.14E-04	2.40E-04	3.56E-06	1.45E-07	8.19E-01
	6.58E+03	7780	9930	1.11E-01	7.83E-04	5.51E-04	1.25E-04	4.41E-04	3.79E-06	1.56E-07	8.72E-01
	0.00E+00	7630	8310	1.03E-01	4.50E-05	4.28E-04	9.20E-05	0.00E+00	3.25E-06	1.37E-07	7.63E-01
351.2+05.2	1.43E+03	-	5920	9.00E-02	2.83E-04	3.93E-04	7.77E-05	7.21E-06	1.86E-06	1.12E-07	6.25E-01
	2.08E+03	-	6050	1.01E-01	3.98E-04	7.70E-04	1.53E-04	9.03E-06	3.23E-06	2.03E-07	7.09E-01
	0.00E+00	-	5810	8.60E-02	9.30E-05	0.00E+00	0.00E+00	4.14E-06	6.30E-07	3.10E-08	5.34E-01
351.6-06.2	1.28E+03	9890	8230	1.34E-01	7.39E-04	6.72E-04	1.93E-04	1.48E-05	7.69E-06	3.14E-07	5.87E-01
	1.56E+03	10100	8310	1.35E-01	8.38E-04	7.58E-04	2.14E-04	1.64E-05	8.49E-06	3.41E-07	6.25E-01
	9.70E+02	9640	8140	1.33E-01	5.89E-04	6.05E-04	1.67E-04	1.23E-05	7.02E-06	2.87E-07	5.54E-01
351.9+09.0	3.41E+02	12700	-	1.03E-01	1.72E-05	3.55E-04	1.03E-04	1.11E-06	1.33E-06	8.53E-08	2.95E-01
	6.31E+02	12800	-	1.04E-01	2.16E-05	3.64E-04	1.06E-04	1.21E-06	1.35E-06	8.80E-08	3.25E-01
	0.00E+00	12600	-	1.02E-01	1.15E-05	3.46E-04	1.00E-04	9.60E-07	1.30E-06	8.13E-08	2.68E-01
351.9-01.9	6.43E+03	9310	12400	1.09E-01	2.68E-04	4.99E-04	1.39E-04	1.35E-05	1.85E-06	3.91E-07	2.64E+00
	8.34E+03	9450	13200	1.13E-01	3.99E-04	5.32E-04	1.47E-04	1.85E-05	2.00E-06	5.30E-07	2.72E+00
	2.40E+03	9150	11900	1.05E-01	0.00E+00	4.40E-04	1.26E-04	2.10E-06	1.68E-06	7.30E-08	2.57E+00
352.0-04.6	3.45E+03	9190	6250	1.42E-01	6.43E-04	2.39E-03	9.15E-04	2.80E-05	2.14E-05	2.60E-07	1.50E+00
	3.81E+03	9380	6790	1.50E-01	6.90E-04	2.97E-03	1.17E-03	3.25E-05	2.50E-05	2.79E-07	1.60E+00

PN G	n_e(SII)	T_e(OIII)	T_e(NII)	He/H	N/H	O/H	Ne/H	S/H	Ar/H	Cl/H	ext.C
	2.94E+03	8970	5930	1.33E-01	5.67E-04	1.34E-03	5.04E-04	2.28E-05	1.59E-05	2.29E-07	1.40E+00
352.1+05.1	3.87E+03	8630	8770	1.31E-01	5.54E-04	6.81E-04	2.71E-04	1.75E-04	5.69E-06	2.36E-07	1.00E+00
	5.70E+03	8860	9230	1.38E-01	8.20E-04	7.69E-04	3.18E-04	3.11E-04	6.40E-06	2.56E-07	1.08E+00
	0.00E+00	8350	8450	1.25E-01	0.00E+00	3.97E-04	1.61E-04	0.00E+00	3.07E-06	2.03E-07	9.51E-01
352.6+03.0	4.12E+03	7900	8970	1.49E-01	6.29E-04	7.07E-04	2.83E-04	1.62E-05	5.52E-06	3.49E-07	2.42E+00
	5.22E+03	7950	9310	1.54E-01	8.74E-04	7.64E-04	3.07E-04	2.01E-05	5.92E-06	4.11E-07	2.47E+00
	6.40E+02	7810	8700	1.45E-01	1.04E-04	2.96E-04	1.18E-04	9.40E-06	5.15E-06	1.95E-07	2.36E+00
353.2-05.2	8.74E+01	9280	8090	1.70E-01	6.94E-04	2.60E-04	1.23E-04	4.38E-06	2.76E-06	3.03E-08	6.75E-01
	1.38E+02	9380	8130	1.72E-01	7.85E-04	2.70E-04	1.35E-04	5.58E-06	2.85E-06	3.25E-08	7.09E-01
	1.12E+01	9180	8020	1.67E-01	5.89E-04	2.44E-04	1.14E-04	3.25E-06	2.66E-06	2.84E-08	6.48E-01
353.3+06.3	6.17E+03	10000	10700	8.70E-02	7.32E-05	2.63E-04	4.79E-05	5.30E-06	8.80E-07	8.47E-08	4.86E-01
	8.02E+03	10100	11400	9.10E-02	9.97E-05	2.83E-04	5.11E-05	6.81E-06	9.28E-07	1.11E-07	5.15E-01
	4.01E+03	9900	10200	8.20E-02	-	2.30E-04	4.14E-05	2.33E-06	8.35E-07	3.32E-08	4.53E-01
353.7+06.3	9.41E+02	7130	7460	1.09E-01	1.24E-04	4.39E-04	8.64E-05	7.91E-06	3.65E-06	1.74E-07	6.37E-01
	1.39E+03	7210	7580	1.11E-01	1.39E-04	4.84E-04	1.08E-04	9.22E-06	4.10E-06	1.89E-07	6.71E-01
	6.01E+02	7060	7350	1.06E-01	1.09E-04	3.78E-04	7.03E-05	6.77E-06	3.29E-06	1.61E-07	5.92E-01
354.5+03.3	2.04E+04	10200	14900	8.90E-02	9.17E-04	6.06E-04	-	2.09E-05	3.07E-06	5.28E-07	3.30E+00
	3.34E+04	10300	20600	9.30E-02	1.40E-03	6.45E-04	-	3.19E-05	3.28E-06	8.05E-07	3.37E+00
	0.00E+00	10000	12600	8.50E-02	5.70E-04	0.00E+00	-	1.32E-05	2.82E-06	4.19E-07	3.23E+00
355.4-02.4	3.14E+03	8190	8690	1.39E-01	1.33E-03	6.97E-04	2.57E-04	2.43E-05	6.20E-06	5.04E-07	1.69E+00
	4.33E+03	8350	9130	1.44E-01	2.01E-03	7.63E-04	2.84E-04	3.25E-05	6.82E-06	6.49E-07	1.84E+00
	0.00E+00	8080	8480	1.30E-01	0.00E+00	5.60E-04	1.92E-04	9.60E-06	5.32E-06	2.71E-07	1.58E+00
355.9+03.6	1.04E+04	10500	15900	5.10E-02	1.79E-05	5.39E-05	1.65E-06	4.82E-06	9.63E-07	3.08E-08	1.07E+00
	1.53E+04	10900	18400	5.30E-02	2.05E-05	5.84E-05	1.94E-06	5.68E-06	1.06E-06	3.51E-08	1.14E+00
	0.00E+00	10200	14500	4.90E-02	1.40E-05	4.26E-05	1.34E-06	3.69E-06	8.49E-07	2.14E-08	9.93E-01
355.9-04.2	6.44E+03	6190	6380	1.30E-01	4.90E-04	1.40E-03	2.08E-04	1.96E-05	7.31E-06	3.49E-07	3.66E-01
	9.45E+03	6260	7760	1.40E-01	5.86E-04	2.17E-03	3.26E-04	2.89E-05	8.27E-06	3.72E-07	4.45E-01
	0.00E+00	6110	6000	1.22E-01	3.82E-04	0.00E+00	1.20E-05	0.00E+00	6.08E-06	3.10E-07	2.79E-01
356.1-03.3	9.51E+02	8520	6160	1.38E-01	7.51E-04	5.00E-03	3.00E-03	2.24E-05	4.47E-06	5.06E-07	1.16E+00
	1.26E+03	8730	6560	1.42E-01	8.76E-04	7.00E-03	4.00E-03	2.61E-05	4.85E-06	5.88E-07	1.25E+00
	6.51E+02	8350	5810	1.32E-01	5.66E-04	2.00E-03	1.00E-03	1.92E-05	3.94E-06	4.05E-07	1.10E+00
356.3-06.2	2.14E+02	9580	8920	1.36E-01	2.65E-04	5.01E-04	-	6.56E-06	2.21E-06	1.81E-07	6.47E-01
	2.70E+02	9640	9000	1.38E-01	2.75E-04	5.22E-04	-	7.31E-06	2.30E-06	1.96E-07	6.79E-01

PN G	n_e(SII)	T_e(OIII)	T_e(NII)	He/H	N/H	O/H	Ne/H	S/H	Ar/H	Cl/H	ext.C
	1.58E+02	9500	8840	1.33E-01	2.51E-04	4.71E-04	-	5.90E-06	2.10E-06	1.53E-07	6.23E-01
356.5-03.6	2.68E+03	8750	7920	1.37E-01	2.94E-04	7.28E-04	-	1.04E-05	4.63E-06	2.70E-07	2.53E+00
	3.05E+03	8860	8010	1.40E-01	3.10E-04	7.70E-04	-	1.15E-05	4.90E-06	2.82E-07	2.59E+00
	2.19E+03	8650	7780	1.34E-01	2.72E-04	6.79E-04	-	9.20E-06	4.40E-06	2.55E-07	2.46E+00
356.8+03.3	8.42E+03	11900	6360	5.90E-02	1.99E-04	5.12E-04	-	2.34E-06	6.40E-07	3.50E-08	1.56E+00
	1.40E+04	13300	7720	6.70E-02	2.85E-04	1.01E-03	-	3.62E-06	8.58E-07	4.50E-08	1.84E+00
	0.00E+00	10500	5750	4.90E-02	0.00E+00	0.00E+00	-	0.00E+00	2.93E-07	1.59E-08	1.34E+00
356.8-05.4	6.70E+01	9200	8030	1.31E-01	1.23E-04	7.15E-04	-	6.42E-06	3.78E-06	9.44E-08	8.92E-01
	1.33E+02	9290	8170	1.33E-01	1.34E-04	7.57E-04	-	6.76E-06	4.05E-06	9.80E-08	9.20E-01
	0.00E+00	9130	7910	1.30E-01	1.12E-04	6.64E-04	-	6.15E-06	3.38E-06	8.85E-08	8.63E-01
356.9+04.4	4.56E+03	11900	7940	7.50E-02	1.04E-04	9.30E-04	1.71E-04	5.86E-06	6.97E-06	1.42E-07	1.20E+00
	5.86E+03	12200	8710	7.90E-02	1.19E-04	1.06E-03	1.96E-04	6.76E-06	7.97E-06	1.59E-07	1.34E+00
	1.50E+03	11600	7210	7.00E-02	8.80E-05	6.23E-04	1.17E-04	4.76E-06	5.19E-06	1.16E-07	1.06E+00
357.0+02.4	1.90E+03	8860	8800	1.36E-01	3.80E-04	7.39E-04	2.31E-04	1.55E-05	6.81E-06	3.94E-07	2.49E+00
	2.15E+03	9040	8930	1.39E-01	4.19E-04	7.95E-04	2.48E-04	1.82E-05	7.38E-06	4.31E-07	2.54E+00
	1.63E+03	8630	8680	1.34E-01	3.52E-04	6.83E-04	2.08E-04	1.38E-05	6.37E-06	3.38E-07	2.43E+00
357.1+03.6	8.74E+01	6970	8030	9.40E-02	4.46E-05	1.71E-03	3.47E-04	1.29E-05	4.63E-06	1.29E-07	2.19E-01
	1.74E+02	7170	8390	1.00E-01	5.07E-05	2.12E-03	4.27E-04	1.59E-05	5.70E-06	1.48E-07	3.33E-01
	0.00E+00	6730	7790	8.90E-02	3.67E-05	1.13E-03	2.62E-04	9.80E-06	3.64E-06	1.12E-07	7.70E-02
357.1+04.4	1.34E+03	6900	10400	1.39E-01	2.34E-05	2.87E-03	1.33E-03	8.86E-06	6.07E-06	1.65E-07	1.46E+00
	1.49E+03	7430	11500	1.41E-01	2.51E-05	3.53E-03	1.69E-03	1.10E-05	6.96E-06	1.87E-07	1.47E+00
	1.18E+03	6580	9400	1.37E-01	2.06E-05	1.12E-03	3.60E-04	4.52E-06	4.14E-06	1.14E-07	1.43E+00
357.1-04.7	1.22E+04	-	5620	1.60E-02	7.68E-05	5.44E-06	-	1.78E-06	5.89E-09	4.03E-08	6.13E-01
	1.89E+04	-	6240	1.70E-02	1.25E-04	7.79E-06	-	3.16E-06	7.70E-09	5.81E-08	6.58E-01
	0.00E+00	-	5100	1.50E-02	2.49E-05	0.00E+00	-	0.00E+00	0.00E+00	0.00E+00	5.67E-01
357.2+02.0	3.61E+03	10000	10500	1.10E-01	8.89E-05	7.31E-04	2.10E-04	5.93E-06	2.34E-06	1.02E-07	2.25E+00
	4.74E+03	10100	10900	1.13E-01	1.04E-04	8.50E-04	2.43E-04	6.64E-06	2.51E-06	1.11E-07	2.32E+00
	1.36E+03	9900	10200	1.07E-01	4.82E-05	3.39E-04	1.12E-04	4.87E-06	2.14E-06	9.00E-08	2.16E+00
357.3+04.0	2.92E+03	8170	12300	1.09E-01	3.27E-05	7.33E-04	1.88E-04	5.46E-06	3.56E-06	1.03E-07	1.19E+00
	3.85E+03	8240	12600	1.13E-01	3.67E-05	7.73E-04	1.96E-04	5.78E-06	3.83E-06	1.11E-07	1.25E+00
	1.68E+03	8110	11800	1.06E-01	2.87E-05	6.92E-04	1.80E-04	4.88E-06	3.27E-06	9.40E-08	1.13E+00
357.5+03.1	1.31E+03	-	10100	-	1.79E-05	5.03E-05	-	7.49E-07	1.24E-07	7.67E-08	1.89E+00
	1.40E+03	-	10800	-	2.12E-05	6.70E-05	-	8.57E-07	1.55E-07	9.46E-08	1.92E+00

PN G	n_e(SII)	T_e(OIII)	T_e(NII)	He/H	N/H	O/H	Ne/H	S/H	Ar/H	Cl/H	ext.C
	1.19E+03	-	9500	-	1.49E-05	2.18E-05	-	6.12E-07	9.30E-08	5.52E-08	1.86E+00
357.5+03.2	1.18E+03	8420	8530	1.21E-01	1.18E-03	1.93E-03	1.01E-03	4.80E-05	1.28E-05	4.68E-07	2.18E+00
	1.64E+03	9580	8690	1.28E-01	1.59E-03	2.57E-03	1.38E-03	7.07E-05	1.65E-05	6.14E-07	2.31E+00
	7.30E+02	7160	8270	1.15E-01	2.50E-04	4.20E-04	0.00E+00	0.00E+00	4.70E-06	8.90E-08	2.02E+00
357.6-03.3	3.21E+02	-	7390	1.49E-01	5.26E-05	5.79E-05	2.47E-05	4.60E-06	4.86E-07	-	1.51E+00
	3.87E+02	-	7550	1.51E-01	5.46E-05	6.02E-05	2.72E-05	4.91E-06	4.96E-07	-	1.52E+00
	2.45E+02	-	7250	1.47E-01	5.06E-05	5.58E-05	2.19E-05	4.25E-06	4.77E-07	-	1.48E+00
357.9-03.8	1.90E+03	21000	21600	1.77E-01	5.30E-06	4.35E-05	1.99E-05	1.47E-07	5.00E-07	1.08E-08	1.48E+00
	2.41E+03	21400	23100	1.78E-01	6.11E-06	4.52E-05	2.10E-05	1.62E-07	5.22E-07	1.16E-08	1.49E+00
	6.80E+02	20600	20600	1.76E-01	4.25E-06	4.19E-05	1.90E-05	1.33E-07	4.81E-07	1.00E-08	1.47E+00
358.0+09.3	1.00E+00	10200	-	1.13E-01	1.95E-05	3.41E-04	9.58E-05	7.79E-07	1.32E-06	3.36E-08	5.12E-01
	1.00E+00	10300	-	1.17E-01	2.05E-05	3.55E-04	9.90E-05	8.63E-07	1.39E-06	3.80E-08	5.78E-01
	0.00E+00	10100	-	1.09E-01	1.76E-05	3.21E-04	9.21E-05	6.90E-07	1.24E-06	3.01E-08	4.45E-01
358.2+03.5	8.37E+03	10900	12400	9.40E-02	1.33E-04	3.30E-04	7.79E-05	5.27E-06	1.09E-06	1.30E-07	2.33E+00
	1.19E+04	11200	13800	9.90E-02	2.20E-04	3.71E-04	8.53E-05	7.03E-06	1.19E-06	1.70E-07	2.41E+00
	1.25E+03	10600	11300	8.90E-02	1.00E-06	2.70E-04	6.50E-05	1.01E-06	9.60E-07	1.90E-08	2.21E+00
358.2+04.2	9.24E+03	7950	9310	1.28E-01	1.95E-04	6.39E-04	2.12E-04	9.31E-06	3.98E-06	2.35E-07	2.05E+00
	1.13E+04	8000	9660	1.31E-01	2.61E-04	7.16E-04	2.32E-04	1.12E-05	4.36E-06	2.73E-07	2.12E+00
	6.20E+03	7900	8970	1.23E-01	5.40E-05	3.61E-04	1.14E-04	5.47E-06	3.66E-06	1.76E-07	1.98E+00
358.5+02.9	7.52E+03	11400	9170	8.00E-02	2.42E-05	3.02E-04	6.66E-05	2.44E-06	8.54E-07	3.79E-08	1.94E+00
	1.11E+04	11900	11700	8.10E-02	3.90E-05	3.42E-04	7.69E-05	3.45E-06	9.27E-07	4.01E-08	1.96E+00
	0.00E+00	11200	6660	7.80E-02	1.06E-05	2.28E-04	4.86E-05	1.86E-06	5.05E-07	3.38E-08	1.91E+00
358.5-04.2	1.34E+04	9630	11600	9.20E-02	8.88E-05	2.28E-04	3.68E-05	1.37E-05	9.41E-07	4.63E-08	1.40E+00
	2.12E+04	9780	14200	9.70E-02	1.18E-04	2.55E-04	4.22E-05	2.43E-05	1.04E-06	5.08E-08	1.50E+00
	0.00E+00	9450	10100	8.60E-02	4.11E-05	0.00E+00	0.00E+00	0.00E+00	8.12E-07	4.19E-08	1.32E+00
358.6+07.8	2.51E+03	8730	11900	1.01E-01	2.43E-05	4.85E-04	1.25E-04	1.07E-05	2.10E-06	9.32E-08	8.31E-01
	3.98E+03	8870	12800	1.06E-01	3.16E-05	5.48E-04	1.37E-04	1.57E-05	2.34E-06	1.03E-07	9.20E-01
	0.00E+00	8550	11200	9.60E-02	1.03E-05	4.39E-04	1.16E-04	0.00E+00	1.88E-06	8.21E-08	7.59E-01
358.6-05.5	1.28E+02	8870	8880	1.52E-01	2.62E-04	5.64E-04	2.31E-04	6.73E-06	4.00E-06	1.19E-07	7.01E-01
	1.94E+02	8950	8980	1.54E-01	2.81E-04	6.47E-04	2.71E-04	7.69E-06	4.60E-06	1.30E-07	7.28E-01
	6.70E+01	8820	8760	1.50E-01	2.43E-04	3.51E-04	1.59E-04	5.71E-06	2.87E-06	1.08E-07	6.68E-01
358.7+05.2	6.21E+03	-	5000	1.90E-02	9.29E-05	7.63E-06	-	2.70E-06	1.41E-07	3.67E-08	2.55E+00
	9.31E+03	-	5010	2.00E-02	1.35E-04	9.80E-06	-	3.93E-06	1.77E-07	5.42E-08	2.62E+00

PN G	n_e(SII)	T_e(OIII)	T_e(NII)	He/H	N/H	O/H	Ne/H	S/H	Ar/H	Cl/H	ext.C
	0.00E+00	-	4990	1.80E-02	0.00E+00	0.00E+00	-	0.00E+00	0.00E+00	0.00E+00	2.47E+00
358.9+03.4	9.21E+03	7020	8880	1.16E-01	7.44E-04	9.41E-04	-	1.10E-04	7.79E-06	2.26E-07	1.45E+00
	1.28E+04	7130	11500	1.20E-01	9.82E-04	1.08E-03	-	1.67E-04	8.46E-06	2.41E-07	1.50E+00
	0.00E+00	6930	8350	1.12E-01	0.00E+00	2.27E-04	-	0.00E+00	7.23E-06	2.10E-07	1.39E+00
359.0-04.1	9.61E+02	8880	8540	1.41E-01	5.22E-04	1.83E-03	8.93E-04	1.50E-05	4.63E-06	2.31E-07	1.03E+00
	1.09E+03	8940	8630	1.43E-01	5.73E-04	2.30E-03	1.11E-03	1.67E-05	4.83E-06	2.56E-07	1.05E+00
	7.27E+02	8810	8480	1.39E-01	4.63E-04	1.23E-03	6.10E-04	1.31E-05	4.45E-06	2.02E-07	9.96E-01
359.2+04.7	6.39E+03	-	6490	2.86E-01	5.16E-05	1.00E-03	-	1.52E-06	6.98E-06	8.66E-07	2.27E+00
	9.38E+03	-	7810	3.96E-01	9.72E-05	2.00E-03	-	2.76E-06	1.29E-05	1.61E-06	2.33E+00
	0.00E+00	-	5590	2.66E-01	0.00E+00	0.00E+00	-	0.00E+00	0.00E+00	0.00E+00	2.20E+00
359.3-01.8	7.46E+03	-	6100	1.40E-02	5.02E-05	1.34E-05	-	1.26E-06	1.05E-07	6.33E-08	2.54E+00
	1.16E+04	-	7200	1.50E-02	5.78E-05	1.76E-05	-	1.52E-06	1.15E-07	8.49E-08	2.66E+00
	0.00E+00	-	5840	1.30E-02	3.58E-05	9.30E-06	-	0.00E+00	9.20E-08	0.00E+00	2.45E+00
359.6-04.8	4.79E+02	13200	17600	1.89E-01	9.36E-06	4.66E-04	1.78E-04	2.70E-06	2.33E-06	8.59E-08	6.56E-01
	5.81E+02	13300	18400	1.91E-01	9.71E-06	4.76E-04	1.81E-04	2.90E-06	2.37E-06	9.43E-08	6.65E-01
	4.13E+02	13100	16900	1.87E-01	9.07E-06	4.56E-04	1.73E-04	2.50E-06	2.30E-06	7.54E-08	6.47E-01
359.7-01.8	1.69E+03	12400	9490	8.60E-02	5.29E-05	3.66E-04	-	2.33E-06	1.29E-06	7.69E-08	1.64E+00
	2.14E+03	12500	9700	8.70E-02	5.97E-05	3.86E-04	-	2.66E-06	1.36E-06	8.39E-08	1.74E+00
	1.09E+03	12200	9250	8.40E-02	4.54E-05	3.52E-04	-	1.94E-06	1.18E-06	6.80E-08	1.56E+00
359.8+02.4	1.03E+04	-	6250	5.40E-02	1.36E-04	3.60E-05	-	2.30E-06	1.59E-06	7.71E-08	2.17E+00
	1.48E+04	-	7110	5.70E-02	1.71E-04	4.25E-05	-	3.06E-06	1.80E-06	9.86E-08	2.28E+00
	0.00E+00	-	6000	5.10E-02	0.00E+00	0.00E+00	-	0.00E+00	0.00E+00	0.00E+00	2.07E+00
359.8+03.7	3.36E+03	8630	8070	9.00E-02	2.73E-05	7.34E-04	-	4.99E-06	3.13E-06	8.72E-08	1.50E+00
	4.37E+03	8750	8740	9.30E-02	2.99E-05	8.68E-04	-	5.75E-06	3.45E-06	9.47E-08	1.56E+00
	8.50E+02	8530	7570	8.80E-02	2.30E-05	4.60E-04	-	4.31E-06	2.84E-06	7.83E-08	1.46E+00
359.8+05.2	1.94E+02	-	-	1.00E-01	6.11E-05	5.10E-05	-	9.09E-06	1.36E-06	1.86E-08	6.00E-01
	2.19E+02	-	-	1.02E-01	6.35E-05	5.33E-05	-	9.83E-06	1.41E-06	2.38E-08	6.41E-01
	1.53E+02	-	-	9.80E-02	5.79E-05	4.84E-05	-	8.32E-06	1.31E-06	1.22E-08	5.64E-01
359.8+05.6	6.21E+03	-	5390	1.22E-02	2.57E-04	9.96E-04	-	1.55E-05	9.31E-07	2.12E-07	5.04E-01
	7.64E+03	-	5780	1.31E-02	4.51E-04	1.92E-03	-	2.84E-05	1.61E-06	3.43E-07	5.43E-01
	4.33E+03	-	5070	1.11E-02	1.89E-04	3.83E-04	-	7.40E-06	6.99E-07	1.23E-07	4.58E-01
359.8+06.9	7.63E+02	9660	10000	1.10E-01	3.50E-04	6.06E-04	2.29E-04	4.09E-05	3.51E-06	1.21E-07	1.48E+00
	8.54E+02	9670	10100	1.12E-01	3.79E-04	6.54E-04	2.51E-04	4.94E-05	3.80E-06	1.25E-07	1.51E+00

PN G	n_e(SII)	T_e(OIII)	T_e(NII)	He/H	N/H	O/H	Ne/H	S/H	Ar/H	Cl/H	ext.C
	6.72E+02	9650	9900	1.08E-01	2.85E-04	5.41E-04	2.08E-04	2.27E-05	3.18E-06	1.16E-07	1.45E+00
359.8-07.2	-	11700	-	8.60E-02	1.01E-05	2.92E-04	6.39E-05	-	9.45E-07	1.12E-07	6.20E-02
	-	11900	-	9.10E-02	1.18E-05	3.06E-04	6.83E-05	-	1.01E-06	1.24E-07	1.08E-01
	-	11600	-	8.10E-02	7.30E-06	2.78E-04	6.12E-05	-	8.86E-07	9.80E-08	6.00E-03
359.9-04.5	7.50E+03	8300	9080	1.23E-01	2.75E-04	8.71E-04	-	4.04E-05	5.72E-06	2.55E-07	8.78E-01
	1.08E+04	8450	9760	1.26E-01	3.33E-04	9.47E-04	-	5.99E-05	6.12E-06	2.70E-07	9.40E-01
	0.00E+00	8210	8680	1.19E-01	1.74E-04	7.85E-04	-	0.00E+00	5.26E-06	2.29E-07	8.18E-01

Appendix G

Metallicity Gradient with PN age classification based on AGB models
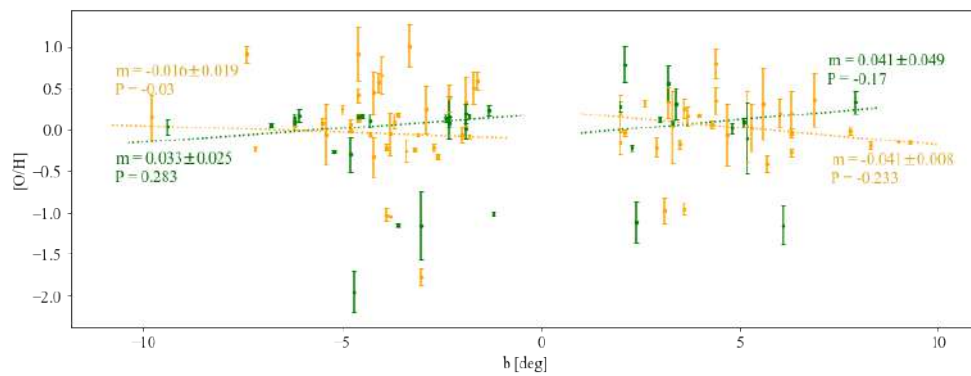
Figure G.1: [O/H] of each PN is plotted against their Galactic latitude. Orange dots are the OPPNe while green bots are the YPPNe. Dashed lines show the error-weighted least squares fitting results. The slope of the best-fit, m, and the Pearson correlation coefficient, r, is shown next to the line.

[1]   A. Acker, J. Marcout, F. Ochsenbein, B. Stenholm, R. Tylenda, and C. Schohn. *The Strasbourg-ESO Catalogue of Galactic Planetary Nebulae. Parts I, II.* 1992.

[2]   A. Ali, M. El-Nawawy, and J. Pfleiderer. "Statistical and physical study of one-sided planetary nebulae". In: *Astrophysics and Space Science* 271.3 (2000), pp. 245–258.

[3]   A. Aller, J. Lillo-Box, D. Jones, L. F. Miranda, and S. B. Forteza. "Planetary nebulae seen with TESS: Discovery of new binary central star candidates from Cycle 1". In: *Astronomy & Astrophysics* 635 (2020), A128.

[4]   A. Aparicio, A. Herrero, F. Sánchez, et al. *Stellar astrophysics for the local group: VIII Canary Islands Winter School of Astrophysics*. Vol. 8. Cambridge University press, 1998.

[5]   J. N. Bahcall and T. Piran. "Stellar collapses in the galaxy". In: *The Astrophysical Journal* 267 (1983), pp. L77–L81.

[6]   B. Balick. "The evolution of planetary nebulae. I-Structures, ionizations, and morphological sequences". In: *The Astronomical Journal* 94 (1987), pp. 671–678.

[7]   B. Balick and F. Adam. "Shapes and shaping of planetary nebulae". In: *Annual Review of Astronomy and Astrophysics* 40 (2002), p. 439.

[8]   B. Balick, A. Frank, and B. Liu. "Models of the Mass-ejection Histories of Pre-planetary Nebulae. IV. Magnetized Winds and the Origins of Jets, Bullets, and FLIERs". In: *The Astrophysical Journal* 889.1 (2020), p. 13.

[9]   T. Bensby, S. Feltzing, A. Gould, J. C. Yee, J. Johnson, M. Asplund, J. Meléndez, S. Lucatello, L. Howes, A. McWilliam, et al. "Chemical evolution of the Galactic bulge as traced by microlensed dwarf and subgiant stars-VI. Age and abundance structure of the stellar populations in the central sub-kpc of the Milky Way". In: *Astronomy & Astrophysics* 605 (2017), A89.

[10]   T. Bensby, J. Yee, S. Feltzing, J. A. Johnson, A. Gould, J. G. Cohen, M. Asplund, J. Melendez, S. Lucatello, C. Han, et al. "Chemical evolution of the Galactic bulge as traced by microlensed dwarf and subgiant stars-V. Evidence for a wide age distribution and a complex MDF". In: *Astronomy & Astrophysics* 549 (2013), A147.

[11]   H. M. Boffin and D. Jones. *The Importance of Binaries in the Formation and Evolution of Planetary Nebulae*. Springer, 2019.

[12]   H. Boffin, F. Dérie, A. Manescau, R. Siebenmorgen, V. Baldini, G. Calderone, R. Cirami, I. Coretti, P. Di Marcantonio, J. Kosmalski, et al. "FORS-Up: Making the most versatile instrument in Paranal ready for 15 more years of operations". In: *Ground-based and Airborne Instrumentation for Astronomy VIII*. Vol. 11447. International Society for Optics and Photonics. 2020, 114477A.

[13]   C. Chiappini, S. Górny, G. Stasińska, and B. Barbuy. "Abundances in the Galactic bulge: results from planetary nebulae and giant stars". In: *Astronomy & Astrophysics* 494.2 (2009), pp. 591–610.

[14]   N. Chornay, N. Walton, D. Jones, H. Boffin, M. Rejkuba, and R. Wesson. "Towards a more complete sample of binary central stars of planetary nebulae with Gaia". In: *Astronomy & Astrophysics* 648 (2021), A95.

[15]   J. Cliffe, A. Frank, M. Livio, and T. W. Jones. "Precessing jets and point-symmetric nebulae". In: *The Astrophysical Journal* 447.1 (1995), p. L49.

[16] R. Corradi and H. Schwarz. "Morphological populations of planetary nebulae: which progenitors? I. Comparative properties of bipolar nebulae." In: *Astronomy and Astrophysics* 293 (1995), pp. 871–888.

[17] R. L. Corradi, J. Garcıéa-Rojas, D. Jones, and P. Rodrıéguez-Gil. "Binarity and the abundance discrepancy problem in planetary nebulae". In: *The Astrophysical Journal* 803.2 (2015), p. 99.

[18] F. Cuisinier, W. Maciel, J. Köppen, A. Acker, and B. Stenholm. "Observations of planetary nebulae in the Galactic Bulge". In: *arXiv preprint astro-ph/9910521* (1999).

[19] H. D. Curtis. "The planetary nebulae". In: *Publications of Lick Observatory* 13 (1918), pp. 55–74.

[20] K. P. Dere, G. Del Zanna, P. R. Young, E. Landi, and R. S. Sutherland. "CHIANTI—an atomic database for emission lines. XV. Version 9, improvements for the X-ray satellite lines". In: *The Astrophysical Journal Supplement Series* 241.2 (2019), p. 22.

[21] K. Dere, E. Landi, H. Mason, B. M. Fossi, and P. Young. "CHIANTI-an atomic database for emission lines-I. Wavelengths greater than 50 Å". In: *Astronomy and Astrophysics Supplement Series* 125.1 (1997), pp. 149–173.

[22] P. G. van Dokkum, J. Bloom, and M. Tewes. "LA Cosmic: Laplacian Cosmic Ray Identification". In: *Astrophysics Source Code Library* (2012), ascl–1207.

[23] A. Escudero and R. Costa. "Abundances of recently discovered planetary nebulae towards the galactic bulge". In: *Astronomy & Astrophysics* 380.1 (2001), pp. 300–308.

[24] A. Escudero, R. Costa, and W. Maciel. "New abundances of planetary nebulae in the Galactic Bulge". In: *Astronomy & Astrophysics* 414.1 (2004), pp. 211–221.

[25] E. L. Fitzpatrick. "Correcting for the effects of interstellar extinction". In: *Publications of the Astronomical Society of the Pacific* 111.755 (1999), p. 63.

[26] *FORS2, FOcal Reducer/low dispersion Spectrograph 2*. 2022. URL: https://www.eso.org/sci/facilities/paranal/instruments/fors/img/cut_col.gif (visited on 02/01/2022).

[27] F. Fragkoudi, P. Di Matteo, M. Haywood, S. Khoperskov, A. Gomez, M. Schultheis, F. Combes, and B. Semelin. "What the Milky Way bulge reveals about the initial metallicity gradients in the disc". In: *Astronomy & Astrophysics* 607 (2017), p. L4.

[28] A. Frank, Z. Chen, T. Reichardt, O. De Marco, E. Blackman, and J. Nordhaus. "Planetary Nebulae Shaped by Common Envelope Evolution". In: *Galaxies* 6.4 (2018), p. 113.

[29] K. Freeman, M. Ness, E. Wylie-de-Boer, E. Athanassoula, J. Bland-Hawthorn, M. Asplund, G. Lewis, D. Yong, R. Lane, L. Kiss, et al. "ARGOS–II. The Galactic bulge survey". In: *Monthly Notices of the Royal Astronomical Society* 428.4 (2013), pp. 3660–3670.

[30] D. J. Frew and Q. A. Parker. "Planetary nebulae: observational properties, mimics and diagnostics". In: *Publications of the Astronomical Society of Australia* 27.2 (2010), pp. 129–148.

[31] M. Galavıs, C. Mendoza, and C. Zeippen. "Atomic data from the IRON Project". In: *Astron. Astrophys. Suppl. Ser* 133 (1998), pp. 245–248.

[32]   J. Garcıéa-Rojas, R. L. Corradi, H. Monteiro, D. Jones, P. Rodrıéguez-Gil, and A. Cabrera-Lavers. "Imaging the elusive H-poor gas in the high ADF planetary nebula NGC 6778". In: *The Astrophysical Journal Letters* 824.2 (2016), p. L27.

[33]   J. Garcıéa-Rojas, C. Morisset, D. Jones, R. Wesson, H. M. Boffin, H. Monteiro, R. L. Corradi, and P. Rodrıéguez-Gil. "MUSE spectroscopy of planetary nebulae with high abundance discrepancies". In: *Monthly Notices of the Royal Astronomical Society* 510.4 (2022), pp. 5444–5463.

[34]   J. Garcıéa-Rojas, M. Pena, C. Morisset, A. Mesa-Delgado, and M. T. Ruiz. "Analysis of chemical abundances in planetary nebulae with [WC] central stars-I. Line intensities and physical conditions". In: *Astronomy & Astrophysics* 538 (2012), A54.

[35]   J. Garcıéa-Rojas, M. Peña, C. Morisset, G. Delgado-Inglada, A. Mesa-Delgado, and M. T. Ruiz. "Analysis of chemical abundances in planetary nebulae with [WC] central stars-II. Chemical abundances and the abundance discrepancy factor". In: *Astronomy & Astrophysics* 558 (2013), A122.

[36]   G. Garcıéa-Segura. "Three-dimensional magnetohydrodynamical modeling of planetary nebulae: The formation of jets, ansae, and point-symmetric nebulae via magnetic collimation". In: *The Astrophysical Journal* 489.2 (1997), p. L189.

[37]   G. Garcıéa-Segura, N. Langer, M. Rożyczka, and J. Franco. "Shaping bipolar and elliptical planetary nebulae: effects of stellar rotation, photoionization heating, and magnetic fields". In: *The Astrophysical Journal* 517.2 (1999), p. 767.

[38]   G. Garcıéa-Segura, P. M. Ricker, and R. E. Taam. "Common envelope shaping of planetary nebulae". In: *The Astrophysical Journal* 860.1 (2018), p. 19.

[39]   G. Garcıéa-Segura, R. E. Taam, and P. M. Ricker. "Common envelope shaping of planetary nebulae. II. Magnetic solutions and self-collimated outflows". In: *The Astrophysical Journal* 893.2 (2020), p. 150.

[40]   K. Gesicki, A. Zijlstra, M. Hajduk, and C. Szyszka. "Accelerated post-AGB evolution, initial-final mass relations, and the star-formation history of the Galactic bulge". In: *Astronomy & Astrophysics* 566 (2014), A48.

[41]   K. Gesicki, A. Zijlstra, and C. Morisset. "3D pyCloudy modelling of bipolar planetary nebulae: evidence for fast fading of the lobes". In: *Astronomy & Astrophysics* 585 (2016), A69.

[42]   C. Giammanco, S. E. Sale, R. L. Corradi, M. J. Barlow, K. Viironen, L. Sabin, M. Santander-Garcıéa, D. J. Frew, R. Greimel, B. Miszalski, et al. "IPHAS extinction distances to planetary nebulae". In: *Astronomy & Astrophysics* 525 (2011), A58.

[43]   O. Gonzalez, M. Rejkuba, M. Zoccali, E. Valent, D. Minniti, and R. Tobar. "Reddening and metallicity maps of the Milky Way bulge from VVV and 2MASS-III. The first global photometric metallicity map of the Galactic bulge". In: *Astronomy & Astrophysics* 552 (2013), A110.

[44]   O. A. Gonzalez. *BEAM - Bulge Extinction and Metallicity Calculator*. 2018. URL: https://www.oagonzalez.net/beam-calculator (visited on 05/18/2022).

[45]   S. Górny. "Spectroscopy of southern Galactic disk planetary nebulae-Notes on chemical composition and emission-line stars". In: *Astronomy & Astrophysics* 570 (2014), A26.

[46] S. Górny, C. Chiappini, G. Stasińska, and F. Cuisinier. "Planetary nebulae in the direction of the Galactic bulge: on nebulae with emission-line central stars". In: *Astronomy & Astrophysics* 500.3 (2009), pp. 1089–1108.

[47] S. Górny, G. Stasińska, A. Escudero, and R. Costa. "The populations of planetary nebulae in the direction of the Galactic bulge-Chemical abundances and Wolf-Rayet central stars". In: *Astronomy & Astrophysics* 427.1 (2004), pp. 231–244.

[48] J. Greaves. "Toroidal magnetic fields around planetary nebulae". In: *Astronomy & Astrophysics* 392.1 (2002), pp. L1–L4.

[49] W. Greig. "The morphological classification of symmetrical nebulae." In: *Astronomy and Astrophysics* 10 (1971), pp. 161–174.

[50] W. J. Henney and G. Stasińska. "Can solid body destruction explain abundance discrepancies in planetary nebulae?" In: *The Astrophysical Journal* 711.2 (2010), p. 881.

[51] R. Henry, K. Kwitter, R. Dufour, and J. Skinner. "A multiwavelength analysis of the halo planetary nebula DdDm-1". In: *The Astrophysical Journal* 680.2 (2008), p. 1162.

[52] R. Henry, B. Stephenson, M. M. Miller Bertolami, K. Kwitter, and B. Balick. "On the production of He, C, and N by low-and intermediate-mass stars: a comparison of observed and model-predicted planetary nebula abundances". In: *Monthly Notices of the Royal Astronomical Society* 473.1 (2018), pp. 241–260.

[53] R. B. Henry, K. Kwitter, and B. Balick. "Sulfur, chlorine, and argon abundances in planetary nebulae. IV. synthesis and the sulfur anomaly". In: *The Astronomical Journal* 127.4 (2004), p. 2284.

[54] R. B. Henry, A. Speck, A. I. Karakas, G. J. Ferland, and M. Maguire. "The curious conundrum regarding sulfur abundances in planetary nebulae". In: *The Astrophysical Journal* 749.1 (2012), p. 61.

[55] G. Hromov and L. Kohoutek. "Morphological study of planetary nebulae. I. Observed forms of planetary nebulae". In: *Bulletin of the Astronomical Institutes of Czechoslovakia* 19 (1968), p. 1.

[56] V. Icke. "Blowing bubbles". In: *Astronomy and Astrophysics* 202 (1988), pp. 177–188.

[57] N. Ivanova, S. Justham, X. Chen, O. De Marco, C. Fryer, E. Gaburov, H. Ge, E. Glebbeek, Z. Han, X.-D. Li, et al. "Common envelope evolution: where we stand and how we can move forward". In: *The Astronomy and Astrophysics Review* 21.1 (2013), p. 59.

[58] G. H. Jacoby, T. C. Hillwig, D. Jones, K. Martin, O. De Marco, M. Kronberger, J. L. Hurowitz, A. F. Crocker, and J. Dey. "Binary central stars of planetary nebulae identified with Kepler/K2". In: *Monthly Notices of the Royal Astronomical Society* 506.4 (2021), pp. 5223–5246.

[59] D. Jones and H. M. Boffin. "Binary stars as the key to understanding planetary nebulae". In: *Nature Astronomy* 1.5 (2017), pp. 1–6.

[60] D. Jones, H. M. Boffin, J. Hibbert, T. Steinmetz, R. Wesson, T. C. Hillwig, P. Sowicka, R. L. Corradi, J. Garcıéa-Rojas, P. Rodrıéguez-Gil, et al. "The post-common-envelope binary central star of the planetary nebula PN G283. 7- 05.1-A possible post-red-giant-branch planetary nebula central star". In: *Astronomy & Astrophysics* 642 (2020), A108.

[61] D. Jones, H. M. Boffin, P. Rodrıéguez-Gil, R. Wesson, R. L. Corradi, B. Miszalski, and S. Mohamed. "The post-common envelope central stars of the planetary nebulae Henize 2-155 and Henize 2-161". In: *Astronomy & Astrophysics* 580 (2015), A19.

[62] D. Jones, R. Wesson, J. Garcıéa-Rojas, R. L. Corradi, and H. M. Boffin. "NGC 6778: Strengthening the link between extreme abundance discrepancy factors and central star binarity in planetary nebulae". In: *Monthly Notices of the Royal Astronomical Society* 455.3 (2016), pp. 3263–3272.

[63] H. Jönsson, N. Ryde, M. Schultheis, and M. Zoccali. "Abundances of disk and bulge giants from high-resolution optical spectra-II. O, Mg, Ca, and Ti in the bulge sample". In: *Astronomy & Astrophysics* 598 (2017), A101.

[64] S. Jordan, K. Werner, and S. J. O'Toole. "Discovery of magnetic fields in central stars of planetary nebulae". In: *Astronomy & Astrophysics* 432.1 (2005), pp. 273–279.

[65] J. Kaler. "Electron temperatures in planetary nebulae". In: *The Astrophysical Journal* 308 (1986), pp. 322–336.

[66] F. Kerber, R. Mignani, R. Smart, and A. Wicenec. "Galactic planetary nebulae and their central stars-II. Proper motions". In: *Astronomy & Astrophysics* 479.1 (2008), pp. 155–160.

[67] R. L. Kingsburgh and M. Barlow. "Elemental abundances for a sample of southern galactic planetary nebulae." In: *Monthly Notices of the Royal Astronomical Society* 271 (1994), pp. 257–299.

[68] R. Kippenhahn, A. Weigert, and A. Weiss. *Stellar structure and evolution*. Vol. 192. Springer, 1990.

[69] J. Krtička, J. Kubát, and I. Krtičková. "Stellar wind models of central stars of planetary nebulae". In: *Astronomy & Astrophysics* 635 (2020), A173.

[70] S. Kwok. "Evolution from the Asymptotic Giant Branch to Planetary Nebulae". In: *AIP Conference Proceedings*. Vol. 804. 1. American Institute of Physics. 2005, pp. 187–196.

[71] S. Kwok. "The origin and evolution of planetary nebulae". In: *The origin and evolution of planetary nebulae/Sun Kwok. Cambridge; New York: Cambridge University Press* (2000).

[72] E. Landi, G. Del Zanna, P. Young, K. Dere, H. Mason, and M. Landini. "CHIANTI—an atomic database for emission lines. VII. New data for X-rays and other improvements". In: *The Astrophysical Journal Supplement Series* 162.1 (2006), p. 261.

[73] J. Lattanzio. *Stellar Evolution Tutorial*. 2003. URL: https://sparky.rice.edu/astr350/stellar_evolution/m5z02evoln.html (visited on 07/13/2022).

[74] X.-W. Liu, S.-G. Luo, M. Barlow, I. Danziger, and P. Storey. "Chemical abundances of planetary nebulae from optical recombination lines—III. The Galactic bulge PN M 1-42 and M 2-36". In: *Monthly Notices of the Royal Astronomical Society* 327.1 (2001), pp. 141–168.

[75] X.-W. Liu, P. Storey, M. Barlow, I. Danziger, M. Cohen, and M. Bryce. "NGC 6153: a super-metal-rich planetary nebula?" In: *Monthly Notices of the Royal Astronomical Society* 312.3 (2000), pp. 585–628.

[76]   W. J. Maciel, R. Costa, and M. Uchida. "An estimate of the time variation of the O/H radial gradient from planetary nebulae". In: *Astronomy & Astrophysics* 397.2 (2003), pp. 667–674.

[77]   W. J. Maciel, R. Costa, and T. E. P. Idiart. "Age distribution of the central stars of galactic disk planetary nebulae". In: *Astronomy & Astrophysics* 512 (2010), A19.

[78]   P. Marigo, L. Girardi, M. Groenewegen, and A. Weiss. "Evolution of planetary nebulae-I. An improved synthetic model". In: *Astronomy & Astrophysics* 378.3 (2001), pp. 958–985.

[79]   I. Martinez-Valpuesta and O. Gerhard. "Metallicity gradients through disk Instability: A simple model for the Milky Way's boxy bulge". In: *The Astrophysical Journal Letters* 766.1 (2013), p. L3.

[80]   C. Mendoza. "Recent advances in atomic calculations and experiments of interest in the study of planetary nebulae". In: *Symposium-International Astronomical Union*. Vol. 103. Cambridge University Press. 1983, pp. 143–172.

[81]   C. Mendoza and C. Zeippen. "Transition probabilities for forbidden lines in the 3 p 2 configuration–II." In: *Monthly Notices of the Royal Astronomical Society* 199.4 (1982), pp. 1025–1032.

[82]   G. Nandakumar, N. Ryde, M. Schultheis, B. Thorsbro, H. Jönsson, P. Barklem, R. M. Rich, and F. Fragkoudi. "Chemical characterization of the inner Galactic bulge: North–South symmetry". In: *Monthly Notices of the Royal Astronomical Society* 478.4 (2018), pp. 4374–4389.

[83]   M. Ness, K. Freeman, E. Athanassoula, E. Wylie-de-Boer, J. Bland-Hawthorn, M. Asplund, G. F. Lewis, D. Yong, R. Lane, L. Kiss, et al. "ARGOS–IV. The kinematics of the Milky Way bulge". In: *Monthly Notices of the Royal Astronomical Society* 432.3 (2013), pp. 2092–2103.

[84]   J. J. Nishiyama. *An Introduction to Planetary Nebulae*. Morgan & Claypool Publishers California, 2018.

[85]   S. Ortolani, A. Renzini, R. Gilmozzi, G. Marconi, B. Barbuy, E. Bica, and R. M. Rich. "Near-coeval formation of the Galactic bulge and halo inferred from globular cluster ages". In: *nature* 377.6551 (1995), pp. 701–704.

[86]   D. E. Osterbrock and G. J. Ferland. *Astrophysics of gaseous nebulae and active galactic nuclei, 2nd*. 2006.

[87]   B. Paczynski. "Evolution of single stars. VI. Model nuclei of planetary nebulae". In: *Acta Astronomica* 21 (1971), p. 417.

[88]   Q. A. Parker, A. Acker, D. J. Frew, M. Hartley, A. E. Peyaud, F. Ochsenbein, S. Phillipps, D. Russeil, S. F. Beaulieu, M. Cohen, et al. "The macquarie/AAO/Strasbourg Hα planetary nebula catalogue: MASH". In: *Monthly Notices of the Royal Astronomical Society* 373.1 (2006), pp. 79–94.

[89]   Q. A. Parker, I. S. Bojicic, and D. J. Frew. "HASH: the Hong Kong/AAO/Strasbourg Hα planetary nebula database". In: *J. Phys. Conf. Ser.* Vol. 728. 2016, p. 032008.

[90]   M. Peimbert and S. Torres-Peimbert. "Type I planetary nebulae". In: *Symposium-International Astronomical Union*. Vol. 103. Cambridge University Press. 1983, pp. 233–242.

[91] R. Porter, G. J. Ferland, P. Storey, and M. Detisch. "Improved He I emissivities in the case B approximation". In: *Monthly Notices of the Royal Astronomical Society: Letters* 425.1 (2012), pp. L28–L31.

[92] S. Pottasch. "Planetary Nebulae: A Study of Late Stages of Stellar Evolution (Dordrecht, Boston, Lancaster: D. Reidel)". In: (1984).

[93] A. Pradhan. "Collision Strengths For [O ii] and [S ii]". In: *Monthly Notices of the Royal Astronomical Society* 177.1 (1976), pp. 31–38.

[94] I. Ramıérez, C. A. Prieto, and D. L. Lambert. "Oxygen abundances in nearby FGK stars and the galactic chemical evolution of the local disk and halo". In: *The Astrophysical Journal* 764.1 (2013), p. 78.

[95] C. Ramsbottom, K. Bell, and F. Keenan. "Effective collision strengths for fine-structure forbidden transitions among the 3s23p3 levels of Ar IV". In: *Monthly Notices of the Royal Astronomical Society* 284.3 (1997), pp. 754–760.

[96] M. Ratag, S. Pottasch, M. Dennefeld, and J. Menzies. "Abundances in planetary nebulae near the galactic centre-I. Abundance determinations". In: *Astronomy and Astrophysics Supplement Series* 126.2 (1997), pp. 297–310.

[97] B. Rees and A. Zijlstra. "Alignment of the angular momentum vectors of planetary nebulae in the Galactic Bulge". In: *Monthly Notices of the Royal Astronomical Society* 435.2 (2013), pp. 975–991.

[98] B. Rees. *A study of planetary nebulae in and towards the Galactic Bulge*. The University of Manchester (United Kingdom), 2011.

[99] M. G. Richer, J. A. López, M. T. Garcıéa-Dıéaz, D. M. Clark, M. Pereyra, and E. Dıéaz-Méndez. "The Evolution of the Kinematics of Nebular Shells in Planetary Nebulae in the Milky Way Bulge". In: *The Astrophysical Journal* 716.1 (2010), p. 857.

[100] A. Ritter and Q. A. Parker. "A Preferred Orientation Angle for Bipolar Planetary Nebulae". In: *Galaxies* 8.2 (2020), p. 34.

[101] A. Rojas-Arriagada, A. Recio-Blanco, V. Hill, P. De Laverny, M. Schultheis, C. Babusiaux, M. Zoccali, D. Minniti, O. Gonzalez, S. Feltzing, et al. "The Gaia-ESO Survey: metallicity and kinematic trends in the Milky Way bulge". In: *Astronomy & Astrophysics* 569 (2014), A103.

[102] A. Rojas-Arriagada, G. Zasowski, M. Schultheis, M. Zoccali, S. Hasselquist, C. Chiappini, R. E. Cohen, K. Cunha, J. G. Fernández-Trincado, F. Fragkoudi, et al. "How many components? Quantifying the complexity of the metallicity distribution in the Milky Way bulge with APOGEE". In: *Monthly Notices of the Royal Astronomical Society* 499.1 (2020), pp. 1037–1057.

[103] C. Rola and D. Pelat. "On the estimation of intensity for low S/N ratio narrow emission lines". In: *Astronomy and Astrophysics* 287 (1994), pp. 676–684.

[104] F. Ruiz-Escobedo and M. Peña. "Abundance discrepancy factors in high-density planetary nebulae". In: *Monthly Notices of the Royal Astronomical Society* 510.4 (2022), pp. 5984–6000.

[105] L. Sabin, A. A. Zijlstra, and J. Greaves. "Magnetic fields in planetary nebulae and post-AGB nebulae". In: *Monthly Notices of the Royal Astronomical Society* 376.1 (2007), pp. 378–386.

[106]   L. Sabin, Q. A. Parker, R. M. Corradi, L. Guzman-Ramirez, R. Morris, A. A. Zijlstra, I. S. Bojičić, D. J. Frew, M. Guerrero, M. Stupar, et al. "First release of the IPHAS catalogue of new extended planetary nebulae". In: *Monthly Notices of the Royal Astronomical Society* 443.4 (2014), pp. 3388–3401.

[107]   R. Sahai, M. R. Morris, and G. G. Villar. "Young planetary nebulae: Hubble Space Telescope imaging and a new morphological classification system". In: *The Astronomical Journal* 141.4 (2011), p. 134.

[108]   R. K. Saito, M. Zoccali, A. McWilliam, D. Minniti, O. A. Gonzalez, and V. Hill. "Mapping the X-shaped Milky Way bulge". In: *The Astronomical Journal* 142.3 (2011), p. 76.

[109]   M. Santander-Garcıéa, D. Jones, J. Alcolea, R. Wesson, and V. Bujarrabal. "The missing mass conundrum of post-common-envelope planetary nebulae". In: *arXiv preprint arXiv:1810.09296* (2018).

[110]   D. Schönberner, R. Jacob, H. Lehmann, G. Hildebrandt, M. Steffen, A. Zwanzig, C. Sandin, and R. Corradi. *A hydrodynamical study of multiple-shell planetary nebulae*. 2014.

[111]   H. Schwarz, R. Corradi, and J. Melnick. "A catalogue of narrow band images of planetary nebulae". In: *Astronomy and Astrophysics Supplement Series* 96 (1992), pp. 23–113.

[112]   P. Scott, N. Grevesse, M. Asplund, A. J. Sauval, K. Lind, Y. Takeda, R. Collet, R. Trampedach, and W. Hayek. "The elemental composition of the Sun-I. The intermediate mass elements Na to Ca". In: *Astronomy & Astrophysics* 573 (2015), A25.

[113]   R. A. Shaw. "Shape, structure, and morphology in planetary nebulae". In: *Proceedings of the International Astronomical Union* 7.S283 (2011), pp. 156–163.

[114]   L. S. Shore. *Growing Up A Star*. 2011. URL: http://www.exo.net/~pauld/ workshops/Stars/HR$%5C%$20Diagram.pdf (visited on 07/13/2022).

[115]   C. L. Smith, A. A. Zijlstra, K. M. Gesicki, and H. L. Dinerstein. "Abundances in Galactic bulge planetary nebulae from optical, ultraviolet and infrared observations". In: *Monthly Notices of the Royal Astronomical Society* 471.3 (2017), pp. 3008–3018.

[116]   P. Sowicka, D. Jones, R. L. Corradi, R. Wesson, J. Garcıéa-Rojas, M. Santander-Garcıéa, H. M. Boffin, and P. Rodrıéguez-Gil. "The planetary nebula IC 4776 and its post-common-envelope binary central star". In: *Monthly Notices of the Royal Astronomical Society* 471.3 (2017), pp. 3529–3546.

[117]   L. Stanghellini, R. L. Corradi, and H. E. Schwarz. "The correlations between planetary nebula morphology and central star evolution". In: *Astronomy and astrophysics* 279 (1993), pp. 521–528.

[118]   G. Stasinska, M. Richer, and M. McCall. "The planetary nebulae populations in five galaxies: abundance patterns and evolution". In: *Astronomy and Astrophysics* 336 (1998), pp. 667–681.

[119]   P. Storey and C. Zeippen. "Theoretical values for the [O III] 5007/4959 line-intensity ratio and homologous cases". In: *Monthly Notices of the Royal Astronomical Society* 312.4 (2000), pp. 813–816.

[120]   N. Strobel. *Astronomy Notes*. 2020. URL: https://www.e-education.psu.edu/ astro801/book/export/html/1756 (visited on 07/13/2022).

[121]   Y. Terzian. *Planetary nebulae: observations and theory*. Vol. 76. Springer Science & Business Media, 1978.

[122]   *The MPIfR's Survey Samplers*. 2020. URL: http://www.mpifr-bonn.mpg.de/survey.html (visited on 07/13/2022).

[123]   Y. Tsamis, J. Walsh, J. Vıélchez, and D. Péquignot. "Chemical abundances in the protoplanetary disc LV 2 (Orion): clues to the causes of the abundance anomaly in H II regions". In: *Monthly Notices of the Royal Astronomical Society* 412.2 (2011), pp. 1367–1380.

[124]   R. Tylenda, N. Siódmiak, S. Górny, R. Corradi, and H. Schwarz. "Angular dimensions of planetary nebulae". In: *Astronomy & Astrophysics* 405.2 (2003), pp. 627–637.

[125]   E. Valenti, M. Zoccali, O. Gonzalez, D. Minniti, J. Alonso-Garcıéa, E. Marchetti, M. Hempel, A. Renzini, and M. Rejkuba. "Stellar density profile and mass of the Milky Way bulge from VVV data". In: *Astronomy & Astrophysics* 587 (2016), p. L6.

[126]   H. Van Winckel. "Post-AGB stars". In: *Annual Review of Astronomy and Astrophysics* 41.1 (2003), pp. 391–427.

[127]   W. Vlemmings. "Magnetic fields around AGB stars and Planetary Nebulae". In: *Proceedings of the International Astronomical Union* 9.S302 (2013), pp. 389–397.

[128]   W. Wang and X.-W. Liu. "Elemental abundances of Galactic bulge planetary nebulae from optical recombination lines". In: *Monthly Notices of the Royal Astronomical Society* 381.2 (2007), pp. 669–701.

[129]   W. Weidmann, R. Gamen, D. Mast, C. Fariña, G. Gimeno, E. O. Schmidt, R. Ashley, L. P. de Arriba, P. Sowicka, and I. Ordonez-Etxeberria. "Towards an improvement in the spectral description of central stars of planetary nebulae". In: *Astronomy & Astrophysics* 614 (2018), A135.

[130]   W. Weidmann and R. Gamen. "Central stars of planetary nebulae: New spectral classifications and catalogue". In: *Astronomy & Astrophysics* 526 (2011), A6.

[131]   W. Weidmann, M. Mari, E. Schmidt, G. Gaspar, M. Bertolami, A. Oio, L. Gutiérrez-Soto, M. Volpe, R. Gamen, and D. Mast. "Catalogue of central stars of planetary nebulae: Expanded edition". In: *arXiv preprint arXiv:2005.10368* (2020).

[132]   R. Wesson, D. Jones, J. Garcıéa-Rojas, H. Boffin, and R. Corradi. "Confirmation of the link between central star binarity and extreme abundance discrepancy factors in planetary nebulae". In: *Monthly Notices of the Royal Astronomical Society* 480.4 (2018), pp. 4589–4613.

[133]   R. Wesson, D. Stock, and P. Scicluna. "Understanding and reducing statistical uncertainties in nebular abundance determinations". In: *Monthly Notices of the Royal Astronomical Society* 422.4 (2012), pp. 3516–3526.

[134]   R. Wesson. "ALFA: An automated line fitting algorithm". In: *Monthly Notices of the Royal Astronomical Society* 456.4 (2016), pp. 3774–3781.

[135]   R. Wesson. *Ranked values of the abundance discrepancy*. https://nebulousresearch.org/adfs/. Accessed: 2022-07-02.

[136]   R. Wesson, M. J. Barlow, R. L. Corradi, J. E. Drew, P. J. Groot, C. Knigge, D. Steeghs, B. T. Gänsicke, R. Napiwotzki, P. Rodriguez-Gil, et al. "A planetary nebula around Nova

V458 Vulpeculae undergoing flash ionization". In: *The Astrophysical Journal* 688.1 (2008), p. L21.

[137] B. E. Westerlund and K. G. Henize. "Dimensions of southern planetary nebulae". In: *The Astrophysical Journal Supplement Series* 14 (1967), p. 154.

[138] P. Young, G. Del Zanna, E. Landi, K. Dere, H. Mason, and M. Landini. "CHIANTI—an atomic database for emission lines. VI. Proton rates and other improvements". In: *The Astrophysical Journal Supplement Series* 144.1 (2003), p. 135.

[139] H.-B. Yuan, X.-W. Liu, D. Péquignot, R. Rubin, B. Ercolano, and Y. Zhang. "Three-dimensional chemically homogeneous and bi-abundance photoionization models of the 'super-metal-rich' planetary nebula NGC 6153". In: *Monthly Notices of the Royal Astronomical Society* 411.2 (2011), pp. 1035–1052.

[140] G. Zasowski, M. Schultheis, S. Hasselquist, K. Cunha, J. Sobeck, J. Johnson, A. Rojas-Arriagada, S. R. Majewski, B. Andrews, H. Jönsson, et al. "APOGEE DR14/DR15 abundances in the inner Milky Way". In: *The Astrophysical Journal* 870.2 (2019), p. 138.

[141] C. Zeippen. "Transition probabilities for forbidden lines in the 2 p 3 configuration". In: *Monthly Notices of the Royal Astronomical Society* 198.1 (1982), pp. 111–125.

[142] C. Zeippen, K. Butler, and J. Le Bourlot. "Effective collision strengths for fine-structure forbidden transitions in the 3p3 configuration of AR IV". In: *Astronomy and Astrophysics* 188 (1987), pp. 251–257.

[143] M. Zoccali, V. Hill, A. Lecureur, B. Barbuy, A. Renzini, D. Minniti, A. Gómez, and S. Ortolani. "The metal content of bulge field stars from FLAMES-GIRAFFE spectra-I. Stellar parameters and iron abundances". In: *Astronomy & Astrophysics* 486.1 (2008), pp. 177–189.

[144] M. Zoccali, A. Lecureur, B. Barbuy, V. Hill, A. Renzini, D. Minniti, Y. Momany, A. Gómez, and S. Ortolani. "Oxygen abundances in the Galactic bulge: evidence for fast chemical enrichment". In: *Astronomy & Astrophysics* 457.1 (2006), pp. L1–L4.